Recrystallization, abnormal grain growth and ultrafine microstructure of ODS ferritic steels

Nicolas Sallez

UNIVERSITÉ DE GRENOBLE

THÈSE

Pour obtenir le grade de

DOCTEUR DE L'UNIVERSITÉ DE GRENOBLE

Spécialité : **Ingénierie Matériaux Mécanique Energétique Environnement Procédé Production**

Arrêté ministériel : 7 août 2006

Présentée par

Nicolas SALLEZ

Thèse dirigée par **Yves BRECHET** et
codirigée par **Patricia DONNADIEU**

préparée au sein du **Laboratoire de Sciences et Ingénierie des Matériaux et des Procédés (SIMaP)**
dans **l'École Doctorale Ingénierie – Matériaux Mécanique Énergétique Environnement Procédés Production (I-MEP2)**

Recrystallization, abnormal grain growth and ultrafine microstructure of ODS ferritic steels

Thèse soutenue publiquement le **19 décembre 2014**,
devant le jury composé de :

Mme Martine BLAT-YRIEIX
Ingénieur EDF Les Renardières, Co-encadrant
M. Andras BORBELY
Professeur à l'Ecole des Mines de Saint Etienne, Président
M. Yves BRECHET
Professeur à Grenoble-INP, Directeur
M. Yann de CARLAN
Ingénieur CEA Saclay, Examinateur
Mme Patricia DONNADIEU
Directeur de recherche à Grenoble INP, Co-directeur
Mme Anne-Françoise GOURGUES-LORENZON
Professeur à l'Ecole des Mines de Paris, Rapporteur
M. Roland LOGE
Professeur à l'Ecole Polytechnique Fédérale de Lausanne, Rapporteur

Remerciements

Si quelqu'un m'avait demandé 4 ans plus tôt si j'envisageais de faire une thèse, je lui aurais probablement demandé ce qui lui passait par la tête… Pourtant aujourd'hui, force est de constater que j'ai vécu une expérience que je ne renierais pour rien au monde, heureux et fier d'avoir participé à cette aventure, je tiens à remercier tous ceux qui, de près ou de loin, y ont pris part !

Tout d'abord, je voudrais remercier Andras Borbèly qui m'a fait l'honneur d'assurer la présidence du jury de thèse ainsi qu'Anne-Françoise Gourgues-Lorenzon et Roland Loge qui ont eu la lourde tâche de rapporter mon travail. Merci, pour l'attention avec laquelle vous avez lu ce manuscrit et pour vos remarques constructives.

A mon arrivée, le premier jour de mon contrat, la première phrase d'Yves fut « Ah tu tombes bien j'ai un jury de thèse sur les aciers ODS demain matin, on prend le train de 5h30 à la gare Grenoble ! ». Malgré un emploi du temps infernal, tu as toujours su te rendre disponible (souvent le week-end !), merci pour ta confiance, pour tes conseils et tes idées qui ont constamment rehaussé l'intérêt de ces travaux et pour tes encouragements constants. Nos régulières discussions tant scientifiques, qu'historiques et politiques du dimanche matin resteront pour moi un moment privilégié.
S'il est une personne que je dois remercier c'est bien ma co-directrice de thèse. Durant ces trois ans tu as été un soutien sans faille, toujours à l'écoute, toujours disponible, proposant de nouvelles idées et trouvant des arguments supplémentaires pour en soutenir d'autres. Merci pour ta bonne humeur et ton enthousiasme quotidien qui ont porté ces trois années de thèses et pour la confiance que tu m'as témoigné. Je garderais la théorie du raisonnement par l'escalier comme la base de toute réflexion !
Je tiens à remercier Martine, ma co-encadrante de thèse pour EDF, et Frédéric Delabrouille, votre implication dans mon travail ainsi que vos précieux conseils au cours des réunions d'avancement m'ont permis de ne pas trop m'éloigner du cadre industriel et de garder en tête la finalité du projet. Merci à tous les deux, ce fut un plaisir de travailler ensemble ces trois années.
Un grand merci également à Yann qui a suivit cette thèse pour le CEA, et dont le scepticisme bienveillant m'a poussé à aller toujours plus loin dans la rigueur de mon travail. Les macarons du dimanche matin, après une semaine de sommeil tout relatif au synchrotron resterons comme l'une de mes expérience gustative les plus réussies !

Une thèse c'est une histoire de rencontre et de gens qui acceptent de vous ouvrir leur porte et de vous faire partager leur connaissances. A ce titre, je dois une reconnaissance toute particulière à Andras, qui, sans faire parti de l'encadrement de cette thèse, m'a

accompagné tout au long de celle-ci au travers de son expertise dans le domaine de la diffraction rayons X. Les travaux présentés dans ce manuscrit lui doivent beaucoup et notamment les résultats obtenus au synchrotron. Andras, merci pour ta patience et pour tes lumières !

A ce titre, mes remerciements vont également à toute l'équipe du laboratoire de microscopie électronique et de spectroscopie du KIT, et notamment à Christian et Eglantine pour l'accueil chaleureux qu'ils nous ont réservé à chacune de nos visites. Les discussions de microscopie que nous avons eues à Karlsruhe comptent parmi les expériences les plus enrichissantes de cette thèse. Merci également à Robby et Delphine pour la qualité des lames FIB qu'ils ont préparé.

Merci à Laurent et Dominique de m'avoir ouvert les portes du laboratoire de microscopie du MAI d'EDF et pour les quelques discussions que nous avons pu partager.

Des remerciements sont également dus à Jean-Luc Béchade du service SRMA du CEA, tant pour sa participation active à notre manip synchrotron que pour son soutien et sa bienveillance constante durant la thèse. Je remercie également Joël, Laurent et Denis pour la préparation des échantillons analysés au cours de cette thèse.

Je retiendrais également les conseils avisés qui m'ont été donnés et les discussions passionnantes que j'ai eues avec Joël, Denis, Bertrand et Frédéric dans le cadre du CPR. Je remercie également tous les thésards du CPR ODISSEE pour leur bonne humeur lors de notre rencontres et notamment Constantin, Caroline, Thomas, Yann, Anne-Laure, Marie, Arun et Hubert. Je remercie tous les membres du CPR ODISSEE.

Le laboratoire MATEIS a lui aussi été un partenaire majeur de cette thèse. En effet, non seulement la partie modélisation écrite dans ce manuscrit doit tout ou presque à Mohammad Abdur Razzak qui m'a permis d'entrer dans la logique de la simulation « AGG-Preciso » qui a été reprise ici et avec qui les discussions sur la croissance anormale ont été riches ! Mais également à Michel Perez et Damien Fabregue qui ont accompagné et agrémenté les discussions sur l'étude de la croissance anormale de leurs avis éclairés. Egalement membre du laboratoire MATEIS et ancien camarade de Phelma, j'ai eu la chance de nouer un partenariat privilégié avec Xavier Boulnat. Durant ces trois années, nous avons pu réaliser ensemble une manip synchrotron inédite. Curieux et motivé, je ne compte plus le nombre de soirées passées ensemble à exploiter les résultats de la manip et à discuter de métallurgie avec un fond musical premium ! Un grand merci à toi, sans ces moments partagés, il est évident que le manuscrit qui suit serait bien moins abouti.

Je voudrais remercier toute l'équipe de la ligne Diffabs du synchrotron SOLEIL, pour l'accueil dans leur local et notamment Dominique Thiaudière et Cristian Mocuta dont l'expertise en Macro Imagej s'est relevée précieuse.

J'adresse également mes remerciements à l'équipe de ILL, à Charles Dewhurtz ainsi qu'à David Bowyer pour la petite visite guidée du réacteur. Merci à Frédéric de Gueuser et Laurent qui m'ont littéralement pris dans leurs bagages sur cette manip.

Durant cette thèse, j'ai également eu la chance de rencontrer de nombreux thésards européens avec lesquels j'ai pu collaborer sur le développement des aciers ODS. Je tiens ici a remercier particulièrement Marta Serrano pour l'organisation de l'école Muneco ainsi que Mickael Gorley et Isabell Hilger (si si les Daft Punk sont bien français !) pour l'organisation du Workshop ODISSEUS.

J'en arrive maintenant à la racine de la thèse, à l'entité sans laquelle rien de ce qui est rédigé plus haut n'est possible. Il s'agit du laboratoire SIMaP et de l'université Grenoble – Alpes. Je tiens à remercier en premier lieu les gestionnaires, qui ont toujours fait en sorte que les missions, conférences, déplacements, inscriptions et démarches en tout genre soient possible même quand le délais qui leur été laissé pour le faire était…disons court ! Alors un grand merci à Virginie et à Jacqueline pour sa bonne humeur et sa réactivité, ainsi qu'à Natalie, Sani, Pascale et Sylvie. J'y ajoute un remerciement particulier à Augustine de l'école doctorale. Merci à Michel Pons de m'avoir accueilli au sein du laboratoire, et à Alexis au sein du groupe Physique du Métal (Quel responsable de groupe amène des thésards faire du canyoning entre 12h et 14h !?).
Plus généralement j'aimerais remercier tous les permanents du groupe PM, eux qui nous ont fait une petite place parmi eux durant ces trois ans. Notamment Frédéric de Gueuser, qui, avec Alexis ont pris le temps de m'inculquer les bases de la diffusion aux petits angles, Muriel qui m'a transmis le virus ASTAR et qui, lorsqu'elle entre par hasard dans une salle de microscopie peut d'un seul coup transformer une séance qui semblait perdue en un moment passionnant ! Merci donc pour ces gros coup de main ponctuels et votre bonne humeur. Mais également Marc V., Fabien, Fredéric L., Marie C., Bruno G., Catherine qui va pouvoir se reposer après avoir couru trois ans après Fanny, Marc M., François avec qui j'ai partagé quelques footings appuyés !, Marc de B., Mireille, Guillaume B., Valentina et Roberta, Gilles et Raphael. Un grand merci également à toute l'équipe de techniciens qui se plient en quatre pour répondre comme ils peuvent à nos demandes pas toujours évidentes et au premier rang desquels Magali leur cheftaine, un merci tout particulier à Alain D., l'inoxydable, l'âme du labo, sans oublier Bruno M., Jean-Louis, Colin, Roman, Stéphane, Julien, Thomas, Alain Mouny et Yannick a qui je dois beaucoup puisqu'en juillet dernier il a miraculeusement ramené mon ordinateur à la vie ! Le SIMaP peut également compter sur une équipe de caractérisation très complète, le CMTC, que je tiens remercier vivement pour leur soutien pendant ma thèse. Stéphane qui m'a présenté la DRX, Alexandre le spécialiste microsonde, Florence l'experte EBSD, et bien sûr Fréderic et Francine pour leurs précieux conseils au MEB. Je remercie également Cécile et Adam mes deux stagiaires qui ont grandement contribués à la partie expérimentale de la thèse.
Si cette thèse a été une aventure humaine formidable, c'est en grande partie grâce aux nombreux thésards qui s'y sont succédés. Bien sûr, honneur aux anciens qui nous ont confié la tâche de perpétuer les quelques traditions du labo et notamment l'immanquable

tarot de midi, la raclette de noël ou encore les barbecues de printemps ! Merci à Guilhem, notre rugbymen, pour ces conseils sur les cartos EBSD et sur le polissage, Jean-Marie notre breton, Quentin, le sage et le lève tôt, Thomas l'un des pilier du groupe parti en Australie, mais également Coraly, Romain, Souad, Christophe et Benjamin. J'ai eu le plaisir pendant ces trois années de partager mon bureau avec Fanny qui ne s'est pas arrêtée une seconde pendant ces trois ans toujours à fond au boulot ou pendant les footings, et Audrey qui m'a fait découvrir les joies d'un thé bien chaud le matin agrémenté de quelques petits gâteaux, merci à elles de m'avoir supporté et soutenu ! Laurent, sur qui j'ai pu compter en toute occasion, je me demande encore comment le labo tournera sans toi ! Qingquan toujours de bonne humeur, Simon et Maxime les deux professeurs en devenir ! Dan et Olivier, le savoyard pur jus. Puis Eva est arrivée, rigueur et douceur version allemande, puis Kitty, Mahmoud, Hasan et Rosen, l'international du groupe, une constellation de pays à lui tout seul. Plus récemment, sont arrivés Solène, Alexis, Martin et Nadia, j'espère qu'ils prendront autant de plaisir que moi pendant leur thèse.

Plus personnellement, je remercie ma famille, mon frère, ma sœur et ma mère qui sont venus aujourd'hui, qui me soutiennent depuis toujours et sans qui je ne serais pas là. Je veux remercier également Yannick, Christine, Emilie et Damien, leur présence aujourd'hui me touche énormément. Merci à Grégoire et Julie ainsi qu'à Guillaume et Apolline d'avoir fait le déplacement pour être là !

Enfin, je remercie tout particulièrement ma plus belle moitié, Mélanie, qui m'a soutenue tout au long de cette thèse et plus encore pendant ce retour dans les années cinquante qu'elle m'a offert pour ce dernier mois et demi de rédaction !!

Content

Symbol list

Γ is the Line tension of a dislocation (energy per unit length stored by a single dislocation)

μ is the shear modulus

ν is the Poisson's ratio

φ is the angle between Burgers vector and the line vector of the dislocation

R_e is the upper cut off radius of a dislocation

R_0 is the inner cut off radius of a dislocation

ρ is the overall dislocation density

ρ_{GND} is the geometrically necessary dislocation density

b is the Burgers' vector modulus

γ_S is the specific energy of a subgrain boundary

γ is the specific energy of a grain boundary

γ_p is the specific interfacial energy between matrix and precipitate

γ_m, θ_m are the parameters of the normalized form of Read Shockley relation

G is the activation energy

V is the activation volume

M_{sg}, M_0 Are respectively the subgrain and the intrinsic mobility

D_S is the coefficient of self diffusion.

α is an interaction factor

v_{sg} is the growth rate of the subgrain

$\dot{G}$ the linear grain growth rate

$\dot{N}$ the nuclei formation rate

F_V is the precipitate volume fraction

k_s and k_v are respectively a geometrical and a volume factor

$\alpha_0$the amplification factor for pinning at special location

d_a is the closest interatomic spacing

Q_0 is the invariant

q is the module of the scattering vector

$\Delta\boldsymbol{\rho}$ is the electronic contrast

$\boldsymbol{C}$ is the contrast factor of dislocations

$\boldsymbol{\varepsilon}$ is the distortion parameter

$\boldsymbol{L}$ is the Fourier series parameter

$\boldsymbol{Q_c}$ is the correlation index

$\boldsymbol{\alpha_T}$ is the dislocation density tensor

$\Delta\boldsymbol{\theta}$ is the neighbouring misorientation

$\boldsymbol{\beta^{el}}$ is the elastic distortion tensor

$\boldsymbol{\epsilon^{el}}$ is the elastic strain tensor

$\boldsymbol{g}$ is a tensor accounting for local rotations

$\Delta\boldsymbol{q}$ is the smallest disorientation between two neighbouring points among all the possible crystal symmetries

$\boldsymbol{m_V}$ is the grain surface curvature

$\boldsymbol{\vartheta_1}$ and $\boldsymbol{\vartheta_2}$ are the principal radii of curvature

$\boldsymbol{K_{gar}}$ is the grain aspect ratio coefficient

$\boldsymbol{f_z}$ is the elementary force exerted by a particle on a grain boundary

$\boldsymbol{\rho_{eff}}$ is the compact efficiency factor

$\boldsymbol{\lambda_{ab}}, \boldsymbol{\lambda_n}$ are geometric factors

$\boldsymbol{\lambda_p}$ is the ratio between the projected surface over the actual surface of the normal grain

$\Delta\boldsymbol{G}^*$ is the driving force for precipitation

$\boldsymbol{k_b}$ is the Boltzmann constant

$\boldsymbol{N_0}$ is the number of nucleation sites per unit volume

$\boldsymbol{Z}$ is the Zeldovich factor

$\boldsymbol{\beta}^*$ is the condensation rate of solute atoms

$\boldsymbol{\tau}$ is the incubation time

$\boldsymbol{R}^*$ is the critical radius for stable precipitates

$\boldsymbol{K_s}$. is the solubility product

$\boldsymbol{\alpha_r}$ is the ratio of matrix to precipitate atomic volumes

Résumé étendu en français

Contexte et objectifs

Le développement économique sans précédent du XXème siècle a permis d'établir une corrélation entre l'accès à l'énergie et l'amélioration des conditions de vie des populations. Néanmoins, en ce début de siècle nouveau, cette course effrénée à l'énergie nous rattrape par ces effets collatéraux. En effet, les émissions produites par les usines (parfois mobiles) de productions d'énergie ont profondément modifié notre écosystème et menacent aujourd'hui de provoquer de graves crises environnementales.

Dans ce contexte ou l'énergie apparait à la fois comme une nécessité pour améliorer les conditions de vie de la population, mais qui, dans le même temps, constitue une menace environnementale globale, l'énergie nucléaire apparait comme étant une partie prépondérante de la solution. En effet, depuis plus de 40 ans, l'énergie nucléaire a démontrée sa capacité à être une source fiable et économique d'électricité tout limitant considérablement l'émission de gaz à effet de serre. Néanmoins, pour éviter de n'être qu'une politique du pire et de remplacer un désastre écologique annoncé par un autre désastre écologique que nous laisserions en héritage, il convient de limiter les risques, extrêmement important, associées à cette énergie.

C'est ce que propose le projet ASTRID (Advanced Sodium Technological Reactor for Industrial Demonstration). La conception de ce réacteur permet de résoudre de nombreux problèmes liés à l'énergie nucléaire :

- En utilisant des neutrons rapides, le réacteur ASTRID permettra de recycler, en tant que combustible, une large proportion du stock actuel de déchets nucléaires composé principalement d'uranium 238 et de Plutonium 239. Cela permet non seulement d'augmenter considérablement la quantité d'uranium disponible à long terme mais également de ferme le cycle combustible.
- En consommant le plutonium 239, il limite la prolifération des matières fissiles.
- Enfin, en fonctionnant à haute température, il améliore la efficacité énergétique par rapport aux actuels Réacteur à Eau Pressurisée (REP).

D'un point de vue matériau, cela impose deux contraintes majeures pour la première barrière de confinement du réacteur : les gaines combustible. Tout d'abord, il leur faudra une meilleure résistance au gonflement sous irradiation, puisque le flux neutronique souhaité atteindra $6.0.10^{15}$ $n.cm^{-2}.s^{-1}$ pour une durée de vie allant jusqu'à 8 ou 10 ans. Cela signifie que les dommages d'irradiation subis par le matériaux dépasserons les 150 dpa. Ensuite, il devra également avoir une bonne résistance à haute température, avec une température de fonctionnement retenue pour les gaines de combustible est d'environ 650°C. Les matériaux utilisés pour les gaines combustible dans les REP (qui constituent

l'intégralité du parc nucléaire français aujourd'hui en fonctionnement), des alliages de Zirconium, n'ont pas une résistance mécanique suffisante à haute température pour pouvoir être utilisés. Les aciers austénitiques ont eux un gonflement sous irradiation trop important alors que les aciers ferritiques, qui ont une bonne résistance au gonflement sous irradiation n'ont pas la résistance au fluage à haute température attendue.

La solution matériau envisagée est d'utiliser un acier dit ODS (Oxide Dispersion Strengthened) qui combine à la fois l'avantage d'avoir un faible gonflement sous irradiation grâce à la matrice BCC de l'acier ferritique avec une très bonne tenu au fluage à haute température due à une dispersion de nano-oxydes d'yttrium. Lors de son élaboration, des poudres aciers ferritiques sont cobroyées avec des poudres d'oxyde d'yttrium afin de faire passer l'yttrium en solution solide dans le matériau et d'obtenir ainsi une précipitation homogène lors du recuit de consolidation. La poudre broyée est ensuite dégazée afin de limiter les pollutions dues au cobroyage, puis, portée à 1100°C, sa température de consolidation. La fabrication est ensuite terminée par une consolidation par extrusion à chaud et un laminage à pas de pèlerin (à froid). Ce processus d'élaboration particulier mène à une microstructure singulière. En effet, après la montée en température à 1100°C, le mécanisme de recrystallisation engendre une microstructure granulaire fortement bimodale. Pendant l'extrusion, les grains les plus gros deviennent extrêmement anisotropes. Cette microstructure est particulièrement néfaste pour les propriétés mécaniques transverses du matériau qui sont pourtant celles qui seront soumises à la pression exercée par les gaz de fission libérés dans la gaine lors des réactions nucléaires.

Cette thèse porte donc sur l'étude des mécanismes de recrystallisation des aciers ODS ferritiques menant à la croissance anormale. Elle se divise en trois parties :

- La caractérisation et la compréhension qualitative et quantitative de l'évolution de la microstructure pendant les phases de recuit du matériau. Cette partie a nécessité la mise en place de méthodes spécifiques de caractérisation, notamment en matière de Diffraction des Rayons X (DRX) et de Microscopie Electronique à Transmission (MET).
- En s'appuyant sur les résultats obtenus dans la partie précédente, réaliser une modélisation permettant de déterminer le type de croissance de la structure granulaire (homogène, normale : tous les grains croissent à la même vitesse ; ou hétérogène, anormale : certains grains croissent beaucoup plus rapidement que d'autres).
- Une dernière partie sera consacrée à l'étude de la pertinence des résultats obtenus précédemment dans le cadre de produits finis et à l'étude plus particulière de l'interaction entre joints de grains et précipités dans les aciers ODS ferritiques.

Au terme de cette étude, l'objectif est d'être en mesure de proposer des solutions concrètes afin de maîtriser la microstructure des aciers ODS lors de leur élaboration et de limiter l'anisotropie microstructurale qui en découle aujourd'hui tout en préservant les propriétés mécaniques adéquates.

Evolution microstructurale de la poudre

Afin de comprendre les conditions de la mise en place de la microstructure anormale, une étude de l'évolution microstructurale de la poudre d'acier ODS pendant la montée jusqu'à la température d'extrusion est réalisée.

Méthodes de caractérisation mises en place

La caractérisation microstructurale sur poudre a nécessité la mise en place de nombreuses techniques tels que la DRX, la Microscopie Electronique à Balayage (MEB), la microsonde de Castaing, le MET, les techniques de diffraction à petits angles (à la fois aux neutrons et aux rayons-X) et la Sonde Atomique Tomographique (SAT). Pour répondre aux problèmes spécifiques de l'étude et notamment dans l'analyse des structures de défauts, des innovations ont été apportées dans le cas des techniques de DRX et de MET.

Diffraction des Rayons X

En utilisant un rayonnement synchrotron, un détecteur et surtout un four permettant des mesures in-situ, il a été possible de reproduire qualitativement la cinétique de la croissance anormale des aciers ODS. En effet, nous avons identifié l'apparition de spots sur les anneaux de diffraction censés être continus dans le cas de polycrystaux fins. Cette ponctualisation des anneaux correspond à l'apparition de grains de taille particulièrement importante par rapport au reste de la microstructure (et donc au début de la signature de la croissance anormale). L'intensité de ces spots étant proportionnelle à la taille des grains, il a été possible de déterminer la cinétique de croissance des grains de taille anormale. En s'appuyant sur la méthode Warren-Averbach modifiée (mWA), méthode quantitative qui permet de calculer la taille de cristallite et la densité de dislocation, et en faisant par ailleurs légèrement évoluer les lois de la méthode de Williamson-Hall modifiée (mWH), il nous a été possible de déterminer directement la taille de cristallite ainsi que la densité de dislocation (en tout cas leur évolution qualitative) à l'aide de cette seconde méthode. L'intérêt d'obtenir ces deux jeux de valeurs qui sont à priori supposés être identiques à partir de ces deux méthodes est qu'elles n'utilisent pas la même portion du diagramme de diffraction pour les déterminer. En effet, la méthode mWH se base sur la mesure de la largeur des pics à mi-hauteur alors que la méthode mWA est basée sur la transformée de Fourier de l'intégralité des pics. De fait, le diagramme de diffraction étant représenté dans l'espace réciproque, plus l'on s'intéresse à un paramètre proche des maximas des pics plus on est sensible aux informations à longue distance dans l'espace réel. Ainsi, la

méthode mWH sera plus sensible au déclenchement de la croissance anormale des grains. De fait la comparaison de l'évolution de la valeur de la taille de cristallite entre les deux méthodes permet d'avoir une bonne idée du moment auquel la croissance anormale des grains commence. Ensuite, il est possible de connaitre précisément la cinétique de croissance des petits cristallites à l'aide de la méthode mWA et celle des cristallites les plus larges à l'aide de l'intensité des spots sur le détecteur 2D.

Microscopie Electronique à Transmission

Au sein du laboratoire SIMaP, Egdar Rauch aidé ensuite par Muriel Véron, a développé une méthode de caractérisation particulière à partir d'un MET. Pour obtenir des cartographies d'orientation cristalline sur des alliages hyper déformés, il a utilisé le mode nanobeam d'un MET afin d'obtenir une diffraction locale du matériau. En comparant cette diffraction avec une base de données contenant des diffractions préenregistrées, il est possible de retrouver l'orientation précise du matériau. En balayant ensuite le matériau, on obtient une cartographie d'orientation point par point de façon similaire à la technique EBSD (Electron BackScattered Diffraction) par MEB avec les diagrammes de Kikuchi.

En partant de ces valeurs obtenues, il est ensuite possible de mesurer la valeur de la densité de dislocation géométriquement nécessaires pour accommoder la désorientation locale en se basant sur l'expression du tenseur de Nye.

Evolution de la microstructure

Microstructure de la poudre co-broyée

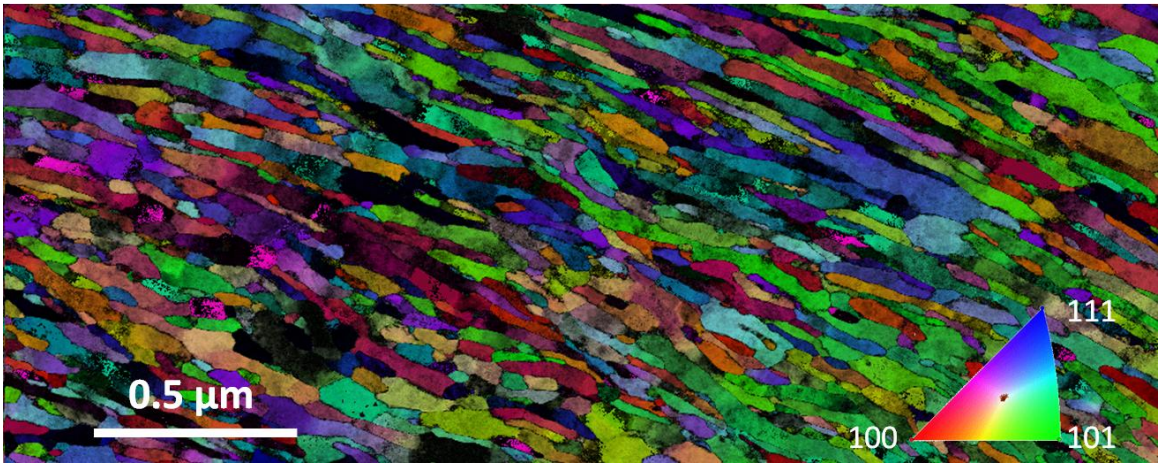

Figure 1: Cartographie d'orientation MET-ACOM d'une section FIB de particule de poudre co-broyée.

Comme le montre la Figure 1, la microstructure granulaire de la poudre co-broyée est particulièrement hétérogène que ce soit au niveau de la taille, de la morphologie ou de la déformation. En effet, si globalement la taille des grains s'établie à 10 000 nm² (0.01 µm²), il existe un ratio bien supérieur à 10^2 entre les plus petits et les plus gros grains. De même, si le facteur de forme moyen est de 5, dans le détail il va de 1 à 30. L'anisotropie des grains est donc non seulement très importante mais également très contrasté d'un

grain à l'autre. Enfin, certaines zones de la microstructure ne semblent pas déformées alors que la désorientation locale mesuré par le KAM (Kernel Average Misorientation) est très forte dans d'autres zones.

Des mesures complémentaires par DRX montrent que la taille de cristallites obtenue en fin de broyage est d'environ 25 nm et la densité de dislocation légèrement supérieure à 1.10^{16} m^{-2}. Le couplage entre les résultats obtenus en DRX et par MET-ACOM ont permis de démontrer que la microstructure était composée de grains très allongés au sein desquels peuvent se trouver des cristallites séparés les uns des autres par des murs de dislocations d'épaisseur variable. Ces cristallites identifiés par KAM comme étant les zones de faibles désorientation locale ont des tailles moyennes correspondant à la taille de cristallite moyenne calculée à partir des diagramme obtenus en DRX.

La distribution chimique des éléments d'alliage c'est relevée relativement homogène après observation par microsonde de Castaing. Un point extrêmement important est qu'il n'a pas été possible de détecter, ni la formation de précipités, ni de quelconques résidus d'oxydes d'yttrium après la mécanosynthèse. Ces expériences qui ont été réalisées à la fois pas SAXS, SANS et par SAT montrent donc une mise en solution solide des oxydes d'yttrium.

Recrystallisation et croissance anormale

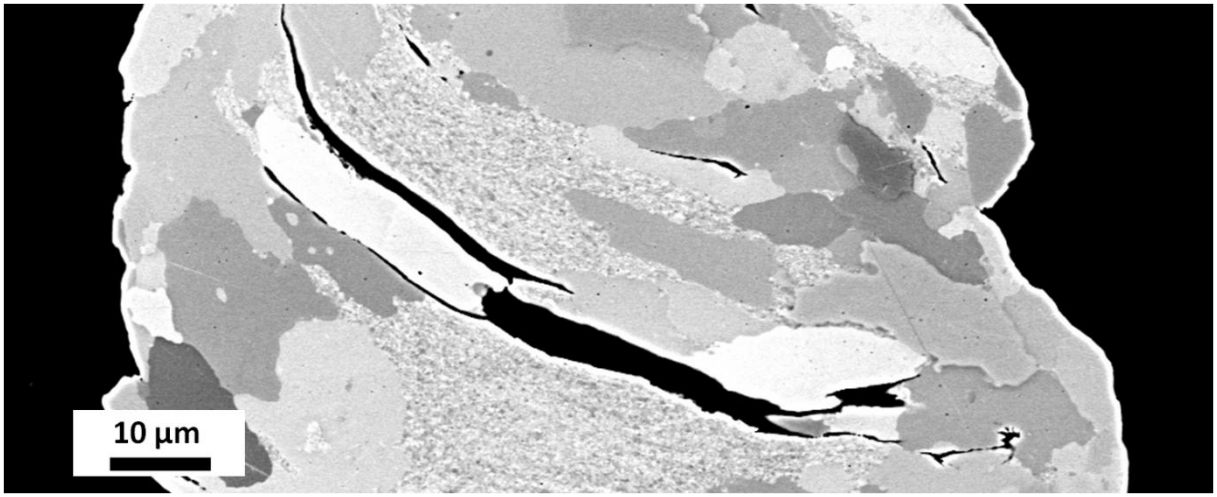

Figure 2 : Microstructure d'une particule de poudre après un recuit à 1100°C.

Comme le montre la Figure 2, la microstructure est bimodale après le recuit portant le matériaux à sa température d'extrusion (1100°C). En effet, il est possible de distinguer deux populations de grains ayant une taille radicalement différente (de l'ordre de 200 µm² pour l'une et de 10^{-2} µm² pour l'autre). Il est également intéressant de noter que cette évolution s'accompagne d'une suppression du caractère anisotrope de la microstructure. Les deux populations de grains sont en effet quasiment isotrope.

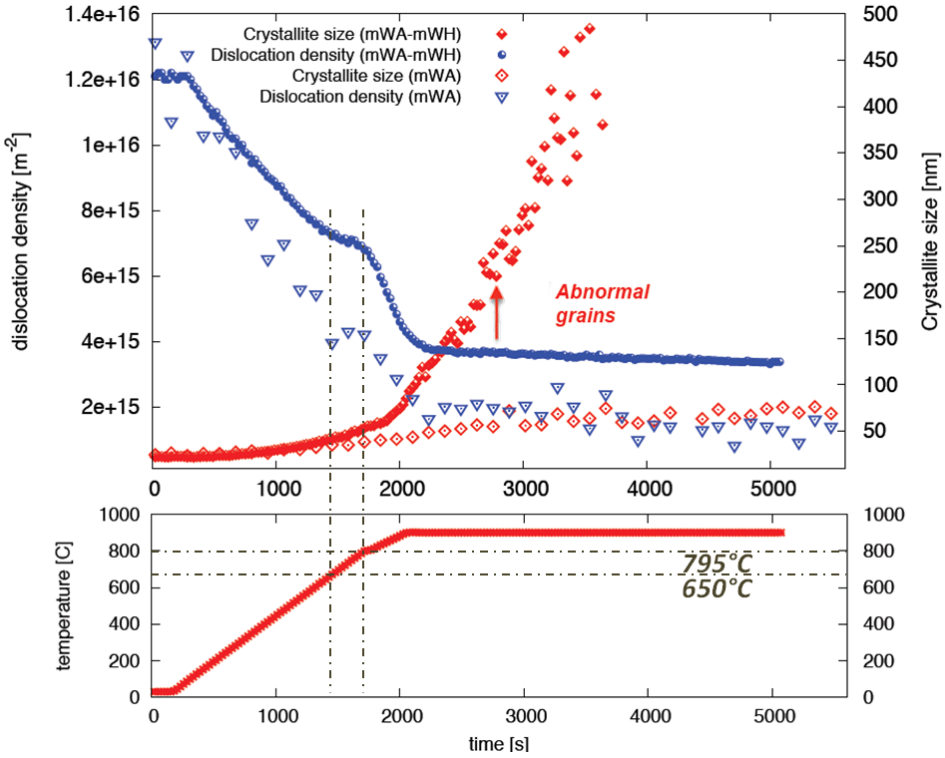

Figure 3 : Densité de dislocation et taille de cristallites déterminées avec la méthode couplée mWA-mWH et la méthode mWA pendant la recuit jusqu'à 900°C suivit d'un maintient à 900°C pendant 1h.

Les mesures faites in-situ au synchrotron SOLEIL permettent de détailler cette évolution. La Figure 3 montre l'évolution de la taille des grains et de la densité de dislocation pendant un recuit jusqu'à 900°C. Il est possible d'identifier plusieurs phases de cette évolution.

Tout d'abord, jusqu'à 650°C l'évolution microstructurale est relativement similaire entre les différentes population de grain mesurées par mWA et mWA-mWH. Celle-ci se caractérise par une forte chute de la densité de dislocation accompagnée d'une faible augmentation de la taille de cristallite. Il convient de noter que cette faible augmentation de la taille de cristallite ne ce matérialise pas lorsque l'on compare les taille de grains des échantillons correspondant aux états brut et recuit à 600°C par mesure MET ou MEB, pour quelque durée que ce soit, celle-ci restant constante. Puisque les parois intergranulaires ne bougent pas, il s'agit donc plus probablement d'un effet directement lié à la réduction de la densité de dislocation qui, en réduisant l'épaisseur des murs de dislocation entre cristallites augmente de fait la taille de celles-ci. Cette plage d'évolution microstructurale peut être identifiée comme étant une étape de restauration.

Ensuite de 650°C à 800°C, la diminution de la densité de dislocation qu'elle soit déterminée par l'une ou l'autre des méthodes de calcul marque un net ralentissement. Ce léger ralentissement est corrélé à une accélération de la croissance de la taille des cristallites (cf. Figure 3). Cette phase peut être assimilée à une recrystallisation de la microstructure. En effet même si la densité de dislocation diminue peu et que la taille de cristallite augmente peu. Il s'agit ici d'une recrystallisation continue qui résulte de

l'augmentation de la désorientation entre deux sous-grains voisins du fait de la réorganisation des dislocations et des parois de dislocations.

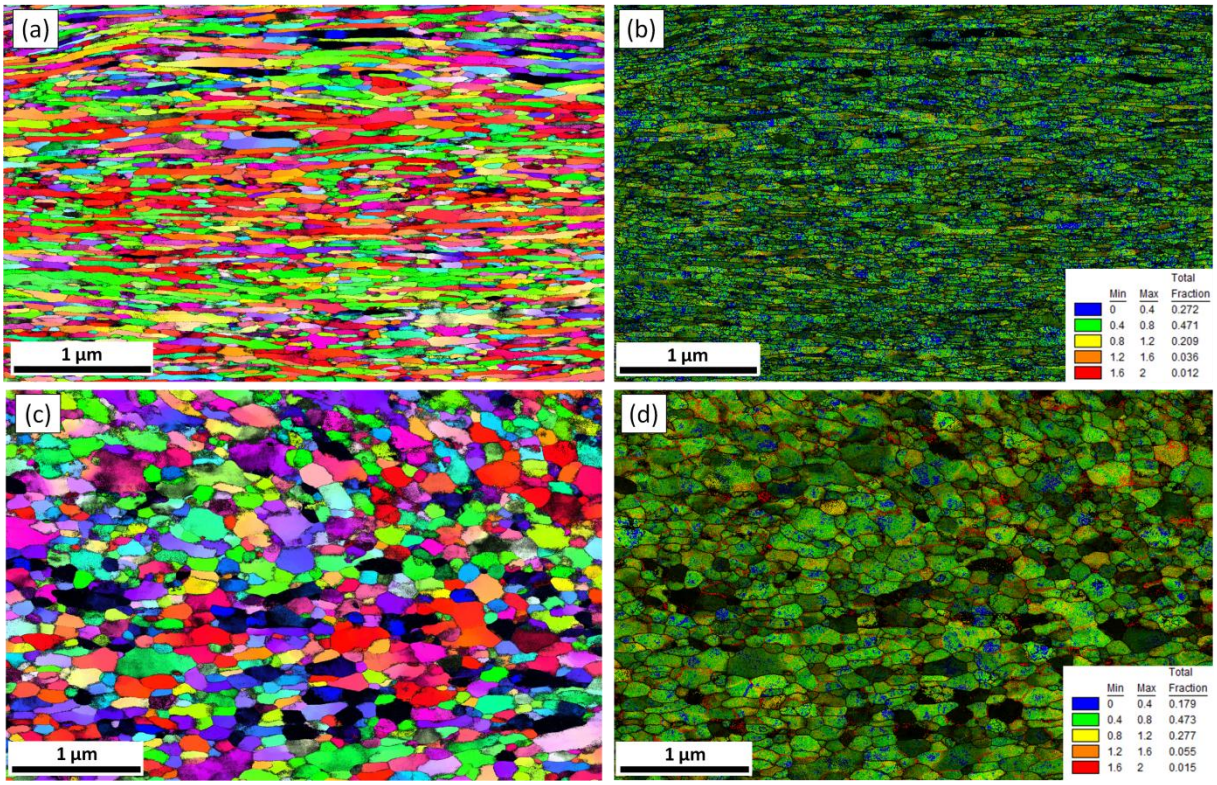

Figure 4 : Cartographies MET-ACOM. a) et b) respectivement cartographie d'orientation et KAM (1er voisin) d'une particule de poudre après un recuit de 5min@600°C, c) et d) même représentations pour une particule de poudre recuit de 5 min@800°C.

La recristallisation est d'ailleurs clairement observée sur la Figure 4 (a et b). En effet, sur cette image on constate que l'on passe d'une microstructure anisotrope après un recuit à 600°C à une microstructure entièrement isotrope après un recuit à 800°C sur une particule de poudre. Cette transformation de la microstructure correspond en tout point à une recristallisation.

Un autre point intéressant est que malgré cette recristallisation, le niveau de déformation mesurée par le KAM est supérieur dans l'échantillon recuit à 800°C par rapport à celui recuit à 600°C. Il a été possible de démontrer que ce phénomène est du à la désorientation locale provoquée par la précipitation qui apparait à cette température.
Enfin, sur la Figure 3, la taille de cristallite déterminée par mWH augmente significativement à partir de 850°C. De plus, elle augmente significativement plus rapidement que la taille de cristallite déterminée par la méthode mWA-mWH. Ce phénomène marque l'apparition de deux populations de taille de cristallites distinctes dans le matériau et donc de la croissance anormale.

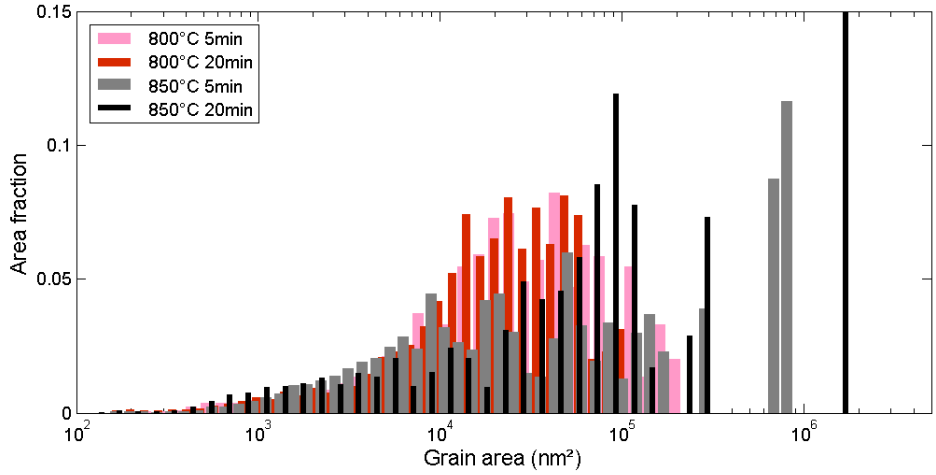

Figure 5 : Histogrammes de la taille de grain pour des particules de poudres.

La Figure 5 apporte la confirmation de l'apparition de la croissance anormale entre 800°C et 850°C. En effet, les histogrammes présentés montrent l'apparition de grains de classe de taille supérieures d'au moins un ordre de grandeur par rapport à la taille moyenne du reste de la population granulaire à 850°C.

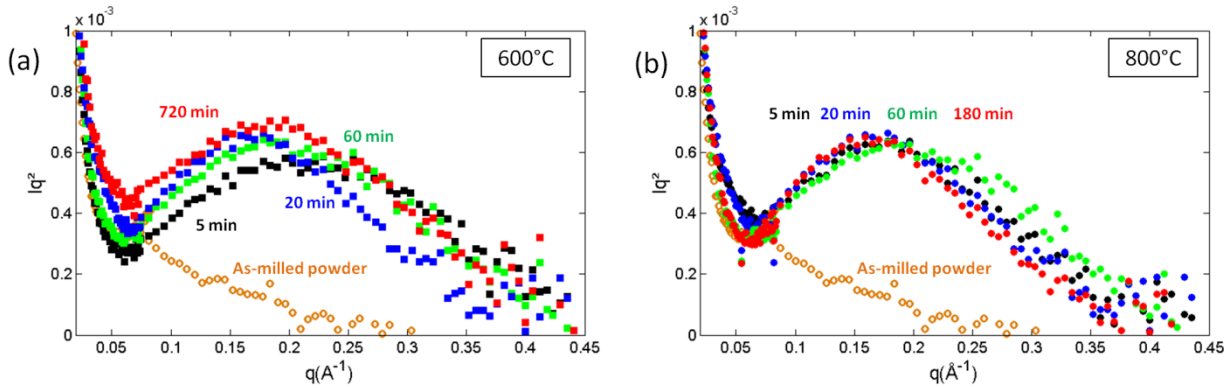

Figure 6 : Résultats de diffusion aux petits angles obtenus sur des poudres d'aciers ODS ferritiques recuits (a) 600°C (b) 800°C.

Un aspect essentiel de l'évolution microstructurale des aciers ferritiques ODS est l'évolution de la précipitation. La Figure 6, montre que la précipitation entre l'état co-broyé et l'état recuit à 600°C évolue fortement. En revanche, une fois la précipitation établie, son évolution est marginale. En effet, celle-ci s'établit à une fraction volumique d'environ 1% et passe d'un rayon de Guinier moyen de 8 Å pour une recuit de 5min à 600°C à 10 Å après une recuit de 3h à 800°C.

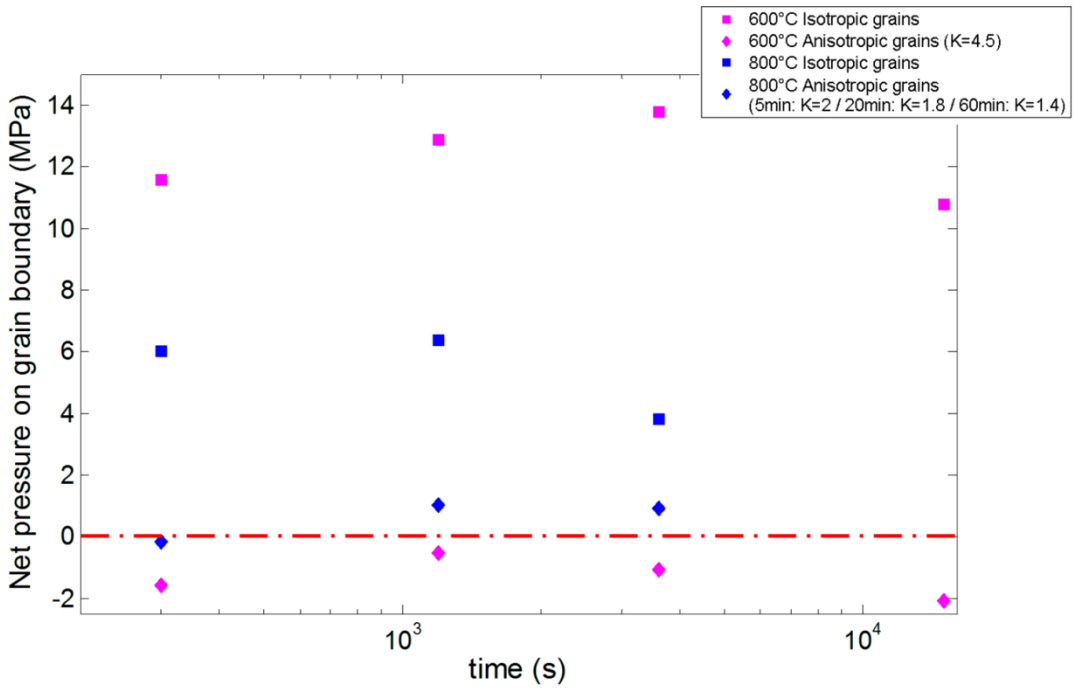

Figure 7 : Effet de l'anisotropie sur la pression exercée sur les grains

L'ensemble des propriétés microstructurales obtenues lors de la caractérisation permettent d'approfondir l'étude par l'intermédiaire de la pression nette exercée sur les joints de grains. Pour cela, la densité de dislocation (en réalité la différence de densité de dislocation entre deux grains voisins) et la taille de grains (l'énergie de surface) sont considérées comme des forces motrices et l'épinglage par les précipités (force de Zener) comme une force de freinage.

La Figure 7 fait le bilan de ce calcul. De manière intéressante, en considérant les grains comme étant isotrope, la pression nette exercée sur les joints de grains est positive que se soit à 600°C ou 800°C. Or, la caractérisation a montré que la croissance de grain n'intervient qu'à partir de 800°C. Par contre en prenant l'anisotropie en compte, alors comme lors de la caractérisation les grains la pression ne devient positive qu'a 800°C. Ce paramètre d'anisotropie est donc essentiel pour expliquer le comportement de la microstructure avant la recristallisation (<800°C).

Effet de la quantité de soluté sur la croissance anormale

La microstructure obtenue après mécanosynthèse combinée avec la précipitation rapide sont théoriquement responsables la croissance anormale du matériau. Afin de contrôler cette croissance anormale et donc les propriétés mécaniques du matériau, des études sur l'évolution microstructurale de matériaux contenant différents taux de renforts en titane et en yttrium ont été réalisée afin d'évaluer l'effet réel de la précipitation sur la croissance anormale.

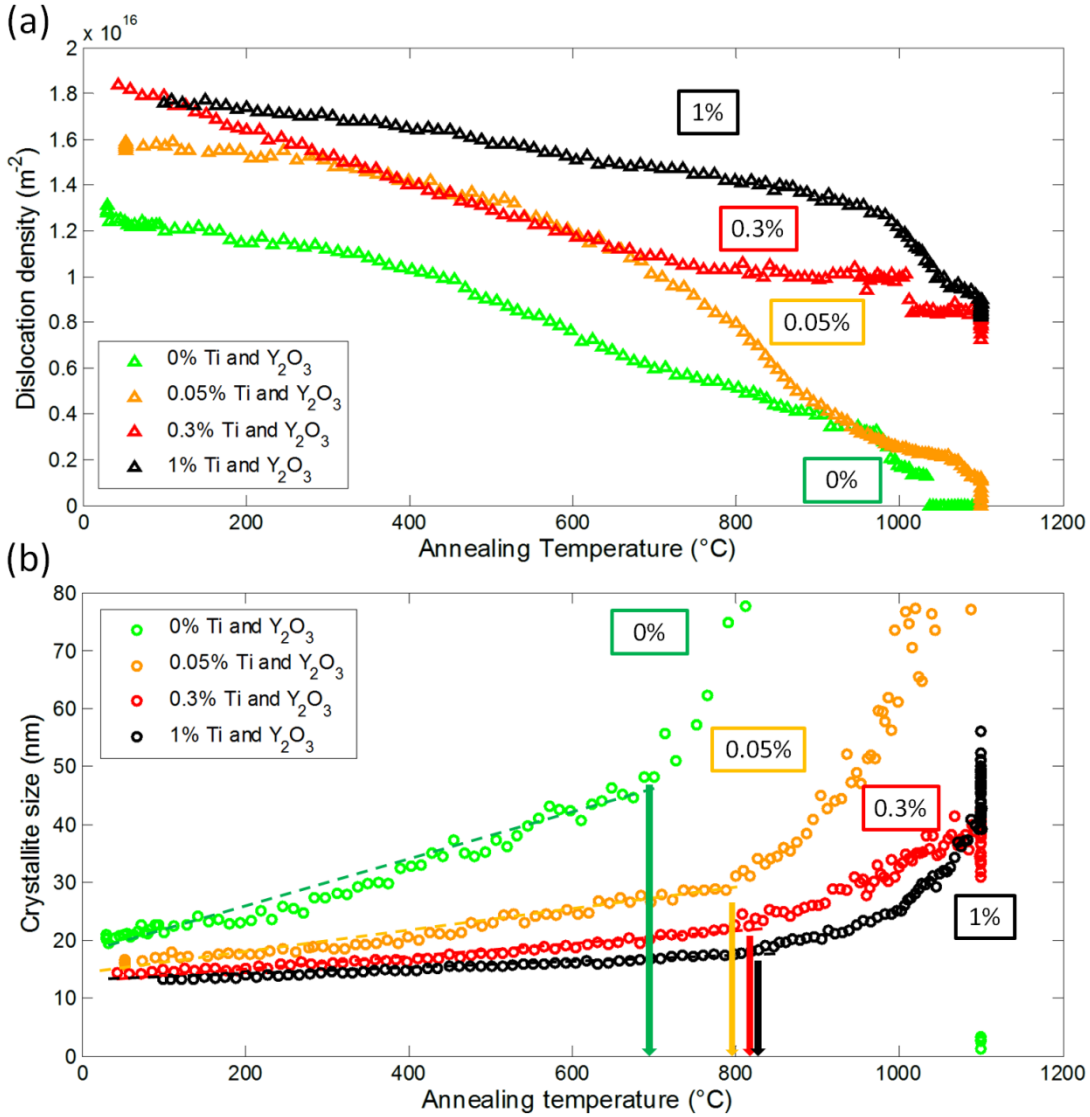

Figure 8 : Comparaison de l'évolution microstructurale de poudre d'acier ODS ferritique ayant différentes quantité de soluté, (a) densité de dislocation (b) taille de cristallite déterminées avec la méthode couplée mWA-mWH pendant un recuit menant à 1100°C suivi d'un maintien à cette température pendant 20 min.

La Figure 8 montre l'évolution microstructurale de poudre d'acier ODS ferritique ayant différentes quantité de soluté pendant un recuit menant à la température d'extrusion puis un maintient 20 min à cette température. Lors de la mécanosynthèse d'une phase métallique ductile avec un oxyde fragile, le durcissement de la phase ductile est d'autant plus important que la fraction volumique d'oxyde est élevée. La poudre est donc d'autant plus fragile et en fin de mécanosynthèse la taille des particules de poudre d'autant plus faible que la quantité d'oxydes est élevée. A l'état cobroyé, la taille de cristallites et la densité de dislocation sont respectivement plus faible et plus élevée lorsque le taux de renfort augmente.

Durant la phase de montée en température, jusqu'à 700°C, pour chacune des poudres il y a une croissance continue de la taille de cristallites s'accompagnant d'une diminution également continue de la densité de dislocation. L'effet de trainage induit par les éléments en solution est mis en lumière par le ralentissement de ces cinétiques (croissance de

cristallites et diminution de la densité de dislocation) qui est corrélé à l'augmentation de la quantité de titane et d'oxyde d'yttrium introduite dans la matrice ferritique. A 700°C, seule la poudre non renforcée recristallise. Les trois poudres renforcées, elles, recristallisent toutes vers 800°C. La recrystallisation n'est donc pas contrôlée par la quantité de soluté mais bien par l'aspect anisotrope de la microstructure tel qu'il est présenté au paragraphe précédent.

Par contre, la quantité de soluté va jouer un rôle important dans le déclenchement de la croissance anormale. En effet, plus la quantité de soluté initiale est importante dans la matrice, plus la température de déclenchement de la croissance anormale est élevée. Cet élément est essentiel puisqu'il permet d'identifier la quantité de soluté comme un moyen de contrôler l'apparition de la croissance anormale. Ainsi, il est envisageable d'augmenter légèrement la quantité de soluté et d'étudier les possibilités de diminuer la température nécessaire à l'extrusion afin de limiter ou même d'empêcher l'apparition de la croissance anormale.
La taille des grains ultrafins est également contrôlable avec la quantité de soluté. Ainsi, une loi définie à partir de la théorie de Zener a pu être établie dans le cas des aciers ODS ferritiques. Cette loi permet de prédire la taille de ces grains ultrafins de manière précise à partir de la fraction volumique et de la taille moyenne des précipités.

Les différents mécanismes contrôlant l'évolution de la microstructure ont été identifiés :

- Jusqu'à 750°C, la restauration de la microstructure, contrôlée par l'anisotropie microstructure, a lieu.
- Ensuite, la recristallisation a lieu et la microstructure devient isotrope. La cinétique de la croissance granulaire ainsi que la taille finale des grains sont alors contrôlées par la précipitation.
- La quantité de soluté est un moyen efficace pour contrôler la température de croissance anormale. Néanmoins, le phénomène intervient quelque soit la quantité de soluté et est contrôlée par la différence d'énergie stockée par densité de dislocation entre grains voisins.
- Le ratio grains ultrafins sur grains larges comme la taille critique de grains ultrafins peuvent être contrôlés par la quantité de soluté. Néanmoins, les grains larges ont la même taille quelque soit la quantité de soluté.

Une simulation pour prédire la croissance anormale

Dans le but prévoir l'apparition de la croissance anormale quelque soit le traitement thermique appliqué. Une simulation a été adapté pour le cas des aciers ODS ferritiques en y ajoutant notamment l'effet de la densité de dislocation. A l'origine, la simulation utilisée a été développée par l'INSA de Lyon au laboratoire MATEIS pour les aciers faiblement alliés. Le principal avantage de ce code est qu'il couple à la fois l'évolution de la structure granulaire avec l'évolution de la précipitation.

La croissance anormale est modélisée en appliquant les hypothèses suivantes : les grains sont considérés comme étant isotropes, le freinage par soluté est négligé par rapport à l'épinglage par les précipités et la précipitation est considérée comme étant homogène. La formulation de la pression exercée pour la croissance des grains (normaux ou anormaux) tiens également compte de l'effet des précipités placés à des endroits spécifiques tels que des points triples ou quadruples. Placés à ces endroits particuliers, les précipités ont un effet d'épinglage supérieur aux précipités placés sur des joints de grains classiques. Ainsi, étant donné que plus les grains sont petits, plus la densité de points spécifiques augmente, les grains les plus petits seront épinglés plus efficacement que les plus larges, ce qui crée de fait une situation favorable à l'apparition de la croissance anormale. Néanmoins, du fait de la très forte densité de précipités dans le matériau, cet effet joue très peu dans le cas des aciers ODS ferritiques. Au final partant de ces hypothèses, il est possible d'établir une condition numérique pour la croissance anormale :

$$\begin{aligned}\frac{d}{dt}\left(\frac{D_{ab}}{D_n}\right) &= \frac{1}{D_n}\frac{dD_{ab}}{dt} - \frac{D_{ab}}{D_n^2}\frac{dD_n}{dt} \\ &= \frac{2\gamma_g M}{D_n^2}\left[\mu - (1-\mu)\left(\frac{D_n}{D_{ab}}\right)^2 + (2\mu - 1)\frac{D_n}{D_{ab}} - \frac{\lambda}{2}\frac{D_{ab}}{D_n}\right] \\ &\quad - \frac{M}{D_n}\left(\frac{D_{ab}}{D_n} + 1\right)(P_C + P_Z) > 0\end{aligned} \tag{1}$$

Ainsi, il y a croissance anormale lorsque les grains les plus larges croissent plus rapidement que le restant de la population de grains.

La modélisation de la précipitation est basée sur la théorie classique de nucléation et de croissance formulée par Langer et Schwartz puis modifiée par Kampmann et Wagner. Les principales hypothèses et simplifications formulées sont : La croissance des précipités est contrôlée par la diffusion des solutés sur de longues distance dans la matrice, les précipités sont sphériques, ils n'induisent pas de champ de déformation dans la matrice, l'énergie d'interface ne dépends ni de la température ni de la taille de précipités et enfin on considère de l'équilibre local est établit à l'interface. De fait, ces hypothèses mènent au contrôle de la croissance des précipités par l'élément diffusant le plus lentement dans la matrice et donc dans le cas présent par l'yttrium. Numériquement, la modélisation de la précipitation est implémentée par une approche de Lagrange multi-classe, pour laquelle la distribution de taille de précipités est discrétisée. Cela permet de résoudre de manière indépendante un nombre variable d'équations donnant à la fois la nucléation et la croissance de chacune des classe de taille de précipitation pour chaque incrément de temps. Il est également important de noter que la diffusion accélérée des éléments aux joints de grain est prise en compte dans la simulation.

La croissance de grains et la précipitation sont interconnectés. En effet, la croissance de grain dépend fortement de l'épinglage. A chaque pas de temps, la distribution de précipité est calculée en premier puis implémentée comme paramètre d'entrée dans la modélisation

de la croissance granulaire. Modélisée de la sorte, les résultats de la simulation sur l'évolution de la microstructure ne prédit que de la croissance normale pour des traitement thermiques allant de 800°C à 900°C et de 5 à 60 min. Or expérimentalement, la croissance anormale est observée dès 850°C et 20 min de recuit lors d'un traitement thermique.

Ce résultat a motivé l'introduction de la densité de dislocation dans la simulation. Les hypothèses retenues pour le faire sont que la densité dislocation est homogène entre les grains de taille normale et est également homogène entre les grains de taille anormale, la densité de dislocation est présente uniquement dans les grain de taille normale donc la densité de dislocation dans les grains les plus larges est égale à zéro. Cette modification de la simulation permet d'obtenir un résultat beaucoup plus conforme aux observations expérimentales puisque celui-ci prédit désormais correctement l'apparition de la croissance anormale. Néanmoins, de nombreux raffinement sont encore nécessaires pour obtenir une simulation réellement prédictive. En effet, celle-ci ne prédit aucune croissance normale ce qui est contraire aux observations expérimentales. De plus, la cinétique de la croissance anormale est trop élevée et est irréaliste. Deux principales améliorations peuvent être envisagée pour la simulation, l'implémentation de la distribution de la taille de grain et l'attribution d'une densité de dislocation indépendante pour chacune des classe de taille de grain.

De la poudre aux matériaux consolidés

Afin de déterminer si les mécanismes identifiés lors des chapitres précédents s'appliquent réellement dans le cas des aciers ODS ferritiques élaborés dans des conditions industrielles, une comparaison détaillée entre les matériaux consolidés et les particules de poudre recuites a été réalisée.

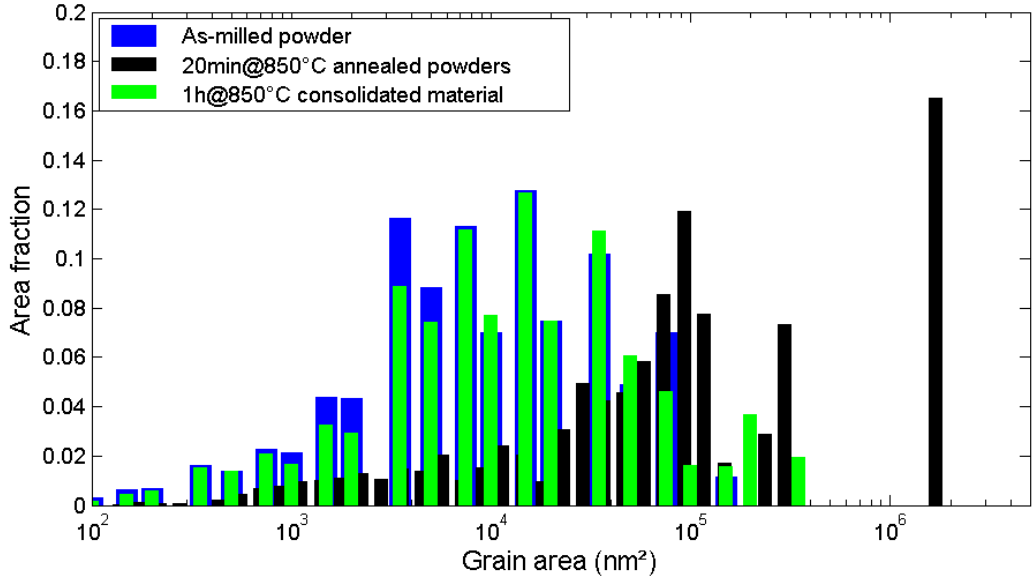

Figure 9 : Comparaison de la distribution de la taille de grains entre la poudre brute de cobroyage, une particule de poudre recuite 20 min à 850°C et la poudre consolidé 1h à 850°C par HIP.

En réalisant cette comparaison à 850°C, soit une température intermédiaire par rapport à la température finale d'extrusion, des différences notables sont observables. Comme le montre la Figure 9, la distribution de la taille de grain est largement différente entre la poudre et le consolidé. En effet, si les deux distributions montrent des signent de croissance anormale avec les classes des grains les plus grands surreprésentées par rapport à une distribution gaussienne classique, la croissance anormale est bien plus avancée dans le cas de la particule de poudre recuite. De même, la microstructure de la poudre est bien plus isotrope que celle du matériau consolidé. De fait, l'évolution de la microstructure est plus importante dans le cas de la poudre recuite. Ceci a pu être expliqué par la plus grande diffusion du titane sur les bords des particules comparé à la diffusion lors de la consolidation. La plus grande surface libre dans le cas des particules crée un environnement favorable pour la diffusion du titane qui est attiré au bord par l'oxygène avec lequel il forme des oxydes. La quantité de titane disponible dans la matrice diminue ce qui provoque une diminution de la densité de précipité ainsi qu'une augmentation de leur taille. Les grains sont donc moins bien épinglés et les joints de grains se déplacent plus vite dans la microstructure. L'effet est donc similaire à celui observé pour l'évolution de la microstructure pour différents taux de renforts.

Néanmoins, après un recuit à 1100°C, les microstructures sont cette fois similaires, à la fois dans la morphologie et dans la taille des différentes populations de grains même si la densité de précipités est légèrement plus faible dans le cas des particules de poudre simplement recuites. Cette similitude montre que les mécanismes identifiés précédemment sont bien valides dans le cas d'une fabrication industrielle de gaines de combustibles en aciers ODS ferritiques.

Des observations particulièrement intéressantes effectuées sur des matériaux extrudés ont conduit à une étude approfondie de l'interaction entre joints de grains et précipités pendant l'extrusion. En effet, observés par MET, les petits précipités se relèvent être cohérents quelque soit leur position dans la microstructure. Or les caractérisations précédentes montrent à la fois que la précipitation à lieu en grande partie avant l'extrusion et que l'extrusion conduit nécessairement à la migration de joints de grains. Si les précipités sont cohérents partout sur la microstructure, cela semble indiquer qu'ils n'ont pas été franchi par un joint de grain. En effet, Si cela avait été le cas leur réseau cristallin serait incohérent vis-à-vis de l'orientation cristalline du nouveau grain dans lesquels ils se trouvent. C'est donc le signe qu'un phénomène spécifique est à l'œuvre. De même, il apparait que la taille des précipités présents sur les joints de grains est plus élevée que celle de ceux présents dans la matrice.

Afin d'étudier le mécanisme d'évolution microstructurale menant à cette microstructure, un échantillon spécifique dont l'extrusion a été interrompue a été élaboré. Ainsi, il a été possible d'étudier trois instants particulier de l'extrusion : la partie consolidée, la partie se

trouvant dans le cône d'extrusion et la partie extrudée. Comme l'illustre la Figure 10, la partie située dans le cône d'extrusion montre une forte hétérogénéité microstructurale. En effet, différentes zones qui peuvent être délimitées parallèlement aux joints de grains sont présentes. Certaines de ces zones sont dégarnies à la fois en précipités mais également en solutés, d'autres sont constitués de précipités d'oxydes mixtes de titane et d'yttrium de taille nanométriques tels qu'ils sont classiquement attendus dans les aciers ODS. Certaines zones sont très riche en yttrium et en titane et constituées de gros précipités. Enfin, les joints de grains sont également riche en éléments d'addition, non seulement par la présence de gros précipités mais également de la plus forte solubilité de l'yttrium et du titane aux joints de grains.

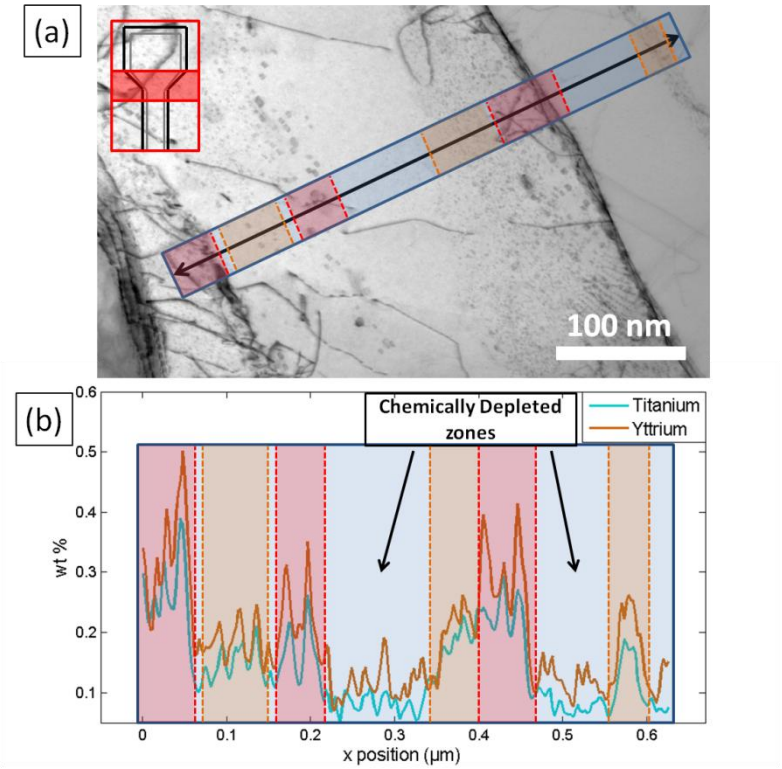

Figure 10 : (a) image MET de l'échantillon prélevé dans le cône d'extrusion (b) profiles de concentration en Y et Ti correspondant à la zone définie par la flèche noire et le rectangle bleu en (a), les zones colorés correspondent respectivement à : zones bleues – zones dénudées, zones oranges – petits précipités , zones rouges – joints de grains et alignements de gros précipités.

La mise en évidence de ces différentes zones plutôt que d'une précipitation parfaitement homogène à l'intérieur des grains à conduit à la proposition d'un mécanisme de dissolution des nanoprécipités aux joints de grains. De façon similaire à un mécanisme proposé par Bouchaud et Naka sur des alliages de titane renforcés par des oxydes d'yttrium, l'idée est que la plus grande solubilité des solutés aux joints de grain, notamment lorsque ceux-ci se déplacent, attire les solutés présents en amont du joints de grain vers celui-ci. Ceci crée une zone de déplétion juste en avant du joint de grain, la concentration en yttrium devient alors plus faible que la concentration d'équilibre et les précipités commencent à se dissoudre. Lorsque le joint de grains atteint sa propre concentration d'équilibre, la concentration en avant du joint de grain remonte, les

précipités ne sont plus dissous et les joints de grains sont a nouveau épinglés. La diffusion accélérée aux joints de grains favorisent alors le mûrissement d'Oswald et la taille des précipités présents sur le joint de grain augmente. La force d'épinglage diminue se qui permet alors au joint de grain de se désancrer et de se déplacer à nouveau, relâchant une partie de la quantité de soluté emmagasinée et dissolvant de nouveau précipités. Les solutés ainsi relâchées précipitent de manière cohérente dans leur nouvelle matrice.
De nouvelles caractérisations ainsi qu'une modélisation sont envisagées afin de valider cette proposition de mécanisme qui répond de parfaitement aux observations expérimentales faites.

Conclusion

Au terme de cette étude, la caractérisation fine de la microstructure complexe des aciers ODS ferritiques a été réalisée par le couplage de nombreuses techniques de caractérisation complémentaires. Celle-ci a permis la mise en lumière des différents stade de l'évolution microstructurale des aciers ODS et des mécanismes qui y prennent part. De même, la modélisation de la croissance anormale et la prévision de celle-ci en fonction d'une microstructure de départ donnée est également réalisée. Ces deux réalisations permettent de donner des préconisations précises aux aciéristes en terme de traitement thermique et d'élaboration en sens large afin de limiter la croissance anormale dans le matériau et de la forte anisotropie des propriétés mécaniques qui en résulte.

De plus, un mécanisme de dissolution des précipités par les joints de grains lors de l'extrusion est proposé et demande a être validé. De même que la modélisation de la croissance anormale offre de nombreuse pistes d'optimisation, l'effet de l'anisotropie granulaire sur la croissance de grain demande a être quantifié.

Enfin, les données expérimentales obtenues dans le cadre de cette thèse pourront largement être utilisées dans d'autres simulations développées au sein du CPR ODISSEE dans lequel cette thèse c'est déroulée mais également pour des travaux à l'INSA de Lyon et au service SRMA du CEA.

General Introduction

Energy supply: a global issue

During the last century, a clear correlation between the increase of energy consumption levels and improvement of the main socio-economic indicators (i.e. increase of life expectancy, years of schooling, improved water access and decrease of infant mortality) has been found [1]. Therefore, energy supply is a priority for many governments, especially in developing countries.

Nevertheless, this exceptional opportunity to access better life conditions is put in danger by a major side effect of energy supply. Indeed, with increasing population and demand, the various emissions produced by energy factories have increased to a point that the ecosystem is no longer able to regulate them. The Intergovernmental Panel on Climate Change (IPCC) has clearly established the involvement of human activities in the major change of climate [2] (cf. Figure 11).

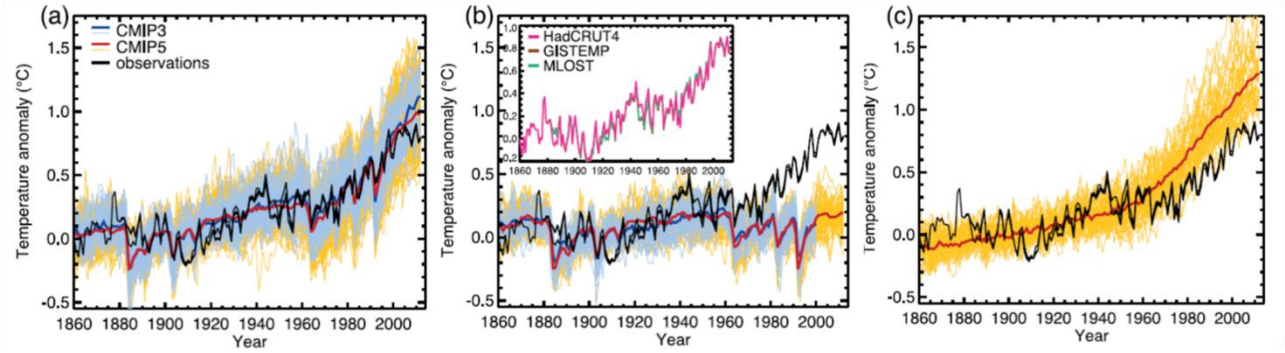

Figure 11: On (a), (b) and (c), three observational estimates of global mean surface temperature (displayed in black lines) are compared to model simulation [CMIP3 models – thin blue lines and CMIP5 models – thin yellow lines, thick red and blue lines are averages across all available CMIP5 and CMIP3 respectively] with (a) both anthropogenic and natural forcing, (b) natural forcing only and (c) greenhouse gas (GHG) forcing only [2].

As outlined by Figure 11, anthropogenic activities exert an extreme pressure on the ecosystem as measured by the anthropogenic radiative forcing. The consequences of this pressure on the environment are already profound. A notorious example is the rise of ocean level which results from its thermal expansion since 1971 (for 40%) and from glacier melting. Over the years, the number of environmental threats a change of climate would cause have raised. A review of the likelihood for these threats to become real has been performed by the IPCC. The different risks under study where, for example, the atlantic meridional overturning circulation[1], the greenland ice sheets decrease in area and volume, the permfrost carbon storage or the atmospheric methane emission from terrestrial and oceanic clathrates [3].

[1] The Atlantic Meridional Overturning Circulation (AMOC) is a major current in the Atlantic Ocean, characterized by a northward flow of warm, and a southward flow of colder water in the deep Atlantic.

Nuclear energy as a part of the solution

Over the past 40 years, nuclear energy, which represents 13% of the global electricity supply, has proved to be an affordable and reliable baseload for the electric supply, at a very low greenhouse gas emission cost [5]. Risks associated to nuclear energy are real and extremely serious to consider. The major issues arising from electric nuclear plants are the following:

- Optimization of fuel resources
- Management of the nuclear waste
- Prevention of fissile materials proliferation
- Safety

Solving these issues is essential to achieve a sustainable nuclear energy. In that prospect, advanced nuclear reactors have been proposed by the Generation IV International Forum. Among them, the concept of Sodium Fast Reactor (SFR) hold a special place. Compared to actual Pressurised Water Reactors (PWRs), SFR main advantages are:

- The fast neutron spectrum of the SFR reactor will allow recycling, as effective fuel, a large quantity of the current stock of nuclear fuel waste (mainly ^{239}Pu and ^{238}U). This capacity allows to largely increase the amount of available fissile resource in the long run (>200 years). More importantly, it allows to drastically reduce the final waste production as it efficiently consumes a significant part of the existing waste. The fuel cycle is closed.
- The direct consumption of ^{239}Pu which directly allows to control its proliferation.
- A higher in service temperature compared to PWRs which enables to reach enhanced thermal cycle efficiency.

SFR spread out in France and in the world

France, from her experience in fast breeders in the 70's (Phenix, Superphenix) is pioneer in SFR development, in which she has been joined by a large community of countries. Under the French leadership, a new European project, the Advanced Sodium Technological Reactor for Industrial Demonstration (ASTRID) is under study with a projected finalized construction around 2030. Other countries such as Russia (BN-series), Japan (Monju), India (Kalpakkam - PFBR), China Experimental Fast Reactor (CEFR) have also established large scale SFR program and contribute to growth in the body of knowledge.

Recent development such as a core with a negative temperature coefficient[2], modular heat exchangers, corium catcher, the possibility of to use a sodium / gas exchanger, bring the

[2] number of neutrons available for new fissions decreases when temperature increase.

level of safety of the new SFR beyond the one of classical PWR.

From nuclear to metallurgy: the ODS steel choice

Neither the Zirconium alloys actually in service in PWRs nor the advanced austenitic alloys used in the previous SFR version can be employed for the ASTRID project with the required efficiency that is imposed by a high burn-up and temperature. To satisfactorily meet the challenge, the chosen material will have to sustain a high operating temperature and a high radiation flux (respectively 650°C and $6.0.10^{15}$ $n.cm^{-2}.s^{-1}$) without having a too large swelling rate. Meanwhile, both safety and economical issues will benefit from a maximization of claddings (and therefore fuel) duration in the reactor. At the present state, the goal is to reach a lifespan of 8 to 10 years in service, which means that the radiation damage induced on the claddings will exceed 150 dpa[3]. In these operating conditions Zirconium alloys simply do not have the necessary resistance while austenitic alloys will importantly swell under radiation. Ferritic steels, additionally to their interesting high thermal conductivity and low thermal expansion coefficient, have a high irradiation swelling resistance. Unfortunately, they display poor high temperature creep properties. To overcome this difficulty, Oxide Dispersion Strengthened (ODS) bcc steels were proposed for the SFR fuel claddings application.

Context of the study

This thesis was conducted within the frame of the four-year (2012-2016) research program ODISSEE (Oxide DIspersion Strengthened StEEls) funded by the CNRS, CEA, EDF, AREVA and Mécachrome. Consisting in a dozen of PhD theses and grouping together nearly as many laboratories, its general aim is to reach a better control degree of the ODS ferritic steel clad fabrication process. The studies range from the atomic scale modelling of the Fe-Cr unmixing to the study of the mechanical response to creep damage accumulation.

More specifically, the present thesis aims at studying the microstructural evolution of the material during its elaboration and more precisely the conditions leading to its abnormal grain growth. This chemical and structural study relies on characterization facilities and the expertise of the SIMaP laboratory for characterization and modelling of the microstructural evolution, and also on a strong collaboration with the SRMA/CEA for alloy elaboration and thermo mechanical treatments. Additionally, important complementary support for characterization was provided by the KMNF - Karlsruhe Institute of Technology (KIT), EDF Les renardières, the METSA network through the Groupe de Physique des Matériaux (GPM) in Rouen and the SOLEIL synchrotron

[3]dpa is the averaged number of displacement per atoms induced by radiation. In PWR it does not exceed 5 dpa for fuel claddings

installation.
An abnormal grain growth modelling will focus on the grain boundary migration coupled to the diffusion and preferential pinning by precipitates at triple junctions. It will then be confronted to characterization results.

Presentation of the manuscript

The first chapter of this thesis will be devoted to a literature review on ODS steels and recrystallization.

The second chapter will present the chosen materials and the thermo mechanical treatments applied will be presented. Characterization methods choices and more importantly characterization methods specifically developed will be detailed.

Then, in chapter 3 the specific powder behaviour will be discussed, both in terms of its response to the different thermal treatments and as a function of its solute content. Results will be confronted to classical pinning models and to a more sophisticated model currently developed by the MATEIS laboratory in Lyon and allowing to estimate the occurrence of abnormal grain growth for a given initial microstructure and thermal treatment.

A second part will be dedicated to the understanding of the microstructural evolution from powder to consolidated material. Observations and possible mechanisms involved in microstructure evolution during extrusion are reported.

Main conclusions and perspectives of this work will be presented as the final part of this manuscript.

General introduction bibliography

[1] Pasten C. et Santamarina J.C. (2012) ENERGY AND QUALITY OF LIFE. *Energy Policy*, **49**, 468‑476. http://dx.doi.org/10.1016/j.enpol.2012.06.051

[2] Bindoff N.L., Stott P.A., AchuttaRao K.M., Allen M.R., Gillett N., Gutzler D., … Zhang X. (2013) 2013: DETECTION AND ATTRIBUTION OF CLIMATE CHANGE: FROM GLOBAL TO REGIONAL. *Climate Change 2013: The Physical Science Basis Contribution of Working Group I to the Fifth Assessment Report of the Intergovernmental Panel on Climate Change*, Cambridge University Press. Stocker, T.F., D. Qin, G.-K. Plattner, M. Tignor, S.K. Allen, J. Boschung, A. Nauels, Y. Xia, V. Bex and P.M. Midgley, Cambridge, United Kingdom and New York, NY, USA.

[3] Collins M., Knutti R., Arblaster J., Dufresne J.-L., Fichefet T., Friedlingstein P., … Wehner M. (2013) 2013: LONG-TERM CLIMATE CHANGE: PROJECTIONS, COMMITMENTS AND IRREVERSIBILITY. *Climate Change 2013: The Physical Science Basis Contribution of Working Group I to the Fifth Assessment Report of the Intergovernmental Panel on Climate Change*, Cambridge University Press. Stocker,

T.F., D. Qin, G.-K. Plattner, M. Tignor, S.K. Allen, J. Boschung, A. Nauels, Y. Xia, V. Bex and P.M. Midgley, Cambridge, United Kingdom and New York, NY, USA.

[4] Fricker A. (2002) THE CONSCIOUS PURPOSE OF SCIENCE IS CONTROL OF NATURE; ITS UNCONSCIOUS EFFECT IS DISRUPTION AND CHAOS. *Futures*, **34**, 535‑546. http://dx.doi.org/10.1016/S0016-3287(01)00079-9

[5] Chu S. et Majumdar A. (2012) OPPORTUNITIES AND CHALLENGES FOR A SUSTAINABLE ENERGY FUTURE. *Nature*, **488**, 294‑303. http://dx.doi.org/10.1038/nature11475

Chapter I
Literature review

1. ODS steels

Historically, ODS alloys have been employed to improve high temperature mechanical properties. In 1910, the first utilization of an oxide dispersion was reported by W.D. Coolidge: using classical powder metallurgy, a tungsten based alloy reinforced with thorium oxides was developed to impede high temperature grain growth and therefore increase the life span of a tungsten filament lamp [1].

After this first development, several other applications with various metallic matrices such as aluminium or nickel were imagined over decades. A notable improvement in the field has been made by J.S. Benjamin at the International Nickel COmpany (INCO) laboratory: he proposed a new elaboration process based on high energy milling powder metallurgy – later called mechanical alloying [2]. This process was introduced in order to obtain a fine and homogeneous oxide dispersion within a nickel matrix. Its aim was to produce high temperature resistant materials for the gas turbine application [3]. Currently, mechanical alloying is still considered as the most effective process to obtain fine and homogeneously distributed precipitates. Rapidly, given the high standard of the technical specifications for the SFR fuel cladding application (cf. §I.1.1), mechanical alloying was integrated to the elaboration process.

The classical processing route used to produce 14Cr ODS ferritic steel cladding tubes therefore highly depends on powder metallurgy (cf. Figure I.1). The first step of the elaboration is the mechanical alloying of both ferritic steel and yttrium oxide powders at high energy and room temperature for several dozens of hours. This step allows to force yttrium into solid solution. The milled powder is then degased around 400°C for 2 hours, and heated up to a consolidation temperature of 1100°C in order to close the last remaining porosities by hot extrusion. Yttrium oxide precipitation occurs during the heating up to 1100°C of this thermo-mechanical treatment. The process is usually terminated by cold rolling. Afterwards, tubes have to be welded to an integrated structure in order to be placed into the reactor. This major technological issue will not be treated here [4,5].

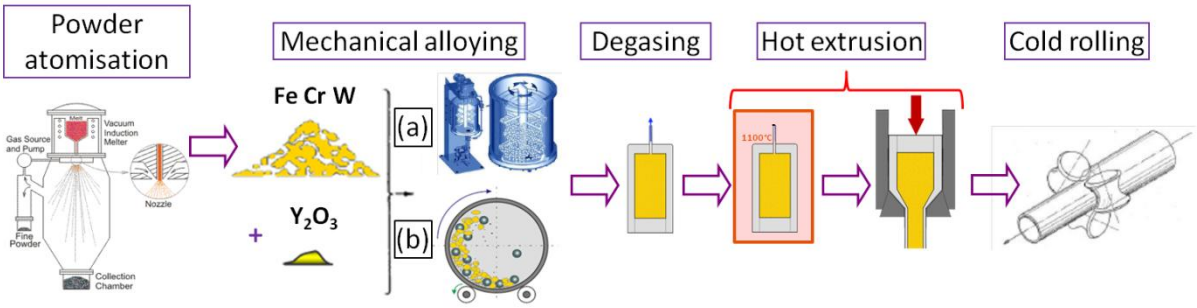

Figure I.1: Classical ODS ferritic steel elaboration process. In case (a) mechanical alloying is performed by an attritor, in case (b) by a ball mill

As explained is the general introduction, ODS steels for nuclear applications have been studied since the 70s by a large worldwide community. In order to introduce the main concepts that will be used this thesis, this review will concentrate on both the general microstructure and mechanical properties of ODS steels, and the phenomenon of recrystallization and related microstructural evolutions.

1.1. Technical specifications

Specifications to obtain agreement for nuclear materials are drastic (design and construction rules for SFR can be found in the RCC-MRx code). The dimensional criteria resulting from the expected operative service conditions define the materials' resistance value of cladding tube. Cladding tube dimensions should be close to a 10.73 mm external diameter, a 0.5 mm thickness and a 3m length [6]. If the ODS steels are to be used in nuclear applications they have to achieve the following set of properties.

First, the fission reaction will continuously release fission products. Consequently, the pressure inside the tube will increase to such a point that it will reach 100 MPa ($\sigma_{\theta\theta}$) at the end of the fuel's life. To be conservative, the material will have to be able to sustain a maximum pressure on the entire service period; which means, following the Larson Miller criterion, 72000 h at 670°C for 100 MPa. The yield stress and the ultimate tensile stress will have to be respectively superior to 100MPa and 300MPa at 670°C.

The complete structure of the assembly has to hold during the whole cycle duration (transportation, manutentioning, storage, etc.). As a result the fracture toughness has to be superior to 20MPa.$m^{1/2}$ and the ductility to 0.5%. Furthermore, the Ductile to Brittle Transition Temperature has to be lower than -30°C.

The material will have to sustain an irradiation dose equivalent to 150dpa with a restrained deformation (< 1,5%). This limitation, which is inferior to the 3% swelling allowed for the austenitic steels is due to the poor ductility properties of the ODS steels. Irradiation may deform the material not only through swelling but also throught irradiation induced creep. An additional reason for dimensional stability is the design for a negative temperature factor which ensures a passive safety and relies on geometry considerations.

Materials should also achieve suitable corrosion properties in order to resist to the chemical reaction with the fuel and to allow the possibility to ease the used fuel reprocessing. Low activation of additional elements is also important, this will restrain the use of compounds such as Molybdenum to improve the properties of the material. Finally, fabricability of the material is also a major concern since the material has not only to be manufactured but it also has to be cost efficient.

1.2. Alloys developed

The first ODS steels have been developed by the CEN-SCK in Belgium during the 70s. In collaboration with the company Dour Metal, they produced two different materials; the DT alloy reinforced with titanium oxides and the DY alloy reinforced with yttrium oxides. Their main particularity was to present a intermetallic brittle χ phase. Later on, MA 956 and MA 957 alloys were commercially developed in England by IncoAlloy and PM2000 by Plansee GmbH in Austria.

Since then, numerous international teams have developed ODS steels; among them we can distinguish the Japan efforts which leads to the elaboration of M and K alloys series, the American (12YWT, 14YWT) and European (Eurofer) series.

Alloy	**Steelmaker**	**Additional elements (wt%)**							
		Cr	Ti	Y_2O_3	W	Al	Mo	Mn	Ni
Eurofer 97 ODS	Plansee [7]	9	-	0.3	1.1	-	-	0.5	-
M11	JAEA [8]	9	0.21	0.37	1.94	-	-	-	0.02
J04	CEA [9]	9	0.22	0.3	1.1	-	-	-	-
12 YWT	Kobe steel [10]	12	0.35	0.25	2.5	-	-	-	-
DT	Dour Metal [11]	13	2.2	-	-	-	1.5	-	-
DY	Dour Metal [11]	13	2.9	0.5	-	-	1.5	-	-
J27	***CEA*** [12]	***13.5***	***0.4***	***0.3***	***0.9***	***-***	***0.27***	***0.32***	***-***
MA 957	IncoAlloy [13]	14	1	0.3	-	-	0.3	-	-
14 YWT	SpecialMetals, Inc. [14]	14	0.4	0.25	3	-	-	-	-
J05	CEA [12]	14	0.3	0.3	1.1	-	-	0.3	-
CPR-BR1	***CEA***	***14***	***0.3***	***0.3***	***1***	***-***	***-***	***-***	***-***
K3	Kobelco [15]	16	0.25	0.3	2	4	-	-	-
J03	CEA [16]	18	0.25	0.55	0.95	-	-	-	-
PM2000	Plansee [17]	19	0.45	0.6	0.04	5.1	-	0.11	-
MA 956	IncoAlloy [17]	21	0.33	0.6	-	5.8	-	0.05	0.11

Table I.1: Chemical composition of the main ODS steels elaborated by powder metallurgy in literature (non exhaustive list). Materials studied in the present thesis appears in bold italics within the table.

1.2.1. A Ferritic-Martensitic Matrix

The fuel claddings to be used in the first ASTRID core, will be manufactured in the already well mastered advanced austenitic steels (15/15 Ti). Nevertheless, they soon will have to be replaced in order to meet the technical specifications, notably concerning the irradiation induced swelling (cf. Figure I.2 and §I.1.1).

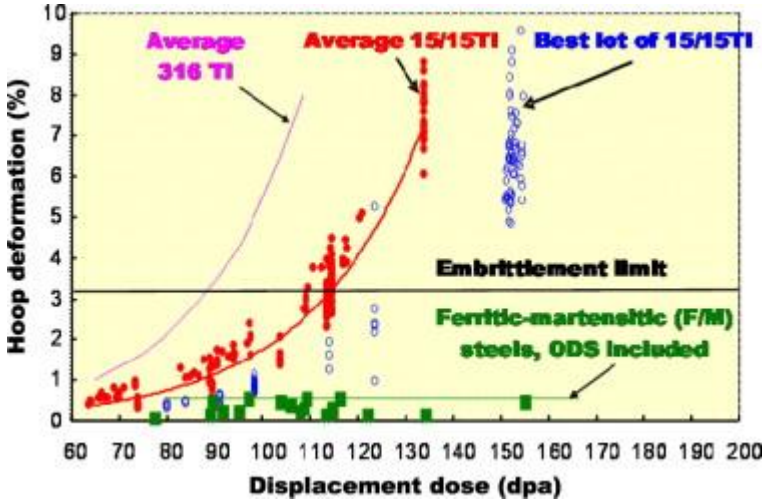

Figure I.2: Irradiation induced swelling resistance for several alloys [18]

The ODS steels under consideration for the future Astrid core have a chromium content ranging from 9 to 20wt% with a very low carbon content. As a result, they have a body-centered cubic crystallographic structure. This structure allows to limit the cavity formation due to void coarsening, and the irradiation induced swelling resistance is further increased by the presence of nanosized precipitates that act as stable sinks for defects such as vacancies and interstitial atoms [19]. Usually, ODS steels are divided into two main series depending upon their chromium content; Ferritic-Martensitic steels with a relatively low chromium content (from 9 to 12 wt%) and ferritic steels with a high chromium content (12 to 20 wt%) (cf. Figure I.3).

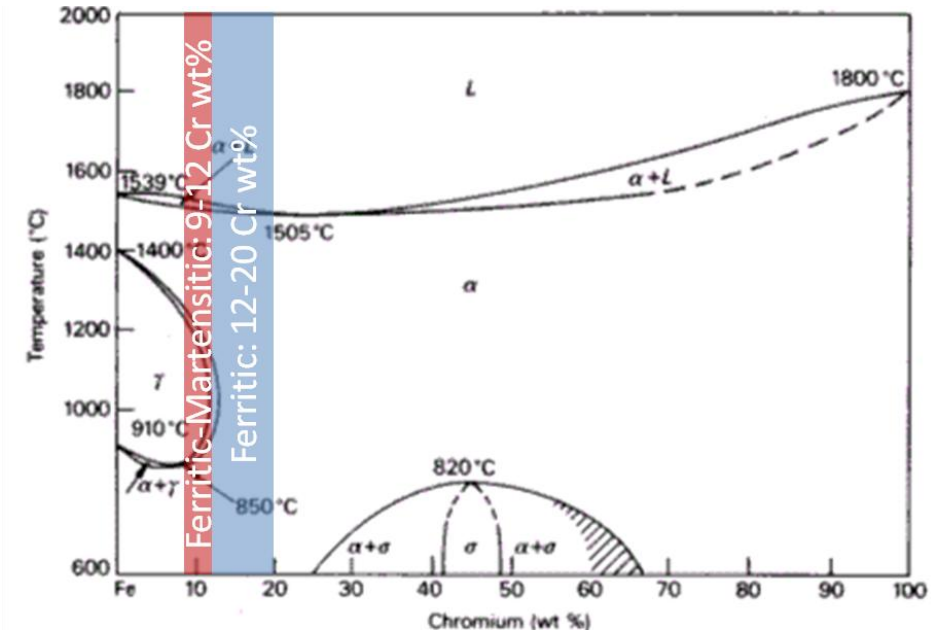

Figure I.3: Fe-Cr phase diagram, the ferritic-martensitic and the ferritic domains are displayed in red and blue respectively.

Martensitic steels exhibit a (α→γ) phase transformation around 850°C. This transformation can be used during manufacturing to obtain isotropic microstructure after cold-rolling, which is of invaluable interest for creep properties. Meanwhile, this phase transformation induces important dimensional variations and inacceptable in-use

modification of mechanical properties. Therefore martensitic steels application is limited to service temperatures under 800°C. Furthermore, if their low chromium content also prevents them from critical embrittlement due to brittle phase precipitates formation [20], it also introduces weaknesses towards corrosion and reprocessing [21].

Ferritic alloys, which will be studied in this manuscript, have a higher chromium content and are indeed more resistant to corrosion [22]. Their reprocessing is eased and they are stable upon the entire temperature range, from room temperature to melting. Nevertheless they present major drawbacks that explains why the choice between the two grades has not yet been made.

The main difficulty to deal with for ferritic ODS steels is their anisotropic microstructure. Indeed, the fabrication process involves extrusion and cold rolling (cf. Figure I.1), which results in a heterogeneous anisotropic microstructure with a strong <110> α-fiber texture, parallel to the rolling direction. These particular features lead to poor mechanical properties in the transverse direction (cf. §I.1.5). Unfortunately, since internal pressure increases in the tube with the accumulation of gas fission products, the major stress component is precisely applied in the transverse direction. The material therefore faces a critical risk of failure. The high chromium content also favours the α/α' demixing and the σ phase precipitation during thermal and irradiation ageing, both introduce hardening and embrittlement [23,24].

1.2.2. Precipitate formation: Yttrium and Titanium addition

Y_2O_3 was already used by Benjamin et al. as oxide dispersion reinforcement when they first developed the mechanical alloying process. Indeed, the main selection criteria to choose a dispersive element are its chemical and morphological stabilities [25]. Regarding stability, Y_2O_3 exhibits spectacular behavior since its standard enthalpy of formation is extremely low (-1920kJ.mol^{-1} at 298K [26]), yttria is therefore still used in recent ODS steels.

Mechanical properties improvement at high temperature is the main favourable effect of oxide reinforcement. Nevertheless, excessive oxides precipitation is known to cause embrittlement and worsen mechanical behaviour. Benjamin and Bomford prove, for example, that the optimum precipitate volume fraction was around 1.5% [25].

Later, following this work, Ukaï laboratory established a reference composition. After demonstrating the significant improvement of thermal creep resistance for Ti and Y_2O_3 content above 0.2wt% [27], they have shown that above 0.25wt%, yttria could risk to impede any recrystallization mechanism [27,28] and proved that high temperature ductility loss occurs for concentrations superior to 0.3wt% [29]. Titanium was also identified as a key element toward precipitation as it allows the formation of nanosized Y-Ti-O precipitates. Indeed, it refines the density and size of precipitates which further

increase creep resistance and nanoprecipitates stability [30–32]. Finally, Ukaï et al. proposed 0.3Ti-0.25Y_2O_3 wt% as an optimum concentration for ferritic ODS steels alloys [33]. The composition of recently developed ODS is still very close to these values (cf. Table I.1).

Using yttria, oxygen is introduced with yttrium in the material. Oxygen is necessary to form nanosized precipitates but excess oxygen content is systematically found after mechanical alloying [34,35]. This contamination could have a important effect and greatly deteriorate the mechanical properties of the material. Nevertheless, after a close study of the subject, Ohtsuka et al. concluded that oxygen excess have to be mastered to a certain level but not be minimized to optimise the final material [36,37].

1.2.3. Additional alloying elements

When developing MA957, J.J. Fisher identified Molybdenum as an important element in order to improve the high temperature mechanical properties [13]. Yet, Mo being highly activated under neutronic flux this element cannot be used for nuclear application. Since then, it has been successfully replaced by Tungsten. To avoid Laves phase formation and subsequent ductility loss, tungsten content is limited to 1 and 2 wt% [38].

The introduction of small Al amounts leads to the formation of Y-Al O phases [39]. These precipitates, larger than the Y-Ti-O oxides induce a drop by 10% of the 700°C UTS and 30% of the uniform elongation [40]. Nevertheless, JAEA is currently developing high Aluminium content (around 3.5wt%) ODS ferritic steel in order to improve oxidation properties. To compensate for this properties degradation, small quantities (~0.7wt%) of Hf or Zr are added to favour the formation of very small precipitates preferentially to Y-Al-O oxides [15,41,42].

1.3. Powder Metallurgy: a unique way to produce ODS steels

1.3.1. Mechanical alloying

High energy ball-milling is currently the most efficient way to produce high quality ODS steels. As a critical and essential step of the ODS steels elaboration, mechanical alloying aims at forcing the chosen oxides into the base metal solid solution. During the process, materials are therefore submitted to severe strains. Numerous materials have already been produced industrially using mechanical alloying (cf. Table I.1). In the case of ODS steel, large industrial quantities have already been produced and an efficient powder elaboration protocol has been stabilized. Nevertheless, the process is currently widely studied and major improvements are still expected from its optimization [31,35,43–48].

During the processing, the base metal powder is placed into a cylinder filled with hard metallic balls. To avoid contamination balls are usually chosen to have a similar composition to the base metal powder. The main principle is to impulse a movement on the cylinder that contain the powders and the balls so that the balls collide (cf. Figure I.1).

Under the impact, the powder particles are plastically deformed which leads to work hardening and fractures (cf. Figure I.4). At the beginning of the milling, the particles are relatively soft, therefore the new surfaces created by fractures enable particles to weld together and form larger particles which leads to an increase in the mean particle size (cf. Figure I.5). As the milling continues, the particles harden and fracture by fragmentation of the brittle flakes or a fatigue failure mechanism. Then, in the absence of other agglomerating force, the fragments may continue to reduce in size. At this stage, the fracturation mechanisms predominate over the cold welding and the mean particle size decreases [49]. At some point, the system will reach a steady-state equilibrium between the welding and the fracturing rates that compensate each other and stabilize to a mean particle size (cf. Figure I.5). During the entire process, crystallographic grain size within the particles constantly decreases to reach a nanosized value by the end of the mechanical alloying.

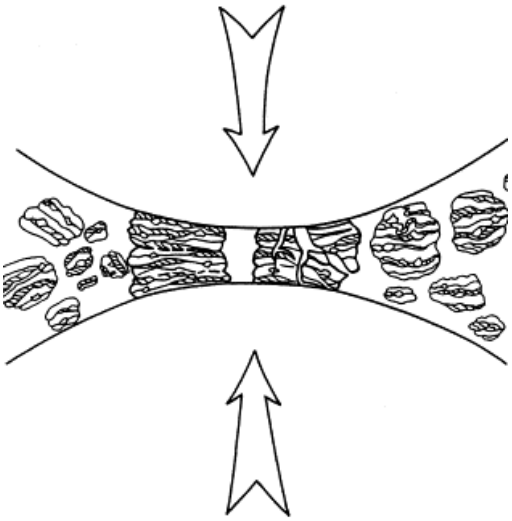

Figure I.4: Ball-powder-ball collision during mechanical alloying [49]

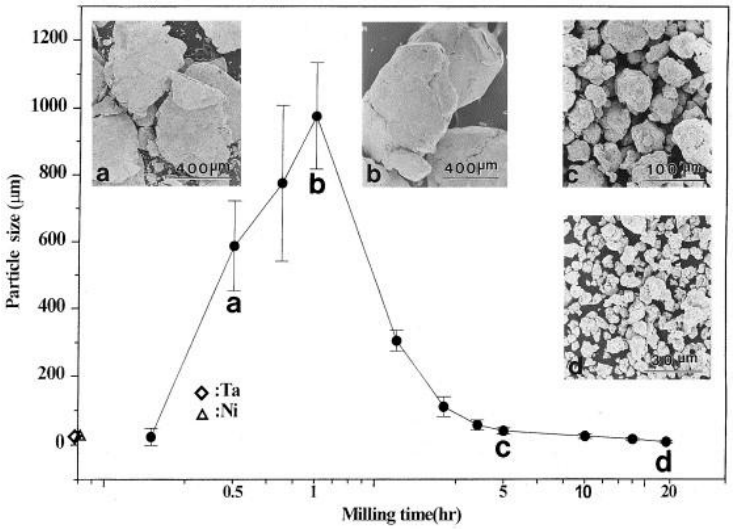

Figure I.5: Particle size distribution as a function of the milling duration [49]

Due to the extreme deformation, a wide range of crystal defects such as dislocations, vacancies, stacking faults and a large number of grain boundaries are present in the base metal powders. As a result, the diffusivity of solutes in the matrix is greatly increased. This enhanced diffusivity combined to the nanosized microstructure are the essential reasons for the high solubility increase after mechanical alloying [49]. In the case of ferritic ODS steel this is the mechanism that allow to force yttrium into solid solution.

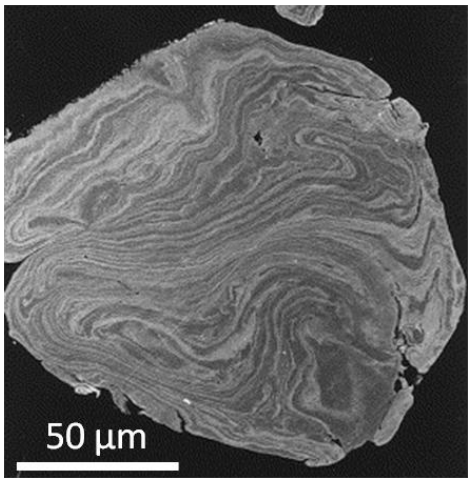

Figure I.6: SEM micrograph depicting the lamellar structure obtained during milling of a ductile-ductile component system (Ag-Cu) [49]

Figure I.6, is a micrograph of the lamellar structure induced by successive fractures and cold welding of a ductile-ductile component system during mechanical alloying. This micrograph depicts the potential extreme complexity of a microstructure deriving from mechanical alloying which goes beyond the sole nanoscale aspect.

Mechanical alloying is the critical elaboration stage. Indeed, the homogeneous distribution of the solute content achieved by ball milling will have a direct effect on the final material properties. Main parameters of mechanical alloying are the design of the milling container which will determine both the optimal amount and ratio of powder and balls. The control of the atmosphere is also very important, since this step is particularly sensitive to contamination [36,44,45]. Finally, intensity and temperature of milling can have a significant effect, notably on final grain size [50].

1.3.2. Casting is cost efficient and straightforward, why not using it ?

In addition to powder metallurgy, casting has been also used to produce ODS alloys for a very long time. Its main advantage is the straightforward industrialisation that casting induce.

However, two major difficulties arise for casting: the wettability of the oxides by the melted steel and the density differences that favours the agglomeration of oxides and therefore create heterogeneities in the precipitate dispersions. Nevertheless, recent studies focusing on a new technique called Disintegrated Melt Deposition technique consisting in the creation of a vortex to enhances stirring [51] or the matrix / oxide wettability [52] are among the encouraging improvement of the method. Casting is still currently seriously studied as a possible elaboration process for the ODS steels [53] but will not be considered in this document.

1.3.3. Mechanically alloyed powder microstructure

Literature on the microstructure of ODS steel powders after ball-milling is quite limited and usually restrained to the determination of yttrium dissolution within the metallic

matrix. Indeed, studies are usually limited to XRD (X-Ray Diffraction) and chemical investigations.

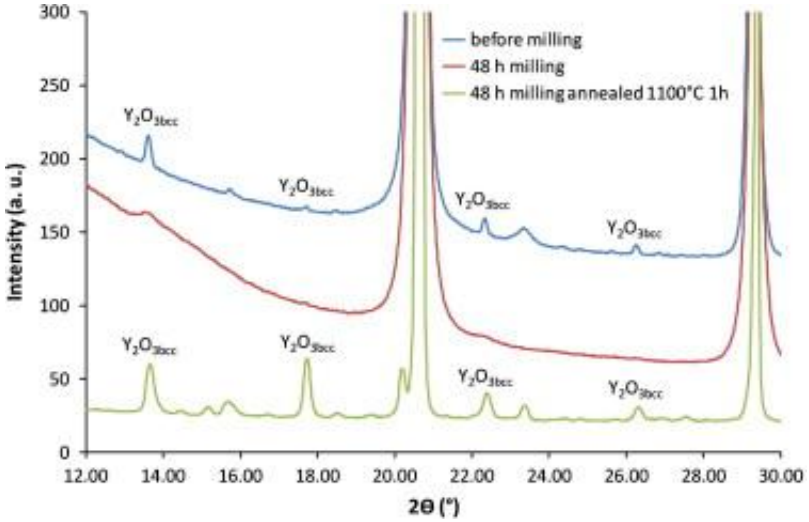

Figure I.7: Transmission XRD diffractogram obtained on a 9%Cr ODS alloy particle. High intensity peaks correspond to the α-Fe phase [54]

Indexation of XRD pattern clearly suggest the dissolution of Yttrium into solid solution within the matrix after milling (cf. Figure I.7) [46,54]. Alinger, Odette and Hoelzer after an extensive work using SANS (Small Angle Neutron Scattering) characterization, reach to the same conclusion [31,55].

The dispersion of elements after milling is generally good enough to obtain an homogeneous distribution of solute within the matrix (cf. Figure I.8) [46,56]. This allow to obtain a suitable special repartition of the precipitates during annealing.

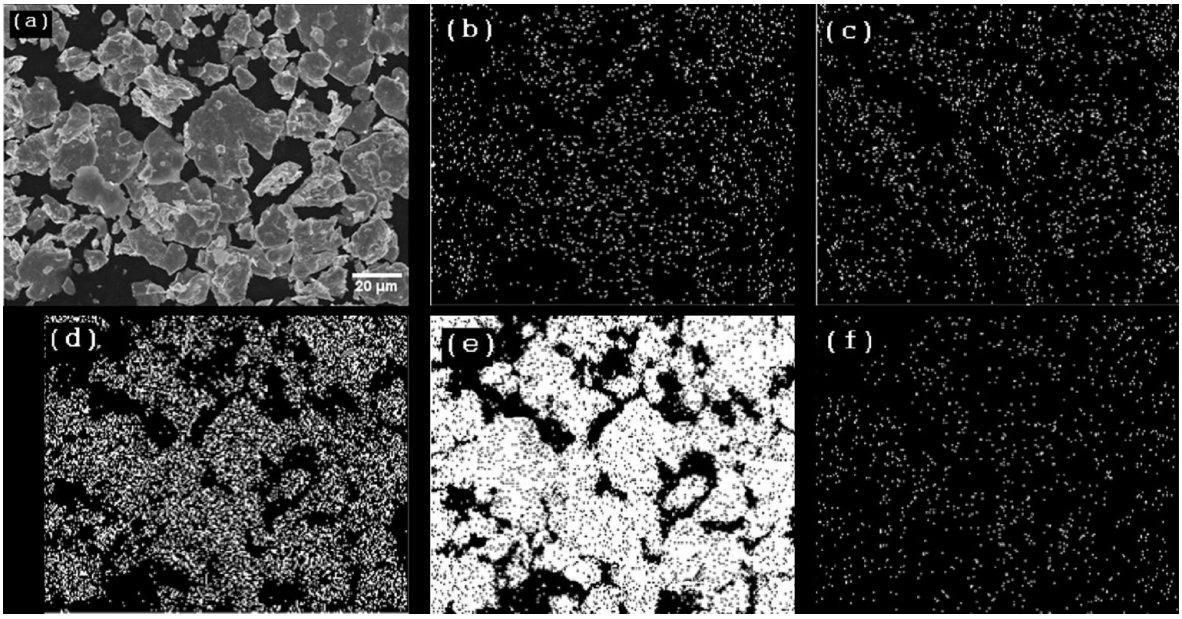

Figure I.8: Chemical map of milled powder after 5 h milling (a) electron image, (b) W, (c) Y, (d) Cr, (e) Fe, (f) Ti [56]

Following XRD results obtained on particles, at the beginning of alloying, crystallite size decreases with increasing milling duration to stabilize to a constant value. There is a large

consensus on the final crystallite size which, assuming isotropic crystallites, is calculated to be close to 20 nm [46,56,57].

Despite the TEM preparation difficulties, several authors managed to obtain suitable samples from particle for observation [58,59]. Because of the high dislocation density, the grain microstructure is difficult to outline, but Kishimoto et al. [59] formulate the hypothesis that grains were anisotropic (which is highly probable looking at the effect of mechanical alloying on other materials: cf. Figure I.6) with length respectively ranging from 25 to 50 nm and 50 to 200 nm, which leads to a grain aspect ratio of about 5.

1.3.4. Sintering

Sintering of ball-milled powder leads to a bimodal microstructure (cf. Figure I.9b) and porosities that do not allow to obtain an optimal consolidation (cf. Figure I.9a).

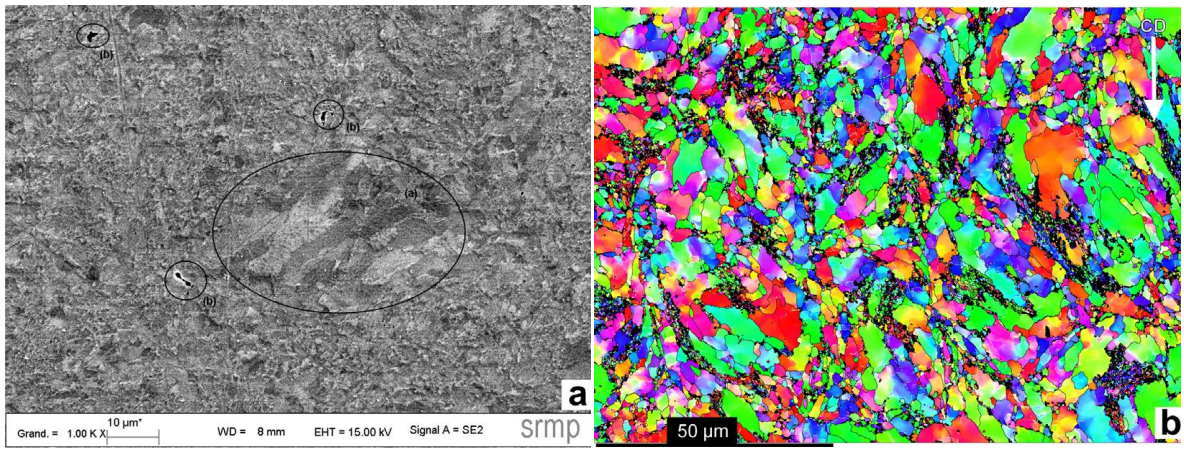

Figure I.9: Hot Uni-axial Pressing material in the longitudinal direction, (a) SEM-FEG image of coarse and fine ferritic grains (b) SEM-EBSD crystallographic orientation map [60]

Recent works on ODS steel sintering demonstrate that an increase in temperature and duration of the sintering allows to improve the relative density of the consolidated material but induces a reciprocal loss of hardness due to grain growth [61]. Interestingly, study on the optimal consolidation pressure shows that increasing the pressure up to 300MPa notably improves the ductility of specimens without any significant microstructural change [62].

1.3.5. Extrusion

To achieve complete consolidation, extrusion is the most commonly used process. After a 2h degassing at 400°C, materials are frequently extruded between 1100°C and 1150°C with a reduction ratio generally close to 15. As a result, in ferritic ODS steels the microstructure obtained is highly textured, and have an anisotropic grain morphology [63]. Indeed, grains exhibit an important aspect ratio, generally around 4 with values as high as 20 for grains which have abnormally grown during the sintering process. Grain dimensions are frequently found to be close to 0.4 µm wide and 1.5 µm long (cf. Figure I.10) [39,64,65].

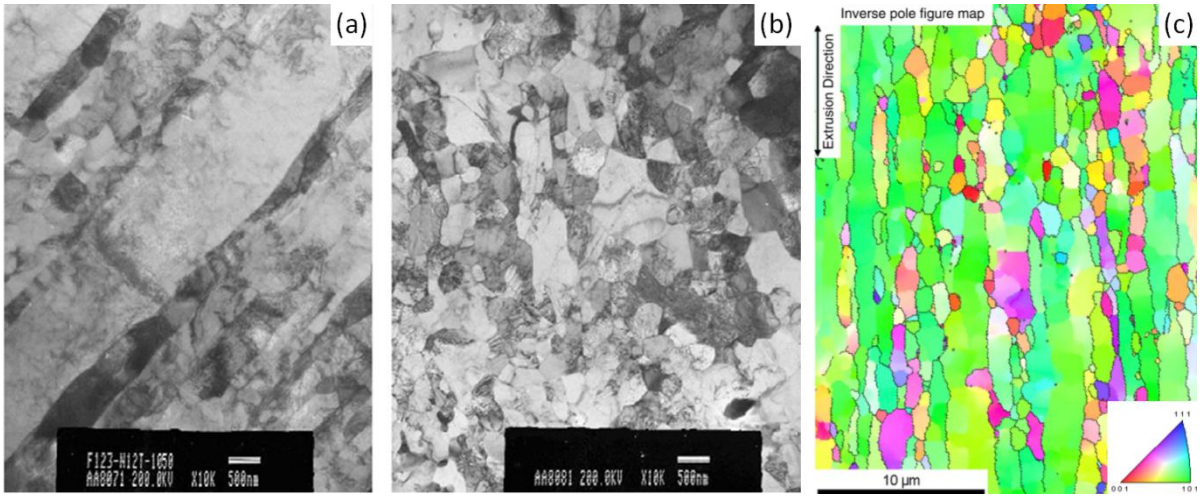

Figure I.10: Bright field micrograph obtained on a Fe14Cr1W0.3Ti0.3Y_2O_3 extruded rod: (a) longitudinal direction, (b) transverse direction [66]; (c) EBSD orientation map obtained on a Fe16.1Cr3.4Al0.09Ti0.27Y_2O_3 [67]

After extrusion, a softening treatment is usually applied to the tubes to ease further cold rolling treatments. This aspect will not be treated in this manuscript, interested readers are referred to the work by H. Réglé [68].

1.3.6. Precipitation

Nanoprecipitation is the essential feature that allows ODS ferritic steels to be considered as serious candidates for fuel cladding application in severe nuclear environment. Indeed, according to [19], even at very low volume fraction (<1 vol%) nanosized oxide dispersion acts as:

- pinning points that impede dislocation movement giving high temperature strength and creep resistance;
- sites for small helium bubbles nucleation, preventing larger bubbles formation, or excessive He migration to grain boundaries which both lead to embrittlement;
- stable sinks for irradiation induced defects such as vacancies and interstitial atoms, reducing hardening defects such as dislocation loops.

Considering the Y/Ti ratio in the precipitates, Sagasegawa et al. established a strong correlation between the size of the precipitates and their yttrium content [69]. No stoichiometric precipitation is found up to ~15nm, larger yttrium, titanium oxygen oxides precipitates are found to be mainly stoichiometric $Y_2Ti_2O_7$. Accordingly, they propose an evolution mechanism of oxides based on Yttrium diffusion. This mechanism is schematised on Figure I.11.

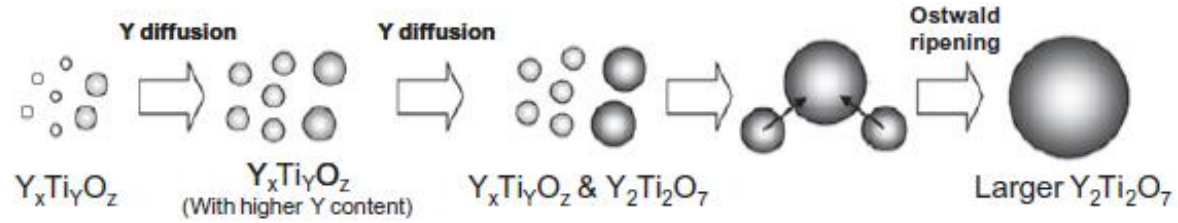

Figure I.11: Schematic illustration for evolution mechanism of oxides [69]

There is six Y-Ti-O oxides with various stoichiometric crystalline structures [70], at least four of them have been reported in ODS steels:

- $Y_2Ti_2O_7$: structure pyrochlore,
- Y_2TiO_5: structure hexagonal,
- $YTiO_3$: structure orthorhombic,
- $Y_{x1}Ti_{y1}O_{z1}$: structure orthorhombic.

Among them, $Y_2Ti_2O_7$ precipitates are the most commonly found, Y_2O_3 are also frequently observed in ODS steels. A description of their structure and relation with the matrix can be found in a HR-TEM study by Ribis et de Carlan (cf. Figure I.12 and Figure I.13) [71]. They highlight the presence of strain field typical of coherent precipitates with small misfit and interpret the low interfacial energy as the main factor for coarsening resistance rather than slow diffusion rate of yttrium.

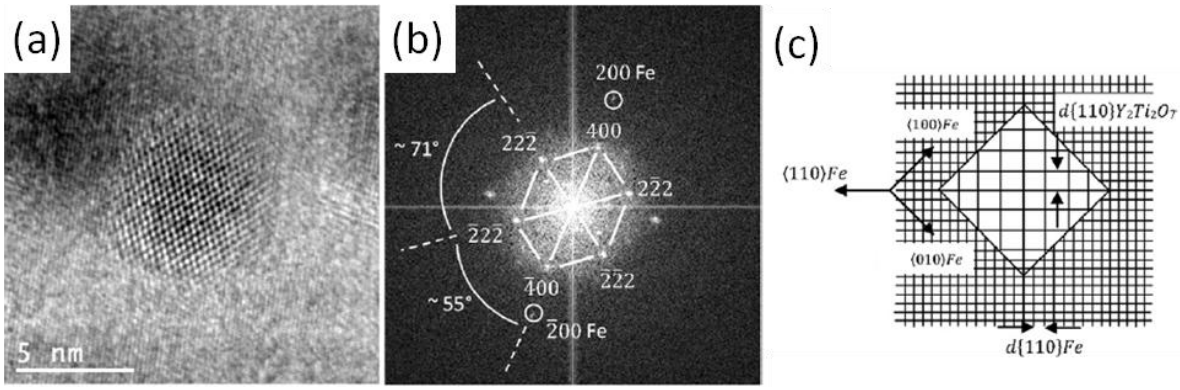

Figure I.12: Cubic particle characterized as $Y_2Ti_2O_7$ type particle: (a) HR-TEM, (b) corresponding FFT showing B=110 of the $Y_2Ti_2O_7$ structure orientation of the Y-pyrochlore-type particle (c) schematic inferred representation of the particle embedded in the α-Fe matrix [71]

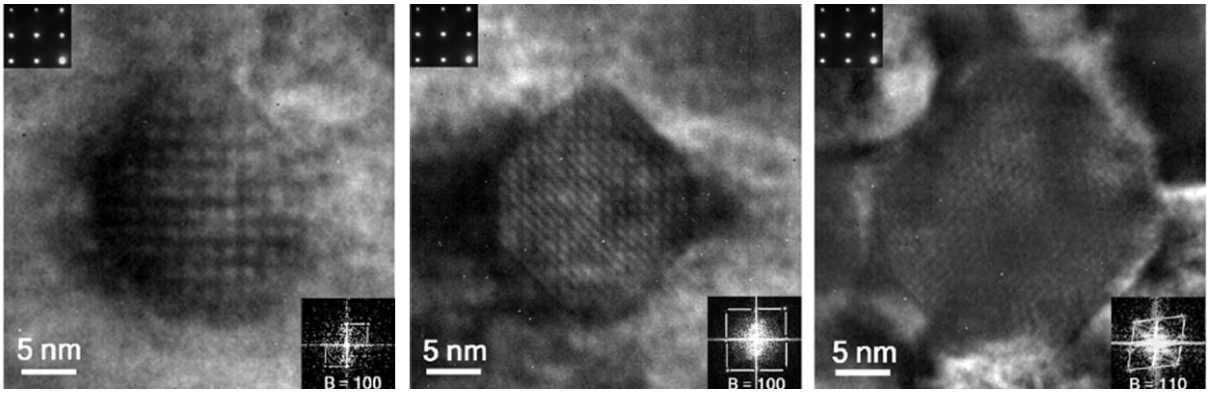

Figure I.13: Y_2O_3 particles observed by TEM and HRTEM : (a) cuboïdal bcc particle and FFT, (b) truncated cuboidal fcc particle and FFT, (c) truncated cuboidal fcc particle and FFT [71]

In addition to Yttrium containing precipitates, material is contaminated by large Ti and Cr oxides, usually located at the boundaries of the former powder particles. The formation of these oxides has to be circumscribed to avoid the deterioration of the global mechanical properties. Other studies, evidencing a core / schell structure with a yttrium core for very small precipitates proposed a precipitates formation mechanism based on the interaction between chromium and yttrium.

Nevertheless, the dense nanoprecipitation is the key factor that allows the ODS steel to achieve the excellent high temperature mechanical behaviour presented in the next section.

1.4. Mechanical resistance of ODS ferritic steels: a promising behaviour for severe nuclear environment

Mechanical resistance achieved by ODS steels largely outperforms classical steels. For example, they exhibit a stress improvement of ~200MPa for a given Larson-Miller parameter compared to nobium reinforced Martensitic steels (cf. Figure I.14). Klueh et al. [17] and Ukai et al. [33] demonstrate tensile stress and creep properties superiority of ODS steels, even towards austenitic steels.

Once again, these properties are largely due to the nanoprecipitates. Furthermore, as shown on Figure I.14, it was reported that the finer the precipitates distribution, the better the creep properties [17,72].

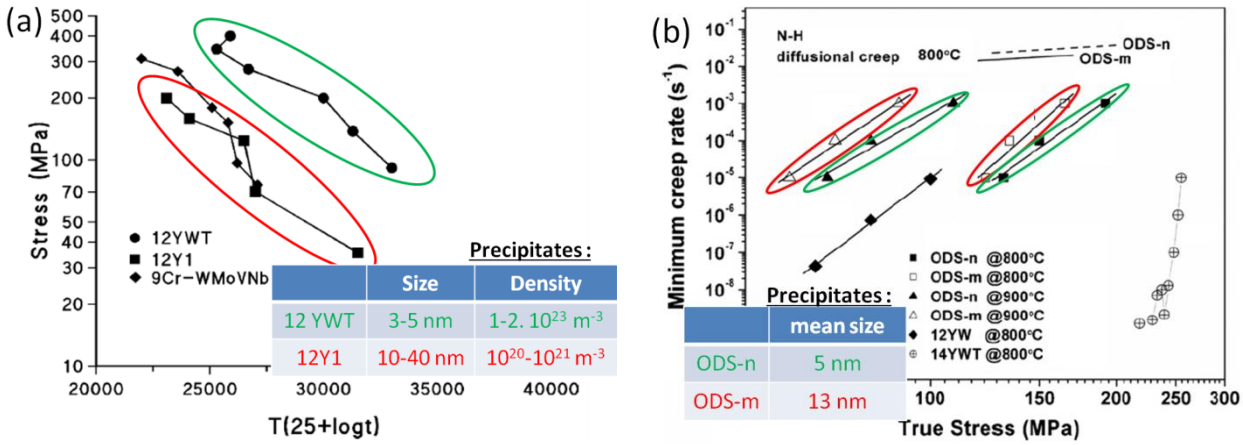

Figure I.14: Influence of nanoprecipitates population on the ODS steels creep properties: (a) Rupture stress vs. Larson Miller parameter for the ODS steels 12Y1 and 12YWT and a conventional Martensitic steel NF616 [17], (b) Strain rate vs. True Stress for two ODS alloys (Fe-12Cr-2W-0.5Y_2O_3 wt%) and comparison with two other literature alloys [72]

According to [17,72], the dominant deformation mechanism is dislocation glide. Creep behaviour is quite complex to describe due to interaction between dislocation and nanoprecipitates. Brandes et al. proposed a mechanism that explain strengthening from nanoprecipitates due to their attractive interaction with glissile dislocations. Creep would therefore be controlled by stress-assisted thermal activation of dislocation movement from precipitates traps [73]. As a result, the distance between nanosized particles is a key

feature that controls the deformation of the material and for a given volumic fraction, the main parameter is the particle size.

1.4.1. Thermal stability

To achieve creep properties meeting the technical specifications, the thermal stability of the final extruded microstructure has to be very high during aging. Indeed, in a MA957 steel, after high temperature long term annealing, Cunningham et al. have demonstrated the extreme stability of the nanoprecipitates under 900°C even for a 20 000h ageing duration. Following this result, a precipitate coarsening model based on yttrium pipe diffusion was proposed [74]. High stability of both ferritic grains and nanoprecipitates had already been pointed out in earlier works by P. Miao and M.K. Miller [65,75]. Nevertheless, thermal ageing is still a important issue and several authors reported hardening leading to embrittlement and ductility loss, due to Al pollution resulting in a nanoprecipitates coarsening (in Fe-14Cr-2W-0.3Ti-Y_2O_3 wt% alloys) [76] or due to formation of α' particles and intermetallic σ phase (in Fe-18Cr-1W-0.3Ti-0.3Y_2O_3 wt% alloys) [77]. Another example can be found in the limited loss in mechanical properties attributed to Ti depletion in the matrix and the following formation of coarse Ti-oxides (cf. Figure I.15).

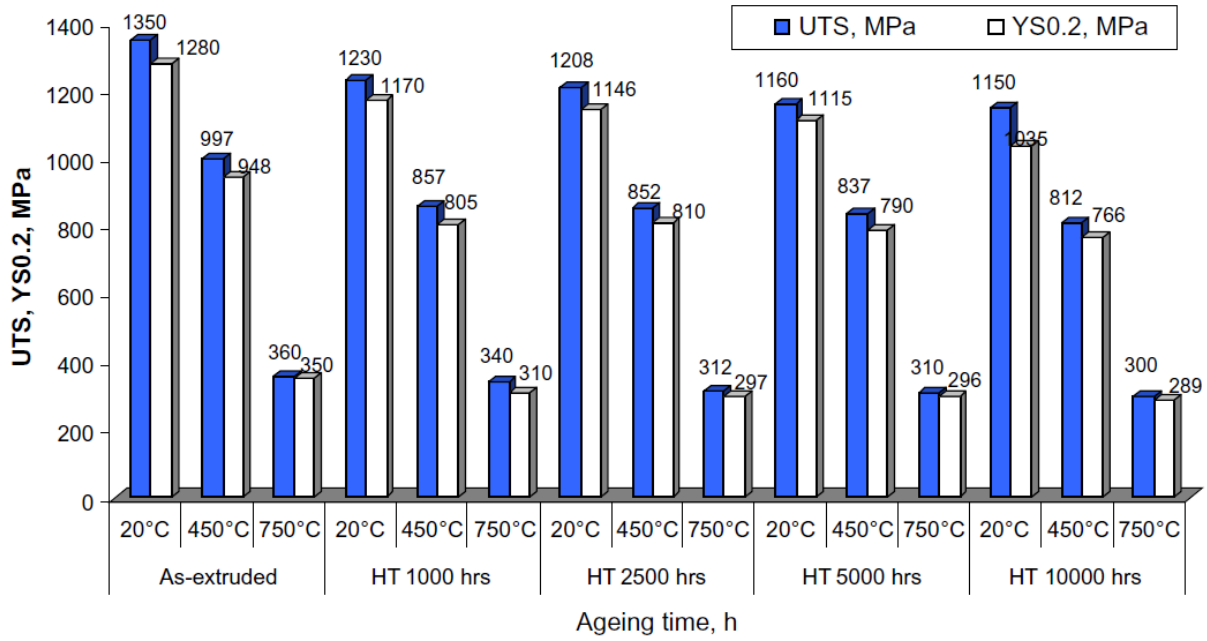

Figure I.15: Ultimate tensile strength and yield strength of a MA957 ODS steel after ageing at 750°C up to 10000h [74]

1.4.2. Stability in nuclear environment

ODS steels mechanical response after irradiation is satisfactory, despite moderate hardening inducing ductility loss and a DBTT shift of (cf. Figure I.16). Still, it remains significantly better than that of conventional ferritic / martensitic steels [78].

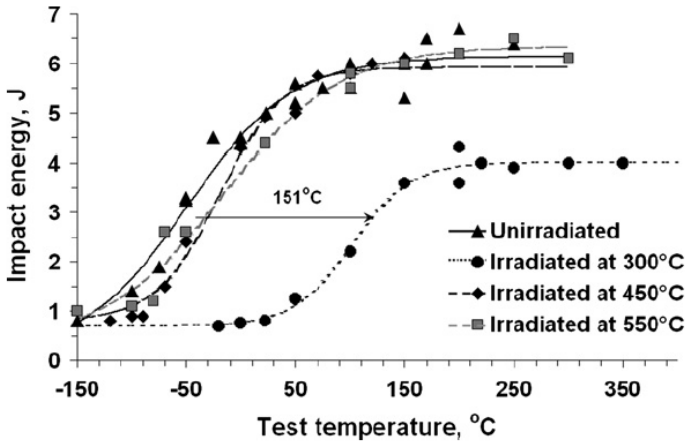

Figure I.16: Charpy impact energy of ODS Eurofer 97 steel irradiated with neutrons (3 dpa) at different temperatures [79]

Noteworthily, material response to irradiation highly depends upon the irradiation temperature. Indeed, temperature activated mechanism allow to partially restore irradiation damage.

Irradiation resistance is highly related to the nanoprecipitation stability. Most studies report only minor changes on the precipitate population and structure during irradiation [80–84] consisting in a slight decrease of precipitate density correlated with an increase of precipitate mean size (cf. Figure I.17). Meanwhile some studies raised question towards the possible dissolution of precipitates under irradiation [85], this phenomenon seems to be more likely to be linked with amorphization of yttrium oxides that with plain dissolution [86].

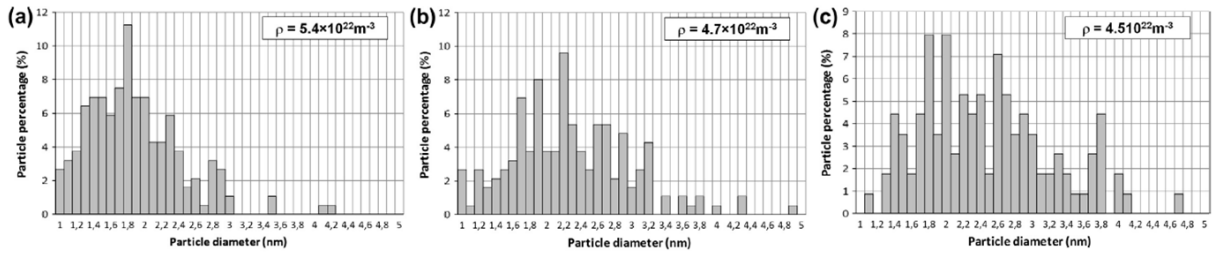

Figure I.17: Evolution of the MA957 ODS steel particle size distribution under ions irradiation ; (a) non-irradiated material (b) after 50 dpa at 412°C (c) after 75 dpa at 430°C [84]

Lescoat et al., using *in-situ* TEM have followed the evolution of several individual nanoprecipitates and report their stability up to 45dpa. They also evidenced interface and shape modification on larger oxides, which seemed more affected by irradiation that nanoparticles [83].

Precipitates interfaces are sinks for irradiation defaults, consequently, Helium released during nuclear reaction has a strong tendency to form bubbles around nanoprecipitates [87,88]. The smaller the precipitates, the smaller the He bubbles and the less cavity formed. Therefore, precipitates size distribution have a major impact on He induced embrittlement; fine and homogeneously dispersed precipitation significantly increase

ODS steels irradiation resistance.

1.5. Mechanical anisotropy: a major weak point

An important step of the ODS ferritic fuel clad manufacturing is the extrusion. The direct consequence of the process is the occurrence of an anisotropic microstructure has evidenced in §1.3.5. This microstructural state will necessarily have some influence on mechanical properties. Indeed, since 1993, Ukaï established the degradation of mechanical properties in the transverse direction compared to the longitudinal direction [89]. This problem is of major importance. Indeed, considering the nuclear aspect of the application, this apparent weakness has to be address or justified by safety authorities to consider ODS steels has in service claddings materials.

In ferritic steels, there is no phase transformation possibility. Therefore, anisotropy seems to be inevitable after extrusion. Indeed, the extrusion process results in a heterogeneous anisotropic microstructure with a strong <110> α-fiber texture, parallel to the rolling direction (cf. Figure I.10c). This is worsened by abnormal grains that results in very elongated and heterogeneous grain shapes. This particular feature leads to poor mechanical properties in the transverse direction [12,67]. Unfortunately, since internal pressure increases in the tube with the accumulation of gas fission products, the major stress component is precisely applied in the transverse direction. As a result, the material faces a critical risk of failure and control of the microstructure is a key issue to ensure that it can fulfil the role of first barrier against radioactive element release.

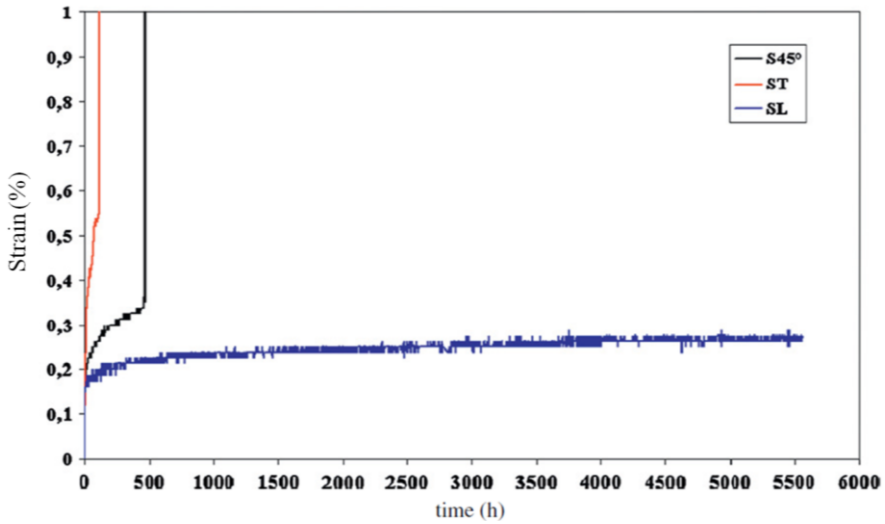

Figure I.18: Thermal creep curves of CEA 18Cr alloy elaborated by hot extrusion, 650°C - 350 MPa [90]

Stress direction appears to have a strong influence upon creep properties and an important lifespan drop of the material is observed when stressed in the transverse direction (cf. Figure I.18) [90]. Furthermore, no measurable tertiary creep stage is observed on ODS steel (even in longitudinal direction), which leads to a fast and non warningly final fracture.

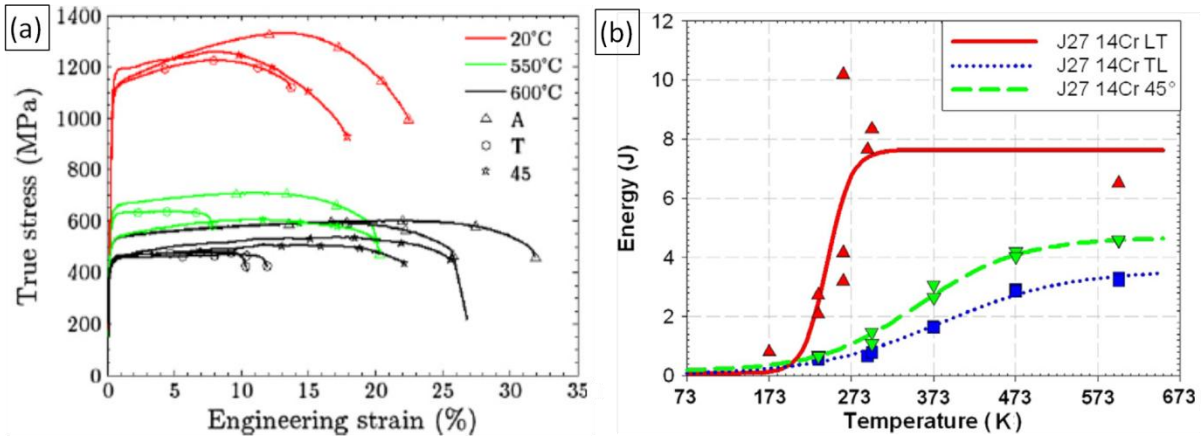

Figure I.19: Mechanical anisotropy; (a) Tensile curves of the J05 ODS steel for three loading directions: axial (A), transverse (T) and rotated by 45° from extrusion direction (45) [64] (b) ductile brittle transition for the J27 ODS steel for three loading directions [12]

This anisotropy can also be evidenced on tensile and toughness properties as reported in many studies (cf. Figure I.19 [12,64]).

So far the only available solution to deal with anisotropy is very high temperature recrystallization which leads to exaggerated grain growth. Indeed, extensive work on cold working stage parameters by A. Alamo and H. Reglé [68,91,92], lead to very high temperature recrystallisation treatment (1350°C) after the extrusion stage. Nevertheless, microstructural anisotropy have to be addressed, and this can only be achieved by a profound microstructural transformation. As expressed earlier, no phase transformation is available for ferritic ODS steels. Recrystallization therefore constitutes the major available mechanism to restrain anisotropy and is a key phenomenon in order to develop proper ferritic ODS steels cladding tube.

2. Deformation and recrystallization

When a material is deformed, a part of the energy used for its deformation is stored within the microstructure. Annealing a deformed material results in different phenomena for which the driving force is the reduction of stored the energy. Those various phenomena can be referred to as recrystallization. Main aspects of recrystallization will be presented here.

2.1. Historical background

In 1829, after studying the acoustic anisotropy of wood and rock [93], Félix Savart managed to reproduce the same effect on various metal specimens, and to demonstrate that metals consisted in crystallized parts of different orientations. He also recorded the first evidence of structure change after deformation and subsequent annealing while he figured out that this treatment was modifying the anisotropic properties of metals [94].

About half a century later, H.C. Sorby by introducing metallographic techniques, reported the formation of an equiaxed grain structure from the annealing of elongated grains in a deformed iron [95]. In 1886, he was the first to termed this process recrystallization.

Despite these fundamental discoveries, recrystallization and grain growth had not been distinguished as separated processes. In the early 1920s', Carpenter and Elam followed by Altherthum clearly established that while grain boundary energy provides driving force for grain growth, stored energy provides driving force for recrystallization. Deformation is then clearly established as the initiating process for recrystallization.

2.2. Deformation in crystals

To account for both the plastic deformation and the relatively low shear stress compared to the theoretical shear stress expected from perfect crystal (~1/10). Polanyi, Orowan and Taylor separately introduced the concept of dislocation in 1934.

A dislocation is a line defect trough the crystal structure along which the crystallographic registry is lost. It is characterized by the Burgers vector (b), representing the magnitude and direction of shear produced by the dislocation and the line vector (t) that points the local direction of the dislocation line. The nature of the distortion associated with the dislocation depends upon the relative orientation of b and t. When the two vector are parallel the dislocation is a screw dislocation, when they are orthogonal the dislocation is an edge dislocation (cf. Figure I.20). In real materials, dislocations are mainly mixed dislocation with a varying angle between Burgers and line vectors.

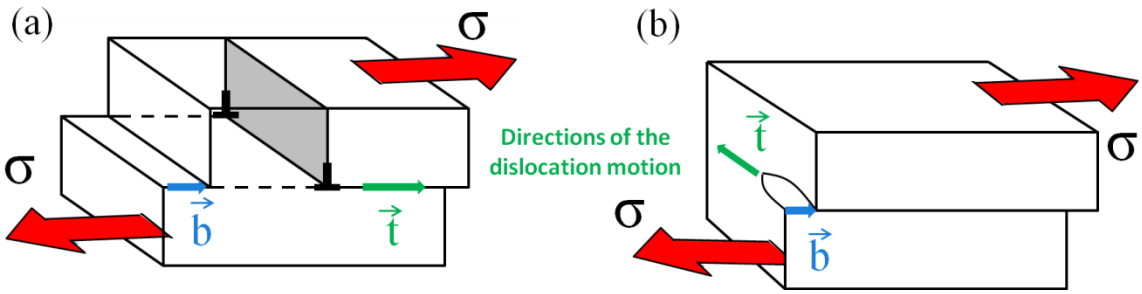

Figure I.20: Direction of the dislocation motion; (a) edge dislocation moved by the applied stress (σ) (b) screw dislocation moved perpendicularly to the applied stress (σ). b: brugers vector, t: line vector

Under an external stress σ, the dislocation produces shear deformation (τ) that will contribute to the macroscopic deformation (cf. Figure I.21). Indeed, it would be extremely difficult to shear a crystal by forcing the glide of atoms planes; one would have to force the simultaneous reconfiguration of every crystal bond that crossed the slip plane. This explains the differences between theoretical and practical shear stresses. A critical stress level τ_c called resolved shear stress is needed to activate slip planes and dislocations gliding,. This stress level increases when dislocation crosses crystal defaults such as precipitates, grain boundaries or other dislocations. The later leads to work hardening: the more deformed the material is, the more energy is needed to deform the material.

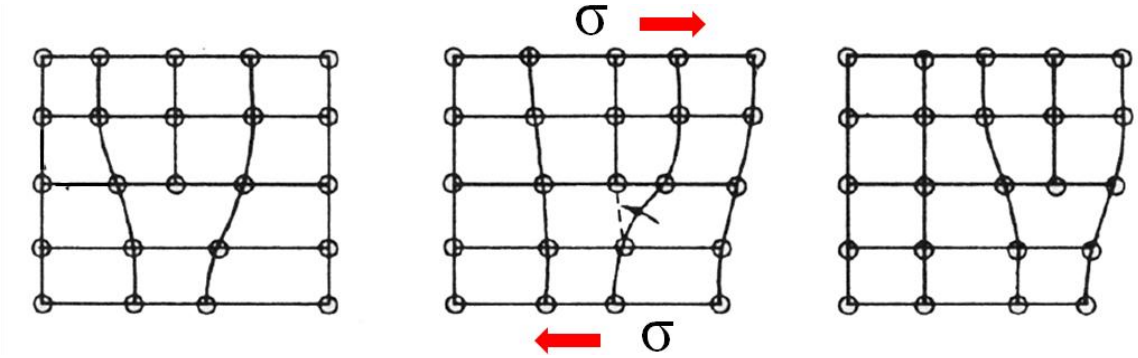

Figure I.21: Dislocation gliding within a simple cubic crystal

About only 1% of the energy consumed to deform a metal remains as stored energy in the material. This energy that will later provides the driving force for microstructural change is stored under the form of dislocations (cf. Figure I.22) and defects accumulation within the crystal lattice. Point defects, generally have such a high mobility that they do not contribute to store the energy of deformation. Therefore, almost the entire stored energy is derived from the accumulation of dislocations and the formation of new interfaces (grain boundaries).

2.3. Energy storage within metallic materials

Energy stored in materials is a key feature when studying recrystallization behaviour. Indeed, heterogeneities in the deformation state of the material provides the necessary driving force for any potential phase transformation. Therefore, understanding of energy storage mechanisms is needed to later be able to measure and interpret recrystallization.

2.3.1. Dislocation stored energy

The origin of the energy stored by a dislocation results from the stress imposed to the atoms neighbouring the dislocation (cf. Figure I.22).

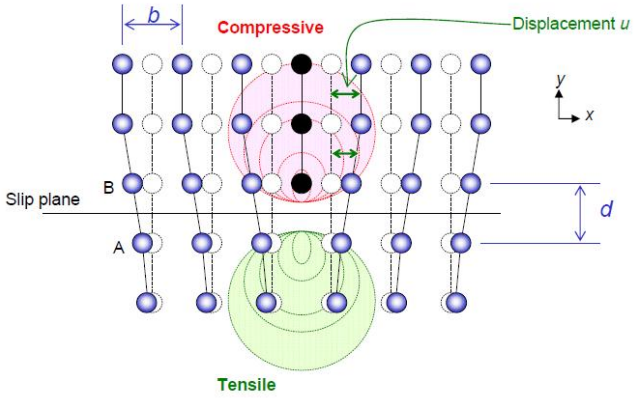

Figure I.22: Origin of a dislocation energy: the distortion associated with the displacement of atoms from their equilibrium position

The energy retained by a single straight dislocation lying in a perfect crystal with an isotropic elasticity can be expressed as follow:

$$\Gamma = \frac{\mu b^2}{4\pi(1-\nu)}(1-\nu\cos^2\varphi)ln\left(\frac{Re}{R_0}\right) \quad \text{(I.1)}$$

Where $\boldsymbol{\Gamma}$ is the energy per unit length stored by a single dislocation, μ is the shear modulus, $\boldsymbol{\nu}$ is the Poisson's ratio, $\boldsymbol{\varphi}$ is the angle between Burgers vector and the line vector of the dislocation, $\boldsymbol{R_e}$ is the upper cut off radius and $\boldsymbol{R_0}$ is the inner cut off radius [96].

The two cut-off radius can be imagined as the influence area of the elastic stress field produced by a dislocation. Equation (I.1) accounts for both the elastic strain energy and the dislocation core energy. The latter being about 1/15 of the total energy, the dislocation core energy is often neglected by taking R_0 between b and $5b$.

For infinite crystals, the upper cut off radius Re tends to diverge as a consequence of the long range character of the elastic strain field around the dislocation ($\propto 1/r$) [97], which would mathematically lead to an infinite amount of stored energy. In a real material containing a dislocation density ρ, dislocations interact with each other via their long range stress field. The outer cut off radius is no longer of the order of the crystal dimension, but it will depend on the dislocation arrangement. For homogeneously distributed dislocations, the common assumption is that stress fields of dislocations cancel each other beyond a critical distance defined as the mean distance between dislocations ($\propto 1/\sqrt{\rho}$) [98]. Therefore, the energy stored by a dislocation highly depends on its neighbouring environment.

Indeed, dislocations' interaction is important as they can exert on each other repulsive and attractive force depending upon their types, signs and orientations. This results in specific dislocation structurization (cf. Figure I.23).

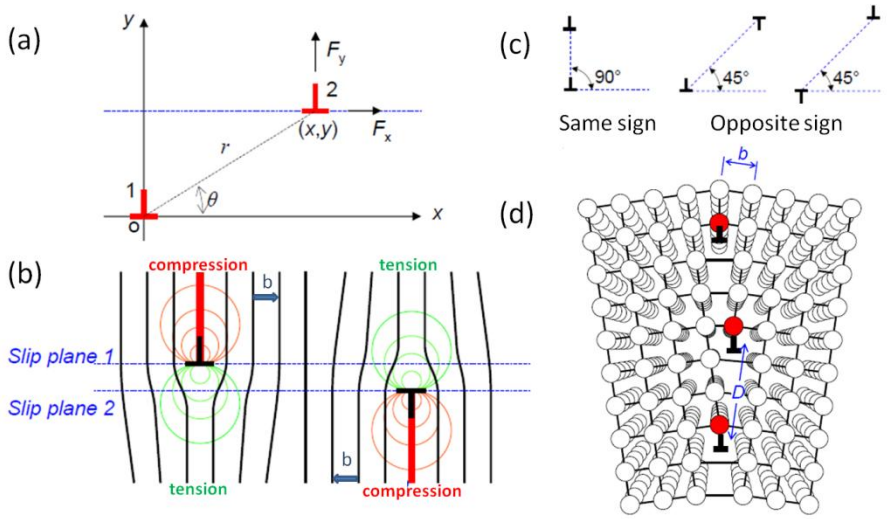

Figure I.23: Dislocation structurization: (a) forces on dislocation can be resumed as Fx (the gliding force) and Fy (the climbing force) (b) depending upon their configuration dislocations will attract or repulse each other, in this situation they are attracting (c) stable position for two edge dislocations (d) low angle boundary formed from edge dislocations.

When the density of dislocation becomes too high, the structurization of dislocation produces self screening features such as dislocation walls which no longer produce long range internal stress ($Re < 1/\sqrt{\rho}$) [99]. Indeed, low energy dislocation structures form during deformation to reduce the total energy of the system. Several factors influence the formation of dislocation structures: intrinsic factors (phase, precipitation, solute texture) and extrinsic factors ($\varepsilon, \dot{\varepsilon}, T, \sigma$). Stacking fault energy has also a strong effect on the structurization of dislocations. Indeed, while in low stacking fault energy materials, the dislocations are mainly restricted to planar slips, in high stacking fault energy materials, dislocations can cross slip and structurization is favoured by this additional degree of freedom.

For a uniform distribution of dislocations or dislocation cells, a direct relation is found between the stored energy and the dislocation density:

$$E_D = \rho . \Gamma \tag{I.2}$$

Considering an equivalent distribution between edge and screw dislocations and disregarding the logarithmic variation of the line tension (elastic energy per unit length) with the dislocation density, the final expression is then approximated to:

$$E_D = \frac{1}{2}\mu b^2 \rho \tag{I.3}$$

When dislocations form low angle grain boundaries (cf. Figure I.23), the stored energy can no longer be measured from the sole dislocation density. It has to be estimated from the subgrain diameter and the specific energy of the low angle grain boundaries which comprise the subgrain walls:

$$E_D = \frac{3\gamma_s \theta}{D\theta_m}\left(1 - \ln\frac{\theta}{\theta_m}\right) \tag{I.4}$$

Where $\boldsymbol{\gamma_S}$ is the specific energy, $\boldsymbol{D}$ the subgrain diameter, $\boldsymbol{\theta}$ the misorientation angle between adjacent subgrains, $\boldsymbol{\theta_m}$ the limiting misorientation angle above which the description of the subgrain by a dislocation array is no longer possible because dislocation cores would overlap.

As pointed out by several authors [100,101], the misorientation between adjacent subgrains is of importance when considering the stored energy.

A strong dependency of the stored energy towards the different texture components has also been reported [102,103]. Indeed, dislocation preferentially takes up on planes with the smallest distance between atoms. In a bcc structure for example, $\{110\}\langle uvw\rangle$ and $\{111\}\langle uvw\rangle$ orientations are reported to be the main dislocation storage component which often results in elongated cells. Meanwhile, $\{211\}\langle uvw\rangle$ and $\{100\}\langle uvw\rangle$ which are low energy component are associated with larger equiaxed cells.

2.3.2. Driving pressure

When the substructure is formed and subgrains or grains are easily identifiable, then grain or subgrain growth (and its reciprocal reduction in boundaries' area) is a net contributor to the driving pressure. This contribution which is enormous in the case of nanosized grains can, in a simple isotropic grains approximation, be expressed as: $E_g = 2\gamma/R$ (γ: grain boundary specific energy, R: main grain radius). The total stored energy contributing to the driving pressure can therefore be expressed as follow:

$$E_T = E_D + E_g \tag{I.5}$$

Comparatively to phase transformation like solid state transformation or the latent heat of fusion for a metal, energies involved in the microstructure evolution during annealing of deformed materials are much smaller. Indeed, energy for recrystallization is about ~10-100 J.mol^{-1} and recovery is about a tenth of it for grain size of 250 nm, compared to respectively ~1 kJ.mol^{-1} for solid state transformation and ~10kJ.mol^{-1} for the latent heat fusion. Thus, annealing a deformed material is a very energy efficient way to modify the microstructure and eventually improve the properties of a material.

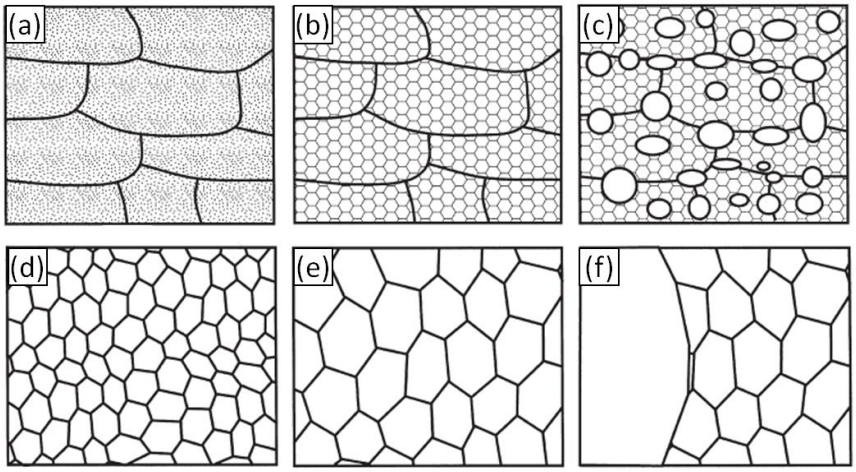

Figure I.24: Schematic diagram of the main microstructural evolutions during annealing; (a) deformed state, (b) recovered, (c) partially recrystallized, (d) fully recrystallized, (e) grain growth, (f) abnormal grain growth [104]

Figure I.24, schematically summarizes the sequence of phenomena occurring when a deformed material is annealed, which starts from the recovery of the microstructure and can lead to abnormal grain growth as developed later (cf. 2.7).

2.4. Recovery

Recovery can be described as the ability of materials to partially restore their microstructure from a non-equilibrium state in which a high density of defects has been introduced into the material. Recovery is primarily due to the reorganization of stored dislocation structures, under the action of both the thermal activation and their internal stresses (cf. Figure I.23).

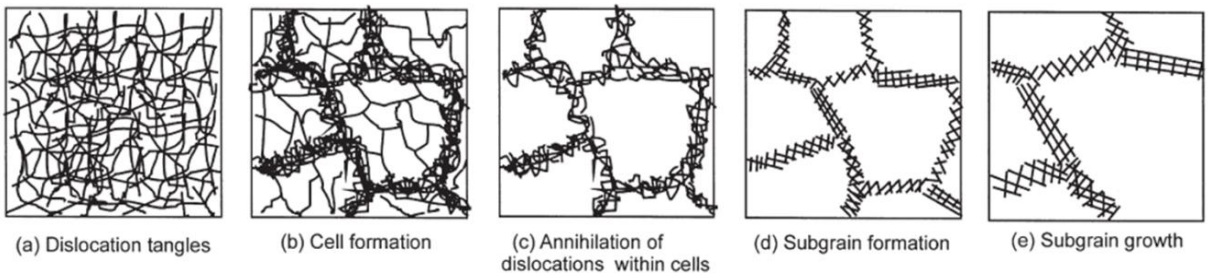

Figure I.25: Recovery stages of a plastically deformed material [104]

The general trend of the dislocation arrangement evolution during recovery has been schematized by Humphreys et Hatherly [104] (cf. Figure I.25). In real materials, some of the stages may have already occurred during deformation or others can significantly overlap between them depending on both the applied treatment and the material characteristics. Description of the recovery process, by a clear distinction between successive recovery stages, is therefore extremely difficult to perform in real materials. The importance of recovery comes from the fact that it consumes the stored energy needed for recrystallization; as a result recovery and recrystallization act as competing processes.

2.4.1. Recovery kinetics and boundary mobility

When reporting on the recovery kinetic, authors have usually emphasized on elementary mechanisms of the cells or subgrain formation (dislocation cross slip) (Kuhlmann [105], Friedel [97]).

If the kinetic of recovery is assumed to be controlled by dislocation climb or thermally activated glide of dislocations, that is to say by dislocation velocity and further assuming a direct correlation between dislocation density and internal stress, this leads respectively:

- For a dislocation climb controlled mechanism to:

$$\frac{1}{\sigma_0^2} - \frac{1}{\sigma^2} = \frac{2D_s c_j}{\alpha^2 G b k T} t \qquad \text{(I.6)}$$

Where c_j is the concentration of jogs.

- For a thermally activated glide of dislocation controlled mechanism to:

$$\sigma = \sigma_0 - \frac{k_b T}{V} \ln\left(1 + \frac{t}{t_0}\right) \quad \text{(I.7)}$$

Where V is the activation volume.

In these models, authors did not specifically consider the microstructure's features (distribution and density of dislocations or cells/subgrains' size).
Experimental measurements of subgrains' growth have been reported to follow the form:

$$D^n - D_0^n = c_1 t \quad \text{(I.8)}$$

Where $\boldsymbol{n}$ is a constant, $\boldsymbol{c_1}$ is a temperature dependant rate constant, $\boldsymbol{D}$ is the subgrain size and $\boldsymbol{D_0}$ is the subgrain size at $\boldsymbol{t = 0}$. $\boldsymbol{C_1}$ contains both a mobility and a driving force (surface energy). As subgrains grow, misorientation tends to increase which reduces the specific energy of the boundary as stressed out in (I.4).

Mobility of grain or subgrain boundaries is thermally dependent and usually follows an Arrhenius type law:

$$M = M_0 exp\left(-\frac{Q}{RT}\right) \quad \text{(I.9)}$$

Where $\boldsymbol{M_0}$ is the intrinsic mobility, $\boldsymbol{Q}$ is the activation energy.

A large number of experimental results points out the stability of activation energy for a range of subgrain sizes and grain boundary misorientation. Those results are consistent with the interpretation made by Sandström [106] that the boundary migration occurs by dislocation climb, at a rate controlled by solute diffusion in the lattice (cf. Table II.6).

T_m (K)	G (GPa)	b (nm)	Qs (kJ.mol^{-1})	Qc (kJ.mol^{-1})	Qb (kJ.mol^{-1})	γ_b (J.m^{-2})
1810	69.2	0.248	239	174	174	0.79

Table I.2: Activation energies for self, core and boundary diffusion of ferritic steel [107]

Considering this mechanism, Sandström [106], and Ørsund and Nes [108] proposed the following expression for low angle grain mobility:

$$M_{sg} = \frac{D_s b}{kT} \quad \text{(I.10)}$$

$\boldsymbol{D_S}$ is the coefficient of self diffusion.

Nevertheless, this expression is not entirely satisfying since it is intrinsically unable to take into account the dependence of the mobility upon the boundary structure misorientation (θ).

2.4.2. Subgrain growth mechanisms

During recovery, two main processes can be encountered for subgrain growth. Subgrain coalescence, originally introduced by Li [109] and further developed by Doherty [110], and subgrain boundary migration for which the reader is referred to the enlightening following articles (Sandström [111] and Furu et al. [112]). Before going further into the

description of those mechanisms it is important to stress out that subgrain growth differs from grain growth. Both are based on the reduction of the global system energy, but grain growth is mainly based on atomic jumps though the grain boundary whereas subgrain growth relies on glide and climb of dislocations in subgrain boundary.

Subgrains are usually misoriented from one another by less than 10°. Coalescence occurs when two neighbouring subgrains arrange their respective crystallographic orientation on one another by the motion of their concomitant dislocations. This can lead to a slight rotation of both subgrains but even if it was already claimed to be observed in 1962 [113], this effect has never been clearly established without suspecting major experimental artefacts. This mechanism is considered to occur less often than its counterpart: subgrain boundary migration that seems to be responsible for subgrain growth in a large majority of cases [104].

In the subgrain boundary migration, the substructure organizes itself under forces arising from the boundaries energy by the movement of triple point Y junctions (cf. Figure I.26a). Considering a 2D model, the triple point A is indeed subjected to the forces F1, F2, F3 from three boundaries. To minimise their length and reduce the global energy of the system, the boundaries migrate in the direction of the arrows. Considering equivalent specific energies for the three boundaries, the system stabilizes when boundaries are straight and angles are at the equilibrium value of 120° (cf. Figure I.26b).

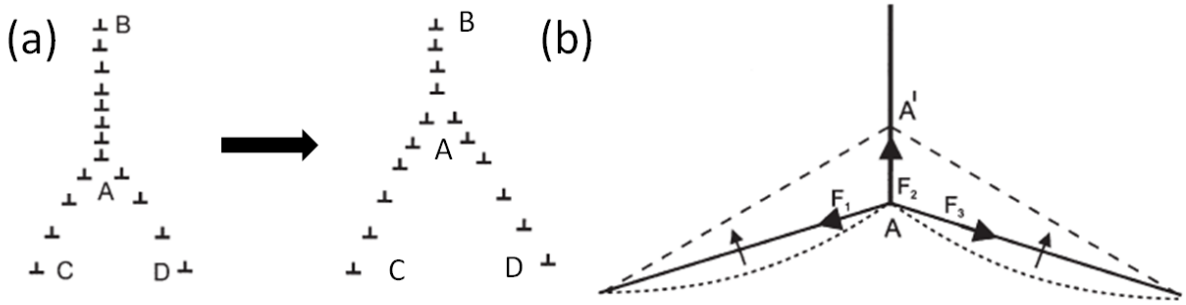

Figure I.26: (a) Migration of a low boundary at triple point and (b) corresponding movement of a Y-junction during subgrain growth [104]

2.4.3. Driving pressure for subgrain growth

During recovery, we can approximate the microstructure as an array of subgrains, with a mean radius and a subgrain boundary energy γ_{sg}. Then, the stored energy (E_{sg}) is $\alpha\gamma_s/R$ (per unit volume). The driving force for subgrain growth therefore arises from the reduction of the energy contained in low angle boundaries as subgrains grow:

$$P = \frac{F}{A} = -\alpha R \frac{d}{dR}\left(\frac{\gamma_{sg}}{R}\right) \quad \text{(I.11)}$$

Where α is a shape factor.

Therefore, the driving pressure evolves during subgrain growth with both the subgrain radius growth and the evolution of γ_{sg} with the misorientation. The growth rate of

subgrains v_{sg} is directly related to the driving pressure by the mobility of subgrains M_{sg}as:

$$v_{sg} = \frac{dR_{sg}}{dt} = M_{sg}P \tag{I.12}$$

When considering the specific energy as independent from the subgrain size R (absence of orientation gradient) the following equation is obtained:

$$\frac{dR}{dt} = \alpha \frac{M_{sg}\gamma_{sg}}{R_{sg}} \tag{I.13}$$

After resolution, integration gives, for subgrain growth, a similar expression that the one used for grain growth:

$$R^2 - R_0^2 = 2\alpha M_{sg}\gamma_{sg}t \tag{I.14}$$

Finally this expression is found to be equivalent to the one obtained on (I.8) with $c_1 = 2\alpha M_{sg}\gamma_s$. Nevertheless, considering highly deformed metals and elongated grains, there is a strong probability that misorientation accumulates over long distances between sub boundaries within the grains. In that case, during subgrain growth, misorientation increase between boundaries and equation (I.14) no longer holds.
Furthermore, boundary specific energy varies with θ according to the Read-Shockley equation [114], in its normalized form:

$$\gamma = \gamma_m \frac{\theta}{\theta_m}\left(1 - \ln\frac{\theta}{\theta_m}\right) \tag{I.15}$$

For small values of θ, $\gamma_s = \theta\gamma_m/\theta_m$ which leads to:

$$\frac{dR}{dt} = \alpha \frac{M_{sg}\theta\gamma_m}{2\theta_m} \tag{I.16}$$

Subgrain growth is then favoured in highly deformed materials as misorientation gradients allow to partially keep its driving force constant. The effect of the misorientation is limited by a saturation phenomenon (cf. §2.4.2), when it is reached, the driving pressure decreases as subgrains grow ($\propto 1/R$).

Nevertheless, in some specific cases (highly deformed material for example), recovery can reach a large extent with important subgrain growth and moderate temperature stability. Still, this phenomenon cannot be assimilated to continuous recrystallization in which the microstructure is mainly constituted by high angles boundaries while a large fraction of low angle boundaries remains in the recovered microstructure.

2.5. Recrystallization

In addition to the recovery process, recrystallization has been identified as a second mechanism for the material to release its excess in stored energy. Contrarily to recovery, recrystallization is a discontinuous process, which means that on different parts of the

material, the transformation is either complete or has not occurred. Recrystallized parts arise in the form of low internal energy crystallites growing in deformed or recovered material from which they are separated by high angle boundaries (i.e. >15° misorientation).

Recrystallization can be divided in three stages; nucleation and grain growth, which are forming the primary recrystallization, and abnormal grain growth which occurs in a fully recrystallized microstructure and is sometimes called secondary recrystallization. Usually, the term recrystallization refers to primary recrystallization.

2.5.1. Nucleation

Recrystallization nucleation relies on the formation of high angles grain boundaries. Over the years many models were proposed to account for nucleation. Burgers in 1941, postulates that recrystallization originates from dislocation cells or subgrains already present in the microstructure after deformation. Therefore, the following points deserved to be highlighted:

- Recrystallization nucleation originates from the transition of a subgrain low angle boundaries structure into high angle boundaries structure, therefore forming recrystallization germs.
- In order to create such high angle boundaries, an important misorientation gradient must be present within the grains. The larger the misorientation gradient, the faster the recovery and the following recrystallization.

Burke and Turnbull in 1952, proposed to adapt the classical nucleation theory applied in phase transformation for recrystallization nucleation. They assume that random atomic thermal fluctuation would end up in the formation of a small crystallite with high angle grain boundaries. However, this theory is rather unlikely for two main reasons:

- The driving force for recrystallization is low comparatively to phase transformation processes.
- The interfacial energy of a high angle grain boundary is elevated.

As a result, the formation of such a nucleus would produce a very important increase of the global system energy, and the probability of embryo formation is negligible even at high temperatures. It is now established that small volumes pre-existing in the deformed material under the form of cells or subgrains acts as nucleation sites as proposed by Burgers.

An interesting mechanism called Strain Induced Boundary Migration (SIBM) was reported by Beck and Sperry (1950) [115]. SIBM relies on the bulging of the boundary between two grains containing two different dislocation densities. Under the pressure resulting from this difference, the boundary moves towards the grain with the highest dislocation density (cf. Figure I.27).

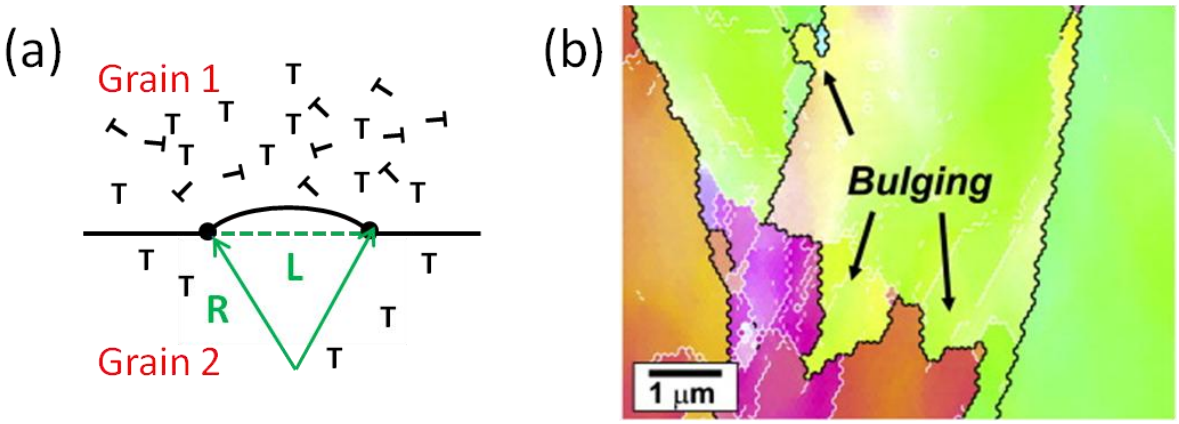

Figure I.27: SIBM nucleation. (a) sketch of a boundary bulging under the pressure arising from the difference of the dislocation density between grain 1 and grain 2, L is the diameter of the bulged area of the spherical shape of radius R (b) experimental evidence of SIBM induced bulging by EBSD [116]

The kinetics of the recrystallization was first studied by Bailey and Hirsh [117], they proposed a nucleation model based on the energy difference between two neighbouring grains leading to:

$$L \geq L_{crit} = \frac{\gamma}{\Delta E_D} \tag{I.17}$$

Where L is the bulging criterion for SIBM mechanism, γ is the specific energy of the grain boundary and ΔE_D is the stored energy difference per unit length.

Following this expression, nucleation occurs only if the energy stored ΔE_D is high enough to compensate for the increasing grain boundary surface energy. Assuming that the dislocation densities remain constant on both sides of the bulge during its displacement, the net pressure on the bulge can be expressed as (cf. equation (I.3)):

$$\Delta E_D = E_D^1 - E_D^2 = \frac{1}{2}\mu b^2(\rho_1 - \rho_2) \tag{I.18}$$

Bate and Hutchinson proposed in 1997 [118] an interesting evolution of this model. They stressed out the fact that whilst the boundary area containing the bulge increases, the number of dislocations contained in the bulging boundary remains constant. As a result, the restraining energy (E_D^2) acting on the concave side of the boundary decreases proportionally to the increase of the bulge area. By taking the following notation $f = E_D^1/E_D^2$, with 1 and 2 denoting grains as defined in Figure I.27a, the nucleation criterion becomes:

$$L_{crit}^{Bate} = \frac{4\gamma}{\mu b \rho_1 \sqrt{1-f}} \leq L_{crit}^{Bailey} \tag{I.19}$$

While valuable experimental studies observed that this mechanism was prominent mainly on low deformed alloys, This approach allows to consider SIBM for highly deformed materials and small ΔE_D implying a significant reduction in the critical bulge size in those cases.

Following this various approaches for recrystallization nucleation, debates around the

possible existence of a mechanism based on abnormal subgrain growth to explain the origin of recrystallization nuclei arose [119].

2.5.2. Grain growth

Grain growth occurring during recrystallization is controlled, by the thermally activated migration of atoms across the grain boundary. It can be described by the velocity of the grain boundary resulting from the combination between the mobility of the grain boundary and the net pressure exerted on it. Using equations already introduced for subgrain growth in the introduced in §2.4.1 and 2.4.3, this leads to:

$$v_{GB} = M_0 exp\left(-\frac{G}{RT}\right) P \tag{I.20}$$

In this expression, the net pressure on the grain boundary can be expressed by taking into account two contributions: the driving pressure and the boundary curvature.
As previously presented, the driving pressure arises from the dislocation density, which provides the stored energy (E_D):

$$P_d = E_D = \alpha \rho G b^2 \tag{I.21}$$

Contrarily, the boundary curvature has a retarding effect on grain growth. Indeed, when considering a grain growing within a deformed material, the creation of additional boundary length has an energy cost. Indeed, the global energy would be lowered if the grain were to shrink, the Gibbs-Thomson relationship gives:

$$P_c = \frac{2\gamma}{R} \tag{I.22}$$

Which results in the following global equation:

$$v_{GB} = M_0 exp\left(-\frac{G}{RT}\right)\left(\alpha \rho G b^2 - \frac{2\gamma_{GB}}{R}\right) \tag{I.23}$$

As both grain size and dislocation density vary during annealing, the grain boundary law changes along recrystallization. It is important to notice here that when subgrains are transformed into proper grains (i.e. they are no longer an additional structure compared to the recovered microstructure), grain growth contributes to lower the global system energy since it reduces the total boundary length, while until then it was increasing it. Then, with the exact same term, grain growth changes from a retarding to a contributing effect to the net pressure on the grain boundary.

2.5.3. Recrystallization kinetic law

In order to quantify recrystallization, the variable X_{rex} which represents the volume fraction of recrystallized matter is currently used. This variable usually used a sigmoid shape as illustrated in Figure I.28. Notability, the low transformation rate on first part of the curve can be related to the nucleation of grains, while on the last part of the curve the slow rate can be attributed to the impingement of growing grains. The recrystallization

temperature is defined as the temperature at which 50% of the material is recrystallized. Obviously, this only applies for an anisothermal annealing. Two main reasons can justify this choice. As previously described, recrystallization initiation is extremely difficult to identify. Therefore, defining the recrystallization temperature as the temperature at which the first subgrain transforms into a high angle grain boundary would systematically lead to overestimate the recrystallization temperature. Secondly, the middle of the sigmoid corresponds to the maximum transformation rate, which makes it both easier to identify and relevant to stress out a transformation process.

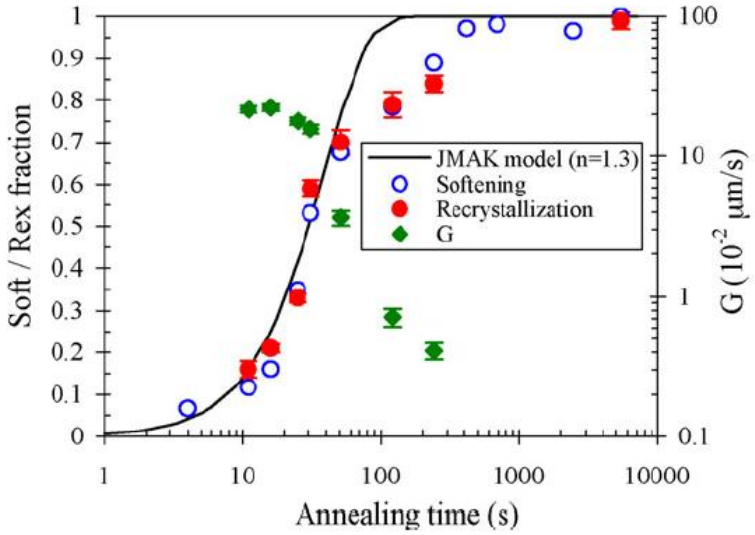

Figure I.28: Evolution of the fractional softening, of the recrystallized volume fraction and of the mean migration rate of the recrystallization front, G, as a function of the annealing time at 600°C on a cold rolled low carbon steel [120]

Sigmoid curves are commonly used to describe transformation reactions which can be modelled in terms of successive nucleation and growth processes. Pioneering work in this area is due to Johnson and Mehl (1939), Avrami (1939) and Kolmogorov (1937) in what is known as the JMAK model. The general form of the kinetic law is:

$$X_{rex} = 1 - exp(-Bt^n) \quad \text{(I.24)}$$

With B=f$\dot{N}\dot{G}^3/4$, the "JMAK equation", where f is $(4\pi/3)$ for spheres, $\dot{N}$ the nuclei formation rate and $\dot{G}$ the linear grain growth rate.

Experimental values ranging from 1 to 4 have been found for the n exponent. JMAK model is generally considered to be too simple to account for the microstructural change occurring during the recrystallization process. Nevertheless, fruitful attempts were made to improve its ability to account for microstructural features evolution, see for example Dunlop et al. [121].

2.6. Effect of second phase particles

During both recovery and recrystallization, the presence of a particle dispersion exerts a retarding force on grain growth. This has a strong effect on the global kinetic of the microstructure transformation during annealing which is known as Zener drag.

The restraining force exerted by a particle interacting with a boundary can be expressed as [122]:

$$F = 2\pi r\gamma \cos\beta \sin\beta \quad \text{(I.25)}$$

It should be noted that when a particle interacts with a grain boundary, the intersecting areas of both the grain boundary and the precipitate with the matrix are effectively removed to create the interaction between the precipitate and the boundary. This lowers the energy of the system. Therefore, boundaries are naturally attracted by particles and this also explains why grain boundaries are often cited as preferential nucleation sites for precipitates.

2.6.1. Influence of the particle shape on their interaction with boundaries

Pinning force may be affected by many features, Nes et al. notably published an extensive review of the interaction between particles and grain boundaries in which they stressed out the importance of the particles' shape and distribution [123]. These early results have later been successfully accounted for by mean field modelling [124].

As reported in §1.3.6, it is very likely that the precipitates found in ODS steels exhibit cubic shapes. Ringer et al. on a Ti microalloyed steel forming coherent TiN precipitates [125], demonstrate that in the maximum interaction case, the pinning by a cubic precipitate was nearly twice as efficient as the one produced by a spherical precipitate of the same volume. They also observed that the pinning strength highly depends upon the orientation of the cube relatively to the boundary.

2.6.2. Effect of the coherency of the particles

The coherency of the precipitates within the matrix also has an important effect on the interaction between particles and grain boundaries, as first emphasised by Ashby in 1969 [126]. Indeed, when a high angle grain boundary passes though a coherent precipitate population, precipitates lose their coherency with the matrix. The energy of an incoherent surface being higher than that of the original coherent interface, the additional energy expense must be provided by the moving boundary. As schematized in Figure I.29, three different bounding energy can be distinguished, γ_{12} between the two grains, γ_{13} between grain 1 and the particle and γ_{23} between the particle and grain 2.

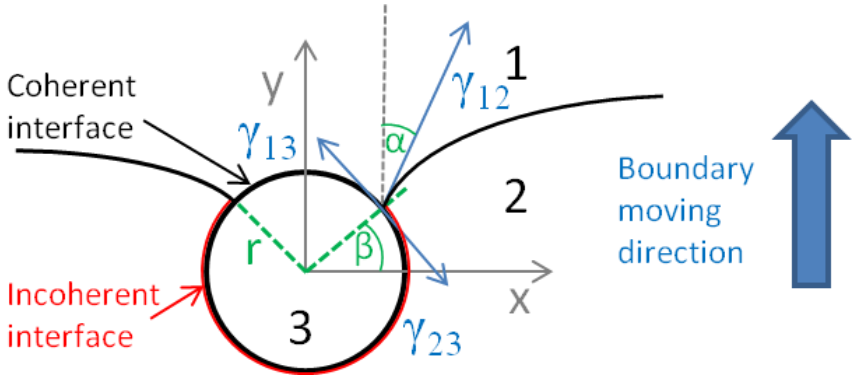

Figure I.29: sketch of the boundary interaction with a coherent particle.

At equilibrium, the following expression applies:

$$\gamma_{23} = \gamma_{13} + \gamma_{12} \cos \alpha \tag{I.26}$$

Then:

$$\cos \alpha = \frac{\gamma_{23} - \gamma_{13}}{\gamma_{12}} \tag{I.27}$$

Using equation (I.25), the pinning force is:

$$F_p = 2\pi r \gamma \cos(\alpha - \beta) \cos \beta \tag{I.28}$$

In the most favourable case, when $\beta = \alpha/2$ and $= 0$; the pinning force is $F_p = 2\pi r\gamma$, which is twice the maximal value obtained for a pinning by incoherent particles of the same size.

2.6.3. Pinning pressure induced by a precipitated distribution

Pinning pressure exerted by particles on a unit area of the boundary is given by the addition of the force (F_p) exerted by each particle intersecting the boundary area (N_s), as:

$$P_z = N_s F_p \tag{I.29}$$

With:

$$N_s = \frac{3F_V}{4\pi r^2} \tag{I.30}$$

Using equations (I.25) to (I.30) and assuming a rigid boundary (β=45°, cf. Figure I.30), the pinning pressure becomes:

$$P_Z = \frac{3F_V \gamma}{2r} \tag{I.31}$$

This expression is clearly not enough elaborated to take into account all the microstructural subtleties of a real material. More rigorous calculations later attempted often ended up to very close results from those obtained with equation (I.31). Indeed, Hundert et al. [127] demonstrates that the Zener pinning is not influenced by the curvature of the boundary in cases where the mean distance between particles is much smaller than the boundary curvature (i.e. curvature is high enough to be short ranged compared to the particle mean distance). Considering the homogenous and high precipitate concentration evidenced in ODS steels, the condition enounced by Hundert et al. is very likely to be fulfilled in our case. Still, the physical ambiguity of the rigid boundary, which implies that as particles are pinning the boundary, others will be pulling it making the resulting net pinning pressure to be nil, remains unclear.

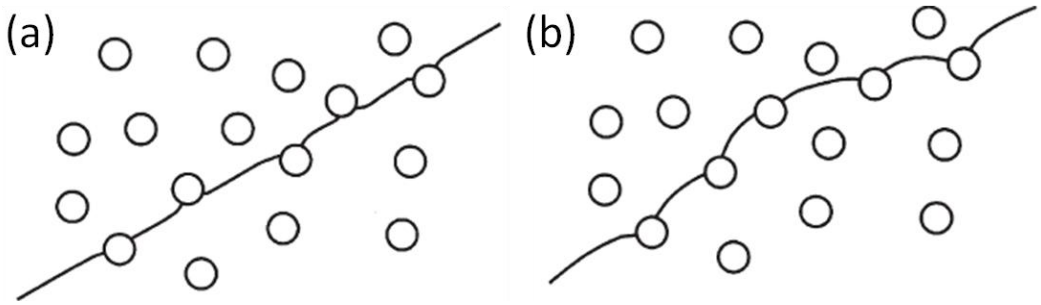

Figure I.30: Interaction of particles with (a) a rigid planar boundary; (b) a flexible boundary.

Finally, a reasonable approximation of pinning force taking into account the shape of the precipitates can be expressed using the classical following expression [128]:

$$P_z = \frac{2k_s}{k_v}\frac{\gamma f_p}{r} \tag{I.32}$$

Where $\boldsymbol{k_s}$ and $\boldsymbol{k_v}$ being respectively a geometrical and a volume factor, $\boldsymbol{\gamma}$ the specific boundary energy, $\boldsymbol{f_p}$ the volume fraction of precipitates and $\boldsymbol{r}$ the particle radius.

Constant values for the shape and geometrical factors k_s and k_v can be found in Table I.3.

2.6.4. Influence of precipitate pinning on grain growth

As depicted above, a precipitate distribution acts as a retarding force for grain growth. This effect is discribed by the pinning pressure P_Z on the grain boundaries. Therefore, the net driving pressure for recrystallization is:

$$P = P_D + P_C - P_Z = \alpha\rho Gb^2 + \frac{2\gamma_b}{R} - \frac{2k_s}{k_v}\frac{\gamma f_p}{r} \tag{I.33}$$

Where $\boldsymbol{P_D}$ is the dislocation driving pressure, $\boldsymbol{P_C}$ is the capillarity pressure (resulting from the boundary surface reduction) and $\boldsymbol{P_Z}$ is the Zener pinning pressure.

In order for the grains to grow, the driving pressure has to be positive. Then, from a given Fv/r ratio, strained as to exceed a critical value to allow the material to recrystallize. Similarly, it is clear from this equation that, for an equivalent volumic fraction, the smaller the precipitates the more efficient the pinning will be. Precipitates are found to be retarding features for both nucleation (by pinning subgrains, and dislocations) and growth (by pinning grains).

Thus, the precipitates introduce a limited grain size as grain growth will cease when $P_C = P_Z$ (neglecting the driving pressure). This limit is known as the Zener limit. With R_{Zener} as the critical grain size this leads to:

$$P_{C_{limit}} = P_Z \rightarrow \frac{\alpha\gamma}{R_{zener}} = \frac{3f_p\gamma}{2r} \tag{I.34}$$

and:

$$R_Z = \frac{4\alpha r}{3F_V} \tag{I.35}$$

Similarly to the pinning pressure, many authors tried to improve the Zener proposition, introducing, for example, a parameter taking into account the ratio between the maximum and the average grain size. It often results in using a α coefficient raging from 0.25 to 0.5 and a critical grain size fitting equation (I.35) (Gladman 1965, Hillert 1975, Manohar 1998).

2.6.5. Influence of special pinning location

Recently, Bréchet et Militzer [128], introduced the concept of corner pinning. Contrary to classical Zener pinning, corner pinning is bring forth by precipitates lying at quadruple junctions. The so called Bréchet Militzer model relies on the two following assumptions:

- Corner pinning is more efficient than conventional Zener boundary pinning.
- Particles first pin quadruple locations, then, when all quadruple points are pinned the remaining particles pin the grain boundaries according to classical Zener pinning.

If n is the number of particles per unit volume and N^* the number of special locations (quadruple points) per unit volume. After the introduction of $K = (K_0/K_V)k_v$ with K_0as the average number of quadruple points per grain and K_V a geometric constant describing the grain shape. Following, the arguments mentioned above, we come to two different situations:

- The number of particles n is smaller than N^*. Then, the expression for the pinning force per unit area is:

$$F_P = \left(\frac{n}{N^*}\right)\frac{K_0\alpha_0 f_z}{K_A D^2} \tag{I.36}$$

With (n/N^*) the fraction of quadruple point effectively occupied, $\alpha_0$the amplification factor for pinning at special location, $K_A D^2$ is the mean boundary area per grain with K_A being a geometrical constant and D the average volumetric grain diameter. Finally, f_z is the elementary force exerted by a particle on a grain boundary ($f_z = k_s\gamma r$). Using equation (I.32) this expression can be written (with $\alpha_1 = \alpha_0 K_V/(2K_A)$):

$$F_P = \alpha_1\frac{D}{r}F_Z \tag{I.37}$$

- The number of particles n is larger than N^*:

$$F_P = \frac{K_0\alpha_0 f_Z}{K_A D^2} + (n - N^*)2rf_Z \tag{I.38}$$

Simplification leads to:

$$F_P = \frac{Kr^3 F_Z}{D^3 f_p}\left(\alpha_1\frac{D}{r} - 1\right) + F_Z \tag{I.39}$$

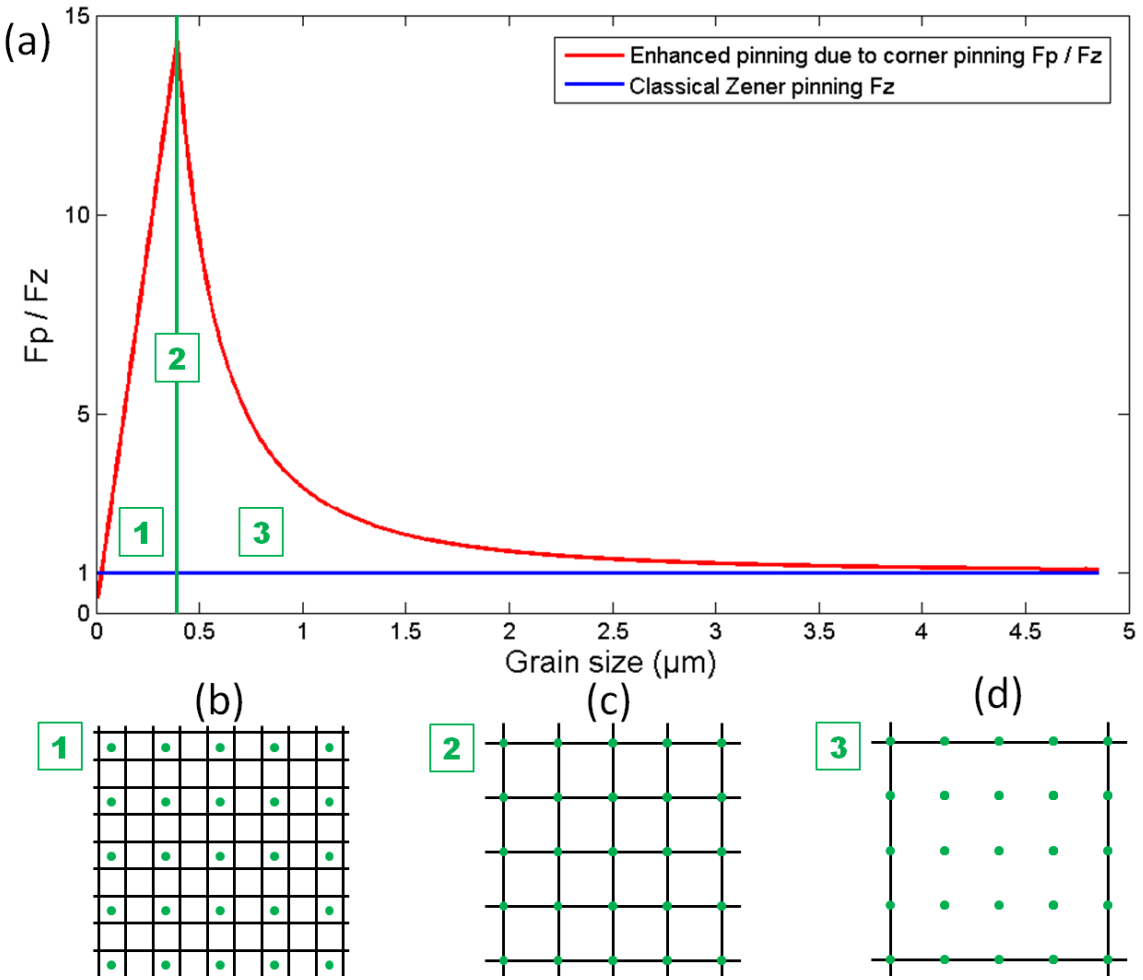

Figure I.31: Influence of the corner pinning on a given precipitation state (here rp = 10nm and fp = 5.10^{-4} %): (a) Curve representing the multiplication factor induced by corner pinning compared to classical Zener pinning, (b) Situation in the first part of the curve: grain size is smaller than the mean precipitate distance (c) At point 2 of the curve the mean precipitate distance equals to the mean grain size (d) After this point grain size is higher than the mean precipitate distance.

As described in Figure I.31, three main situations can be distinguished if the corner pinning approach applies:

- Mean distance between precipitates is larger than the grain size (cf. Figure I.31b); as grains grow precipitates locate on the special locations and consecutively pinning force rapidly increases,
- Comparatively, corner pinning force reach a maximum when the grain size equals to the mean distance between precipitates. Indeed in this situation every precipitates are located at a corner point and every corner points are pinned by a precipitate (cf. Figure I.31c).
- Then, when the grain size increases, precipitates begin to locate on standard boundary locations and the contribution of corner pinning weakens as the proportion of precipitates at special locations decreases. When the grain size reaches a certain point, the two pinning forces equal each other and classical Zener pinning theory perfectly applies.

As stated in [128], this model gives rise to two important considerations. First, given the typical values encountered in nanocrystalline materials, corner pinning force is expected to be particularly efficient in those materials. This efficiency is proposed as one of the reasons for the particular stability of nanosized microstructure. Secondly, as we have shown in Figure I.31, once the maximum pinning efficiency is reached, the pinning force decreases very rapidly with the grain size. Therefore, a larger grain among the grain population will be less efficiently pinned and will further increase its growth rate compared to smaller grains. This mechanism can be a determining factor for abnormal grain growth.

	Equiaxed grains, spherical precipitates	**Equiaxed grains, cubic precipitates**
K_V^a	$(1.1)^3\,\pi/6$	$(1.1)^3\,\pi/6$
K_A^a	$(1.1)^2\,\pi/2$	$(1.1)^2\,\pi/2$
K_0	5	5
k_v	$4\pi/3$	8
k_s	π	4
$K^* = K_0/K_V$	$30/(1.1)^3\pi$	$30/(1.1)^3\pi$
$K = k_v K^* = k_v K_0/K_V$	$40/(1.1)^3$	$240/(1.1)^3\pi$

Table I.3: Values of the different constants for simple geometrical assumptions

2.7. Abnormal grain growth

Until this section, grain growth has been considered as a global phenomenon, shifting the grain size distribution to larger mean values but keeping the shape of the distribution unchanged. This is referred to as Normal Grain Growth (NGG), in opposition to Abnormal Grain Growth (AGG) which corresponds to microstructural instability where a little number of grains grow excessively compared to the others (cf. Figure I.32).

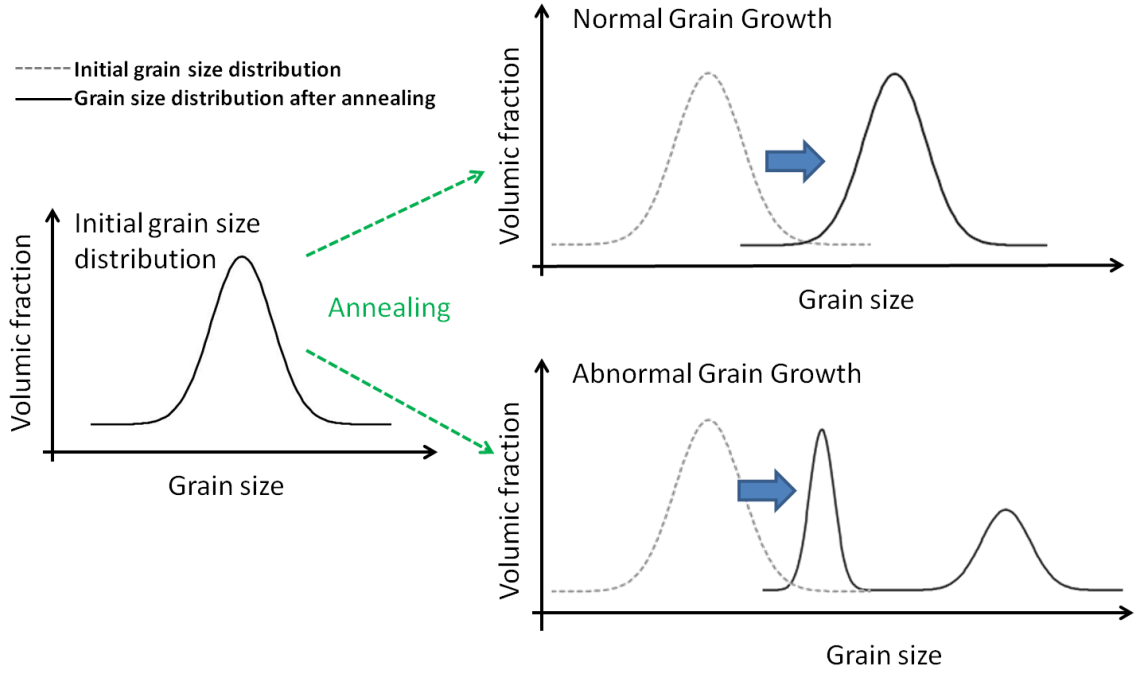

Figure I.32: Comparative sketch of a normal and an abnormal grain growth distribution after annealing.

Several microstructural factors have been identified to explain the kinetic advantages of abnormally growing grains over their neighbouring grains. Two factors are principally considered in litterature: texture (i.e. different boundary mobility over the material) [129] and second phase particles. In addition to precipitate induced pinning, the solute drag effect can also significantly affect AGG [130]. Considering ODS steels, precipitate induced mechanisms will be favoured given the high precipitate density expected within the material. As an introduction to second phase particle effect, readers are reported to the early works initiated by Hillert [131] and to the review made by Gladman [132].
Two basic assumptions can be made to account for abnormal grain growth:

- Abnormal grains have to grow:

$$\frac{dD_{ab}}{dt} > 0 \tag{I.40}$$

- Abnormal grains have to grow faster than normal grains:

$$\frac{d}{dt}\left(\frac{\overline{D}_{ab}}{\overline{D}}\right) > 0 \tag{I.41}$$

Where D_{ab} is the mean diameter of the coarse grains (at least $2 \times D$) and D is the normal sized grain mean size.

To describe this mechanism, Andersen et al. have established a simple criterion for the initiation of abnormal grain growth under different pinning conditions (cf. Figure I.32). In addition, they also built a mechanism map that systemically described the conditions for AGG to occur (cf. Figure I.33) [133]:

$$\left[\frac{\left(\frac{2}{c_3}\right)\frac{\overline{D}}{\overline{D}_{ab}}}{\tan\left[\frac{\pi}{4}\frac{\overline{D}}{\overline{D}_{ab}} - \frac{\pi}{12}\left(\frac{\overline{D}}{\overline{D}_{ab}}\right)^2\right]} - \frac{2\sqrt{3}}{c_3}\frac{\overline{D}}{\overline{D}_{ab}} - \frac{\overline{D}_{ab}}{\overline{D}}\right] \Big/ \left[1 - \frac{\overline{D}_{ab}}{\overline{D}}\right] > \frac{\overline{D}}{\overline{D}_{Lim}} \tag{I.42}$$

Later, based on the pinning model formulated by Bréchet et Militzer [128] (cf. §2.6) this model was further improved by M. Perez and his collaborators. First by taking into account the entire precipitate size distribution and adding the hypothesis that the larger precipitates were preferentially located at quadruple points [134]. Then, based on 3D geometrical considerations, Razzak et al. [135] obtained the following condition for abnormal grain growth to occur (Considering that for the second condition to be true, the first condition presented in equation (I.40) has to be true, only the second condition (I.41) is taken into account here):

$$\frac{d}{dt}\left(\frac{D_{ab}}{D_n}\right) = \frac{1}{D_n}\frac{dD_{ab}}{dt} - \frac{D_{ab}}{D_n^2}\frac{dD_n}{dt}$$
$$= \frac{2\gamma M}{D_n^2}\left[\mu - (1-\mu)\left(\frac{D_n}{D_{ab}}\right)^2 + (2\mu - 1)\frac{D_n}{D_{ab}} - \frac{\lambda}{2}\frac{D_{ab}}{D_n}\right] \quad \text{(I.43)}$$
$$- \frac{M}{D_n}\left(\frac{D_{ab}}{D_n} + 1\right)(P_C + P_Z)$$

Where $\mu = \rho/(4\lambda_p)$, ρ is the compact efficiency factor, λ_p is the ratio between the projected surface over the actual surface of the normal grains and λ is a geometrical factor.

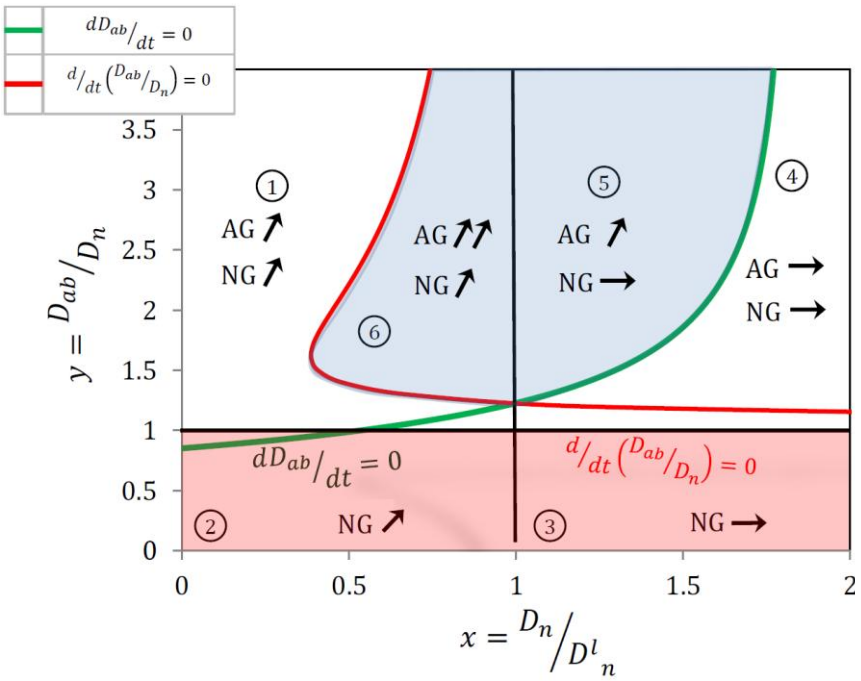

Figure I.33: AGG mechanism map [135]

3. Recrystallization of ODS steels

Few studies have been conducted on the recrystallization of ODS steels. Furthermore, the large majority of them focuses on the softening treatment after consolidation. In particular, we can distinguish the work realized on MA957 alloys. H. Réglé et al. have shown that a partial control over the recrystallization temperature could be lowered by several hundred degrees (starting at 750°C) by applying controlled deformation level. Doing so, abnormal grain growth mechanism was favored over normal grain growth that involves significantly higher recrystallization temperatures (1350°C). Additionally, they also stressed out the importance of texture and precipitates on the recrystallization mechanisms [68].

Bhadeshia and colleagues [136–138], also extensively studied the recrystallization of MA 956 and MA957 ODS steels. Notably, they proposed a recrystallization mechanism based on the very small size of the ODS steel grains. For nanosized grains, grain boundary junctions can play the role of pinning points for grain growth. This is expected to explain

the exceptional grain stability at high temperatures. On 12Cr ODS ferritic steels [33], S.Ukaï et al. have evidenced the importance of intermediate softening treatment to control the grain morphology during cold working and the correlation between Y_2O_3 and Ti solute content with the recrystallization degree.

The importance of recrystallization on mechanical properties of ODS steels has also been demonstrated. Indeed, a recrystallized microstructure exhibits a more isotropic behaviour with a higher ductility and better creep properties for long rupture times despite its higher DBTT [78].

4. Synthesis and key points

The main points arising from this literature review are the following:

- ODS ferritic steels exhibit particular microstructural features that are of interest towards the technical specification of the tube claddings application for SFR.
- Those particular features involve an ultrafine grain microstructure and a dense nanosized precipitation.
- Abnormal grain growth occurs during the processing of the ODS ferritic steels and results in poor transverse properties that are detrimental for the fuel cladding application.
- For a given microstructure, the annealing related phenomena depend primarily on the precipitation states, the grain size and the stored energy.

Literature review bibliography

[1] Coolidge W.D. (1910) DUCTILE TUNGSTEN. *American Institute of Electrical Engineers, Transactions of the*, **XXIX**, 961‑5.

[2] Benjamin J.S. et Volin T.E. (1974) THE MECHANISM OF MECHANICAL ALLOYING. *Metallurgical Transactions*, **5**, 1929‑34.

[3] Benjamin J.S. (1970) DISPERSION STRENGTHENED SUPERALLOYS BY MECHANICAL ALLOYING. *Metallurgical Transactions*, **1**, 2943‑51.

[4] Chen C.-L., Tatlock G.J. et Jones A.R. (2010) MICROSTRUCTURAL EVOLUTION IN FRICTION STIR WELDING OF NANOSTRUCTURED ODS ALLOYS. *Journal of Alloys and Compounds*, **504**, S460‑6.

[5] Han W.T., Wan F.R., Leng B., Ukai S., Tang Q.X., Hayashi S., He J.C. et Sugino Y. (2011) GRAIN CHARACTERISTIC AND TEXTURE EVOLUTION IN FRICTION STIR WELDS OF NANOSTRUCTURED OXIDE DISPERSION STRENGTHENED FERRITIC STEEL. *Science and Technology of Welding and Joining*, **16**, 690‑6.

[6] Mignot G., Klein J.C., Chenaud M.S., Thevenot C., Ravenet A., Valentin M.P.B., … Massara S. (2008) STUDIES ON FRENCH SFR ADVANCED CORE DESIGNS.

[7] Lindau R., Möslang A., Rieth M., Klimiankou M., Materna-Morris E., Alamo A., … Dietz W. (2005) PRESENT DEVELOPMENT STATUS OF EUROFER AND ODS-EUROFER FOR APPLICATION IN BLANKET CONCEPTS. *Fusion Engineering and Design*, **75–79**, 989‑96.

[8] UKAI S., MIZUTA S., FUJIWARA M., OKUDA T. et KOBAYASHI T. (2002) DEVELOPMENT OF 9CR-ODS MARTENSITIC STEEL CLADDINGS FOR FUEL PINS BY MEANS OF FERRITE TO AUSTENITE PHASE TRANSFORMATION. *Journal of Nuclear Science and Technology*, **39**, 778‑88.

[9] Toualbi L., Cayron C., Olier P., Malaplate J., Praud M., Mathon M.-H., Bossu D., Rouesne E., Montani A., Logé R. et de Carlan Y. (2012) ASSESSMENT OF A NEW FABRICATION ROUTE FOR FE–9CR–1W ODS CLADDING TUBES. *Journal of Nuclear Materials*, **428**, 47‑53.

[10] Klueh R.L., Maziasz P.J., Kim I.S., Heatherly L., Hoelzer D.T., Hashimoto N., Kenik E.A. et Miyahara K. (2002) TENSILE AND CREEP PROPERTIES OF AN OXIDE DISPERSION-STRENGTHENED FERRITIC STEEL. *Journal of Nuclear Materials*, **307–311, Part 1**, 773‑7.

[11] Zakine C., Prioul C. et François D. (1996) CREEP BEHAVIOUR OF ODS STEELS. *Materials Science and Engineering: A*, **219**, 102‑8.

[12] Fournier B., Steckmeyer A., Rouffie A.-L., Malaplate J., Garnier J., Ratti M., Wident P., Ziolek L., Tournie I., Rabeau V., Gentzbittel J.M., Kruml T. et Kubena I. (2012) MECHANICAL BEHAVIOUR OF FERRITIC ODS STEELS – TEMPERATURE DEPENDANCY AND ANISOTROPY. *Journal of Nuclear Materials*, **430**, 142‑9.

[13] Fischer J.J. (US4075010 A, 1978.) CHROMIUM, TITANIUM, YTTRIA, IRON.

[14] Miller M.K., Russell K.F. et Hoelzer D.T. (2006) CHARACTERIZATION OF PRECIPITATES IN MA/ODS FERRITIC ALLOYS. *Journal of Nuclear Materials*, **351**, 261‑8.

[15] Kimura A., Kasada R., Iwata N., Kishimoto H., Zhang C.H., Isselin J., … Abe T.F. (2011) DEVELOPMENT OF AL ADDED HIGH-CR ODS STEELS FOR FUEL CLADDING OF NEXT GENERATION NUCLEAR SYSTEMS. *Journal of Nuclear Materials*, **417**, 176‑9.

[16] De Carlan Y., Bechade J.-L., Dubuisson P., Seran J.-L., Billot P., Bougault A., … Mathon M.H. (2009) CEA DEVELOPMENTS OF NEW FERRITIC ODS ALLOYS FOR NUCLEAR APPLICATIONS. *Journal of Nuclear Materials*, **386–388**, 430‑2.

[17] Klueh R.L., Shingledecker J.P., Swindeman R.W. et Hoelzer D.T. (2005) OXIDE DISPERSION-STRENGTHENED STEELS: A COMPARISON OF SOME COMMERCIAL AND EXPERIMENTAL ALLOYS. *Journal of Nuclear Materials*, **341**, 103‑14.

[18] Yvon P. et Carré F. (2009) STRUCTURAL MATERIALS CHALLENGES FOR ADVANCED REACTOR SYSTEMS. *Journal of Nuclear Materials*, **385**, 217‑22.

[19] Toloczko M.B., Garner F.A., Voyevodin V.N., Bryk V.V., Borodin O.V., Mel'nychenko V.V. et Kalchenko A.S. ION-INDUCED SWELLING OF ODS FERRITIC ALLOY MA957 TUBING TO 500 DPA. *Journal of Nuclear Materials*,.

[20] Séran J.L., Alamo A., Maillard A., Touron H., Brachet J.C., Dubuisson P. et Rabouille O. (1994) PRE- AND POST-IRRADIATION MECHANICAL PROPERTIES OF FERRITIC-MARTENSITIC STEELS FOR FUSION APPLICATIONS: EM10 BASE METAL AND EM10/EM10 WELDS. *Journal of Nuclear Materials*, **212–215, Part 1**, 588‑93.

[21] Gwinner B., Auroy M., Mas D., Saint-Jevin A. et Pasquier-Tilliette S. (2012) IMPACT OF THE USE OF THE FERRITIC/MARTENSITIC ODS STEELS CLADDING ON THE FUEL REPROCESSING PUREX PROCESS. *Journal of Nuclear Materials*, **428**, 110‑6.

[22] Pint B.A. et Wright I.G. (2002) LONG-TERM HIGH TEMPERATURE OXIDATION BEHAVIOR OF ODS FERRITICS. *Journal of Nuclear Materials*, **307–311, Part 1**, 763‑8.

[23] Dubuisson P., Gilbon D. et Séran J.L. (1993) MICROSTRUCTURAL EVOLUTION OF FERRITIC-MARTENSITIC STEELS IRRADIATED IN THE FAST BREEDER REACTOR PHÉNIX. *Journal of Nuclear Materials*, **205**, 178‑89.

[24] Lee J.S., Jang C.H., Kim I.S. et Kimura A. (2007) EMBRITTLEMENT AND HARDENING DURING THERMAL AGING OF HIGH CR OXIDE DISPERSION STRENGTHENED ALLOYS. *Journal of Nuclear Materials*, **367–370, Part A**, 229‑33.

[25] Benjamin J.S. et Bomford M.J. (1974) EFFECT OF YTTRIUM OXIDE VOLUME FRACTION AND PARTICLE SIZE ON ELEVATED TEMPERATURE STRENGTH OF A DISPERSIC STRENGTHENED SUPERALLOY. *Metallurgical Transactions*, **5**, 615‑21.

[26] Swamy V., Seifert H.J. et Aldinger F. (1998) THERMODYNAMIC PROPERTIES OF Y2O3 PHASES AND THE YTTRIUM–OXYGEN PHASE DIAGRAM. *Journal of Alloys and Compounds*, **269**, 201‑7.

[27] Ukai S., Mizuta S., Yoshitake T., Okuda T., Fujiwara M., Hagi S. et Kobayashi T. (2000) TUBE MANUFACTURING AND CHARACTERIZATION OF OXIDE DISPERSION STRENGTHENED FERRITIC STEELS. *Journal of Nuclear Materials*, **283–287, Part 1**, 702‑6.

[28] UKAI S., NISHIDA T., OKADA H., OKUDA T., FUJIWARA M. et ASABE K. (1997) DEVELOPMENT OF OXIDE DISPERSION STRENGTHENED FERRITIC STEELS FOR FBR CORE APPLICATION, (I). IMPROVEMENT OF MECHANICAL PROPERTIES BY RECRYSTALLIZATION PROCESSING. *Journal of Nuclear Science and Technology*, **34**, 256‑63.

[29] Ukai S., Harada M., Okada H., Inoue M., Nomura S., Shikakura S., Asabe K., Nishida T. et Fujiwara M. (1993) ALLOYING DESIGN OF OXIDE DISPERSION STRENGTHENED FERRITIC STEEL FOR LONG LIFE FBRS CORE MATERIALS. *Journal of Nuclear Materials*, **204**, 65‑73.

[30] Kim I.-S., Choi B.-Y., Kang C.-Y., Okuda T., Maziasz P.J. et Miyahara K. (2003) EFFECT OF TI AND W ON THE MECHANICAL PROPERTIES AND MICROSTRUCTURE OF 12% CR BASE MECHANICAL-ALLOYED NANO-SIZED ODS FERRITIC ALLOYS. *ISIJ International*, **43**, 1640‑6.

[31] Alinger M.J., Odette G.R. et Hoelzer D.T. (2009) ON THE ROLE OF ALLOY COMPOSITION AND PROCESSING PARAMETERS IN NANOCLUSTER FORMATION AND

DISPERSION STRENGTHENING IN NANOSTUCTURED FERRITIC ALLOYS. *Acta Materialia*, **57**, 392‑406.

[32] Tanno T., Ohtsuka S., Yano Y., Kaito T., Oba Y., Ohnuma M., Koyama S. et Tanaka K. (2013) EVALUATION OF MECHANICAL PROPERTIES AND NANO-MESO STRUCTURES OF 9–11%CR ODS STEELS. *Journal of Nuclear Materials*, **440**, 568‑74.

[33] UKAI S., OKUDA T., FUJIWARA M., KOBAYASHI T., MIZUTA S. et NAKASHIMA H. (2002) CHARACTERIZATION OF HIGH TEMPERATURE CREEP PROPERTIES IN RECRYSTALLIZED 12CR-ODS FERRITIC STEEL CLADDINGS. *Journal of Nuclear Science and Technology*, **39**, 872‑9.

[34] Brocq M., Radiguet B., Poissonnet S., Cuvilly F., Pareige P. et Legendre F. (2011) NANOSCALE CHARACTERIZATION AND FORMATION MECHANISM OF NANOCLUSTERS IN AN ODS STEEL ELABORATED BY REACTIVE-INSPIRED BALL-MILLING AND ANNEALING. *Journal of Nuclear Materials*, **409**, 80‑5.

[35] Lucks I., Lamparter P. et Mittemeijer E.J. (2001) UPTAKE OF IRON, OXYGEN AND NITROGEN IN MOLYBDENUM DURING BALL MILLING. *Acta Materialia*, **49**, 2419‑28.

[36] Ohtsuka S., Ukai S., Fujiwara M., Kaito T. et Narita T. (2004) IMPROVEMENT OF 9CR-ODS MARTENSITIC STEEL PROPERTIES BY CONTROLLING EXCESS OXYGEN AND TITANIUM CONTENTS. *Journal of Nuclear Materials*, **329–333, Part A**, 372‑6.

[37] Ohtsuka S., Ukai S., Fujiwara M., Kaito T. et Narita T. (2005) NANO-STRUCTURE CONTROL IN ODS MARTENSITIC STEELS BY MEANS OF SELECTING TITANIUM AND OXYGEN CONTENTS. *Journal of Physics and Chemistry of Solids*, **66**, 571‑5.

[38] Abe F., Noda T., Araki H. et Nakazawa S. (1991) ALLOY COMPOSITION SELECTION FOR IMPROVING STRENGTH AND TOUGHNESS OF REDUCED ACTIVATION 9CR-W STEELS. *Journal of Nuclear Materials*, **179–181, Part 1**, 663‑6.

[39] Sakasegawa H., Chaffron L., Legendre F., Brocq M., Boulanger L., Poissonnet S., de Carlan Y., Bechade J., Cozzika T. et Malaplate J. (2009) EVALUATION OF THRESHOLD STRESS OF THE MA957 ODS FERRTIC ALLOY. *Journal of Nuclear Materials*, **386–388**, 511‑4.

[40] Ohtsuka S., Kaito T., Inoue M., Asayama T., Kim S.W., Ukai S., Narita T. et Sakasegawa H. (2009) EFFECTS OF ALUMINUM ON HIGH-TEMPERATURE STRENGTH OF 9CR–ODS STEEL. *Journal of Nuclear Materials*, **386–388**, 479‑82.

[41] Takaya S., Furukawa T., Müller G., Heinzel A., Jianu A., Weisenburger A., Aoto

K., Inoue M., Okuda T., Abe F., Ohnuki S., Fujisawa T. et Kimura A. (2012) AL-CONTAINING ODS STEELS WITH IMPROVED CORROSION RESISTANCE TO LIQUID LEAD–BISMUTH. *Journal of Nuclear Materials*, **428**, 125‑30.

[42] Ningshen S., Sakairi M., Suzuki K. et Ukai S. (2014) THE CORROSION RESISTANCE AND PASSIVE FILM COMPOSITIONS OF 12% CR AND 15% CR OXIDE DISPERSION STRENGTHENED STEELS IN NITRIC ACID MEDIA. *Corrosion Science*, **78**, 322‑34.

[43] Fecht H.-J. (1995) NANOSTRUCTURE FORMATION BY MECHANICAL ATTRITION. *Nanostructured Materials*, **6**, 33‑42.

[44] Koch C.C. (1997) SYNTHESIS OF NANOSTRUCTURED MATERIALS BY MECHANICAL MILLING: PROBLEMS AND OPPORTUNITIES. *Nanostructured Materials*, **9**, 13‑22.

[45] Koch C.C. (2003) OPTIMIZATION OF STRENGTH AND DUCTILITY IN NANOCRYSTALLINE AND ULTRAFINE GRAINED METALS. *Scripta Materialia*, **49**, 657‑62.

[46] Iwata N.Y., Kimura A., Fujiwara M. et Kawashima N. (2007) EFFECT OF MILLING ON MORPHOLOGICAL AND MICROSTRUCTURAL PROPERTIES OF POWDER PARTICLES FOR HIGH-CR OXIDE DISPERSION STRENGTHENED FERRITIC STEELS. *Journal of Nuclear Materials*, **367–370, Part A**, 191‑5.

[47] Iwata N.Y., Liu T., Dou P., Kasada R., Kimura A., Okuda T., Inoue M., Abe F., Ukai S., Ohnuki S. et Fujisawa T. (2011) EFFECTS OF MA ENVIRONMENT ON THE MECHANICAL AND MICROSTRUCTURAL PROPERTIES OF ODS FERRITIC STEELS. *Journal of Nuclear Materials*, **417**, 162‑5.

[48] Olier P., Couvrat M., Cayron C., Lochet N. et Chaffron L. (2013) INCIDENCE OF MECHANICAL ALLOYING CONTAMINATION ON OXIDES AND CARBIDES FORMATION IN ODS FERRITIC STEELS. *Journal of Nuclear Materials*, **442**, S106‑11.

[49] Suryanarayana C. (2001) MECHANICAL ALLOYING AND MILLING. *Progress in Materials Science*, **46**, 1‑184.

[50] Kim J.H. et Park C.H. (2014) EFFECT OF MILLING TEMPERATURE ON NANOCLUSTERS AND ULTRA FINE GRAINED MICROSTRUCTURE OF OXIDE DISPERSION STRENGTHENED STEEL. *Journal of Alloys and Compounds*, **585**, 69‑74.

[51] Hemanth J. (2009) DEVELOPMENT AND PROPERTY EVALUATION OF ALUMINUM ALLOY REINFORCED WITH NANO-ZRO2 METAL MATRIX COMPOSITES (NMMCS). *Materials Science and Engineering: A*, **507**, 110‑3.

[52] Sobczak N., Nowak R., Radziwill W., Budzioch J. et Glenz A. (2008) EXPERIMENTAL COMPLEX FOR INVESTIGATIONS OF HIGH TEMPERATURE CAPILLARITY PHENOMENA. *Materials Science and Engineering: A*, **495**, 43‑9.

[53] Verhiest K., Mullens S., De Graeve I., De Wispelaere N., Claessens S., De Bremaecker A. et Verbeken K. (2014) ADVANCES IN THE DEVELOPMENT OF CORROSION AND CREEP RESISTANT NANO-YTTRIA DISPERSED FERRITIC/MARTENSITIC ALLOYS USING THE RAPID SOLIDIFICATION PROCESSING TECHNIQUE. *Ceramics International*, **40**, 14319‑34.

[54] Béchade J.-L., Menut D., Lescoat M.-L., Sitaud B., Schlutig S., Solari P.L., Llorens I., Hermange H., de Carlan Y., Ribis J. et Toualbi L. (2012) APPLICATION OF SYNCHROTRON RADIATION TO ANALYZE THE PRECIPITATION IN ODS MATERIALS BEFORE IRRADIATION IN FE–9%CR SINGLE GRAIN OF POWDER AND CONSOLIDATED FE–18%CR. *Journal of Nuclear Materials*, **428**, 183‑91.

[55] Alinger M.., Odette G.. et Hoelzer D.. (2004) THE DEVELOPMENT AND STABILITY OF Y–TI–O NANOCLUSTERS IN MECHANICALLY ALLOYED FE–CR BASED FERRITIC ALLOYS. *Journal of Nuclear Materials*, **329–333, Part A**, 382‑6.

[56] Pandey A., Palneedi H., Jayasankar K., Parida P., Debata M., Mishra B.K. et Saroja S. (2013) MICROSTRUCTURAL CHARACTERIZATION OF OXIDE DISPERSION STRENGTHENED FERRITIC STEEL POWDER. *Journal of Nuclear Materials*, **437**, 29‑36.

[57] Rahmanifard R., Farhangi H., Novinrooz A.J. et Afshari N. (2010) INVESTIGATION OF MICROSTRUCTURAL CHARACTERISTICS OF NANOCRYSTALLINE 12YWT STEEL DURING MILLING AND SUBSEQUENT ANNEALING BY X-RAY DIFFRACTION LINE PROFILE ANALYSIS. *Journal of Materials Science*, **45**, 6498‑504.

[58] Cayron C., Rath E., Chu I. et Launois S. (2004) MICROSTRUCTURAL EVOLUTION OF Y2O3 AND MGAL2O4 ODS EUROFER STEELS DURING THEIR ELABORATION BY MECHANICAL MILLING AND HOT ISOSTATIC PRESSING. *Journal of Nuclear Materials*, **335**, 83‑102.

[59] Kishimoto H., Alinger M.J., Odette G.R. et Yamamoto T. (2004) TEM EXAMINATION OF MICROSTRUCTURAL EVOLUTION DURING PROCESSING OF 14CRYWTI NANOSTRUCTURED FERRITIC ALLOYS. *Journal of Nuclear Materials*, **329–333, Part A**, 369‑71.

[60] Sornin D., Grosdidier T., Malaplate J., Tiba I., Bonnaillie P., Allain-Bonasso N. et Nunes D. (2013) MICROSTRUCTURAL STUDY OF AN ODS STAINLESS STEEL OBTAINED

BY HOT UNI-AXIAL PRESSING. *Journal of Nuclear Materials*, **439**, 19‑24.

[61] Chen C.-L. et Dong Y.-M. (2011) EFFECT OF MECHANICAL ALLOYING AND CONSOLIDATION PROCESS ON MICROSTRUCTURE AND HARDNESS OF NANOSTRUCTURED FE–CR–AL ODS ALLOYS. *Materials Science and Engineering: A*, **528**, 8374‑80.

[62] Oksiuta Z., Ozieblo A., Perkowski K., Osuchowski M. et Lewandowska M. (2014) INFLUENCE OF HIP PRESSURE ON TENSILE PROPERTIES OF A 14CR ODS FERRITIC STEEL. *Fusion Engineering and Design*, **89**, 137‑41.

[63] Leng B., Ukai S., Sugino Y., Tang Q., Narita T., Hayashi S., Wan F., Ohtsuka S. et Kaito T. (2011) RECRYSTALLIZATION TEXTURE OF COLD-ROLLED OXIDE DISPERSION STRENGTHENED FERRITIC STEEL. *ISIJ International*, **51**, 951‑7.

[64] Steckmeyer A., Rodrigo V.H., Gentzbittel J.M., Rabeau V. et Fournier B. (2012) TENSILE ANISOTROPY AND CREEP PROPERTIES OF A FE–14CRWTI ODS FERRITIC STEEL. *Journal of Nuclear Materials*, **426**, 182‑8.

[65] Miao P., Odette G.R., Yamamoto T., Alinger M. et Klingensmith D. (2008) THERMAL STABILITY OF NANO-STRUCTURED FERRITIC ALLOY. *Journal of Nuclear Materials*, **377**, 59‑64.

[66] Olier P., Malaplate J., Mathon M.H., Nunes D., Hamon D., Toualbi L., de Carlan Y. et Chaffron L. (2012) CHEMICAL AND MICROSTRUCTURAL EVOLUTION ON ODS FE–14CRWTI STEEL DURING MANUFACTURING STAGES. *Journal of Nuclear Materials*, **428**, 40‑6.

[67] Kasada R., Lee S.G., Isselin J., Lee J.H., Omura T., Kimura A., Okuda T., Inoue M., Ukai S., Ohnuki S., Fujisawa T. et Abe F. (2011) ANISOTROPY IN TENSILE AND DUCTILE–BRITTLE TRANSITION BEHAVIOR OF ODS FERRITIC STEELS. *Journal of Nuclear Materials*, **417**, 180‑4.

[68] Regle H. et Pineau A. (1994) ALLIAGES FERRITIQUES QUATORZE ET VINGT POUR CENT DE CHROME RENFORCES PAR DISPERSION D'OXYDES: EFFETS DES PROCEDES DE MISE EN FORME SUR LES TEXTURES DE DEFORMATION, LA RECRISTALLISATION ET LES PROPRIETES DE TRACTION = OXIDE DISPERSION STRENGTHENED FERRITIC ALLOYS, FORTY AND TWENTY PERCENT CHROMIUM: EFFECTS OF HOT AND COLD WORKING PROCESSES ON DEFORMATION TEXTURES, RECRYSTALLISATION AND TENSILE PROPERTIES [Internet] [Text]. Université de Paris 11, Orsay, France.

[69] Sakasegawa H., Legendre F., Boulanger L., Brocq M., Chaffron L., Cozzika T., Malaplate J., Henry J. et de Carlan Y. (2011) STABILITY OF NON-STOICHIOMETRIC

CLUSTERS IN THE MA957 ODS FERRTIC ALLOY. *Journal of Nuclear Materials*, **417**, 229‑32.

[70] Klimiankou M., Lindau R. et Möslang A. (2004) TEM CHARACTERIZATION OF STRUCTURE AND COMPOSITION OF NANOSIZED ODS PARTICLES IN REDUCED ACTIVATION FERRITIC–MARTENSITIC STEELS. *Journal of Nuclear Materials*, **329–333, Part A**, 347‑51.

[71] Ribis J. et de Carlan Y. (2012) INTERFACIAL STRAINED STRUCTURE AND ORIENTATION RELATIONSHIPS OF THE NANOSIZED OXIDE PARTICLES DEDUCED FROM ELASTICITY-DRIVEN MORPHOLOGY IN OXIDE DISPERSION STRENGTHENED MATERIALS. *Acta Materialia*, **60**, 238‑52.

[72] Susila P., Sturm D., Heilmaier M., Murty B.S. et Subramanya Sarma V. (2011) EFFECT OF YTTRIA PARTICLE SIZE ON THE MICROSTRUCTURE AND COMPRESSION CREEP PROPERTIES OF NANOSTRUCTURED OXIDE DISPERSION STRENGTHENED FERRITIC (FE–12CR–2W–0.5Y2O3) ALLOY. *Materials Science and Engineering: A*, **528**, 4579‑84.

[73] Brandes M.C., Kovarik L., Miller M.K., Daehn G.S. et Mills M.J. (2012) CREEP BEHAVIOR AND DEFORMATION MECHANISMS IN A NANOCLUSTER STRENGTHENED FERRITIC STEEL. *Acta Materialia*, **60**, 1827‑39.

[74] Cunningham N., Wu Y., Klingensmith D. et Odette G.R. (2014) ON THE REMARKABLE THERMAL STABILITY OF NANOSTRUCTURED FERRITIC ALLOYS. *Materials Science and Engineering: A*, **613**, 296‑305.

[75] Miller M.K., Hoelzer D.T., Kenik E.A. et Russell K.F. (2005) STABILITY OF FERRITIC MA/ODS ALLOYS AT HIGH TEMPERATURES. *Intermetallics*, **13**, 387‑92.

[76] Oksiuta Z., Lewandowska M. et Kurzydłowski K.J. (2013) MECHANICAL PROPERTIES AND THERMAL STABILITY OF NANOSTRUCTURED ODS RAF STEELS. *Mechanics of Materials*, **67**, 15‑24.

[77] Rouffié A.L., Crépin J., Sennour M., Tanguy B., Pineau A., Hamon D., Wident P., Vincent S., Garat V. et Fournier B. (2014) EFFECT OF THE THERMAL AGEING ON THE TENSILE AND IMPACT PROPERTIES OF A 18%CR ODS FERRITIC STEEL. *Journal of Nuclear Materials*, **445**, 37‑42.

[78] Alamo A., Bertin J.L., Shamardin V.K. et Wident P. (2007) MECHANICAL PROPERTIES OF 9CR MARTENSITIC STEELS AND ODS-FECR ALLOYS AFTER NEUTRON IRRADIATION AT 325 °C UP TO 42 DPA. *Journal of Nuclear Materials*, **367–370, Part A**, 54‑9.

[79] Luzginova N.V., Nolles H.S., ten Pierick P., Bakker T., Mutnuru R.K., Jong M. et Blagoeva D.T. (2012) IRRADIATION RESPONSE OF ODS EUROFER97 STEEL. *Journal of Nuclear Materials*, **428**, 192‑6.

[80] Kishimoto H., Yutani K., Kasada R., Hashitomi O. et Kimura A. (2007) HEAVY-ION IRRADIATION EFFECTS ON THE MORPHOLOGY OF COMPLEX OXIDE PARTICLES IN OXIDE DISPERSION STRENGTHENED FERRITIC STEELS. *Journal of Nuclear Materials*, **367–370, Part A**, 179‑84.

[81] Kishimoto H., Kasada R., Hashitomi O. et Kimura A. (2009) STABILITY OF Y–TI COMPLEX OXIDES IN FE–16CR–0.1TI ODS FERRITIC STEEL BEFORE AND AFTER HEAVY-ION IRRADIATION. *Journal of Nuclear Materials*, **386–388**, 533‑6.

[82] Chen J., Jung P., Henry J., de Carlan Y., Sauvage T., Duval F., Barthe M.F. et Hoffelner W. (2013) IRRADIATION CREEP AND MICROSTRUCTURAL CHANGES OF ODS STEELS OF DIFFERENT CR-CONTENTS DURING HELIUM IMPLANTATION UNDER STRESS. *Journal of Nuclear Materials*, **437**, 432‑7.

[83] Lescoat M.-L., Ribis J., Gentils A., Kaïtasov O., de Carlan Y. et Legris A. (2012) IN SITU TEM STUDY OF THE STABILITY OF NANO-OXIDES IN ODS STEELS UNDER ION-IRRADIATION. *Journal of Nuclear Materials*, **428**, 176‑82.

[84] Ribis J. et Lozano-Perez S. (2014) NANO-CLUSTER STABILITY FOLLOWING NEUTRON IRRADIATION IN MA957 OXIDE DISPERSION STRENGTHENED MATERIAL. *Journal of Nuclear Materials*, **444**, 314‑22.

[85] Liu C., Yu C., Hashimoto N., Ohnuki S., Ando M., Shiba K. et Jitsukawa S. (2011) MICRO-STRUCTURE AND MICRO-HARDNESS OF ODS STEELS AFTER ION IRRADIATION. *Journal of Nuclear Materials*, **417**, 270‑3.

[86] Ribis J., Lescoat M.-L., de Carlan Y., Costantini J.-M., Monnet I., Cozzika T., Delabrouille F. et Malaplate J. (2011) STABILITY OF NANO-OXIDES UPON HEAVY ION IRRADIATION OF AN ODS MATERIAL. *Journal of Nuclear Materials*, **417**, 262‑5.

[87] Ryazanov A.I., Chugunov O.K., Ivanov S.M., Latushkin S.T., Lindau R., Möslang A., Nikitina A.A., Prikhodko K.E., Semenov E.V., Unezhev V.N. et Vladimirov P.V. (2013) TENSILE PROPERTIES AND MICROSTRUCTURE OF HELIUM IMPLANTED EUROFER ODS. *Journal of Nuclear Materials*, **442**, S153‑7.

[88] Chen J., Jung P., Rebac T., Duval F., Sauvage T., de Carlan Y. et Barthe M.F. (2014) HELIUM EFFECTS ON CREEP PROPERTIES OF FE–14CRWTI ODS STEEL AT 650 °C. *Journal of Nuclear Materials*, **453**, 253‑8.

[89] Ukai S., Harada M., Okada H., Inoue M., Nomura S., Shikakura S., Nishida T., Fujiwara M. et Asabe K. (1993) TUBE MANUFACTURING AND MECHANICAL PROPERTIES OF OXIDE DISPERSION STRENGTHENED FERRITIC STEEL. *Journal of Nuclear Materials*, **204**, 74‑80.

[90] Ratti M. (2009) DEVELOPPEMENT DE NOUVELLES NUANCES D'ACIERS FERRITIQUES / MARTYENSITIQUES POUR LE GAINAGE D'ELEMENTS COMBUSTIBLES DES REACTEURS A NEUTRONS RAPIDES AU SODIUM. Institut National Polytechnique de Grenoble - INPG.

[91] Alamo A., Regle H., Pons G. et Béchade J.L. (1992) MICROSTRUCTURE AND TEXTURES OF ODS FERRITIC ALLOYS OBTAINED BY MECHANICAL ALLOYING. *Materials Science Forum*, **88-90**, 183‑90.

[92] Regle H. et Alamo A. (1993) SECONDARY RECRYSTALLIZATION OF OXIDE DISPERSION STRENGTHENED FERRITIC ALLOYS. *Le Journal de Physique IV*, **03**, C7‑727 ‑ C7‑730.

[93] Savart F. (1829) RESEARCHES ON THE ELASTICITY OF REGULARLY CRYSTALLIZED BODIES. *The Edinburgh Journal of Science*, **1**, 141‑7.

[94] Savart F. (1829) RESEARCHES ON THE STRUCTURE OF METALS, AS INDICATED BY THEIR ACOUSTIC PROPERTIES. *The Edinburgh Journal of Science*, **2**, 104‑11.

[95] Sorby H.C. (1886) ON THE MICROSCOPIC STRUCTURES OF IRON AND STUDY OF MICROSCOPIC STRUCTURES OF STEEL. *Journal of Iron and Steel Instrumentation*, **1**, 140.

[96] Hull D. et Bacon D.J. (2011) INTRODUCTION TO DISLOCATIONS. Elsevier.

[97] Friedel J. (1964) DISLOCATIONS. Pergamon Pr., Oxford.

[98] Kubin L.P. (2006) DISLOCATION PATTERNING. *Materials Science and Technology*, Wiley-VCH Verlag GmbH & Co. KGaA.

[99] Mughrabi H. (1983) DISLOCATION WALL AND CELL STRUCTURES AND LONG-RANGE INTERNAL STRESSES IN DEFORMED METAL CRYSTALS. *Acta Metallurgica*, **31**, 1367‑79.

[100] Nes E. (1997) MODELLING OF WORK HARDENING AND STRESS SATURATION IN FCC METALS. *Progress in Materials Science*, **41**, 129‑93.

[101] Doherty R.D., Hughes D.A., Humphreys F.J., Jonas J.J., Jensen D.J., Kassner M.E., King W.E., McNelley T.R., McQueen H.J. et Rollett A.D. (1997) CURRENT ISSUES IN RECRYSTALLIZATION: A REVIEW. *Materials Science and Engineering: A*, **238**,

219‑74.

[102] Dillamore I.L., Morris P.L., Smith C.J.E. et Hutchinson W.B. (1972) TRANSITION BANDS AND RECRYSTALLIZATION IN METALS. *Proceedings of the Royal Society of London A Mathematical and Physical Sciences*, **329**, 405‑20.

[103] Hutchinson B. (1999) DEFORMATION MICROSTRUCTURES AND TEXTURES IN STEELS. *Philosophical Transactions of the Royal Society of London Series A: Mathematical, Physical and Engineering Sciences*, **357**, 1471‑85.

[104] Humphreys F.J. et Hatherly M. (2004) RECRYSTALLIZATION AND RELATED ANNEALING PHENOMENA. Elsevier.

[105] Kuhlmann D. (1951) ON THE THEORY OF PLASTIC DEFORMATION. *Proceedings of the Physical Society Section A*, **64**, 140.

[106] Sandsttröm R. (1977) SUBGRAIN GROWTH OCCURRING BY BOUNDARY MIGRATION. *Acta Metallurgica*, **25**, 905‑11.

[107] Frost H.J. et Ashby M.F. (1982) DEFORMATION MECHANISM MAPS: THE PLASTICITY AND CREEP OF METALS AND CERAMICS [Internet]. Pergamon Press, Oxford, UK.

[108] Ørsund R. et Nes E. (1989) SUBGRAIN GROWTH DURING ANNEALING OF HEAVILY DEFORMED METALS. *Scripta Metallurgica*, **23**, 1187‑92.

[109] Li J.C.M. (1962) POSSIBILITY OF SUBGRAIN ROTATION DURING RECRYSTALLIZATION. *Journal of Applied Physics*, **33**, 2958‑65.

[110] Doherty R.D. et Szpunar J.A. (1984) KINETICS OF SUB-GRAIN COALESCENCE—A RECONSIDERATION OF THE THEORY. *Acta Metallurgica*, **32**, 1789‑98.

[111] Sandström R. (1977) ON RECOVERY OF DISLOCATIONS IN SUBGRAINS AND SUBGRAIN COALESCENCE. *Acta Metallurgica*, **25**, 897‑904.

[112] Furu T., Ørsund R. et Nes E. (1995) SUBGRAIN GROWTH IN HEAVILY DEFORMED ALUMINIUM—EXPERIMENTAL INVESTIGATION AND MODELLING TREATMENT. *Acta Metallurgica et Materialia*, **43**, 2209‑32.

[113] Hsun H. (1962) MICROBANDS IN A ROLLED SI-FE CRYSTAL AND THEIR ROLE IN RECRYSTALLIZATION. *Acta Metallurgica*, **10**, 1112‑6.

[114] Read W.T. et Shockley W. (1950) DISLOCATION MODELS OF CRYSTAL GRAIN BOUNDARIES. *Physical Review*, **78**, 275‑89.

[115] Beck P.A. et Sperry P.R. (1950) STRAIN INDUCED GRAIN BOUNDARY MIGRATION IN HIGH PURITY ALUMINUM. *Journal of Applied Physics*, **21**, 150‑2.

[116] Tikhonova M., Kaibyshev R., Fang X., Wang W. et Belyakov A. (2012) GRAIN BOUNDARY ASSEMBLES DEVELOPED IN AN AUSTENITIC STAINLESS STEEL DURING LARGE STRAIN WARM WORKING. *Materials Characterization*, **70**, 14‑20.

[117] Bailey J.E. et Hirsch P.B. (1962) THE RECRYSTALLIZATION PROCESS IN SOME POLYCRYSTALLINE METALS. *Proceedings of the Royal Society of London Series A Mathematical and Physical Sciences*, **267**, 11‑30.

[118] Bate P. et Hutchinson B. (1997) A RE-EVALUATION OF THE MECHANISM OF SIBM. *Scripta Materialia*, **36**, 195‑8.

[119] Holm E.A., Miodownik M.A. et Rollett A.D. (2003) ON ABNORMAL SUBGRAIN GROWTH AND THE ORIGIN OF RECRYSTALLIZATION NUCLEI. *Acta Materialia*, **51**, 2701‑16.

[120] Oyarzábal M., Martínez-de-Guerenu A. et Gutiérrez I. (2008) EFFECT OF STORED ENERGY AND RECOVERY ON THE OVERALL RECRYSTALLIZATION KINETICS OF A COLD ROLLED LOW CARBON STEEL. *Materials Science and Engineering: A*, **485**, 200‑9.

[121] Dunlop J.W.C., Bréchet Y.J.M., Legras L. et Zurob H.S. (2007) MODELLING ISOTHERMAL AND NON-ISOTHERMAL RECRYSTALLISATION KINETICS: APPLICATION TO ZIRCALOY-4. *Journal of Nuclear Materials*, **366**, 178‑86.

[122] Ashby M.F., Harper J. et Lewis J. (1969) THE INTERACTION OF CRYSTAL BOUNDARIES WITH SECOND-PHASE PARTICLES. *Trans Met Soc AIME*, **245**, 413‑20.

[123] Nes E., Ryum N. et Hunderi O. (1985) ON THE ZENER DRAG. *Acta Metallurgica*, **33**, 11‑22.

[124] Chang K., Feng W. et Chen L.-Q. (2009) EFFECT OF SECOND-PHASE PARTICLE MORPHOLOGY ON GRAIN GROWTH KINETICS. *Acta Materialia*, **57**, 5229‑36.

[125] Ringer S.P., Li W.B. et Easterling K.E. (1989) ON THE INTERACTION AND PINNING OF GRAIN BOUNDARIES BY CUBIC SHAPED PRECIPITATE PARTICLES. *Acta Metallurgica*, **37**, 831‑41.

[126] Asle Zaeem M., El Kadiri H., Wang P.T. et Horstemeyer M.F. (2011) INVESTIGATING THE EFFECTS OF GRAIN BOUNDARY ENERGY ANISOTROPY AND SECOND-PHASE PARTICLES ON GRAIN GROWTH USING A PHASE-FIELD MODEL. *Computational*

Materials Science, **50**, 2488‑92.

[127] Hundert O., Nes E. et Ryum N. (1989) ON THE ZENER DRAG—ADDENDUM. *Acta Metallurgica*, **37**, 129‑33.

[128] Bréchet Y. et Militzer M. (2005) A NOTE ON GRAIN SIZE DEPENDENT PINNING. *Scripta Materialia*, **52**, 1299‑303.

[129] Rollett A.D. et Mullins W.W. (1997) ON THE GROWTH OF ABNORMAL GRAINS. *Scripta Materialia*, **36**, 975‑80.

[130] Kim S.G. et Park Y.B. (2008) GRAIN BOUNDARY SEGREGATION, SOLUTE DRAG AND ABNORMAL GRAIN GROWTH. *Acta Materialia*, **56**, 3739‑53.

[131] Hillert M. (1965) ON THE THEORY OF NORMAL AND ABNORMAL GRAIN GROWTH. *Acta Metallurgica*, **13**, 227‑38.

[132] Gladman T. (1966) ON THE THEORY OF THE EFFECT OF PRECIPITATE PARTICLES ON GRAIN GROWTH IN METALS. *Proceedings of the Royal Society of London Series A Mathematical and Physical Sciences*, **294**, 298‑309.

[133] Andersen I. et Grong Ø. (1995) ANALYTICAL MODELLING OF GRAIN GROWTH IN METALS AND ALLOYS IN THE PRESENCE OF GROWING AND DISSOLVING PRECIPITATES—I. NORMAL GRAIN GROWTH. *Acta Metallurgica et Materialia*, **43**, 2673‑88.

[134] Leguen C. (2010) PRIOR AUSTENITE GRAIN SIZE CONTROLLED BY PRECIPITATES [Internet]. INSA de Lyon.

[135] Razzak M. abdur, Perez M., Sourmail T., Cazottes S. et Frotey M. (2012) A SIMPLE MODEL FOR ABNORMAL GRAIN GROWTH. *ISIJ International*, **52**, 2278‑82.

[136] Chou T.S. et Bhadeshia H.K.D.H. (1994) RECRYSTALLIZATION TEMPERATURES IN MECHANICALLY ALLOYED OXIDE-DISPERSION-STRENGTHENED MA956 AND MA957 STEELS. *Materials Science and Engineering: A*, **189**, 229‑33.

[137] Bhadeshia H.K.D.H. (1997) RECRYSTALLISATION OF PRACTICAL MECHANICALLY ALLOYED IRON-BASE AND NICKEL-BASE SUPERALLOYS. *Materials Science and Engineering: A*, **223**, 64‑77.

[138] Sha W. et Bhadeshia H.K.D.H. (1997) MODELLING OF RECRYSTALLISATION IN MECHANICALLY ALLOYED MATERIALS. *Materials Science and Engineering: A*, **223**, 91‑8.

[139] Miao P., Odette G.R., Yamamoto T., Alinger M., Hoelzer D. et Gragg D. (2007) EFFECTS OF CONSOLIDATION TEMPERATURE, STRENGTH AND MICROSTRUCTURE ON FRACTURE TOUGHNESS OF NANOSTRUCTURED FERRITIC ALLOYS. *Journal of Nuclear Materials*, **367–370, Part A**, 208‑12.

[140] Oksiuta Z. (2011) MICROSTRUCTURAL CHANGES OF ODS FERRITIC STEEL POWDERS DURING MECHANICAL ALLOYING. *Acta Mechanica et Automatica*, **Vol. 5, no. 2**, 74‑8.

[141] Oksiuta Z., Hosemann P., Vogel S.C. et Baluc N. (2014) MICROSTRUCTURE EXAMINATION OF FE–14CR ODS FERRITIC STEELS PRODUCED THROUGH DIFFERENT PROCESSING ROUTES. *Journal of Nuclear Materials*, **451**, 320‑7.

Chapter II
Characterization methods and related specific developments

As explained in details in the chapter devoted to the literature review and in the general introduction, the aims of the thesis are to analyse and explain the microstructural evolution of the ODS steel ferritic steels developed to be used as sodium nuclear reactor fuel claddings. In order to be able to explain this evolution, the material has to be characterized all along the numerous processing steps. Due to their particular features, ODS ferritic steels and particularly in their ball milled states are particularly difficult to characterize and specific characterization methods will be proposed. First, the various steps in the process which have been characterized are presented in section §1, especially the very first step such as the annealed powders and an intermediate stage of consolidation. Then the choice of suitable methods for a quantitative characterization of such specific materials (abnormal grain distribution, nanoscale precipitation, high dislocation density) will be detailed. The classical methods used, will be briefly recalled, then advanced characterization methods such as Atom probe Tomography (APT) or SAS (Small Angle Scattering) will be presented. Finally, a more detailed presentation of recently available characterization techniques such as Automatic crystallographic Orientation Mapping – Transmission Electron Microscopy (ACOM-TEM) and of the specific developments made on classical methods X-Ray Diffraction (XRD) will be explored.

1. Material state selection

During the fabrication of ODS cladding tubes, the ball milled powder is degassed, heated up to the consolidation temperature and extruded (cf. Literature review). In order to identify and understand the key features of the microstructural evolution, key states of the fabrication will be reproduced and in particular: annealings on as-milled powder to study the conditions that lead to abnormal grain growth. In addition, several consolidated samples were studied, these samples are particularly important to account for the compatibility between the results obtained on powders and the effective evolution of the microstructure during the cladding tube fabrication (cf. Figure II.1).

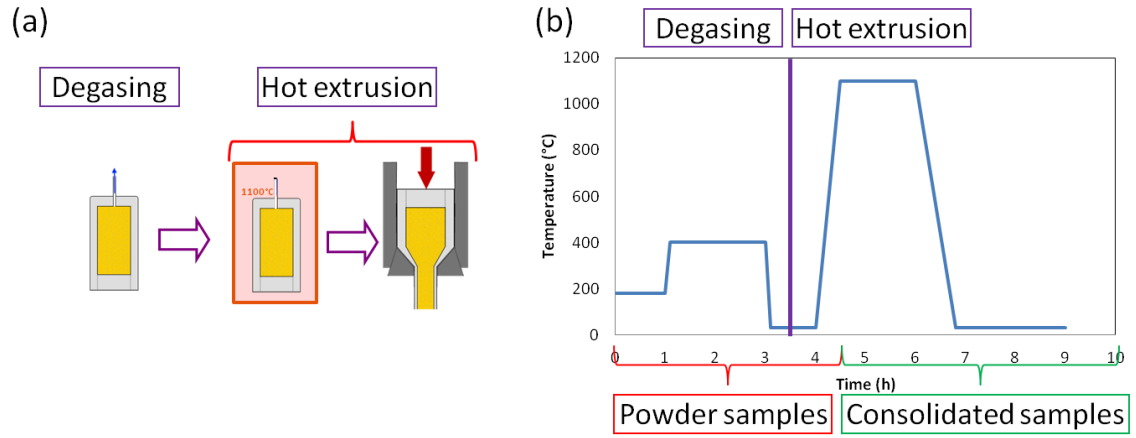

Figure II.1: Fabrication steps of interest (a) sketch of the steps (b) thermal history and material state of the sample during the considered elaboration step

1.1. Summary table of the studied materials

	Elaboration			Expected outcomes
	Initial powder	Milling condition	Consolidation temperature	
Powder				
9073		Plansee	-	- Identify the key temperatures of the recrystallization mechanism leading to abnormal grain growth. - Analyse the causes leading to abnormal grain growth - Account for the effect of the solute content on abnormal grain growth
9074 A	-	-	-	
9074	9074 A	CEA	-	
9077	9074 A	Mécachrome	-	
UP25		CEA	-	
UP26		CEA	-	
UP29		CEA	-	
UP49		CEA	-	
Consolidated				
K10	9067		850°C	- Identify the effects of thermo mechanical processing compared to purely thermal processing
HIP-INSA	9073		1160°C	
Extruded				
K71-Fi	9077		1100°C	- Study the evolution of the microstructure all along the extrusion step and more precisely the interaction between grain boundaries and precipitates at high temperature.
J27	9067		1130°C	

1.2. ODS steel particles

The ODS steel particles mainly studied in this thesis have been obtained from powders produced by gas atomization performed by Aubert & Duval. The powder resulting from this process consists in spherical particles with an average diameter of 70 µm. Its composition is : Fe-14 Cr-1 W-0.3 Ti (wt%) and ~0.3wt% of manganese and silicon. The atomized powder was then milled with yttria particles (having a diameter inferior to 100

nm) by Plansee SE in an industrial high-energy attritor under hydrogen atmosphere. No premixing of the powder is performed, powders are shaken by a vertical shaft for 12 hours to optimise the homogeneity towards the contamination (essentially carbon, oxygen and Nitrogen) which can result from both the atmosphere and the contact with other materials within the attritor. At the end of the milling, powder particles have an average diameter of 77 µm and an average shape factor of 1.8. Within the CEA this powder is referred to as 18R-9073.

A second similar grade (cf. Table II.1) powder referred to as K75-9077 has been prepared by Aubert & Duval, Mécachrome and the CEA. Only a limited characterization campaign focusing on the similarity between the powders' evolution during annealing was performed.

	Fe	Cr	Ni	Ti	W	Si	N	Mn	Y	O
Mesured composition (%wt)	81.56	14.5	0.2	0.32	0.94	0.15	0.136	0.35	0.25	0.13

Table II.1: Composition of the K75-9077 powder measured by microprobe

In order to identify the effect of the solute content on ODS steels, specific powders were produced at the CEA. These powders are also used here to specifically account for the solute effect on abnormal grain growth. The base powder of high-chromium ferritic steel was gas atomized by Aubert & Duval similarly than what was done for the other grades. This powder was then milled with respectively 0, 0.05, 0.3 and 1 wt% of yttrium and titanium in a high-energy attritor for 10 hours at the CEA.

1.3. Consolidated samples

Two consolidated samples have been studied. The first has the following nominal composition: Fe-14Cr-1W-0,4Ti-0,3Y2O3. It is issued from the 16R-9067 powder (cf. Table II.2) which has been consolidated at 850°C for 1h under 450 bars and is referenced K10.

The second consolidated sample, fabricated through Hot Isostatic Pressing (HIP) for 3h at 1160°C under 1000bars was also studied. This sample is issued from the powder extensively studied here, i.e. 18R-9073 grade. This sample was supplied by the MATEIS laboratory at the INSA Lyon and Cefival, it will be referred to as HIP-INSA.

1.4. Extruded samples:

To study the evolution of the microstructure during extrusion, a specific sample has been fabricated. K75-9077 powder was pre-heated for 1h at 1100°C and the extrusion, performed with an extrusion ratio of 3.6 at 1100°C, was interrupted. The resulting material presented in Figure II.2, will be referred to as K71-Fi.

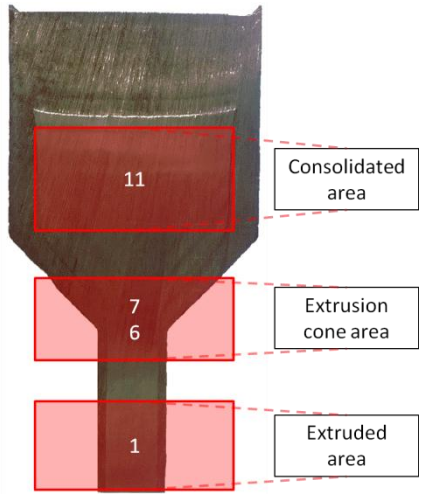

Figure II.2: Section of the interrupted extrusion sample, locations of the sampling zones are specified

An extruded rod was also studied during the thesis. With a nominal composition of Fe-14Cr1W0.3Ti $0.3Y_2O_3$, it was originally designed for the European program GETMAT. Once again matrix base powder was supplied by Aubert & Duval (P-9066) and ball milled with yttria particles by Plansee (P-9067) (cf. Table II.2). Consolidation was performed by Cefival with a pre heating of 3h at 1130°C followed by extrusion with an aspect ratio of 3.16 and a final softening of 1.5h at 1050°C.

	Mn	Ni	Ti	W	C	H	N	O	Cr	Y_2O_3
Before Milling (P9066)	0.287	0.160	0.368	1.045	0.007	$<10^{-4}$	0.004	0.026	13.47	-
After Milling (P9067)	0.309	0.165	0.351	0.975	0.034	0.001	0.136	0.228	12.96	0.29

Table II.2: Composition evolution during mechanical alloying for the 16R-9067 powder used for the extruded sample J27 as well as for the consolidated sample K10

2. Classical characterization methods

For an initial examination, classical characterization methods have been used to obtain basic information on the microstructural evolution of the materials.

Scanning electron microscope

Scanning Electron Microscope (SEM) was used to study microstructures of powders and consolidated materials, images were taken on a FEG ZEISS Ultra 55. Powders were mounted on a specific conductive resin and polished up to a 1µm alumina solution and colloidal silica for several minutes.

Electron microprobe

Electron microprobe allows to perform quantitative analysis on chemical elements within solid samples. In mapping mode measurements spatial resolution was about 1µm it has been used here to evaluate the repartition of solute within the powder and to examine the chemical heterogeneities during extrusion. Experiments were carried out on a CAMECA SX50.

3. Advanced characterization methods for nanoprecipitation

As presented in II.§1.2.2, a key feature of the ODS steels is the yttrium based nanoprecipitation that gives rise to a very specific microstructure and worthwhile mechanical properties. It is therefore of prime importance to be able to fully characterize this nanoprecipitation evolution. This has been performed using the advanced characterization methods presented below.

3.1. Atom Probe Tomography

Atom Probe Tomography (ATP) is an essential characterization tool for ODS steels since it is actually the only method which enables to obtain reliable information on the yttrium oxides nanoprecipitates' composition. The APT results presented here have been carried out at the "Groupe de Physique des Matériaux" (GPM) in Rouen. The main goals are to show evidence of the precipitation even at low annealing temperature, to determine their composition evolution upon annealing and to detect the main elements' solute segregation at grain boundaries.

3.1.1. Basic principle

ATP principle has been extensively presented in many reference works, notably in review articles [1]. Only a short presentation of the basic principle of the method will be done here. The method consists in extracting, layer after layer, the atoms at the tip shaped sample surface by field evaporation, and to project them on a specific detector (cf. Figure II.3a). This detector is able to register the impact position and the time of flight of each impacting atom. Using those two parameters, it is then possible to reconstruct the 3D volume of the sample both in space and in composition.

To evaporate, an atom at the surface of a sample needs to get over the energy barrier $Q_{0,n}$ which depends on the ionisation level and the nature of the material ($Q_{0,n} = \Lambda + \sum I_n - n\Phi$, cf. Figure II.3b). An electric field is introduced in order to modify atomic and ionic potentials and lower the energy barrier Q_n. This electric field is the evaporation field ($E_{n,e} \approx Q_{0,n}^2 \frac{4\pi\varepsilon_0}{n^3 e^3}$, with ε_0 as the permittivity constant of the free space, n the ionisation level and e the elementary charge of an electron). If the energy barrier is low enough, an atom can jump out by tunnel effect or thermal activation, this phenomenon is called field evaporation.

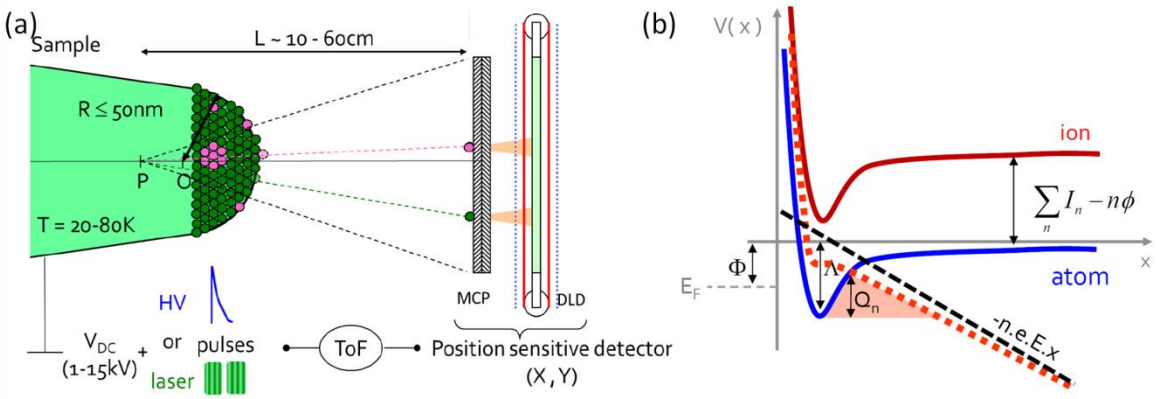

Figure II.3: Schematic diagram of an APT analysis. Courtesy of B. Radiguet GPM Rouen

3.1.2. Sample preparation principle

To evaporate atoms, an intense electric field needs to be created at the sample surface (from 10 to 40 V.nm^{-1}). This is usually obtained by shaping the sample as a needle. Indeed, when an electric potential is applied to a needle shaped sample, the electric field created at the surface is: $E = V/\beta.R$, with V as the electric potential, β is a form factor (ranging from 3 to 8) and R is the curvature radius at the sample tip. A curvature radius smaller than 50 nm is therefore required to evaporate atoms under an electrical potential superior to 10kV.

3.1.3. Experimental conditions

Analyses have been performed with Cameca Laser Assisted Wide Angle Tomographic Atom Probe (LAWATAP), using femtosecond laser pulses and a pulse repetition rate equal to 100 kHz from the Groupe de Physique des Matériaux. In order to optimize the measurement accuracy, the APT analyses have been performed using a UV laser at 40K and at an equivalent pulse fraction of 25%.

3.1.4. Limits

The ODS steels case is particularly difficult for APT analysis and this is essentially due to the fact that analysing ODS particles means to analyse oxides within a metallic matrix. That results in very different evaporation fields and creates errors in both size and composition. These artefacts have to be corrected [2–4]. Redundancy analysis on several sample issued from the same material is systematically used to compensate from the main criticism made towards APT (i.e. its small sampling area and therefore the relevance of the result for the general material behaviour). Still, it is very interesting to be able to perform APT measurement since it is a complementary method to TEM or with Small Angle Scattering techniques [5] which provide more global information on the materials.

3.2. Small Angle Scattering

Small Angle Scattering (SAS) techniques are characterization methods using small angle scattering signals (X-ray or neutron) to extract quantitative information on nanoscale microstructural features. Giving information on the material fluctuations within the

reciprocal space, they allow to study a wide range of topics such as phase transformation, structural defects (voids, radiation damage, dislocations), or even to characterize thin films in the case of Grazing Incidence SAS. Using variable X-Ray wavelength and the so-called "anomalous scattering", it is also possible to access the chemical composition of precipitates. Within the frame of this manuscript the main objectives with SAS are:

- Measure the precipitation state evolution upon annealing up to the consolidated temperature.
- Measure the precipitation state on consolidated samples

3.2.1. Basic principle

Similarly to what has been done for ATP only a short presentation of the basic principle of SAS will be done here. Interested readers for reviews on the subject are reported to [6–8]. Based on the measurement of the scattering of an incident wave due to heterogeneities within the material, depending on the type of particle (i.e. photon or neutron) the scattering factor of atoms changes as the nature of the scattering interaction changes: X-Rays will interact with the electron cloud whereas neutrons will interact with atoms' nucleus. Therefore different microstructural information can be obtained by changing the source type. With X-Rays, the diffusion factor is proportional to the electronic density. Consequently, SAXS (Small Angle X-ray Scattering) will be very sensible to the fluctuations of atomic number (and composition) between the precipitate and the matrix within the studied sample. SANS (Small Angle Neutron Scattering) will probe fluctuations of atomic scattering cross-section (which are not proportional to the atomic number but are still dependant on the scattering elements), SANS is also very sensible to magnetic contrasts of phases with different magnetic properties.
Comparative advantages of the two methods are the following:

- For system with high electronic contrast, SAXS is already very efficient even with laboratory sources. Effective signal can be greatly increased with synchrotron sources, which also allows to perform in-situ measurement. Given the low Z-contrast between the expected precipitates and the matrix in the ODS case, the only advantage for the SAXS method here is the possibility to perform laboratory measurements.
- Given the low electron density contrast in ODS steels, the high Z-number of precipitates, the low volume fraction and the fact that the two phases have very different magnetic properties. SANS measurements are particularly suited to study ODS steels.

3.2.2. Theory

The scattering angle range is confined between 0 and π/d_a where d_a is the closest interatomic spacing (cf. Figure II.4). In bcc materials and more precisely on ferritic ODS steels $d_a = a\sqrt{3}/2$, with a = 2,88 Å, which leads to maximal q range of 1,27 $Å^{-1}$.

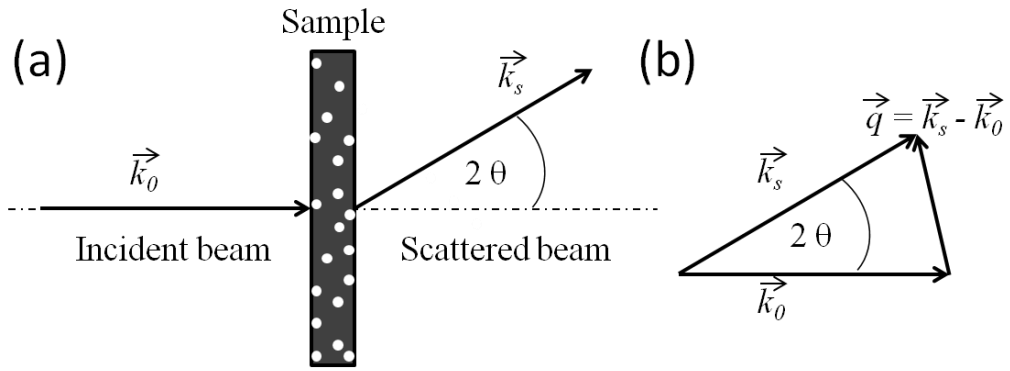

Figure II.4: Schematic diagram of small angle scattering (a) beam diffusion (b) scattering vector. With $k = \frac{2\pi}{\lambda}$, and $q = \frac{4\pi \sin\theta}{\lambda}$

3.2.3. Calculation

Equations describing SAS will not be developed here and can be found in literature [6–8]. The analysis of the results obtained from SAS methods is based on the integrated intensity, the invariant Q_0, which is proportional to the precipitate volume fraction. Considering isotropic conditions, the invariant Q_0 can be written:

$$Q_0(\lambda) = \iiint_V I(q_x, q_y, q_z)\, dq_x dq_y dq_z = \int_0^\infty I(q) q^2 dq = 2\pi^2 |\Delta\rho(\lambda)|^2 f_v (1 - f_v) \quad \text{(II.1)}$$

Where $I(q)$ is the scattered intensity, q is the module of the scattering vector as : $q = 4\pi \sin\theta/\lambda$, f_v is the volume fraction of scattering objects, and $\Delta\rho(\lambda)$ is the electronic contrast, defined as the difference in electronic density between the scattering particle and the matrix ($|\Delta\rho| = |\rho_{ppt} - \rho_m|$).

Considering a size dispersion function $f(R)$ corresponding to a precipitate population of size R, the total intensity can be written:

$$I(q) = \int_0^\infty f(R) I_1(q, R) dR \quad \text{(II.2)}$$

Different methods allow to retrieve function $f(R)$ from a scattered intensity. Very efficient methods, though time consuming, are indirect Fourier transform [9] or the maximum entropy method [10]. Within the frame of the thesis, we consider spherical precipitates of radius R and use the following model fitting approach:

$$f(R) = \frac{1}{\sqrt{2\pi}\sigma R} exp\left(-\frac{1}{2}\left(\frac{\ln(R_m/R)}{\sigma}\right)^2\right) \quad \text{(II.3)}$$

And:

$$I_1(q, R) = \left(\rho_p - \rho_m\right)^2 V_p^2 \left(\frac{\sin \mathrm{qR} - \mathrm{qR}\cos \mathrm{qR}}{(qR)^3}\right)^2 \quad \text{(II.4)}$$

Equations (II.1) from (II.4) allow to obtain the precipitate size distribution, and the volume fraction of a given material. It has been shown to adequately match observations made by transmission electron microscopy [11].

As expressed in (II.1), the calculation of Q necessitates an integration between 0 and ∞, which is impossible. Practically, Q is decomposed as a sum between directly measurable Q_2 and non-directly measurable parameters Q_1 and Q_3 as:

$$Q_0 = \int_0^{q_{min}} I(q)q^2dq + \int_{q_{min}}^{q_{max}} I(q)q^2dq + \int_{q_{max}}^{\infty} I(q)q^2dq = Q_1 + Q_2 + Q_3$$

To account for Q_1 and Q_3 two approximations are made. First, the integrated intensity within the q-range between 0 and q_{min} (Q_1) is defined as a triangle between the origin, (q_{min}, Iq_{min}^2) and $(q_{min}, 0)$, then, for the q-range above q_{max} (Q_3) the intensity is assumed to follow the so-called Porod law K_p/q^{-4}. Finally, (II.1) becomes:

$$Q_0 \approx \frac{I(q_{min})q_{min}^3}{2} + \int_{q_{min}}^{q_{max}} I(q)q^2dq + \frac{K_p}{q_{max}}$$

With K_p determined by fitting $I_{raw}q^4 \underset{q\to\infty}{\equiv} K_p + I_{Laue}q^4$, I_{Laue} being the remaining background noise (independent of q). The fitting model is only used between q_{min} and q_{max}.

Since λ and $\Delta\rho(\lambda)$ as well as the data correction methods used are different from SAS techniques, it is necessary to distinguish the analyses made from SAXS and SANS. Indeed, to obtain the proper intensity scattered by the precipitates, data correction and normalization have to be performed in order to get rid of the various background signals registered by the detectors and the different instrumental factors. General data correction methods can be found, respectively for SAXS and SANS in [12] and [13] and will not be detailed here.

3.2.4. SANS

3.2.4.1. Experimental condition

SANS experiments were performed in beamline D11 at the ILL reactor in Grenoble. The beamline is equipped with a collimator optical, an electromagnet and a 2D detector. To probe a large q-range, three different sample-detector distances have been used (1.6, 8 and 34m) offering a q-range ranging from 0.003 to 0.45 $Å^{-1}$ (i.e. to observe objects with a radius ranging from 0.4 to 65 nm). Wavelengths were selected to be above 4.15 Å and therefore suppress any Bragg diffraction possibility.

Additionally, a magnetic field of 1.6T was applied to the sample in order to access both magnetic and nuclear contrast of the scattering objects.

During this experiment, powders have been encapsulated in a specific quartz holder (transparent to the neutrons), the actual thickness of the sample is 1 mm and the incident beam surface is 6x12 mm, which means that the analysed volume is close to 70 mm^3 (cf. Figure II.5).

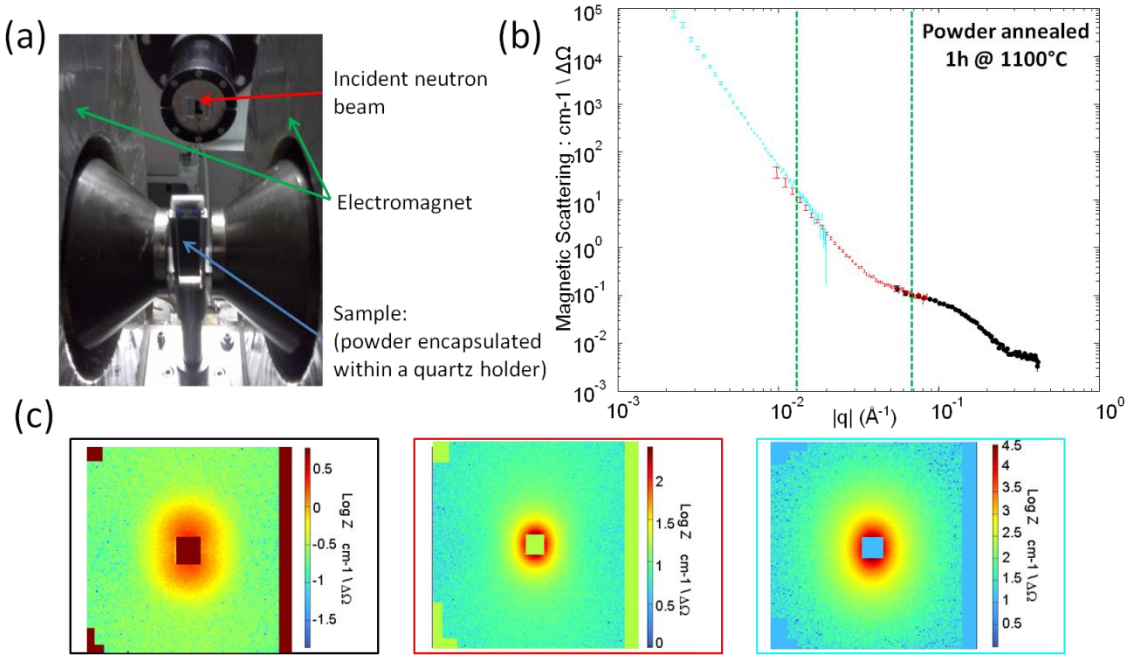

Figure II.5: Experimental set up of the SANS experiment and results. (a) sample positioning (b) Final scattering intensity obtained on an ODS ferritic powder P9073 annealed 1h@1100°C after adjusting the three different distances used (c) images of the detector at the three different distances

3.2.4.2. Contrast factors

SANS signal results from both the interaction between neutrons and atoms and the interaction between neutrons and the magnetic moment of the nucleus. Therefore we have to calculate two different contrast factors, which will depend on the crystallographic structure, on the chemical composition and on the magnetic moment of the matrix and the precipitates. To calculate these contrasts and access to the volume fraction of the analysed samples, a hypothesis has to be previously made on the precipitate composition. Based on a SAXS study by Dumont et al. [15], and confirmed by previous TEM results [16–18], the precipitate composition was assumed to be an intermediate between Y_2TiO_5 and $Y_2Ti_2O_7$ precipitates.

Nuclear contrast

	Fe	Cr	W	Ti	Y	O
Diffusion length (10^{-12}cm)	0.945	0.3635	0.4887	-0.337	0.775	0.5803

Table II.3:Diffusion length of the main ODS precipitates elements [19]

The nuclear contrast depends on the diffusion length of elements as:

$$\Delta\rho_{nucl} = \frac{b_p}{V_p} - \frac{b_m}{V_m}$$

With b_p and b_m being respectively the mean diffusion length for the precipitate $b_p = \sum_i b_i\, c_{i,p}$ and the matrix $b_m = \sum_i b_i\, c_{i,m}$. Where b_i is the diffusion length of the element i and $c_{i,m}$ its concentration within the matrix m.

Magnetic contrast

The magnetic contrast is defined as:

$$\Delta\rho_{mag} = a\left(\frac{\mu_p}{V_p} - \frac{\mu_m}{V_m}\right)$$

With a a constant equal to $0.2695.10^{-12}$ cm^{-2}. Å^3, μ_p and μ_m mean magnetic moments for atoms under a saturating magnetic field respectively for precipitate and the matrix. For the matrix, the mean magnetic moment per atom is [20] $\mu_m = (2.2 - 2.39.C_{Cr})\mu_B = 1.078.10^{-4} eV.T^{-1}$, where μ_b is the Bohr magneton and C_{Cr} is the chromium concentration. In our hypothesis, precipitates are oxides, which means that $\mu_p = 0$.

The average atomic volumes of the considered elements are:

	$V_{Fe-\alpha}$	$V_{Y_2TiO_5}$	$V_{Y_2Ti_2O_7}$
Atomic volume (Å^3)	11.77	13.46	11.69

Table II.4: Mean atomic volume for the yttrium precipitates and the ferritic matrix [21]

Finally the resulting contrast factors are:

	Y_2TiO_5	$Y_2Ti_2O_7$
$\Delta\rho^2_{nucl}$ (10^{-12} cm.Å^{-3})^2	$1.186.10^{-3}$	$1.172.10^{-3}$
$\Delta\rho^2_{magn}$ (10^{-12} cm.Å^{-3})^2	$1.777.10^{-3}$	$1.777.10^{-3}$

Table II.5: Calculated contrast factors for Y_2TiO_5 and $Y_2Ti_2O_7$ precipitates

Since both considered precipitates are oxides, their magnetic contrast is identical and for the study it will be taken to be $1.777.10^{-3}$ (10^{-12} cm.Å^{-3})^2. The final nuclear contrast is also very close (i.e. the difference between the two chosen precipitates is negligible compared to the measure errors) and will be taken as equal to $1.18.10^{-3}$ (10^{-12} cm.Å^{-3})^2.

3.2.5. SAXS

3.2.5.1. Experimental conditions

SAXS experiments were performed both at ESRF synchrotron source in Grenoble and using a laboratory source.

For experiments performed with a synchrotron source at 5.983keV, 2 distances (20cm and 1.65m) were used. Laboratory experiments were performed using a rotating Molybdenum anode source at 17.479 keV at two distances (30 and 50 cm).

ESRF experiments were carried out by F. de Gueser and L. Couturier (SIMaP laboratory).

3.2.5.2. Diffusion factors

The SAXS signal results from the interaction between X-rays and electrons. The electronic density contrast $\Delta\rho$ is calculated using:

$$\Delta\rho = \rho_p - \rho_m = \frac{\sum_i f_i C_i^p}{V_{at}^p} - \frac{\sum_i f_i C_i^m}{V_{at}^m} \quad \text{(II.5)}$$

In this expression, C_i^p and C_i^m respectively represent the atomic concentration of element i in the matrix and in the precipitate, V_{at} is the atomic volume and f_i are the diffusion factors of elements i equals to:

$$f_i = Z_i + f_i' + i.f_i'' \quad \text{(II.6)}$$

Where Z_i is the atomic number of the element i and f_i' and f_i'' are energy dependent terms.

		Fe	Cr	W	Ti	Y	O
Atomic number Z		$2.6.10^1$	$2.4.10^1$	$7.4.10^1$	$2.2.10^1$	$3.9.10^1$	8.00
$E = 5.983\ keV$	f_i'	-1.645	-6.82	-3.97	$-7.15.10^{-1}$	$8.36.10^{-2}$	$7.98.10^{-2}$
	f_i''	$6.37.10^{-1}$	$4.57.10^{-1}$	8.91	2.91	3.386	$5.96.10^{-2}$
$E = 17.479\ keV$	f_i'	$3.49.10^{-1}$	$3.23.10^{-1}$	$-7.6.10^{-1}$	$2.8.10^{-1}$	-2.79	$1.08.10^{-2}$
	f_i''	$8.46.10^{-1}$	$6.26.10^{-1}$	6.88	$4.47.10^{-1}$	3.57	$6.04.10^{-3}$

Table II.6 : Atomic number (Z) and diffusion factors f_i' and f_i'' of the major elements present in the ODS ferritic steels for the two incident energy used during this thesis [14]

Table II.6 allows to calculate the electronic density contrast using equations (II.5) and (II.6).

3.2.6. Limits

The low contrast of yttrium nanoprecipitates prevents from the possibility to perform in-situ SAXS characterisation, which would have enabled a direct access to the evolution of the precipitate distribution upon annealing.

4. Advanced characterization methods for structural defects: crystallite and grain size, dislocation density and local texture

ODS steels are likely to involve important microstructural evolution: recovery, recrystallization and grain growth that can be concomitant and are unpropitious to quantify in a time resolved manner. Yet, for powder metallurgy, kinetic studies of the microstructural evolution starting from the as-milled powder and during subsequent annealing are essential to detect the beginning of a critical phenomenon like abnormal grain growth.

X-Ray Diffraction (XRD) proved to be very accurate to describe dislocation density and crystallite size [22–25] which are suitable microstructural features for monitoring phenomena such as recovery, recrystallization and grain growth. To obtain physically interpretable data, an original 2D detection method which allowed to follow the growth of both Ultra Fine Grains (UFGs) and abnormal grains have been introduced on classical

XRD interpretation methods.

Nevertheless, XRD studies give global information that can overlook the local heterogeneities; grain morphology, local texture as well as grain misorientation are out of reach of a XRD diffraction approach. As proven by many recrystallization and microstructural studies during the last decade, the Scanning Electron Microscopy – Electron BackScatter Diffraction (SEM - EBSD) technique should be more appropriate to perform a recrystallization study. Unfortunately it is not possible to index EBSD patterns from highly deformed materials like as-milled ODS steel particles and the ODS steels' early processing stages. An innovative TEM (Transmission Electron Microscopy) technique called ACOM-TEM (Automatic Crystallographic Orientation Mapping – TEM), based on the scanning of a thin foil by a narrow parallel beam with simultaneous recording and indexation of the diffraction pattern has been used to overcome this problem.

4.1. X-Ray diffraction

XRD will be used here in order to obtain the evolution of the crystallite size and the dislocation density during annealing. We will first report the basic physical principles of crystalline defects study with XRD. Then, developments realized within the frame of this thesis will be presented.

4.1.1. General background

X-Rays are electromagnetic waves. When they reach a metallic material, they are able to produce vibration of the atom electron cloud. In return, these vibrations of the electronic cloud cause a secondary emission of electronic wave, each atom becomes the center of a diffusing wave which will interfere with the wave produced by the other atoms of the material. In crystalline material, like steels, the periodicity of atomic arrangement (and therefore of the electronic cloud or electronic density) is the cause for constructive and destructive interferences between the diffusing waves. The distance between the atomic layers defines a precise angle for constructive waves which creates peaks on the diffraction pattern.

4.1.1.1. Historic

Here, we will briefly recall the key dates for the diffraction peak analysis. XRD analyses have historically played a very important role in the study of heavily deformed materials.
In 1930, the first diffraction experiments on highly plastically deformed materials revealed that the matter was still ordered. The diffraction peaks were drastically broadened but still well defined while it was thought that intensely deformed materials would produce amorphous diffraction patterns due to the high lattice distortion. Following this discovery, which is concomitant with the introduction of the concept of dislocation by Orowan, Polanyi and Taylor (1934) (cf. Chapter I §2.2), Stokes and Wilson (1944) tried to calculate the effect of a dislocation on the broadening of a diffraction peak [26].

Then, in 1950, Wilson demonstrates that in materials with both lattice distortion and crystallite size effect, Fourier coefficients issued from diffracted intensities were the product of a size coefficient (A_L^S), a distortion coefficient (A_L^S) and a coefficient resulting from instrumental broadening effects (A_L^I) (with L the Fourier series parameter). This statement supposes that the asymmetrical character of the line profile is neglected. A_L can therefore be expressed as:

$$A_L = A_L^S . A_L^D . A_L^I$$

Warren and Averbach, between 1950 and 1959, introduced the first theory on diffraction peak broadening due to crystal defects. It involves the expression of peak intensity in terms of a Fourier sum, which can be summed up as the following equation [27,28]:

$$A_L = A_L^S . \exp\left(-2\pi^2 L^2 \langle \varepsilon_g \rangle^2\right) \quad \text{(II.7)}$$

Meanwhile, Williamson and Hall, introduced their own formula based on the analysis of the diffraction pattern (i.e. the reciprocal space) [29]:

$$\Delta K = \frac{1}{d} + \Delta\varepsilon_{hkl} K \quad \text{(II.8)}$$

Parameters of equation (II.8) are detailed in §4.1.2.2. Obviously, from (II.7) the mean difficulty is to get quantitative information from the distortion parameter ε. In 1963, Krivoglaz introduced the idea that distortion is statistically distributed due to dislocations, which leads to [30]:

$$\langle \varepsilon \rangle^2 = \left(\frac{b}{2\pi}\right)^2 \pi\rho C log\left(\frac{d}{L}\right) \quad \text{(II.9)}$$

Where C is the contrast factor of dislocations. This constituted a major improvement but also led to a logarithmic aberration which links d (the crystallite size) to the dislocation density. Equation (II.9) was corrected in 1970 by Wilkens which replaced d in the same equation by the parameter R_e (i.e. the effective outer cut off radius of dislocation) presented earlier (cf. Chapter II §4.1.5.2).

4.1.1.2. Influence of cristal defects on diffraction pattern

In the hypothetic case where the diffracting material is a perfect crystal (i.e. acts as an infinite array of plans with a perfectly constant interplanar distance), each diffraction peak would have a Dirac peak shape.

Crystal defects such as dislocation, grain boundaries, sub-boundaries stacking faults, etc. introduce local modifications of the interplanar distance or modulations in the integration domain of the diffraction intensity. A review of the mean effects of crystals defects on diffraction peak has notably been done by Ungàr [31] (cf. Figure II.6).

Sources of strain	Peak aberrations				
	Peak shift	Peak broadening	Peak asymmetry	Anisotropic peak broadening	Peak shape
Dislocations		+	+	+	+
Stacking faults	+	+	+	+	+
Twinning	+	+	+	+	+
Microstresses		+			
Long-range internal stresses	+		+		
Grain boundaries	+	+			
Sub-boundaries	+	+			
Internal stresses	+				
Coherency strains	+	+	+		
Chemical heterogeneities	+	+	+		
Point defects					+
Precipitates and inclusions			+		+
Crystallite smallness		+		+	+

Figure II.6: Typical correlations between diffraction peak aberrations and the different elements of the microstructure.

Broadening of the diffraction peaks can be due to two main classes of microstructural effects. On the one hand, the reduction of crystallite domain, grain, and twinning or stacking faults which are all considered as "size effects"; on the other hand, an increase of lattice distortions, such as the ones produced by inhomogeneous strains or dislocations. The peak profile can also be asymmetric or undergo shifts with respect to its expected Bragg position or shape modifications. Within all these complex phenomena, dislocations hold a particular place: they are always present either as the major, and in many cases the only component of lattice defects which distorts the crystal lattice to such an extent that it becomes visible by a line broadening. That is the reason why, for the sake of simplicity, we will consider them as the only lattice distortion effect responsible for peak broadening. This approximation will result in a systematic overestimation of the dislocation density. In addition, to account for the peak broadening, we will take into account the crystallite size.

4.1.2. Separation of the broadening effects

Analysis of the Bragg peaks broadening is widely used to determine the stress state and the diffracting crystallite domain. The principle of this analysis will be presented here.

4.1.2.1. Effect of the coherent domain size

Scherrer in 1918 [32], using an analogy with optical lattices, established a link between the integral breath of diffraction peaks and the apparent crystallite size (d).

$$B = \frac{\lambda}{d.\cos(\theta_0)} \tag{II.10}$$

Where $B = \frac{\int_{-\infty}^{+\infty} I(2\theta)d(2\theta)}{I_{max}}$, θ_0 is the Bragg' angle and 2θ the diffraction angle.

It has been shown that the diffracted peak intensity can be decomposed in Fourier transform series (cf. for example work by Warren [28]). Considering a infinite crystal, diffraction on the (hkl) plans is identical to a Fourier transform of an infinite distribution of Dirac peaks. Whereas, for a finite crystal, diffraction is equivalent to a Fourier transform of the product between a rectangular function and a Dirac comb. The Fourier transform of a Dirac comb is a Dirac comb and the Fourier transform of a rectangle is a cardinal sine function. Therefore, the resulting signal produced by the diffraction of such

a crystal lattice is the convolution between a Dirac comb and a squared cardinal sine function that is a squared cardinal sine function comb. This squared cardinal sine function comb constitutes the basis of the well known diffraction patterns shape. The important feature here is the independence of the crystallite size towards the diffraction peak (i.e. it can be measured equivalently on each peak, cf. Figure II.7).

4.1.2.2. Effect of the distorted lattice

To analyse the effect of a distortion of a lattice on a diffraction pattern one has to study the evolution of the interplanar distances between the crystal lattices. Indeed, according to Bragg's law peak position are defined by $K = \frac{2\sin\theta}{\lambda} = \frac{1}{d^0_{hkl}}$ The derivative of K gives:

$$\frac{\Delta K}{K} = \frac{{}^1/_{d_{hkl}} - {}^1/_{d^0_{hkl}}}{{}^1/_{d^0_{hkl}}} = \varepsilon_{hkl}$$

Where d_{hkl} the actual interplanar distance, d^0_{hkl} the interplanar distance for a non distorted lattice and ε_{hkl} the crystal distortion. Importantly, the peak shift ΔK is proportional to the product between the diffraction vector and the crystal distortion peak (cf. Figure II.7). Considering a distribution of distortions $\Delta\varepsilon_{hkl}$ they produce in return a distribution of peaks around the perfect lattice peak position K. Therefore the final resulting signal is a peak diffraction with a width equal to $K\Delta\varepsilon_{hkl}$, which means that the distortion effect will depend on the affected peak.

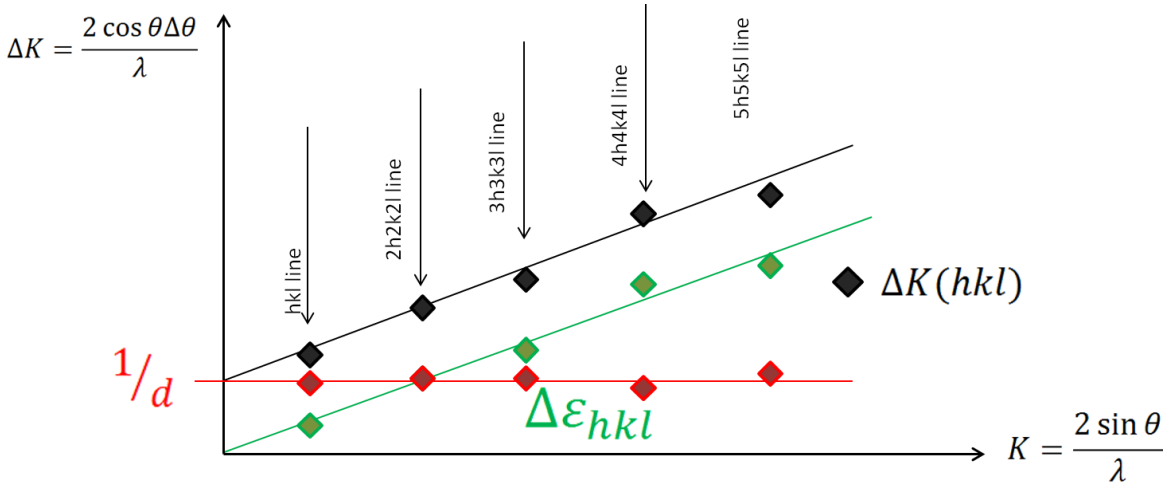

Figure II.7: Schematic diagram of the evolution of the peak broadening of a function of the diffraction vector K. The red points correspond to the size contribution to broadening, the green points to the contribution of the distorted lattice effect, and the black points are the actual peak broadening.

This separation introduces the basis of the diffraction pattern analysis respectively proposed by Warren and Averbach in 1950 [27] and Williamson and Hall in 1953 [29].

4.1.3. Diffraction analysis methods

Numerous methods exist to analyse diffraction patterns, the principal methods will be presented here.

4.1.3.1. Introducing the dislocation contrast factor into classical Warren – Averbach and Williamson- Hall methods

The crystal lattices are commonly anisotropic, which means that the strain produced by an isotropic stress will not by equal for the different directions of the crystal. Concretely, this means that the broadening produced on a {110} or a {211} plane will differ for an equivalent stress (more than it should from the simple diffraction vector proportionality) to account for it and be able to use every diffracted peaks a dislocation contrast factor has been introduced. The dislocation contrast factor C depends on the elastic constants of the studied material and on the relative orientations of the line and Burgers vectors of dislocation and the diffraction vector. This effect has been introduced by Ungàr and Borbèly by modifying Warren-Averbach and Williamson-Hall methods [22]. Borbèly et al. have notably set up a program that allows to calculate the desired dislocation contrast from the elastic constants of the stress tensor [33]. It can be openly used on the internet at the following address: http://metal.elte.hu/anizc/

Modified Williamson-Hall method

Originally the formula of the modified Williamson-Hall (mWH) method introduced by Ungàr and Borbèly was:

$$\Delta K = \frac{0.9}{d} + \left(\frac{\pi A b^2}{2}\right)^{1/2} \rho^{1/2} \left(K\bar{C}^{1/2}\right) + \left(\frac{\pi A' b^2}{2}\right) Q^{1/2}(K^2\bar{C})$$

Where A and A' are parameters determined by the effective outer cut of radius of dislocation , R_e, and the auxiliary parameters R_1 and R_2. Q is related to fluctuation of the dislocation density. The quadratic part of the equation involving Q is particularly important when studying monocrystals or large grained polycrystals [22]. In the case of ODS steels, this term will be neglected. Importantly we can note that in the case of a distorted crystal, the proper scaling parameter is no longer the reciprocal vector K but $K\bar{C}^{1/2}$.

Modified Warren-Averbach method

Mathematically, it involves the expression of peak intensity in terms of a Fourier sum. Therefore, the W-A method describes the Fourier transform of the intensity distribution (only at small values of L). The modified Warren-Averbach (mWA) formula introduced in 1996 is:

$$lnA_n(L) \cong A^s(L) - \rho B L^2 ln\left(\frac{R_e}{L}\right)(K^2\bar{C}) + QB^2L^4 ln\left(\frac{R_1}{L}\right) ln\left(\frac{R_2}{L}\right)(K^2\bar{C})^2 \qquad \text{(II.11)}$$

Where $B = \pi b^2/2$. Similarly to what was stated in §0, the quadratic term will be neglected in the case of ODS steel powders. The remaining strain parameters R_e and ρ were evaluated by fitting the plot of $\left(\frac{\pi}{2}\right)\rho b^2 L^2 ln\left(\frac{R_e}{L}\right)$ vs. L according to eq. (II.11).

Comparing the modified Williamson-Hall and modified Warren-Averbach method

The mWH method, based on the Full Width at Half Maximum (FWHM) of the diffraction peaks, is distinctly different from the mWA method which takes the entire peak into account. Indeed, since it characterizes peak broadening closer to the maximum, mWH. is more sensitive to correlations between atom-pair positions corresponding to larger distances in real space. Whereas the mWA method is based on the asymptotic behaviour of the Fourier transform of the peak profile. The peak tails (and the mWA method) will be more sensitive to the average atomic structure at small real space distances (for example dislocation interaction), while the FWHM (mWH) is more sensitive to the structure over large distances. Therefore, it is expected that in the case of a crystallite size distribution the mWH will be more sensitive to larger crystallites and the mWA method to the averaged distribution of coherent domains.

The accurate theory is the mWA but for recrystallization study, comparison between mWA and mWH, due to the above mentioned sensitivity of the FWHM to larger grains, could give qualitative indicators on the onset of abnormal grain growth. Indeed, a significant deviation of the grain growth determined by the two methods could indicate the onset of abnormal grain growth.

4.1.3.2. Whole powder pattern modelling

The most commonly used method to access to physical values is the Whole Powder Pattern Modelling (WPPM). The principle of these methods is to reconstruct the experimental diffraction pattern by fitting it using calculated profile intensities. These profiles contain a lot a physical parameters (ρ, M, R_e, etc.) and even include stacking faults and twinning [34–36]. It is generally treated using the Rietveld method. Major difficulties can arise from the utilisation of such programs. Indeed, it is generally impossible to access the source, therefore the user has no information on how calculations are performed. Besides, the number of parameters is often very important, which facilitates the fit but also rises questions about the physical meaning of the results obtained. Furthermore, those methods are very sensible to the initial parameters introduced.

4.1.3.3. Momentum method

For the evaluation of size and strain parameters, a momentum method can be considered. It is based on the asymptotic behaviour of different order momentums which are theoretically defined functions [37,38]. Those functions are then calculated by integrating the experimental data to obtain parameters which lead to the size and strain values. The advantages of the momentum method are several. First, during integration, statistical errors in the intensity measurement may cancel out. It is possible to directly check on the moment functions if they match with the theoretically expected shapes. It then makes it very easy to control if the assumed broadening source is present or not. This is out of

reach for the recent WPPM methods. According to the moment method theory established by Wilson and Groma [37,38], the second and fourth order restricted momentums have the following form:

$$M_2(q) = \frac{1}{\pi^2 d} q - \frac{1}{4\pi^2}\frac{L}{K^2 d^2} + \frac{1}{2\pi^2}\Lambda\rho ln\left(\frac{q}{q_0}\right)$$

$$M_4(q) = \frac{1}{3\pi^2 d} q - \frac{\Lambda\rho}{4\pi^2} + \frac{L}{K^2 d^2} + \frac{3\Lambda\rho}{(2\pi)^4 d}\frac{ln(q/q_2)}{q}$$

Where q is the deviation from the reciprocal lattice point, d is the crystallite size, ρ is the dislocation density, K is the Scherrer constant, L is the taper parameter and Λ, q_0 and q_2 are constants [39]. The asymptotical behaviour of the second fourth order restricted momentums at large q values allows to deconvolute the size and strain effects:

- M_2 and M_4 linear: size effect only
- M_2 logarithmic and M_4 linear: dislocation effect only
- Cross effect: linear terms are dominants but there is an important contribution of the dislocation term (M_2) and from the cross term (M_4).

This method is very relevant form a physical point of view and allows to determine the physical parameters on each peak. Nevertheless it requires to work on very high resolution peaks (i.e. ~250 points per peaks).

4.1.4. Instrumental conditions

The instability and rapid evolution of the ferritic microstructure requires the use of fast and precise *in-situ* characterization methods. To be able to follow it with a sufficient time and intensity resolution the ODS steel particles were studied under a synchrotron radiation at the DIFFABS beamline of the synchrotron SOLEIL.

Laboratory experimental conditions

To get first hints on the microstructure and to prepare these experiments, several laboratory measurements were also conducted. XRD laboratory experiments were carried out directly on the powders. Patterns have been recorded on a PanAlytical X'pert Pro MPD laboratory diffractometer with a Cobalt Kα radiation source (1.78896 Å). Diffractograms were recorded with a small angle step (0.017°), deviation from monochromaticity was 5.10^{-3} Å^{-1}. Intensity profiles have been analyzed with the modified Williamson & Hall method [15] and the Whole Powder Pattern Modelling (WPPM) approach using the PM2K software [16]. Both methods have been employed to obtain the domain size and dislocation density.

In-situ synchrotron experimental conditions

Using a furnace dedicated to powder heating, anisothermal treatments from room temperature up to five different soaking temperatures (T = 600°C; 800°C; 850°C; 900°C and 1100°C) were performed under vacuum. The heating rate was chosen low enough (~30°C.min^{-1}) to ensure that the acquisition time induces a temperature shift of only few

degrees. The powder was put onto a boron nitride sample holder that was heated by direct contact with a resistor. This experimental set-up was mounted on a rotating board that allowed the rotation around the axis perpendicular to the incident photon flux. A transparent Kapton window ensured the transmission of incident and scattered photons. A vacuum system allowed to rapidly obtain a secondary vacuum of around 3.10^{-5} Pa within the furnace chamber.

Various XRD experiments have shown the benefits of the synchrotron source to study recrystallization kinetics [25,40]. Furthermore, kinetic studies, have been successfully carried out by combining synchrotron XRD with fast 2D detectors to obtain timely well resolved diffraction peaks [40,41]. A last generation 2D detector XPAD S140 composed of chips containing $120x80$ pixels with $130mmx130mm$ dimensions were used to record independently each studied diffraction peak [42] (cf. Figure II.8).

During this study, incident energy of photons was selected to be 19 keV, which corresponds to a wavelength of 0.0653 nm. This energy allows optimizing the penetration depth, the number of available peaks and peak width; each of these values being essential for the precision of the results. At this energy, the penetration depth of the beam into the powder was around 25 µm for the (211) planes. 11 X-ray peaks can be detected in a 2θ range from 15 to 67°. Samples were tilted to 15° with respect to the axis parallel to the incident beam in order to minimize the geometrical spread of the beam on the powder. Given these parameters, the 4 most intense diffraction peaks (110), (200), (211), (220), are respectively located at 18.5°, 26.3°, 32.3° and 37.5° in a 2θ range. *In-situ* X-ray diffractograms of these 4 peaks were recorded.

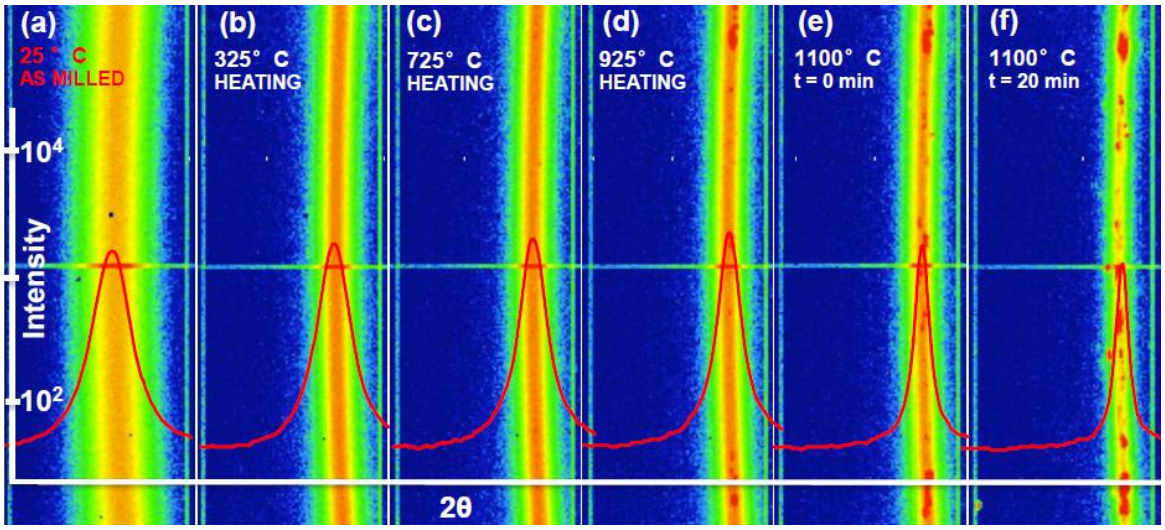

Figure II.8: Evolution of the 2D diffraction ring corresponding to the peak (211) from the ferritic ODS steel powder P9073, from (a) as-milled powder to various annealed states (b-f) during annealing up to 1100°C. The converted $I(2\theta)$ plot is also reported.

The resulting 1D diffractograms were obtained for a radial 2θ range of 7° and from an integration of the 6° azimuthal ψ-range. Each peak was detected in a single detection

sequence, leading to 4 different detection phases in order to center the 2θ domain around each peak maximum. Acquisition time was chosen at 2s.peak^{-1}, leading to a good statistics (peak intensity of more than 1 million of counted photons, giving a signal to noise ratio of more than 500 for the silicon reference sample; for the ODS samples the resulting maximum intensity over background ratio is 85). Taking into account the XPAD displacement time from a peak position to the next and the acquisition time of the four peaks took 15 s. A temperature error depending on the heating rate is introduced between the (110 and the 220) peaks, this error corresponds to 15s heating seconds. Thus, considering a heating rate of 0.5°C.s^{-1}, the temperature variation during a diffractogram acquisition upon heating was less than 10°C. Consequently, the whole diffractogram was approximated as being isothermal. With 10 additional seconds for returning to the initial position, diffractograms were measured every 25 s, the effective temperature can therefore be estimated with an error of 13°C.

Instrumental broadening

In addition to the broadening due to microstructural characteristics of the material, there is always some additional sources of broadening due to the instrumental set up. Those sources can be multiple, for example the slit widths, the sample size, the penetration length in the sample, an imperfect focusing, etc. . The instrumental broadening contribution was measured with a reference silicon powder mounted on a zero background sample holder. Two different methods were used to account for the instrumental broadening of mWH and mWA methods.

First, for mWH method, it was found that instrumental broadening follows a Caglioti function that is when fitted by a parabolic function $\beta_{inst} = f(\theta^2)$ [43]. Since pseudo-Voigt functions were used to fit the diffraction peaks, the Full Width at Half Maximum (FWHM) of the sample profile is given by the following equation (cf. [44]):

$$\beta_{raw}^2 = \beta_{sample}\beta_{raw} + \beta_{inst}^2$$

Where β_{raw}, β_{ODS}, and β_{inst} are the FWHM respectively of the raw diffraction profile, the profile of the sample studied and that of the instrument.

In the mWA case, the instrumental contribution was corrected by the considering that the Fourier coefficients of the total diffraction profile A_n^{raw} are the product of the Fourier coefficients resulting from the sample contribution A_n^{sample} by instrumental Fourier coefficients A_n^{inst}.

$$A_n^{sample} \times A_n^{instr} = A_n^{raw}$$

Instrumental coefficients were calculated by an interpolation of the neighbouring silicon peak coefficients weighted by their respective distance to the ODS steel peaks according to the Cagliotti formula.

4.1.5. Revisiting the Williamson-Hall modified method

The initial goal of the in-situ experiment was to use the momentum methods in order to obtain as reliable results as possible. Unfortunately, the too limited resolution of the diffracted peaks prevented from doing so. Therefore, a particular interest was given to the modified Warren Averbach (mWA) and modified Williamson-Hall (mWH) methods.

4.1.5.1. Initial modified Williamson-Hall formula

The initial Ungàr and Borbèly formula has been significantly reinterpreted during the last 15 years on somehow debatable physical justification. Indeed, the first version of the formula published by Ungàr et Borbély in 1996 is:

$$\Delta K = \frac{0.9}{d} + \left(\pi A \frac{b^2}{2}\right)^{1/2} \rho^{1/2} \left(K\bar{C}^{1/2}\right) + \left(\pi A' \frac{b^2}{2}\right)^{1/2} Q^{1/2}(K^2\bar{C}) \quad \text{(II.12)}$$

Then, few years later with Gubicza, Hanàk and Alexandrov, Ungàr published the simplified form [45]:

$$\Delta K = \frac{\gamma}{d} + \left(\pi M^2 \frac{b^2}{2}\right) \rho^{1/2}(K^2\bar{C}) + O(K^4\bar{C}^2) \quad \text{(II.13)}$$

Where M is the Wilkens parameter with $M = R_e\sqrt{\rho}$. Since then, this version of the formula is often found within the literature [25,46]. Therefore it is this version of the formula that will be used here.

4.1.5.2. Physical parameters M and R_e

The mWH method may seem to be too simple to account for microstructural evolution. However, as stated in II§4.1.3.1, mWH allows to obtain information on the onset of recrystallization and abnormal grain growth, it is then a very interesting method within the frame of this study. Since the dislocation density is a key parameter to account for the occurrence of recrystallization. It seems therefore relevant to take into consideration the unknown Wilkens parameter M evolution which accounts for the dislocation rearrangement. Indeed, the outer cut off radius is a key parameter to obtain dislocation density from mWH methods. The idea here is to obtain the unknown Wilkens parameter M from the accurate mWA method in order to take into account the physics of the dislocation density. Nevertheless, it seems impossible to impose M to calculate ρ since by definition $M = R_e\sqrt{\rho}$. It would therefore necessarily impose two different values of ρ within the same equation. What we propose here is to take into account the physics of the rearrangement through the outer cut off radius parameter R_e determined with the mWA. In order to achieve this, the modified Williamson-Hall method was adjusted by coupling it with the evolution of $R_e(t)$ upon annealing.

4.1.5.3. The coupled modified Warren-Averbach / modified Williamson-Hall methods (mWH-mWA)

This modification leads to the coupled mWA-mWH method and the following formula:

$$\Delta K = \frac{0.9}{d} + \left(\pi R_{e\,WA}^2 \frac{b^2}{2}\right)\rho^{3/2}(K^2\bar{C}) + O(K^4\bar{C}^2) \quad \text{(II.14)}$$

Equation (II.14) takes partially into account dislocation rearrangement upon heating. R_e is no longer a fitting parameter but is evaluated by the modified Warren-Averbach method. Based on the sensitivity of the FWHM to larger grains this implies that we impose the same Re in small and large grains. Figure II.9 shows that the approximation is reasonable up to temperatures of 1000°C when R_e increases from 23nm to about 35nm.

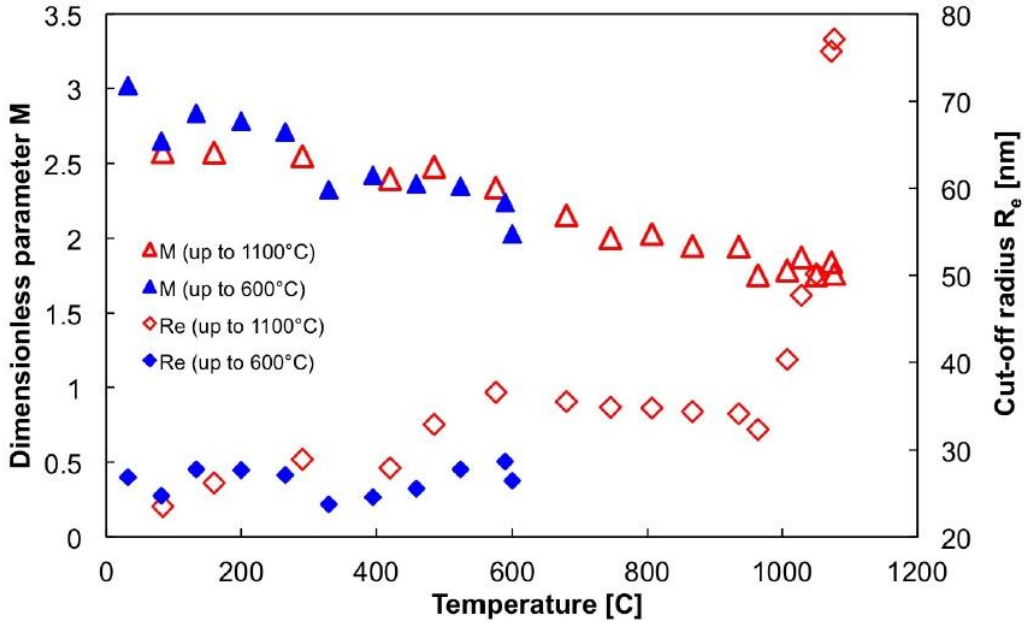

Figure II.9: Evolution of Re and M parameters during annealings of the P9073 powder at 600°C and 1100°C

The coupled mWA-mWH method was applied to *in-situ* diffraction patterns acquired during several non-isothermal treatments from room temperature to 600°C and 1100°C.

4.1.6. Detection of the abnormal grain growth

Using the dynamic and the resolution of the detector 2D used, very interesting information has been obtained towards abnormal grain growth. First, the 2D diffraction rings were integrated to separate ultra-fine grain and coarse grain signals. Indeed, when abnormal microstructure was obtained, individual spots correspond to abnormal grains whereas continuous intensity is due to the ultrafine grains' signal. This step was carefully performed by customized routines in order to eliminate reconstruction artefacts that can arise during evaluation [42].

Concomitant measurement of the kinetic evolution of both ultrafine grains and coarse grains is difficult to achieve since this requires getting access to the spatial distribution of grains at every time during annealing. Recent publications report the growth of 6 individual recrystallized grains that have been quantified on rolled high-purity aluminium [40,47,48]. What is proposed here is to quantify the growth kinetics of abnormal grains detected. When abnormal growth occurs the intensity in the powder diffractogram is no longer continuously distributed over the range but it becomes spotty (cf. Figure II.8). The

intensity of the corresponding diffraction contribution of each grain was integrated at each time step of the annealing process. The 2D diffraction ring was integrated in selected ψ and 2θ ranges so that only the intensity due to individual coarse grains is taken into account. Since diffraction intensity is proportional to the volume of the selected grain, this allows measuring the increase in volume as a function of the annealing time.
The relationship between the intensity of a nanocrystalline material and that of a single grain can be given by [28]:

$$V_{grains} = m \times \frac{I_{int}^{gr}}{I_{int}^{tot}} \times \frac{\sin(2\theta)}{4\sin(\theta)} \times V_{probed}$$

Where V_{grains} is the volume of the corresponding single grain, m the crystallographic multiplicity ($m = 8$ for bcc structure), I_{int}^{gr} and I_{int}^{tot} are the diffraction intensities of the single grains and te entire samples, respectively, V_{probed} is the volume of the sample probed by the X-ray incident beam. The equivalent sphere radius can be obtained as:

$$R_{eq}(t) = \sqrt[3]{\frac{3}{4\pi} \times V_{grain}(t)}$$

This study, using a 2D detector, allowed for the first time to obtain information on the onset of abnormal grain growth and kinetic evolution information. The experimental results obtained here will allow to fully discuss the evolution of ultra-fine grains and coarser recrystallized grains leading to abnormal grain growth during heating.

4.2. Automatic Crystallographic Orientation Mapping-Transmission Electronic Microscopy (ACOM-TEM)

TEM's main characteristic is to allow a direct observation. This may seem obvious stated this way, but this fundamental characteristic gives TEM a very particular position within the variety of characterisation equipments. Indeed, TEM allows a remarkable complementarity with other techniques. It can be used either as a local probe with indirect technique studying large volumes (such as XRD [49,50] or SAS [11,51]), or, as a larger scale method to account for the validity and the representativeness of very local characterisation techniques (such as APT [52–54]). Nevertheless TEM cannot be reduced to a simple intermediate scale characterization technique. Indeed, it offers a wide range possibility, from conventional imaging to High Resolution imaging (HRTEM) through chemical or holographic studies. Here the focus will be made on a newly developed TEM method so-called ACOM-TEM that allows to get information on the crystal orientation of each point of a sample. ACOM-TEM is therefore a very interesting method for studying both the grain size and the lattice deformation within highly deformed materials. The mean development presented here, is the possibility to access to the dislocation density through local misorientation.

4.2.1. ACOM-TEM presentation

The ACOM-TEM method was originally developed to obtain crystal orientation maps on severely deformed metals [55]. It is therefore particularly well suited to study the grain size and texture of ball-milled materials with high deformation. EBSD-SEM technique,

which also provides local orientation information (from Kikuchi lines indexation), could not resolve these systems due to the high deformation level. Whereas, since it is based on the indexation of Bragg spot diffraction patterns, ACOM-TEM method is operative whatever the amount of strain.

The ACOM-TEM system uses a nano-probe scanning electron beam synchronized with a high speed external camera that allows to record diffraction patterns through the TEM front window (cf. Figure II.10).

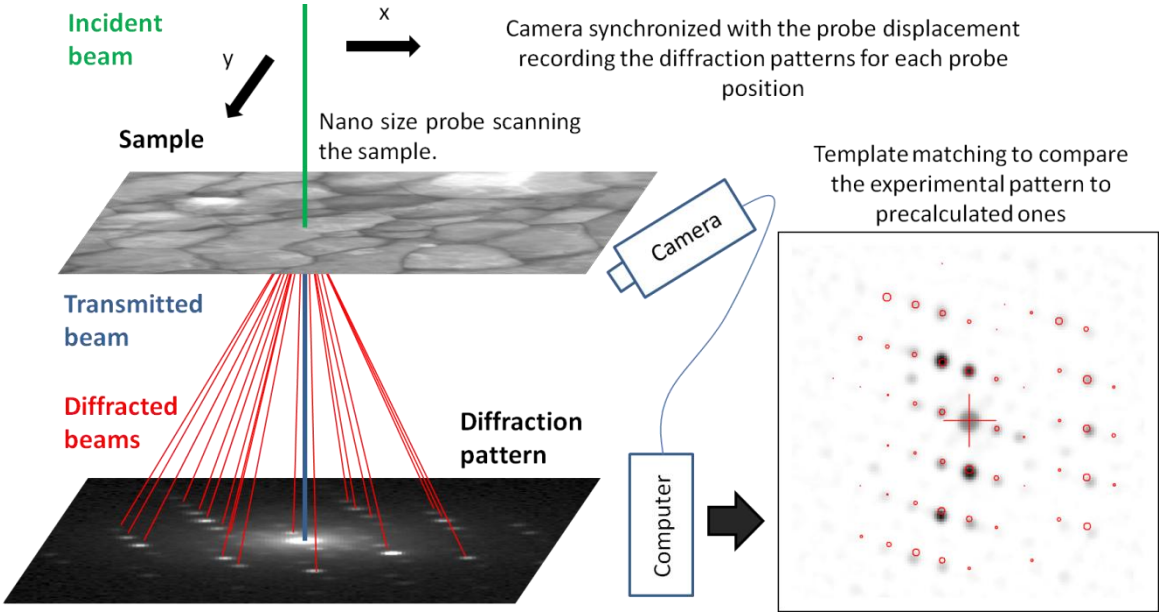

Figure II.10: Schematic presentation of the ACOM TEM method

After acquisition of the diffraction pattern, indexing is performed by a method developed in [56]. Recorded patterns are compared with the complete set of patterns with different orientations calculated in kinematic conditions for the expected phases (i.e. for each phase expected in the material, a complete data base is built by the user with a chosen misorientation between the templates, cf. [56,57]). The detailed orientation determination method which is called "template matching strategy" can be found in more details elsewhere [57].

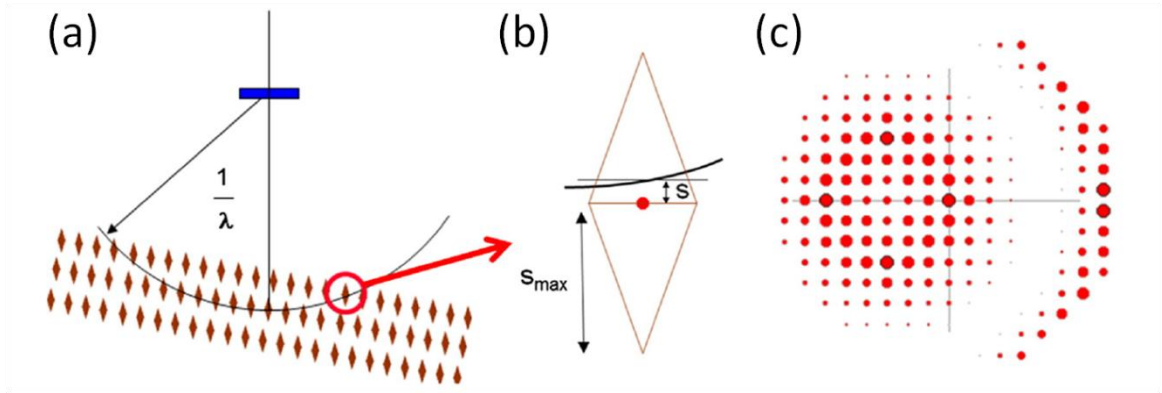

Figure II.11: Schematic view of a template construction : a) the Ewald sphere intercept nodes of the rotated reciprocal lattice; b) the shape of the nodes is representative of the decrease of the spot intensity with increasing deviation from the Bragg condition. The decrease is set linear up to a maximum value S_{max} of the deviation from

Bragg conditions; c) the resulting template is a first order estimate of the diffraction pattern pertaining to kinematical conditions [57]

The orientation identification procedure can be described as an image correlation. Here, the goal is to find the template with the highest correlation degree with the recorded diffraction pattern among the set of pre-calculated orientation. For each pixel (x, y), the following correlation index is calculated for each pre-calculated template [56]:

$$Q_c(i) = \frac{\sum_{j=1}^{m} P(x_j, y_j) T_i(x_j, y_j)}{\sqrt{\sum_{j=1}^{m} P^2(x_j, y_j)} \sqrt{\sum_{j=1}^{m} T_i^2(x_j, y_j)}} \quad \text{(II.15)}$$

$P(x, y)$ and $T_i(x, y)$ being respectively the intensity of the recorded pattern and the simulated pre-calculated template i for a point with coordinates (x,y). The template reaching the highest Q value is considered as the best solution.

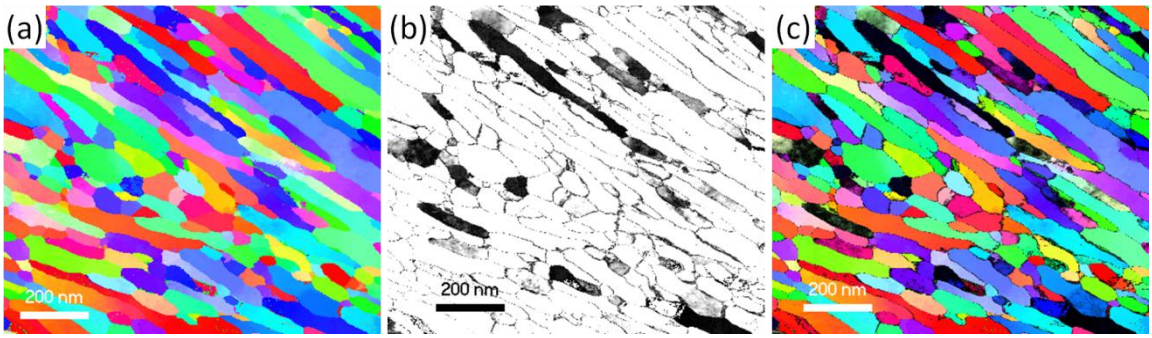

Figure II.12: Orientation map of a low temperature annealed ODS ferritic steel obtained with ACOM-TEM. (a) orientation map (b) reliability map (value ranging from 0 (black, hazardous indexation), to 25 (white, confident indexation), (c) crystallographic orientation map overlapped with the reliability map.

If two Q_c values are close, the software will choose the highest and give its orientation as the final result. Nevertheless close Q_c values means that the confidence that can be put into the result is compared to cases where a Q_c is significantly higher than the others. Therefore, the interpretation that can be made from those two different results is diverging and it is important to address the reliability of the orientation obtained. The reliability is calculated as:

$$R = 1 - \frac{Q_{max}^{2nd}}{Q_{max}^{1st}}$$

With Q_{max}^{1st} and Q_{max}^{2nd} being respectively the best and the second best indexations solutions. The template matching strategy will always provide a solution. Then, the problem is to know whether or not this solution is reliable (cf. Figure II.12). Therefore, special care was given to obtain orientation maps with the best reliability.

To improve the quality of the orientation maps, the sources of low reliability indexation need to be minimized. For instance, working on very thin areas is necessary to be as close to kinematical conditions as possible. Studying nanoscaled grain sizes with a high grain overlapping potential, working on thin areas is also important to limit grain overlap. Indeed, indexing is considered to be meaningful for a maximum of three overlapping grains contributing to the recorded pattern. Also, particular attention has been given to

record diffracted intensity at high angles in the diffraction patterns to avoid ambiguous indexations resulting from bcc crystal symmetries. In order to optimize the confidence in the given orientations, a minimum value of 10 and 150 was chosen respectively for the reliability R and the correlation index Q_c.

Once indexation is achieved, ACOM-TEM provides orientation maps very similar to the ones obtained by EBSD. Using the dedicated data analysis software OIM^{TM} (Orientation Imaging Microscopy), information like grain size, grain shape, grain boundary identification, dislocation density (more precisely the Geometrically Necessary Dislocations GND), misorientation profile and texture can be derived [58].

4.2.2. Spatial and angular resolution of ACOM-TEM

4.2.2.1. Spatial resolution

Spatial resolution is determined by the chosen step size and the beam probe size. For a parallel nanosized beam, the enlargement by propagation of the beam within the studied sample is limited (~1nm using the column approximation [59]). To avoid oversampling and reduce acquisition time step size was chosen as 1nm larger than the size of the beam plus its enlargement (2.75nm).

4.2.2.2. Angular resolution

As explained in §4.2.1, the basic template matching procedure finds the orientation for each point of the map with a precision which equals the misorientation chosen by the user when building its data base. Nevertheless, this value can be greatly improved. Indeed, it is possible to use a refinement procedure in order to improve the orientation resolution for each point. The refinement procedure is based on a finer discretization of the orientation space around the 1°(or the misorientation chosen by the user) orientation precision using a simplex algorithm. It is then possible to slightly modify the matching pre-calculated template orientation. At each step a test is performed to verify if the newly obtained template has a better match with the recorded pattern. The algorithm allows to explore the reciprocal space around the pre-calculated template and then optimise the orientation by successive iterations. The angular range for exploration can be chosen as well as the number of steps within the angular range. On the disorientation curve presented in Figure II.13, subgrain cells with a respective disorientation inferior to 0.3° can be clearly distinguished. Therefore the angular precision of the method can be estimated to be at least 0.3°.

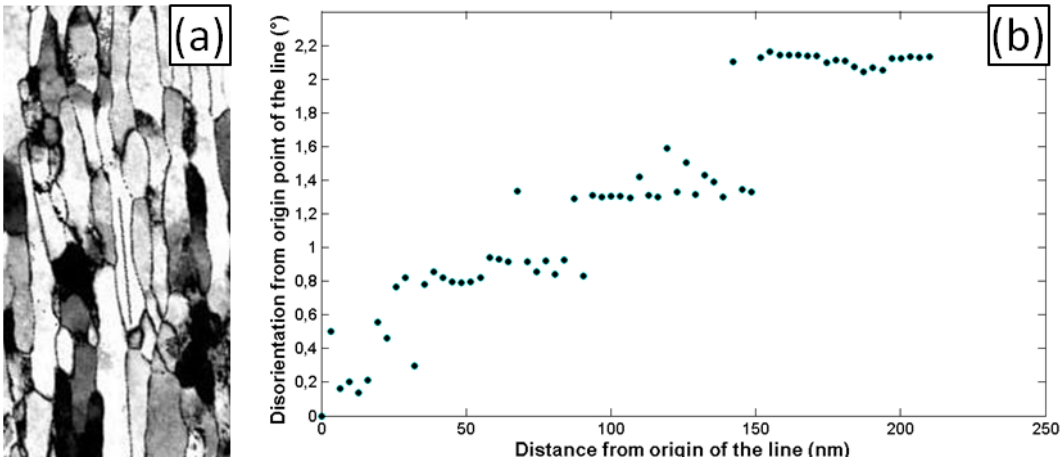

Figure II.13: Orientation map of a low temperature annealed ODS ferritic steel obtained with ACOM-TEM. (a) reliability map (value ranging from 10 (black, hazardous indexation), to 70 (white, confident indexation), (b) disorientations corresponding to the black line within the white (a) (b) grain

In [57], authors demonstrate that the orientation resulting from this procedure is as good as what can be deduced from Kikuchi patterns. Therefore, given these successive results, this refinement procedure results in orientation map with a precision of about 0.1-0.2°, an example of the refinement procedure effect is presented in Figure II.14.

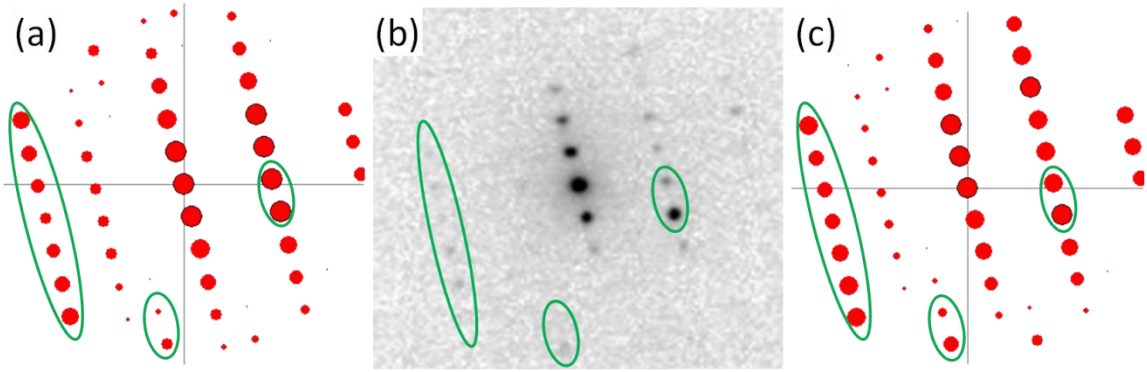

Figure II.14: refinement procedure example. (a) original matching template, (b) recorded diffraction pattern, (c) refined matching template. The global misorientation between pattern a and c is 0.631°, main differences between the patterns are highlighted by green circles

4.2.3. Dislocation density measurements

Strain affects the grains through local misorientation that can be measured using the diffraction pattern indexation. This effect will allow in return to access to the dislocation density. Generally, distinction is made between two different types of dislocations: Statistically Stored Dislocations (SSDs) and Geometrically Necessary Dislocations (GNDs). SSDs are randomly distributed among dislocation whereas GNDs account for the lattice continuity in the presence of curvature [60,61]. For example, GNDs are measured through SEM-EBSD using orientation measurements [62].

4.2.3.1. Dislocation density tensor

Along the dislocation line, the crystalline lattice is distorted which induces both a local displacement and a rotational field. Using their main characteristics (i.e. Burgers vector b and line vectors at position r), Nye introduced a dislocation density tensor [63]:

$$\alpha_{T_{ij}} = b_i t_j \delta(r - r_0) \tag{II.16}$$

A direct relation between the dislocation density tensor and the elastic distortion can be written [64,65]:

$$\alpha_T(r) = \sum_i b_i \otimes t_i \delta(r - r_i) = -\nabla \times \beta^{el} \tag{II.17}$$

With β^{el} being the elastic distortion tensor. Elastic distortion consists in the sum of the elastic strain tensor ϵ^{el} and a tensor accounting for local rotations g:

$$\alpha_{T_{ij}} = -\epsilon_{jkl}\beta^{el}_{il,k} = -\epsilon_{jkl}(\epsilon^{el}_{il,k} + \omega_{il,k}) \tag{II.18}$$

When ignoring elastic strain, the equation simplifies into: $\alpha_{T_{ij}} = -\epsilon_{jkl}\omega_{il,k}$.

4.2.3.2. Local lattice rotation

The local lattice rotation can be related to the local lattice orientation ([64,66]):

$$\Delta\vec{w} = \frac{2\, arccos\Delta q_0}{\sqrt{1 - \Delta q_0^2}}\Delta\vec{q} \tag{II.19}$$

With Δq, the disorientation between two neighbouring points. Δq is chosen as the smallest disorientation among all the possible crystal symmetries (cf. [65]). Then, the lattice curvature tensor κ_{kl} can be introduced to measure the distortion value between two adjacent pixels:

$$\kappa_{kl} = \frac{dw_k}{dx_l} \tag{II.20}$$

From the six accessible curvature components accessible in 2 dimensions, five of the nine components of the dislocations density tensor can be calculated. That leads to the following accessible values for $\alpha_{T_{ij}}$:

$$\alpha_{T_{12}} = \kappa_{21} \qquad \alpha_{T_{13}} = \kappa_{31} \qquad \alpha_{T_{33}} = -\kappa_{11} - \kappa_{22}$$
$$\alpha_{T_{21}} = \kappa_{12} \qquad \alpha_{T_{23}} = \kappa_{32} \tag{II.21}$$

4.2.3.3. 2D dislocation density measurements

The global dislocation density can be obtained from the components of the dislocation density tensor:

$$\rho_{2D}^{GND} = \frac{1}{b}\sqrt{\left(\alpha_{T_{12}}^2 + \alpha_{T_{13}}^2 + \alpha_{T_{21}}^2 + \alpha_{T_{23}}^2 + \alpha_{T_{33}}^2\right)} \tag{II.22}$$

Obviously, this sum is only the apparent dislocation density as all the tensor components cannot be calculated in 2 dimensions. Nevertheless, this method theoretically allows to measure the full dislocation density tensor, which has been done in [67] using EBSD combined with successive FIB cuts, every curvature components are then accessible.

Gao et al. [68] and Kubin et Mortensen [69], assuming that GNDs produce pure tilt have obtained the following simplified expression:

$$\rho_{GND} = \frac{\Delta\theta}{b\delta} \tag{II.23}$$

Where, $\Delta\theta$ is the neighbouring misorientation, δ the step size and b the Burgers vector. First we will use this approximation to compare GNDs in our different samples.

Dislocation density measurements

The calculated local misorientation / curvature, and the resulting dislocation density largely depend upon the experience parameters. Dislocations causing misorientation on a smaller range than the step size were not taken into account in the measure. This therefore results in the overestimation of the dislocation density measurement as the step size decreases [70]. There is no point in performing study with too small a step size without the sufficient angular resolution to account for the dislocation density. For example, with a step size of 3nm and an angular resolution of 0.2°, the minimum dislocation density calculated is 5.10^{-14} m^{-2}.

****

Parts of this work can be found within the following articles :

Sallez N., Donnadieu P., Courtois-Manara E.,Chassaing D., Kübel C., Delabrouille F., Blat-Yrieix M., Carlan Y. de, Bréchet Y., ON BALL-MILLED ODS FERRITIC STEEL RECRYSTALLIZATION: FROM AS-MILLED POWDER PARTICLES TO CONSOLIDATED STATES. *Journal of Materials Science*, **50**, pp 2202-2217

Sallez N., Boulnat X., Borbély A., Béchade J.L., Fabrégue D., Pérez M., Carlan Y. de, Hennet L., Mocuta C., Thiaudière D., Bréchet Y., IN SITU CHARACTERIZATION OF MICROSTRUCTURAL INSTABILITIES: RECOVERY, RECRYSTALLIZATION AND ABNORMAL GROWTH IN NANO-REINFORCED STEEL POWDER. *Acta Materialia*, **87**, pp 377–389

Chapter II bibliography

[1] Miller M.K. et Forbes R.G. (2009) ATOM PROBE TOMOGRAPHY. *Materials Characterization*, **60**, 461‑9.

[2] Williams C.A., Haley D., Marquis E.A., Smith G.D.W. et Moody M.P. (2013) DEFINING CLUSTERS IN APT RECONSTRUCTIONS OF ODS STEELS. *Ultramicroscopy*, **132**, 271‑8.

[3] Larson D.J., Gault B., Geiser B.P., De Geuser F. et Vurpillot F. (2013) ATOM PROBE TOMOGRAPHY SPATIAL RECONSTRUCTION: STATUS AND DIRECTIONS. *Current Opinion in Solid State and Materials Science*, **17**, 236‑47.

[4] Boutard J.-L., Badjeck V., Barguet L., Barouh C., Bhattacharya A., Colignon Y., Hatzoglou C., Loyer-Prost M., Rouffié A.L., Sallez N., Salmon-Legagneur H. et Schuler T. (2014) OXIDE DISPERSION STRENGTHENED FERRITIC STEELS: A BASIC RESEARCH JOINT PROGRAM IN FRANCE. *Journal of Nuclear Materials*, **455**, 605‑11.

[5] Bergner F., Pareige C., Kuksenko V., Malerba L., Pareige P., Ulbricht A. et Wagner A. (2013) CRITICAL ASSESSMENT OF CR-RICH PRECIPITATES IN NEUTRON-IRRADIATED FE–12 AT%CR: COMPARISON OF SANS AND APT. *Journal of Nuclear Materials*, **442**, 463‑9.

[6] Guinier A., Fournet G., Walker C.B. et Vineyard G.H. (1956) SMALL-ANGLE SCATTERING OF X-RAYS. *Physics Today*, **9**, 38.

[7] Bacon G.E. (1975) NEUTRON DIFFRACTION. 3. EDITION.

[8] De Geuser F. et Deschamps A. (2012) PRECIPITATE CHARACTERISATION IN METALLIC SYSTEMS BY SMALL-ANGLE X-RAY OR NEUTRON SCATTERING. *Comptes Rendus Physique*, **13**, 246‑56.

[9] Glatter O. (1977) A NEW METHOD FOR THE EVALUATION OF SMALL-ANGLE SCATTERING DATA. *Journal of Applied Crystallography*, **10**, 415‑21.

[10] Tatchev D. et Kranold R. (2004) MAXIMUM-ENTROPY METHOD AS A ROUTINE TOOL FOR DETERMINATION OF PARTICLE SIZE DISTRIBUTIONS BY SMALL-ANGLE SCATTERING. *Journal of Applied Crystallography*, **37**, 32‑9.

[11] Perrard F., Deschamps A., Bley F., Donnadieu P. et Maugis P. (2006) A SMALL-ANGLE NEUTRON SCATTERING STUDY OF FINE-SCALE NBC PRECIPITATION KINETICS IN THE A-FE–NB–C SYSTEM. *Journal of Applied Crystallography*, **39**, 473‑82.

[12] Fribourg G. (2009) COUPLAGES ENTRE PRÉCIPITATION ET PLASTICITÉ DANS UN ALLIAGE D'ALUMINIUM 7XXX : APPLICATION À DES TRAITEMENTS THERMOMÉCANIQUES DE RÉDUCTION DES DISTORSIONS DANS DES COMPOSANTS AÉRONAUTIQUES [Internet]. Institut National Polytechnique de Grenoble - INPG.

[13] Brocq M. (2010) SYNTHESE ET CARACTERISATION D'UN ACIER ODS PREPARE PAR UN PROCEDE INSPIRE DU BROYAGE REACTIF - ETUDE DE L'INFLUENCE DES CONDITIONS DE BROYAGE ET RECUIT. Université de Rennes 1. PhD thesis.

[14] Cromer D.T. et Liberman D.A. (1981) ANOMALOUS DISPERSION CALCULATIONS NEAR TO AND ON THE LONG-WAVELENGTH SIDE OF AN ABSORPTION EDGE. *Acta Crystallographica Section A*, **37**, 267‑8.

[15] Dumont M., Commin L., Morfin I., DeGeuser F., Legendre F. et Maugis P. (2014) CHEMICAL COMPOSITION OF NANO-PHASES STUDIED BY ANOMALOUS SMALL-ANGLE X-RAY SCATTERING: APPLICATION TO OXIDE NANO-PARTICLES IN ODS STEELS. *Materials Characterization*, **87**, 138‑42.

[16] Lescoat M.-L., Ribis J., Gentils A., Kaïtasov O., de Carlan Y. et Legris A. (2012) IN SITU TEM STUDY OF THE STABILITY OF NANO-OXIDES IN ODS STEELS UNDER ION-IRRADIATION. *Journal of Nuclear Materials*, **428**, 176‑82.

[17] Ribis J., Lescoat M.-L., Zhong S.Y., Mathon M.-H. et de Carlan Y. (2013) INFLUENCE OF THE LOW INTERFACIAL DENSITY ENERGY ON THE COARSENING RESISTIVITY OF THE NANO-OXIDE PARTICLES IN TI-ADDED ODS MATERIAL. *Journal of Nuclear Materials*, **442**, S101‑5.

[18] Ribis J. et de Carlan Y. (2012) INTERFACIAL STRAINED STRUCTURE AND ORIENTATION RELATIONSHIPS OF THE NANOSIZED OXIDE PARTICLES DEDUCED FROM ELASTICITY-DRIVEN MORPHOLOGY IN OXIDE DISPERSION STRENGTHENED MATERIALS. *Acta Materialia*, **60**, 238‑52.

[19] Sears V.F. (1992) NEUTRON SCATTERING LENGTHS AND CROSS SECTIONS. *Neutron News*, **3**, 26‑37.

[20] Aldred A.T., Rainford B.D., Kouvel J.S. et Hicks T.J. (1976) FERROMAGNETISM IN IRON-CHROMIUM ALLOYS. II. NEUTRON SCATTERING STUDIES. *Physical Review B*, **14**, 228‑34.

[21] Jiang Y., Smith J.R. et Robert Odette G. (2010) PREDICTION OF STRUCTURAL, ELECTRONIC AND ELASTIC PROPERTIES OF Y2TI2O7 AND Y2TIO5. *Acta Materialia*, **58**, 1536‑43.

[22] Ungar T. et Borbely A. (1996) THE EFFECT OF DISLOCATION CONTRAST ON X-RAY LINE BROADENING: A NEW APPROACH TO LINE PROFILE ANALYSIS. *Applied Physics Letters*, **69**, 3173‑5.

[23] Ungár T., Dragomir I., Révész A. et Borbély A. (1999) THE CONTRAST FACTORS OF DISLOCATIONS IN CUBIC CRYSTALS: THE DISLOCATION MODEL OF STRAIN ANISOTROPY IN PRACTICE. *Journal of Applied Crystallography*, **32**, 992‑1002.

[24] Shintani T. et Murata Y. (2011) EVALUATION OF THE DISLOCATION DENSITY AND DISLOCATION CHARACTER IN COLD ROLLED TYPE 304 STEEL DETERMINED BY PROFILE ANALYSIS OF X-RAY DIFFRACTION. *Acta Materialia*, **59**, 4314‑22.

[25] Renzetti R.A., Sandim H.R.Z., Bolmaro R.E., Suzuki P.A. et Möslang A. (2012) X-RAY EVALUATION OF DISLOCATION DENSITY IN ODS-EUROFER STEEL. *Materials Science and Engineering: A*, **534**, 142‑6.

[26] Stokes A.R. et Wilson A.J.C. (1944) THE DIFFRACTION OF X RAYS BY DISTORTED CRYSTAL AGGREGATES - I. *Proceedings of the Physical Society*, **56**, 174.

[27] Warren B.E. et Averbach B.L. (1950) THE EFFECT OF COLD #X2010;WORK DISTORTION ON X #X2010;RAY PATTERNS. *Journal of Applied Physics*, **21**, 595‑9.

[28] Warren B.E. (1959) X-RAY STUDIES OF DEFORMED METALS. *Progr in Metal Phys*, **Vol: 8**.

[29] Williamson G.K. et Hall W.H. (1953) X-RAY LINE BROADENING FROM FILED ALUMINIUM AND WOLFRAM. *Acta Metallurgica*, **1**, 22‑31.

[30] Krivoglaz M.A. et Azároff L.V. (1970) THEORY OF X-RAY AND THERMAL NEUTRON SCATTERING BY REAL CRYSTALS. *Physics Today*, **23**, 78.

[31] Ungár T. (2004) MICROSTRUCTURAL PARAMETERS FROM X-RAY DIFFRACTION PEAK BROADENING. *Scripta Materialia*, **51**, 777‑81.

[32] Scherrer P. (1918) BESTIMMUNG DER GRÖßE UND DER INNEREN STRUKTUR VON KOLLOIDTEILCHEN MITTELS RÖNTGENSTRAHLEN. *Nachrichten von der Gesellschaft der Wissenschaften zu Göttingen, Mathematisch-Physikalische Klasse*, **1918**, 98‑100.

[33] Borbély A., Dragomir-Cernatescu J., Ribárik G. et Ungár T. (2003) COMPUTER PROGRAM *ANIZC* FOR THE CALCULATION OF DIFFRACTION CONTRAST FACTORS OF DISLOCATIONS IN ELASTICALLY ANISOTROPIC CUBIC, HEXAGONAL AND TRIGONAL CRYSTALS. *Journal of Applied Crystallography*, **36**, 160‑2.

[34] Scardi P., Leoni M. et Dong Y.H. (2000) WHOLE DIFFRACTION PATTERN-FITTING OF POLYCRYSTALLINE FCC MATERIALS BASED ON MICROSTRUCTURE. *The European Physical Journal B - Condensed Matter and Complex Systems*, **18**, 23‑30.

[35] Scardi P. et Leoni M. (2001) DIFFRACTION LINE PROFILES FROM POLYDISPERSE CRYSTALLINE SYSTEMS. *Acta Crystallographica Section A Foundations of Crystallography*, **57**, 604‑13.

[36] Scardi P. et Leoni M. (2002) WHOLE POWDER PATTERN MODELLING. *Acta Crystallographica Section A Foundations of Crystallography*, **58**, 190‑200.

[37] Wilson A.J.C. (1962) ON VARIANCE AS A MEASURE OF LINE BROADENING IN DIFFRACTOMETRY GENERAL THEORY AND SMALL PARTICLE SIZE. *Proceedings of the Physical Society*, **80**, 286‑94.

[38] Groma I., Ungar T. et Wilkens M. (1988) ASYMMETRIC X-RAY-LINE BROADENING OF PLASTICALLY DEFORMED-CRYSTALS .1. THEORY. *Journal of Applied Crystallography*, **21**, 47‑53.

[39] Borbély A. et Groma I. (2001) VARIANCE METHOD FOR THE EVALUATION OF PARTICLE SIZE AND DISLOCATION DENSITY FROM X-RAY BRAGG PEAKS. *Applied Physics Letters*, **79**, 1772‑4.

[40] Lauridsen E.., Jensen D.J., Poulsen H.. et Lienert U. (2000) KINETICS OF INDIVIDUAL GRAINS DURING RECRYSTALLIZATION. *Scripta Materialia*, **43**, 561‑6.

[41] Malinov S., Sha W., Guo Z., Tang C.C. et Long A.E. (2002) SYNCHROTRON X-RAY DIFFRACTION STUDY OF THE PHASE TRANSFORMATIONS IN TITANIUM ALLOYS. *Materials Characterization*, **48**, 279‑95.

[42] Le Bourlot C., Landois P., Djaziri S., Renault P.-O., Le Bourhis E., Goudeau P., Pinault M., Mayne-L'Hermite M., Bacroix B., Faurie D., Castelnau O., Launois P. et Rouzière S. (2011) SYNCHROTRON X-RAY DIFFRACTION EXPERIMENTS WITH A PROTOTYPE HYBRID PIXEL DETECTOR. *Journal of Applied Crystallography*, **45**, 38‑47.

[43] Caglioti G., Paoletti A. et Ricci F.P. (1958) CHOICE OF COLLIMATORS FOR A CRYSTAL SPECTROMETER FOR NEUTRON DIFFRACTION. *Nuclear Instruments*, **3**, 223‑8.

[44] Balzar D. (1999) VOIGT-FUNCTION MODEL IN DIFFRACTION LINE-BROADENING ANALYSIS. *Defect and Micorstructure Analysis from Diffraction*, R.L. Snyder, H.J. p. 94‑126.

[45] Ungár T., Gubicza J., Hanák P. et Alexandrov I. (2001) DENSITIES AND CHARACTER OF DISLOCATIONS AND SIZE-DISTRIBUTION OF SUBGRAINS IN DEFORMED METALS BY X-RAY DIFFRACTION PROFILE ANALYSIS. *Materials Science and Engineering: A*, **319–321**, 274‑8.

[46] Rahmanifard R., Farhangi H., Novinrooz A.J. et Afshari N. (2010) INVESTIGATION OF MICROSTRUCTURAL CHARACTERISTICS OF NANOCRYSTALLINE 12YWT STEEL DURING MILLING AND SUBSEQUENT ANNEALING BY X-RAY DIFFRACTION LINE PROFILE ANALYSIS. *Journal of Materials Science*, **45**, 6498‑504.

[47] Lauridsen E.M., Poulsen H.F., Nielsen S.F. et Juul Jensen D. (2003) RECRYSTALLIZATION KINETICS OF INDIVIDUAL BULK GRAINS IN 90% COLD-ROLLED ALUMINIUM. *Acta Materialia*, **51**, 4423‑35.

[48] Poulsen S.O., Lauridsen E.M., Lyckegaard A., Oddershede J., Gundlach C., Curfs C. et Juul Jensen D. (2011) IN SITU MEASUREMENTS OF GROWTH RATES AND GRAIN-AVERAGED ACTIVATION ENERGIES OF INDIVIDUAL GRAINS DURING RECRYSTALLIZATION OF 50% COLD-ROLLED ALUMINIUM. *Scripta Materialia*, **64**, 1003‑6.

[49] Hayoune A. et Hamana D. (2010) A DILATOMETRIC AND HIGH-TEMPERATURE X-RAY DIFFRACTION STUDY OF COLD DEFORMATION EFFECT ON THE INTERACTION BETWEEN PRECIPITATION, RECOVERY AND RECRYSTALLIZATION REACTIONS IN AL–12 WT.% MG ALLOY. *Materials Science and Engineering: A*, **527**, 7261‑4.

[50] Jimenez-Melero E., Blondé R., Sherif M.Y., Honkimäki V. et van Dijk N.H. (2013) TIME-DEPENDENT SYNCHROTRON X-RAY DIFFRACTION ON THE AUSTENITE DECOMPOSITION KINETICS IN SAE 52100 BEARING STEEL AT ELEVATED TEMPERATURES UNDER TENSILE STRESS. *Acta Materialia*, **61**, 1154‑66.

[51] Coppola R., Klimiankou M., Lindau R., May R.. et Valli M. (2004) SANS AND TEM STUDY OF Y2O3 PARTICLE DISTRIBUTIONS IN OXIDE-DISPERSION STRENGTHENED EUROFER MARTENSITIC STEEL FOR FUSION REACTORS. *Physica B: Condensed Matter*, **350**, E545‑8.

[52] Marquis E.A. (2008) CORE/SHELL STRUCTURES OF OXYGEN-RICH NANOFEATURES IN OXIDE-DISPERSION STRENGTHENED FE–CR ALLOYS. *Applied Physics Letters*, **93**, 181904.

[53] Certain A.G., Field K.G., Allen T.R., Miller M.K., Bentley J. et Busby J.T. (2010) RESPONSE OF NANOCLUSTERS IN A 9CR ODS STEEL TO 1 DPA, 525 °C PROTON IRRADIATION. *Journal of Nuclear Materials*, **407**, 2‑9.

[54] Hirata A., Fujita T., Wen Y.R., Schneibel J.H., Liu C.T. et Chen M.W. (2011) ATOMIC STRUCTURE OF NANOCLUSTERS IN OXIDE-DISPERSION-STRENGTHENED STEELS. *Nature Materials*, **10**, 922‑6.

[55] Máthis K. et Rauch E.F. (2007) MICROSTRUCTURAL CHARACTERIZATION OF A FINE-GRAINED ULTRA LOW CARBON STEEL. *Materials Science and Engineering: A*, **462**, 248‑52.

[56] Rauch E. et Dupuy L. (2005) RAPID SPOT DIFFRACTION PATTERNS IDENTIFICATION THROUGH TEMPLATE MATCHING RID C-9852-2011. *Archives of Metallurgy and Materials*, **50**, 87‑99.

[57] Rauch E.F. et Véron M. (2014) AUTOMATED CRYSTAL ORIENTATION AND PHASE MAPPING IN TEM. *Materials Characterization*, **98**, 1‑9.

[58] Sallez N., Donnadieu P., Courtois-Manara E., Kübel C., Chassaing D., Blat-Yrieix M., de Carlan Y. et Bréchet Y. ON BALL-MILLED ODS FERRITIC STEEL RECRYSTALLIZATION: FROM AS-MILLED POWDER PARTICLE TO CONSOLIDATED STATES. *submitted to Materials Characterization on the 03/08/2014,*.

[59] Williams D.B. et Carter C.B. (1996) THE TRANSMISSION ELECTRON MICROSCOPE. *Transmission Electron Microscopy*, Springer US. p. 3‑17.

[60] Kocks U.F. (1966) A STATISTICAL THEORY OF FLOW STRESS AND WORK-HARDENING. *Philosophical Magazine*, **13**, 541‑66.

[61] Ashby M. (1970) DEFORMATION OF PLASTICALLY NON-HOMOGENEOUS MATERIALS. *Philosophical Magazine*, **21**, 399 ‑ &.

[62] Ruggles T.J. et Fullwood D.T. (2013) ESTIMATIONS OF BULK GEOMETRICALLY NECESSARY DISLOCATION DENSITY USING HIGH RESOLUTION EBSD. *Ultramicroscopy*, **133**, 8‑15.

[63] Nye J.. (1953) SOME GEOMETRICAL RELATIONS IN DISLOCATED CRYSTALS. *Acta Metallurgica*, **1**, 153‑62.

[64] He W., Ma W. et Pantleon W. (2008) MICROSTRUCTURE OF INDIVIDUAL GRAINS IN COLD-ROLLED ALUMINIUM FROM ORIENTATION INHOMOGENEITIES RESOLVED BY ELECTRON BACKSCATTERING DIFFRACTION. *Materials Science and Engineering: A*, **494**, 21‑7.

[65] Demir E., Raabe D., Zaafarani N. et Zaefferer S. (2009) INVESTIGATION OF THE

INDENTATION SIZE EFFECT THROUGH THE MEASUREMENT OF THE GEOMETRICALLY NECESSARY DISLOCATIONS BENEATH SMALL INDENTS OF DIFFERENT DEPTHS USING EBSD TOMOGRAPHY. *Acta Materialia*, **57**, 559‑69.

[66] Beausir B., Fressengeas C., Gurao N.P., Tóth L.S. et Suwas S. (2009) SPATIAL CORRELATION IN GRAIN MISORIENTATION DISTRIBUTION. *Acta Materialia*, **57**, 5382‑95.

[67] Calcagnotto M., Ponge D., Demir E. et Raabe D. (2010) ORIENTATION GRADIENTS AND GEOMETRICALLY NECESSARY DISLOCATIONS IN ULTRAFINE GRAINED DUAL-PHASE STEELS STUDIED BY 2D AND 3D EBSD. *Materials Science and Engineering: A*, **527**, 2738‑46.

[68] Gao H., Huang Y., Nix W.D. et Hutchinson J.W. (1999) MECHANISM-BASED STRAIN GRADIENT PLASTICITY— I. THEORY. *Journal of the Mechanics and Physics of Solids*, **47**, 1239‑63.

[69] Kubin L.. et Mortensen A. (2003) GEOMETRICALLY NECESSARY DISLOCATIONS AND STRAIN-GRADIENT PLASTICITY: A FEW CRITICAL ISSUES. *Scripta Materialia*, **48**, 119‑25.

[70] Jiang J., Britton T.B. et Wilkinson A.J. (2013) MEASUREMENT OF GEOMETRICALLY NECESSARY DISLOCATION DENSITY WITH HIGH RESOLUTION ELECTRON BACKSCATTER DIFFRACTION: EFFECTS OF DETECTOR BINNING AND STEP SIZE. *Ultramicroscopy*, **125**, 1‑9.

CHAPTER III
Microstructural evolution of the powder

As presented in the introduction, microstructural anisotropy of the classically fabricated ODS steel tubes results in low transverse mechanical properties (cf. Chapter I§1.5) that come from the extrusion step of the fabrication process. Nevertheless, abnormal grain growth significantly aggravates the phenomenon (cf. Chapter I§1.5). Therefore, in order to understand the occurrence conditions of abnormal grain growth, the evolution of as-milled powder microstructure during annealing and the effect of solute content on the occurrence of abnormal grain growth will be studied experimentally.

1. Introductory section: As milled powder microstructure

To adequately describe the microstructural evolution of the ODS steel powder during annealing, it is necessary to obtain a detailed characterization of the as-milled state. This first section will try to perform it as finely as possible.

1.1. Sample preparation

Regarding sample preparation, part of the information can be found in (cf. chapter II§2) and specific sample preparation for ATP experiment in (cf. chapter II§3.1.2). Only complementary information is given below.

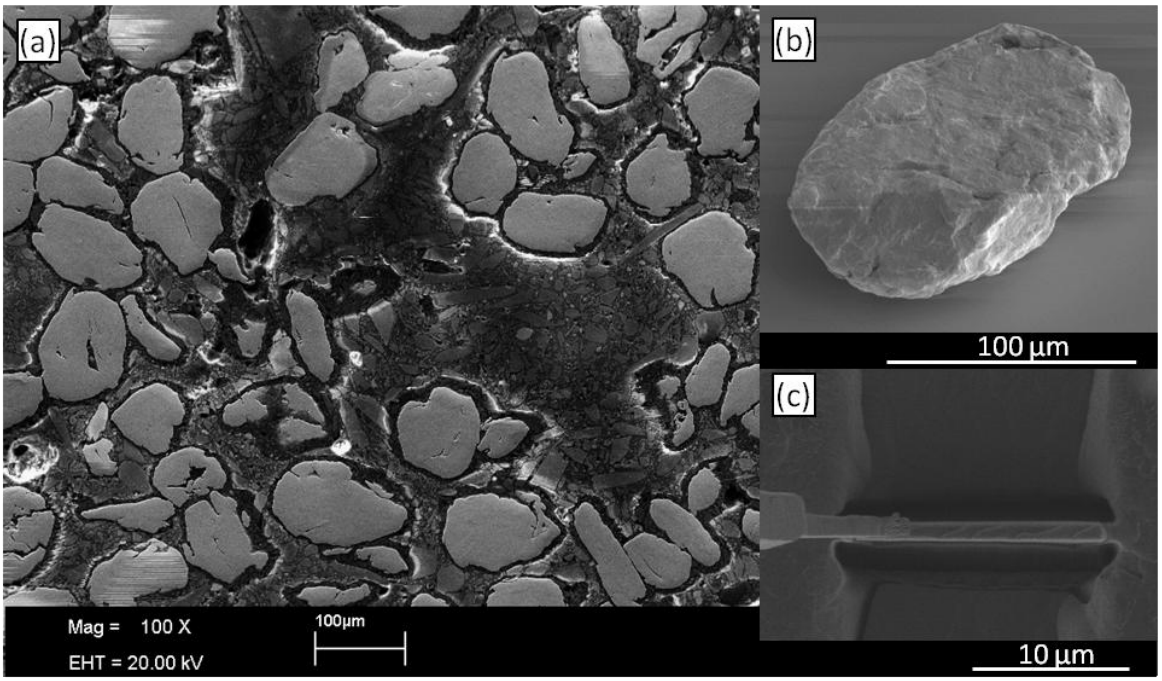

Figure III.1: SEM images of as-milled powder particles. (a) mounted as-milled powder particles (b) image of an isolated powder particle (c) FIB lift out technique applied on the ODS steel powders for specimen preparation

Diffraction measurements have been performed directly on powder particles (cf. Figure III.1b) on a sample holder or on double sided adhesive tape. For scanning electron microscopy observations, powder particles are mounted in a conductive resin and final polishing is performed with colloidal silica to provide a nearly deformation free surface (cf. Figure III.1a). For transmission electron microscopy, FIB (Focus Ion Beam) cross section where directly carried out from powder particles or from resin mounted powder particles (cf. Figure III.1c).

1.2. Particles morphology

After ball-milling, powder particles have a flat ellipsoidal shape (cf. Figure III.1a and b). The size given by SEM measurements are an average length of 95µm for an average width of 58µm which gives a 2D morphological anisotropy factor of 1,8 for the powder particles. Accurate 3D information and shape particle measurements would need a dedicated study and are out of the scope of this thesis.

1.3. Chemical distribution

In previous works on ODS steels, yttrium, titanium and oxygen are often considered to be homogeneously distributed within the ferritic matrix [1,2].

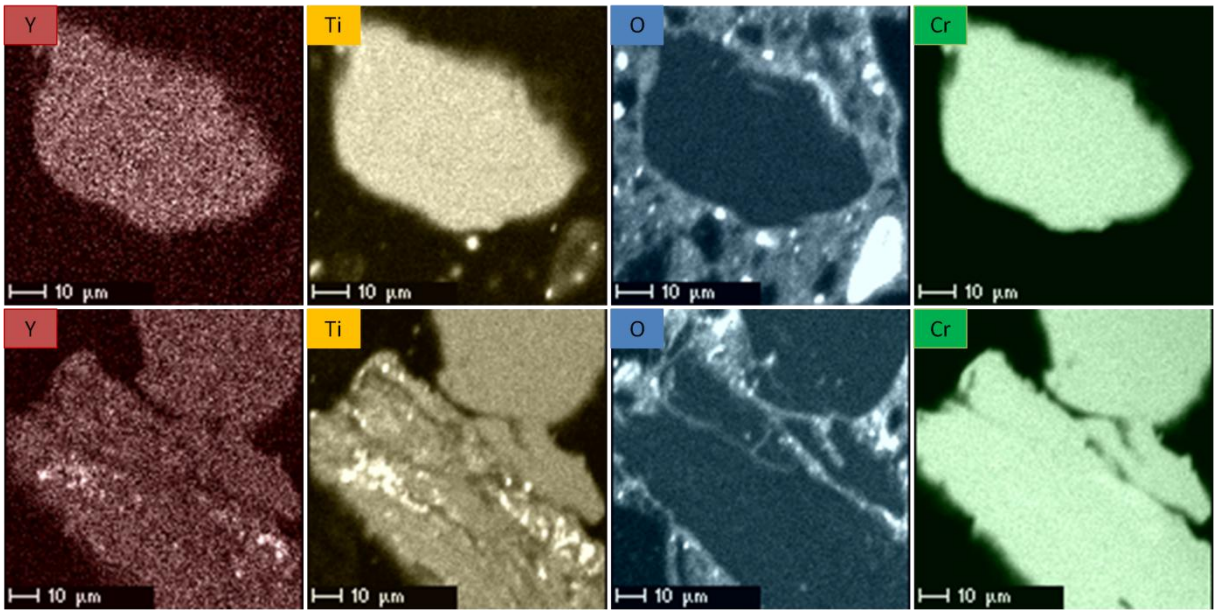

Figure III.2: Electron micro probe elements cartography of two different P9073 as-milled particles.

Figure III.2 shows the chemical maps obtained by electron microprobe on two types of powder, homogeneity is efficiently achieved for each element on most of the powder particles (we recall here that it is the whole point of the mechanical alloying processing step). Nonetheless some local heterogeneous distribution within particles can be observed for Y and Ti. High Ti and high Y concentration areas correlate. The oxygen concentration within the powder is quite low and oxygen content of the mounting resin overshadows it.

1.4. Microstructure detailed overview

As illustrated in Figure III.3, several classical characterization tools have been considered

to study the as-milled powder particle microstructure.

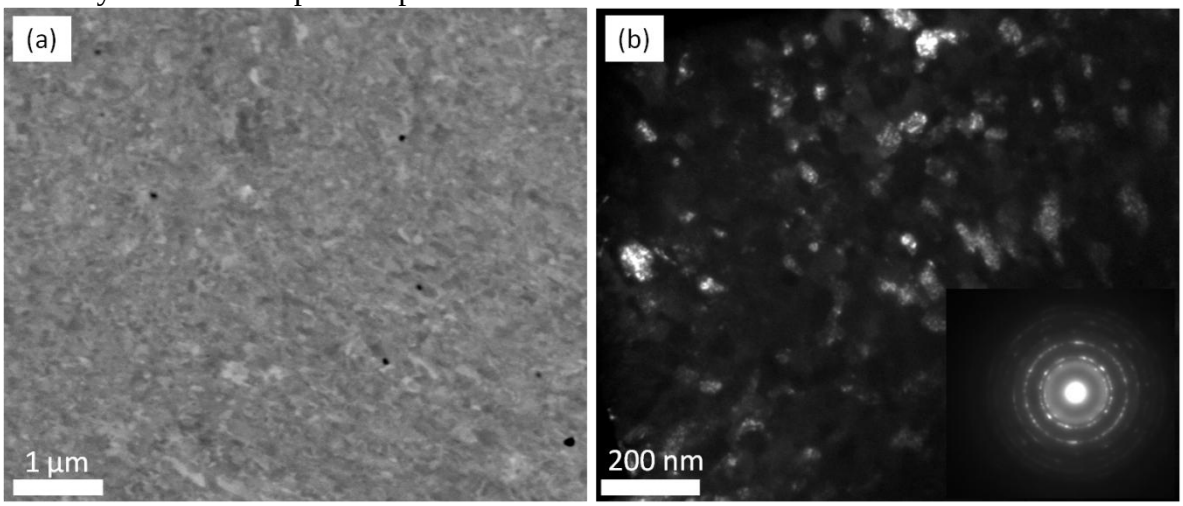

Figure III.3: a) SEM image of the as-milled powder b) Dark Field TEM image of the as milled powder P9073

SEM analysis was first attempted using the electron backscattered mode, but the SEM contrast does not allow for reliable grain detection (cf. Figure III.3a). This is partially due to the large amount of dislocations present in the material combined with the ultrafine grain microstructure. Instead, TEM-DF (Dark Field) imaging was carried out (cf. Figure III.3b) showing that the microstructure consists of crystallites of about 50 nm. However, TEM-DF images only provide a partial view of the microstructure: i.e. limited to the crystallites contributing to the diffraction intensity selected by the contrast aperture. Using the mWA-mWH method (cf. II§4.1.5), crystallite size was measured to be 25 nm and dislocation density to be $1{,}2.10^{16}$ m^{-2} (cf. Figure III.4). This result is consistent, though smaller, with the TEM-DF one.

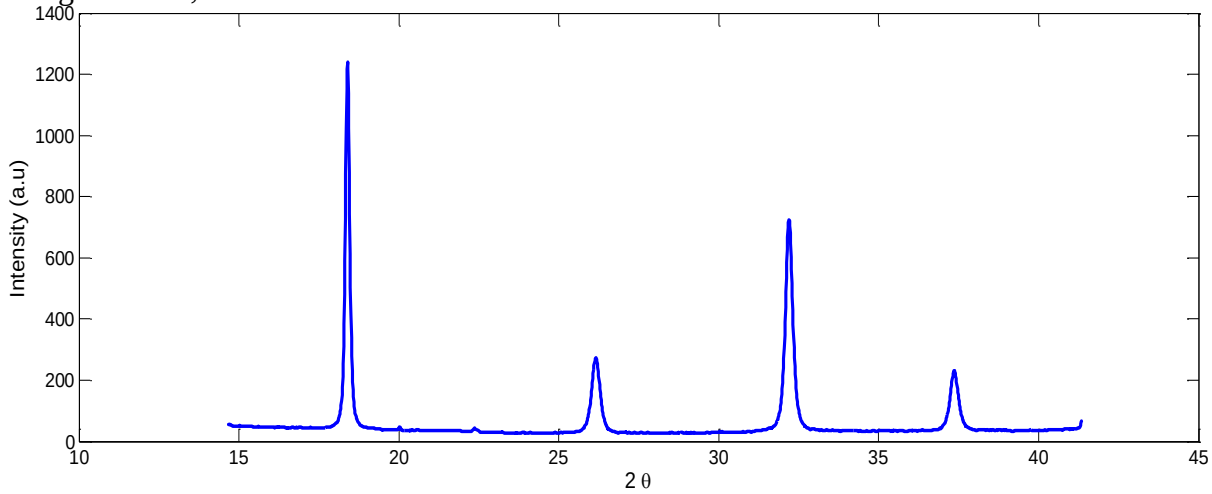

Figure III.4: Diffraction pattern obtained for an as-milled powder P9073 ($\lambda = 19\ keV$).

Obviously, in such finely nanostructured systems, classical characterization tools deliver only partial and scattered information. Given this, applying the ACOM-TEM method is all the more appealing.

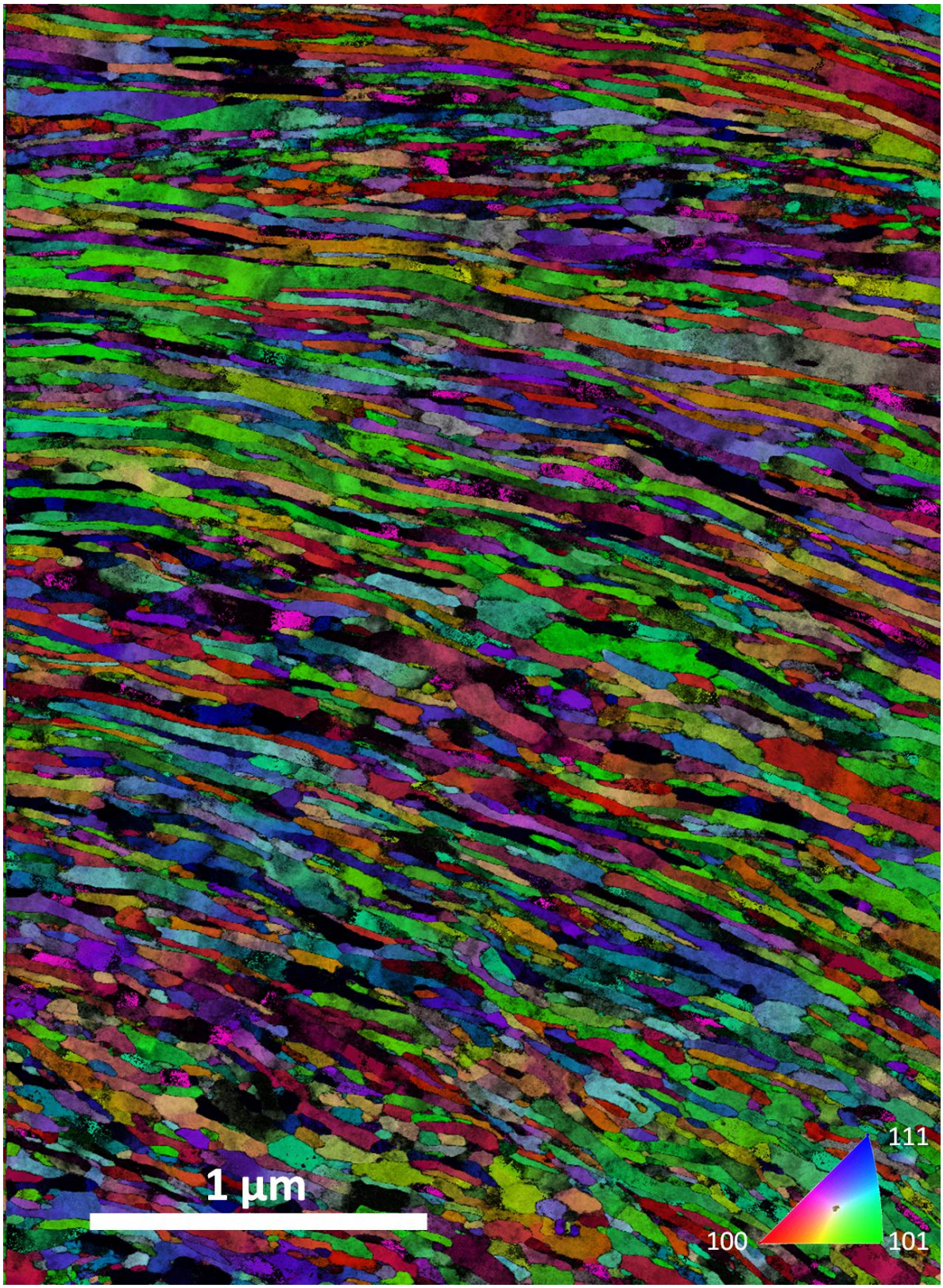

Figure III.5: ACOM-TEM orientation map of an as-milled powder particle. Grains with a lengh of several microns can be observed. Many of them have a very high shape factor, numerous grains are spanning across the area. The overlaid reliability map evidences that low reliable data is often confined to specific grains.

Figure III.5 displays an ACOM-TEM orientation map of a FIB section prepared from an as-milled ODS powder particle obtained with a probe size of 1nm and a step size of 2.75nm. The striking feature here is the presence of numerous anisotropic grains. Those

grains evidenced in the map are linked by an orientation correlation which results in a local texture within the material. For clarity, it is worth indicating that the point to point disorientation threshold to define grain boundaries has been set to 15°. In Figure III.5, the colour coded orientation map is overlaid with the reliability (cf. II§4.2.2). The ACOM-TEM map reveals a microstructure with a highly anisotropic morphology for the as-milled powder particles. This striking feature was not expected from X-ray and classical TEM measurements. More precisely, three main grain morphologies can be distinguished:

- small equiaxed grains with a diameter close to 50 nm,
- very long grains of more than 1µm in length with a shape factor of 5 to more than 30 (for details see Figure III.5),
- grains consistent with a flake-like shape with a size of 300 to 500 nm in length and a main shape factor ranging from 2.5 to 5.

It cannot be excluded that what is interpreted as small grains and flakes might respectively be long cylinder shaped grains cut along their transverse and longitudinal directions. But as the particles were prepared by ball milling this hypothesis seems to be unlikely. Furthermore, cross-section FIB cuts were performed within the same particles and the same grain morphology was observed for transverse and parallel directions to the particle long axis. The mean particles area measured from the orientation map is ~10000 nm² and the mean grain shape factor is 5. On the map, the green colour predominates which corresponds to numerous grains oriented in the same direction, in other words there is a local texture in the as-milled particle. However, in many elongated grains, colour variation indicates important intra-granular misorientations occurring throughout the grains. In the as-milled state, the microstructure of the ferritic ODS steels is already heterogeneous. There is a surface ratio larger than 10^2 between the largest and the smallest grains (cf. Figure III.6). Therefore, it can be stated that in the as-milled powder, microstructural conditions are already very favourable for the expected abnormal grain growth. Indeed, large grains will benefit from a size effect to grow faster that their neighbouring smaller grains (cf. I§2.7, [3]).

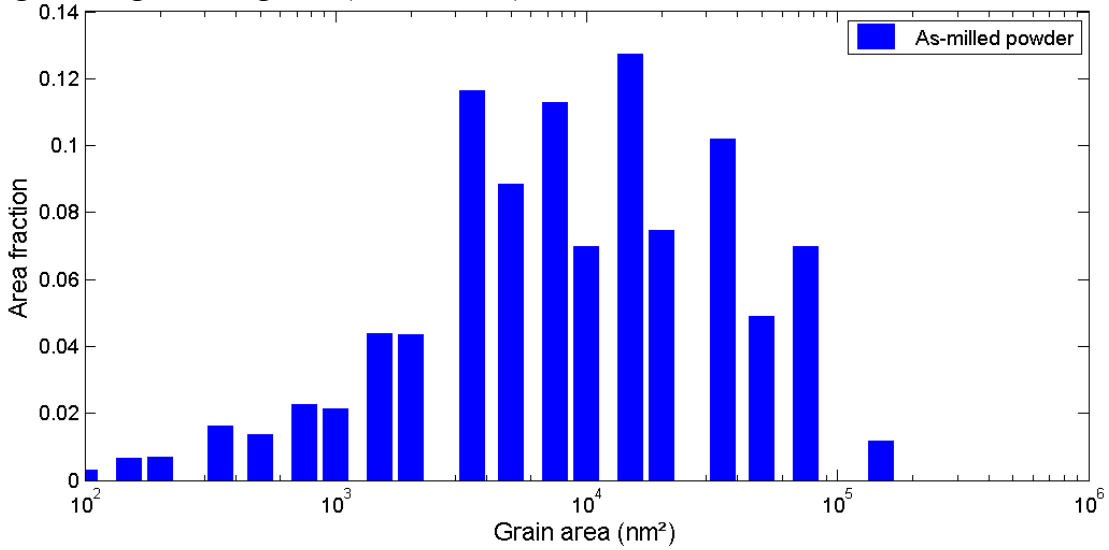

Figure III.6: Grain size distribution within the as-milled powder

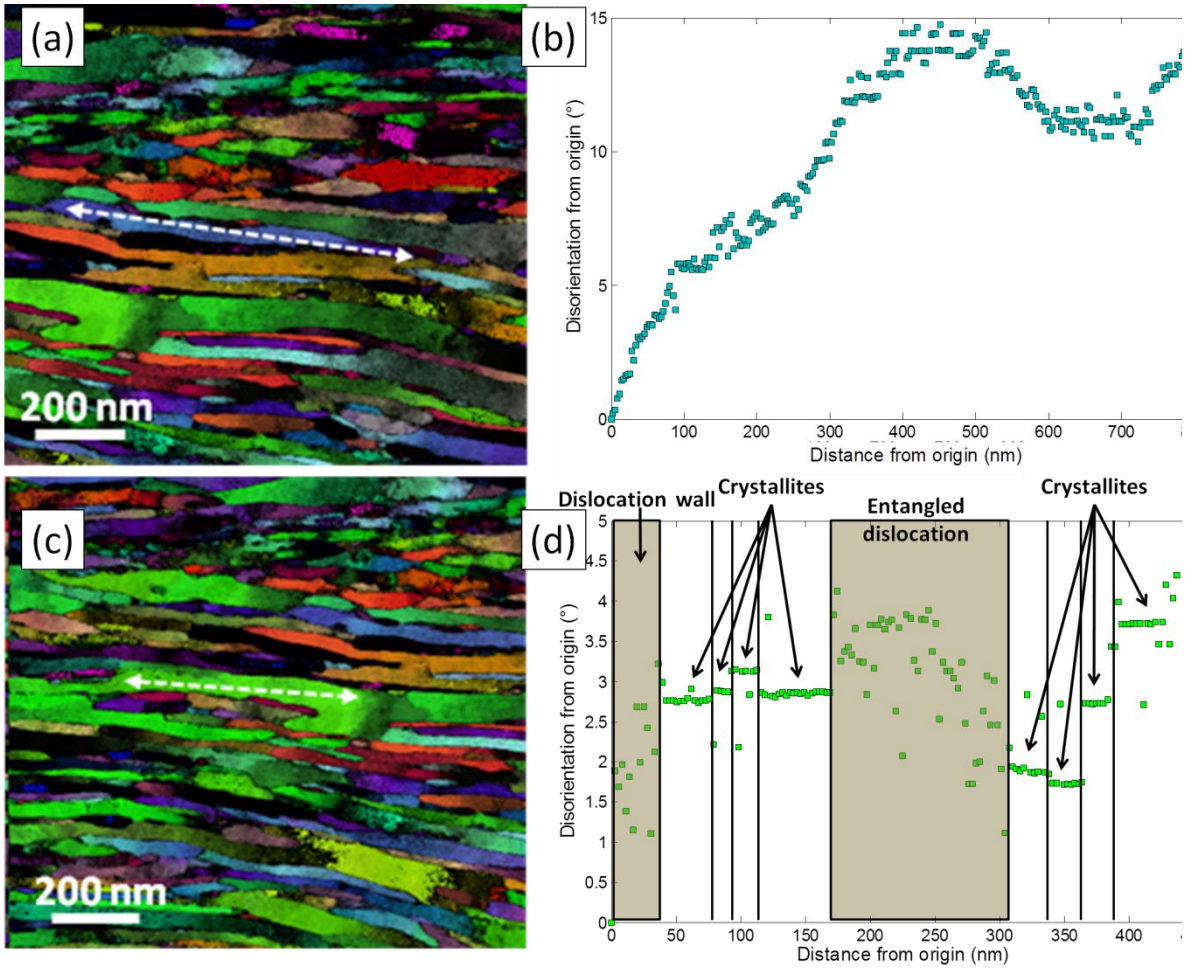

Figure III.7: ACOM-TEM maps of an as-milled powder particle. The misorientation profiles displayed on the right are taken within the grains, as shown by the white arrows on the figures on the left

Misorientation profiles taken across different grains (cf. Figure III.7) allow investigating the substructure within the grains. In Figure III.7b, the profile shows continuous misorientation along the grain length. This type of profile is the most frequently observed. However, in some grains (Figure III.7d), profiles reveal domains of about 30-50 nm with constant orientation separated by thin or thick areas showing high misorientations. These misorientation profiles can be interpreted in terms of crystallites and dislocations: domains with constant orientation correspond to crystallites; large areas with high misorientations are consistent with a large amount of entangled dislocations; the thin disoriented areas between crystallites are dislocation walls.

The crystallite size given by the misorientation profile is in agreement with the coherent domain size given by XRD. Furthermore, crystallite domains enlarged by dislocation walls are compatible with the domains imaged in the TEM experiments. Nevertheless, despite their undisputable interest, the misorientation profiles do not give a global overview of the local misorientations. Therefore, to have a better overview the orientation maps have been derived to obtain the so called Kernel Average Misorientation (KAM) and Grain Average Misorientation (GAM) calculations, that respectively evaluate the mean misorientation between one point and its neighbours, and the misorientation average within each grain separately. These two maps allow to build a 2D representation

of the local misorientation [4].

KAM maps are very enlightening as illustrated by the one obtained for the as milled state (cf. Figure III.8). Here, only the first layer of neighbouring points was considered.

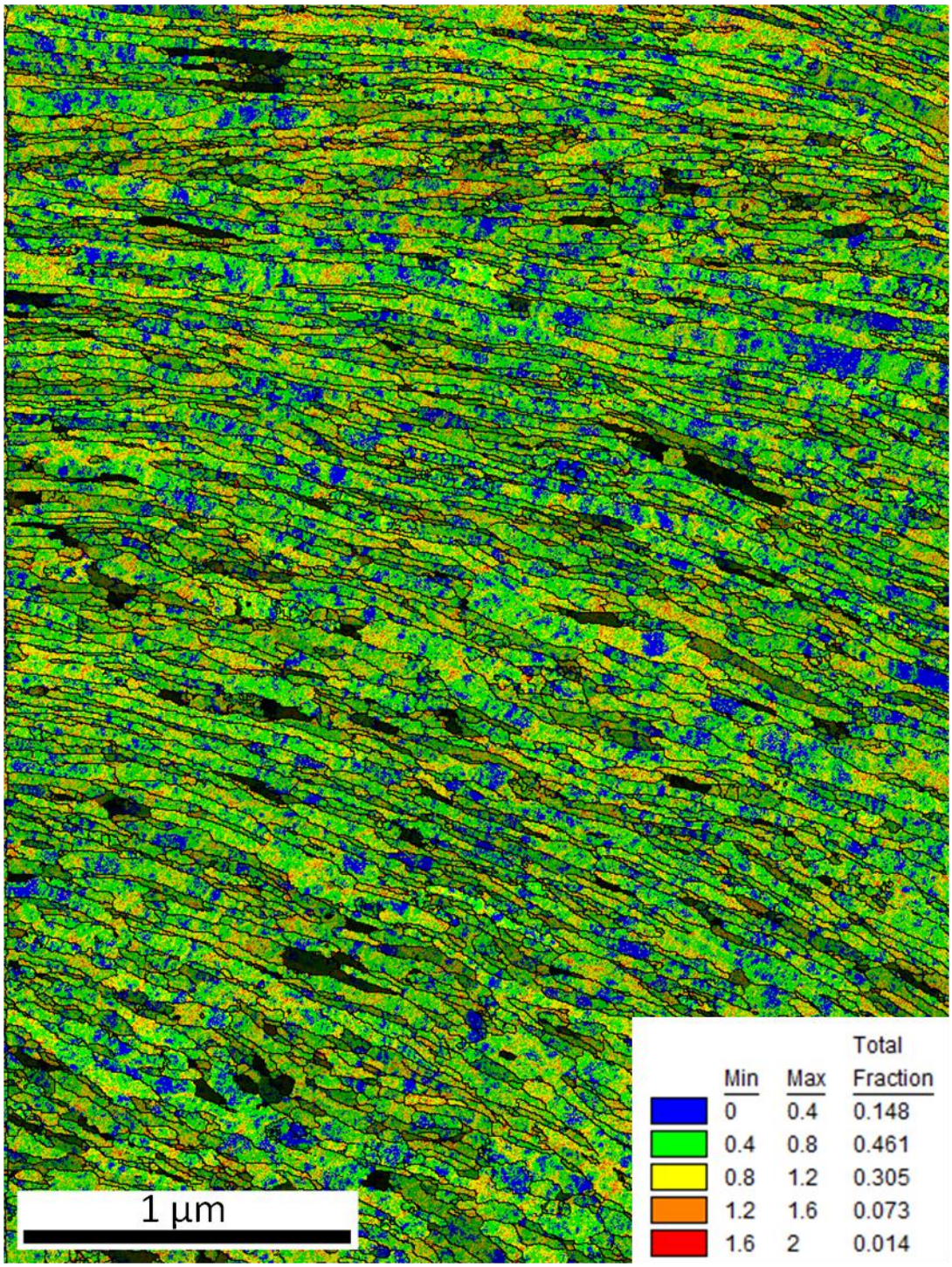

Figure III.8: KAM (1st neighbour) calculated from the as-milled particle orientation map, maximum disorientation=2°

The KAM map in Figure III.8 displays the misorientation with the following colour code: from blue for low disorientation to red for high disorientation (for more precise values see insert on Figure III.8). At first, the as-milled particle KAM map reveals an important misorientation all over the sample area (mean value: 0.69°). Using Gao et al.'s formula

(cf. chapter II §4.2.3.3, [5]), the dislocation density is calculated to $9.7.10^{15}$ m^{-2}. Some domains of low misorientation are visible (in blue), they are ~30nm sized and bound to more disoriented areas. Actually, the blue domain on the KAM map directly points out the crystallites earlier identified by the misorientation profiles. The elongated grains appear on the KAM map as formed by successive crystallites separated by thick domains of high misorientation or, in other words thick dislocation walls. From the GAM measurement it is evidenced that the disorientation is independent of the grain size or grain shape.

1.5. Precipitation state

Precipitation state of the as-milled powders has been much debated within the ODS steels scientific community. Indeed, as presented in the literature review, if some authors claim the presence of nanosized precipitates in the as-milled powder [2,6] others claim that no precipitate can be found at this state [7,8].

Specific TEM sessions have been dedicated to the search of precipitates. However with such small size objects (i.e. 1-2nm) the limit of the technique is reached and no precipitates have been observed with classical TEM until annealing up to 800°C. SANS measurements have been performed and neither the magnetic nor the nuclear scatterings allow to detect any nanosized objects (cf. Figure III.9).

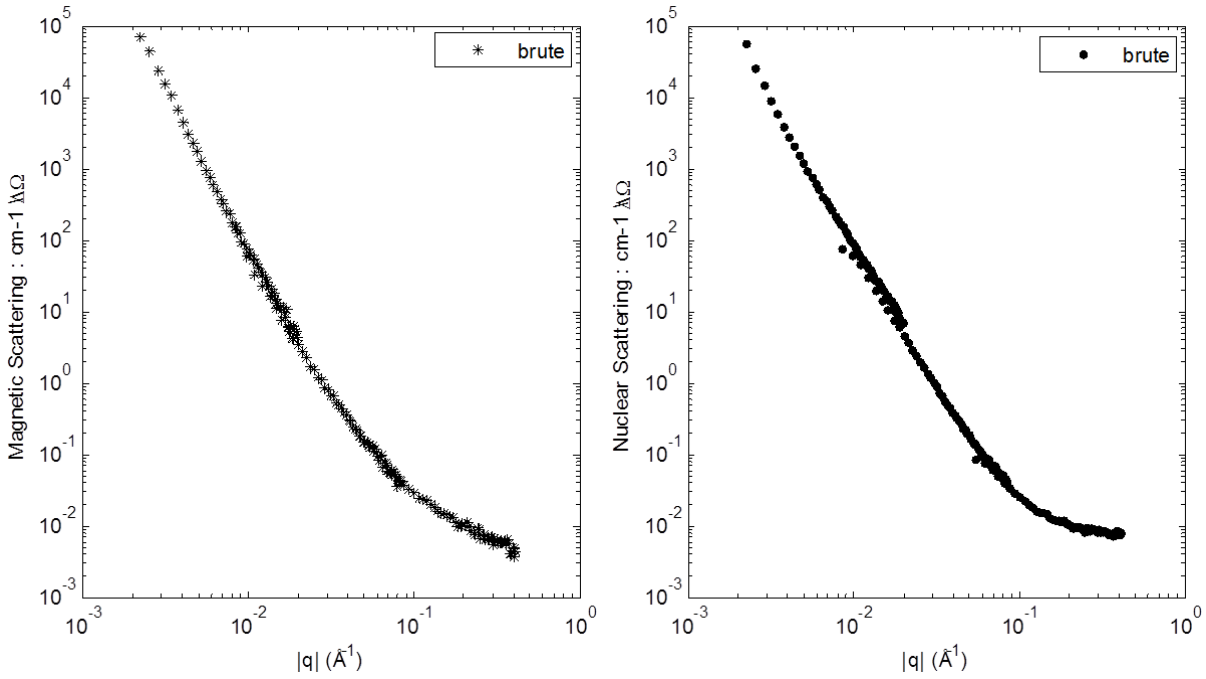

Figure III.9: Magnetic and nuclear scattering of the as-milled P9073 powder issued from SANS measurements (results obtained on the as-milled P9079 powder are almost identical)

Furthermore, APT analysis was performed by C. Hatzouglou [9] on the as-milled powder. It has concluded to the absence of clusters within the as-milled state (cf. Figure III.9). It will therefore be considered that no precipitation has occurred during milling. The heterogeneities evidenced by EPMA (cf. III§1.3) are considered as milling imperfections.

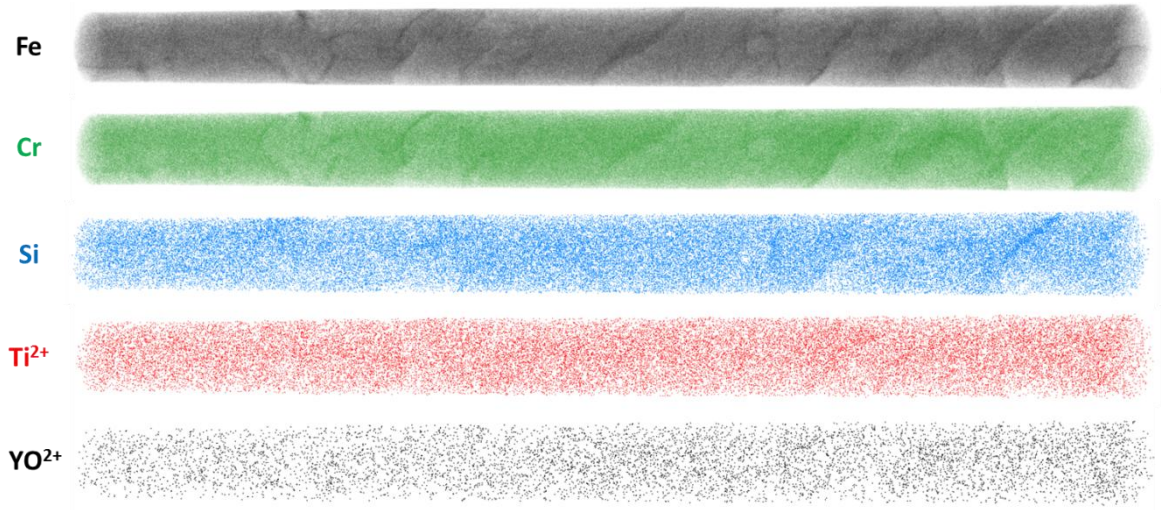

Figure III.10: APT reconstruction of the as-milled P9079 powder, 28x28x396 nm. Courtesy of C. Hatzoglou. GPM Rouen

1.6. Key features of the powder particle microstructure

- Chemical distribution can be considered as homogeneous even if some of the particles may have local heterogeneities.
- The microstructure is mainly constituted of elongated grains. Grain can be very distorted, some are constituted of crystallites separated from each other by dislocation walls.
- The grain size distribution is heterogeneous with a surface ratio of more than 10^2 between the smallest and the largest grains.
- No precipitation is evidenced after mechanical alloying.

2. Part I : Annealing conditions for recrystallization and abnormal grain growth

After ball-milling, the powder particles have a high potential for microstructural change during heat treatment, with a high dislocation density and a large grain boundary area. Their microstructural evolution during various annealing treatments will be reported here. Abnormal grain growth will be observed if the larger grains grow faster than the mean grain growth rate. Grains will be considered to be abnormal if they are twice as large as the mean grain size.

2.1. Low temperature annealing (600°C).

During preliminary XRD investigations, 600°C has been identified as an interesting temperature for microstructural evolution. We will therefore describe here the microstructural evolutions occurring during a 600°C annealing.

2.1.1. Chemical distribution

Compared to the chemical distribution observed on the as-milled powder, a noticeable evolution is the increase of the Ti concentration on the internal free zones of the particles (cf. Figure III.11). This may result from a Ti diffusion towards the particles' surfaces. Indeed, titanium diffusion coefficient within steels is high ($D_0 = 6.8 \times 10^{-3}\ m^2.s^{-1}$ [10]) and many works are actually trying to block its diffusion within stainless steel [11]. In addition, titanium is a well known oxygen getter and will therefore be further attracted by the high oxygen content at the particles' surface.

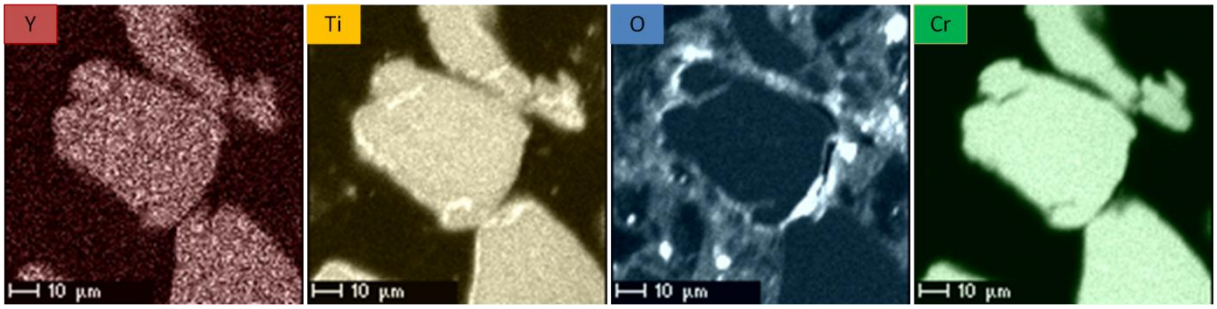

Figure III.11: Electron microprobe analysis of the P9073 powder annealed 1h@600°C

2.1.2. Grain microstructure

According to *in-situ* XRD diffraction dislocation density and crystallite size evolution upon heating up to 600°C vary as shown on Figure III.12. Before heating, the initial powder contains coherent domains with a diameter size of ~23 nm, demonstrating the efficiency of high-energy attrition to produce nanostructured materials (cf. III§1.4, [12–14]). The dislocation density is $1.2.10^{-16}$ m^{-2}, which is consistent with what is observed *ex-situ* by XRD or electron microscopy (cf. III §1.4). A considerable amount of plastic work is stored during milling. Indeed, a first stage of rapid crystallite growth occurs at low temperatures (20-600°C), as illustrated in Figure III.12. During these early stages of heating, annealing induces a decrease in dislocation density from $1.2.10^{-16}$ m^{-2} to 6.10^{-15} m^{-2}, while crystallite size increases from 23 to 33 nm. During the soaking time, a reduction of the crystallite growth rate is observed while the dislocation density decreases

remain constant. This change can be interpreted as a transition from dislocations annihilation within the cells to a real increase of the crystallite size with moving crystallite boundaries.

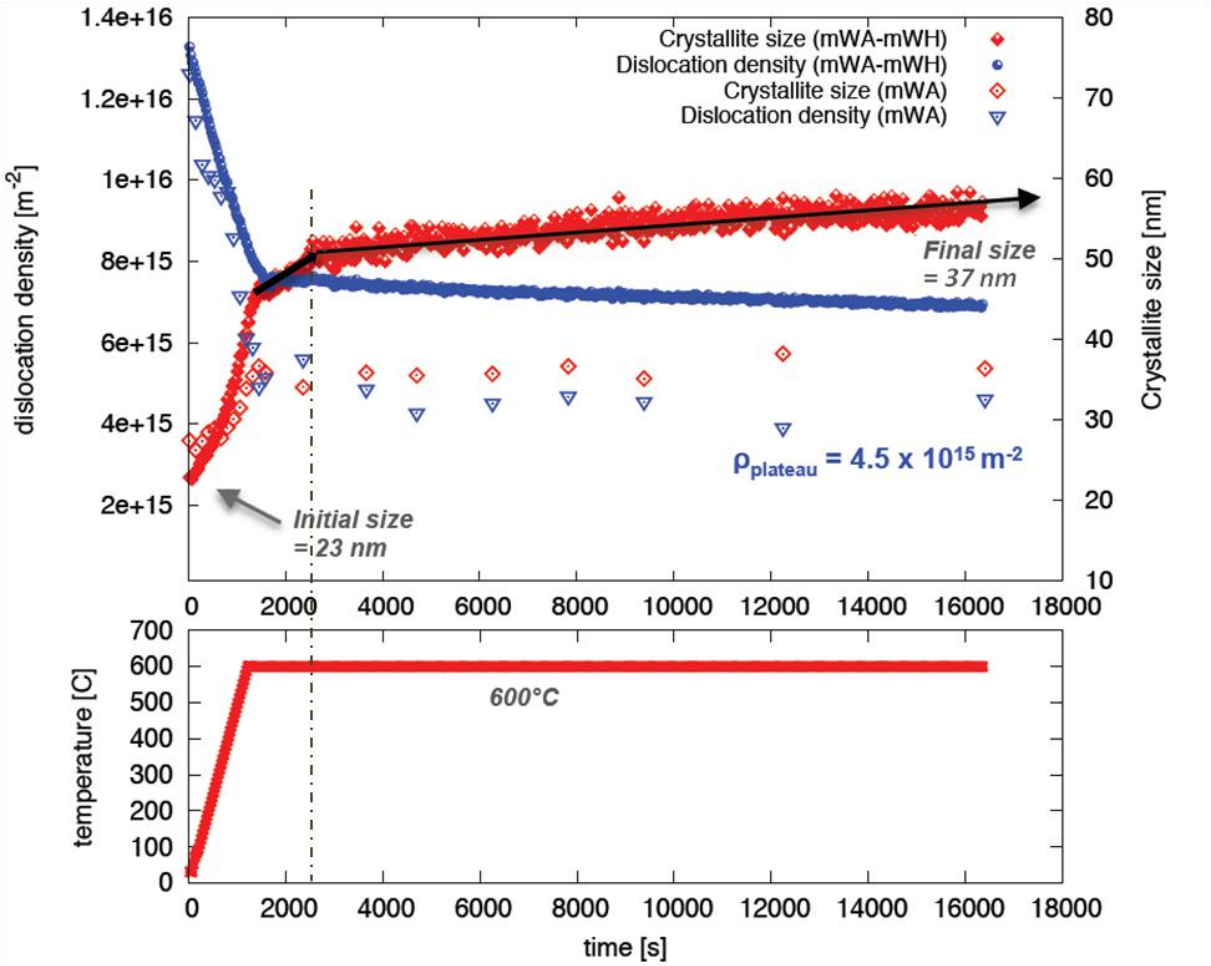

Figure III.12: Dislocation density and crystallite size determined with the coupled mWA-mWH method and the mWA method during heating up to 600°C and consecutive annealing for 4h

A slow increase of crystallite size is observed until the end of the soaking stage (>5 hours) at 600°C, with no slope variation, final crystallite size is then 40 nm. Meanwhile, a plateau was observed for the dislocation density at $4.5.10^{15}$ m^{-2}. This microstructural evolution is characteristical of microstructure recovery. The mWA and mWA-mWH methods give identical results (both for *D* and ρ) at the beginning of the *in-situ* heating, but results differ before attaining the temperature of 600°C. At the end of the heating cycle, the two corresponding dislocation densities deviate from their average value of $5.5.10^{15}m^{-2}$ only by about 20%, which is within the error of the evaluation method. The difference between them is still small indicating that larger and small grains have nearly the same recovered dislocation structure.

From XRD measurement, the general crystallites and global strain behaviours are described. The understanding of this microstructural behaviour can be deepened by the ACOM-TEM technique by the analysis of the grain scale microstructural evolutions.

As it can be observed on the orientation map (cf. Figure III.13a), the grain morphology

after 5 min at 600°C is still characterized by very thin and elongated grains. The KAM map on Figure III.13b, shows that crystallites have grown, and it can be seen that the global misorientation level as decreased (0.58°). Nevertheless, misorientation is still high and crystallites are separated from each other by large high misorientation areas.

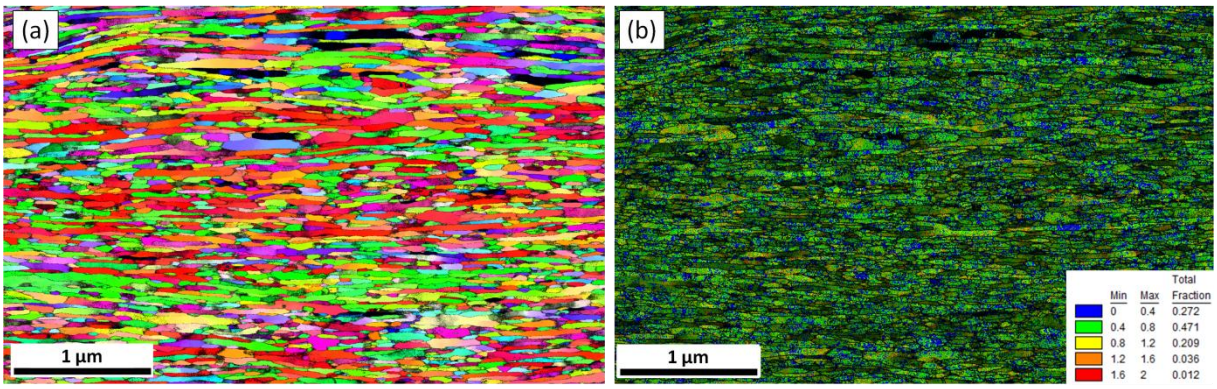

Figure III.13: Microstructure of the P9073 powder after a 5min@600°C annealing. (a) ACOM-TEM orientation cartography (b) KAM (1st neighbour)

The powder particle annealed for 1h@600°C ACOM-TEM orientation cartography shows that the microstructure is still heterogeneous and contains many anisotropic grains (cf. Figure III.14a). The grain mean shape factor is 4.5, while the grain area distribution is narrower than in the as-milled state with an equivalent average value of ~10000 nm² (0.01 µm²). In addition, the grain boundaries are thinner and the KAM map mean distortion (0.53°) is significantly smaller than for the as-milled powder (0.69°) (cf. Figure III.14b), also the calculated dislocation density is $1{,}9.10^{15}$ m^{-2}. Indeed, the low misoriented (blue domains) area fraction is ~30% of the total area which is twice the one observed in the as-milled state (15 %) and slightly superior to what is observed for the 5min annealing (~19%). The increase of the low misoriented area fraction results from the slight enlargement of crystallites and evolution of the thick walls into crystallites and thinner walls. Compared to the as-milled states there is much less highly deformed zones (red areas). This decrease has occurred homogenously within the sample. The slight increase of crystallite domain size (~40 nm) and the decrease of the global disorientation value are in very good agreement with XRD results (cf. III §3.1).

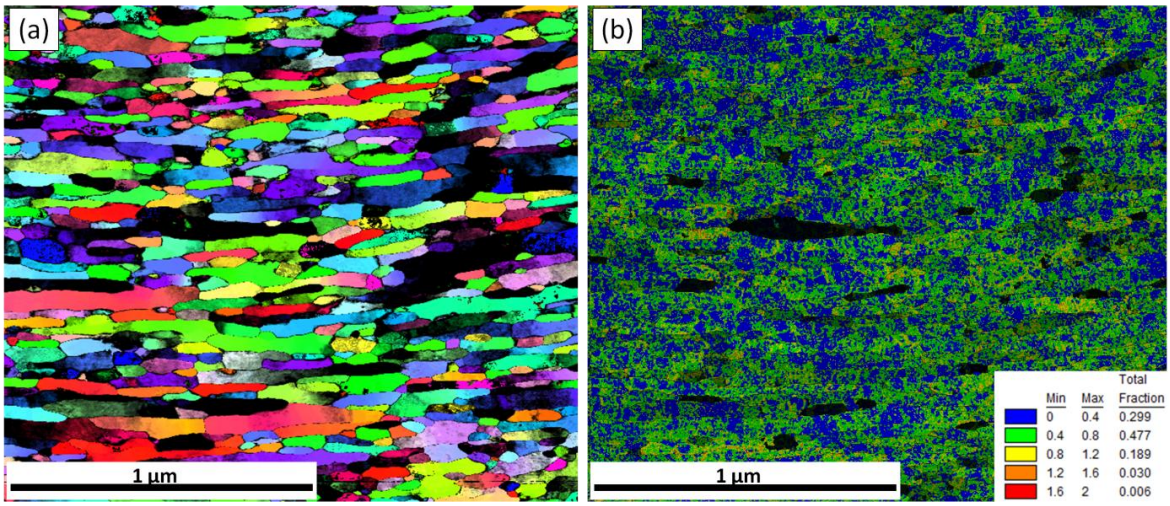

Figure III.14: Microstructure of the P9073 powder after a 1h@600°C annealing. (a) ACOM-TEM orientation cartography (b) KAM (1st neighbour)

Therefore the *in-situ* XRD and TEM-ACOM results are in good agreement. Both indicate the presence of two successive microstructural recovery mechanisms with first the formation of numerous crystallites within the highly deformed microstructure and then their growth.

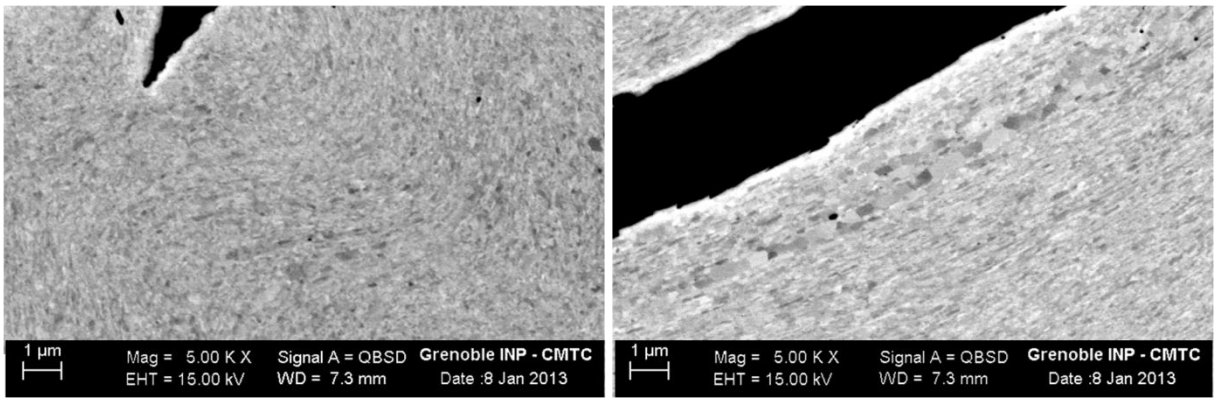

Figure III.15: SEM images of a 12@600°C annealed powder P9073

Interestingly, during a very long annealing at 600°C, larger grains are evidenced on particular locations where the microstructure seems to be highly deformed (cf. Figure III.15). It can be interpreted as recrystallization located in what seems to be former cold weld areas in which the deformation level reached during the mechanical alloying is particularly high.

2.1.3. Precipitation state

Similarly to what was concluded from TEM experiment on the as-milled powder, conventional TEM limits are reached and no precipitates were found. Using SANS however, it has been possible to identify a scattering signal in the 600°C annealed powders. For the study proposed, the as-milled powder will be considered as the reference state and its signal will be used for normalisation on the other samples (cf. Figure III.16).

		5 min	20 min	60 min	720 min
600°C	R_g (Å)	7.53	8.25	8.66	9.04
	f_v (%)	1.03	0.99	1.07	1.14

Table III.1: Mean parameters of the precipitate distributions of the 600°C annealed powders

The mean radius of the precipitates evidenced at 600°C is around 8.5 Å, with a volume fraction being close to 1% (cf. Table III.1). The calculation of the precipitate volume fraction and mean radius, detailed on (cf. II§3.2.3) is based on the assumption that the precipitation is constituted by an equilibrate concentration of $Y_2Ti_2O_7$ and Y_2TiO_5. Nevertheless, precipitation of such phases is highly unlikely at this state since their nucleation temperature has been simulated to be close to 700°C [15]. Broad size distribution of the objects and their relatively small scattering intensity, the precipitation state is more likely to correspond to clustering atoms or clusters than to well defined precipitates. It can be noticed that the signal does not change much over the annealing at 600°C.

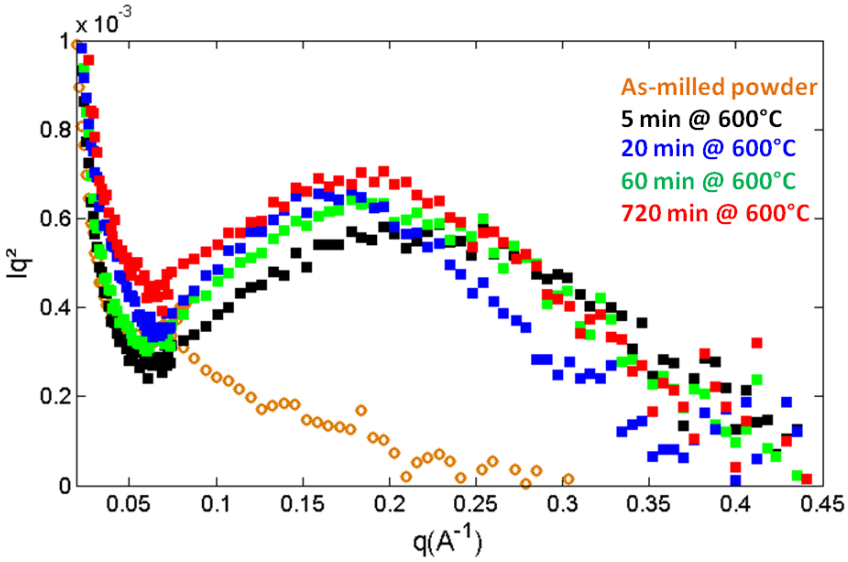

Figure III.16: SANS results obtained on the P9073 powder after different 600°C annealings

2.1.4. Key points

- At 600°C recovery has occurred.
- The recovery is achieved in two successive steps identified by two distinct crystallite growth kinetic during the *in-situ* XRD experiment. This result is confirmed by ACOM-TEM.
- During recovery the dislocation density significantly decreases from its high as-milled value. This is due to the rearrangement of dislocations into subgrain walls.
- This microstructure at 600°C is constituted of anisotropic grains formed by successive crystallites.
- High stability of the microstructure at 600°C.
- Precipitation or clustering

2.2. High temperature annealing (>800°C)

During a 600°C annealing, material evidences a reduced potential for microstructural evolution, nevertheless abnormal grain growth is occurring on ODS ferritic steels. To explain the transition from the recovery mechanisms to abnormal grain growth, results obtained during annealings from 800°C to 1100°C will be exposed here.

2.2.1. Chemical distribution

On the powder annealed at 800°C, chemical maps (cf. Figure III.17) show that a high titanium concentration can be found at the edges of the powder particles. This may have important consequences for precipitate formation, since, as well established by the literature review (cf. I§1.2.2), titanium allows for the formation of a denser and smaller yttrium oxide precipitate population.

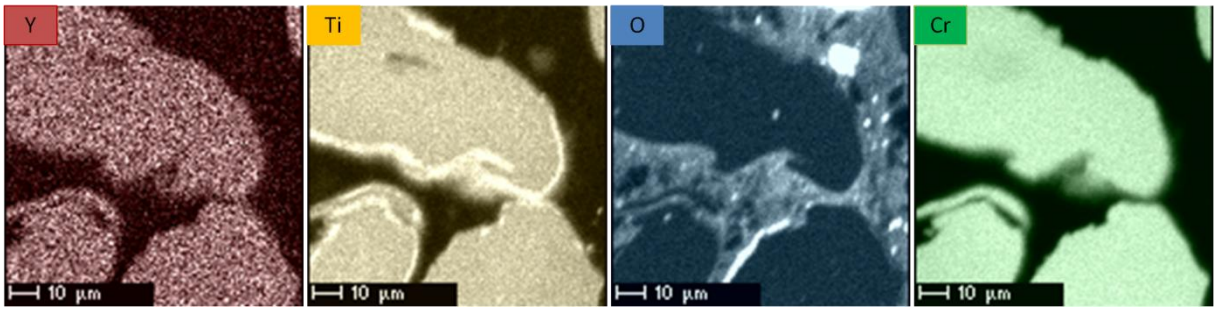

Figure III.17: Electron microprobe analysis of the P9073 powder annealed 1h@800°C

The Ti concentration ratio at the particles' boundaries compared to the bulk increases with the increase of the annealing temperature (cf. Figure III.18 and Figure III.19).

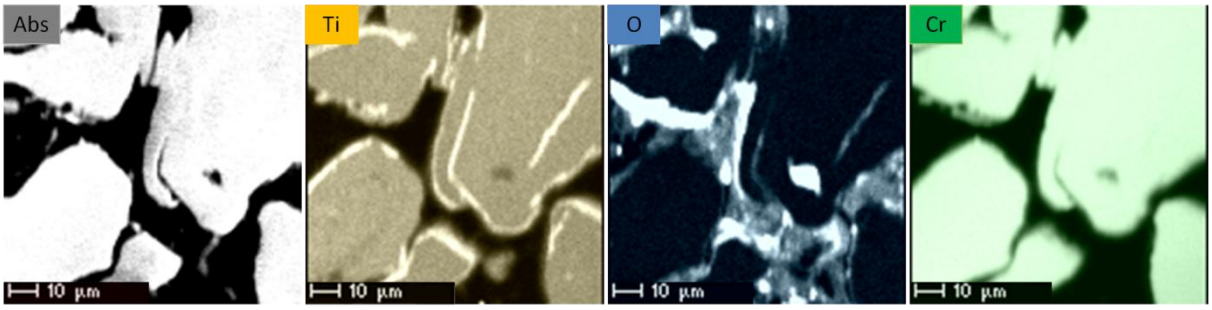

Figure III.18: Electron microprobe analysis of the P9073 powder annealed 1h@850°C

Yttrium concentration is not reported on the 850°C and 1100°C, since at the EPMA scale, this concentration appears to be homogeneous.

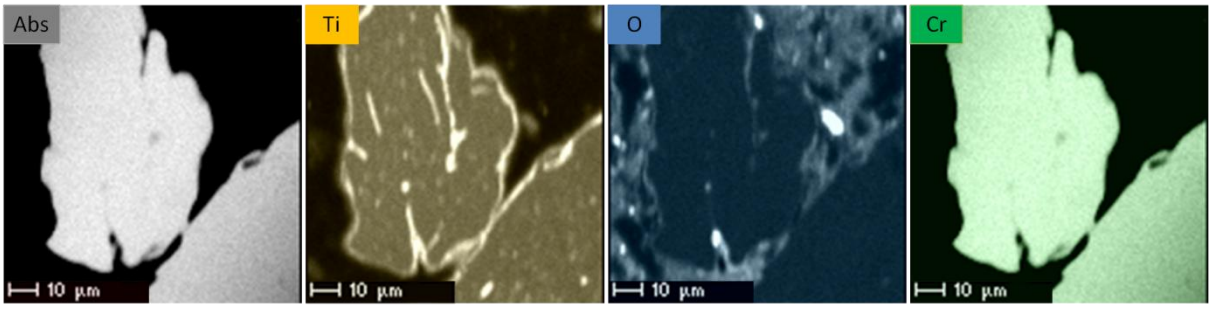

Figure III.19: Electron microprobe analysis of the P9073 powder annealed 20min@1100°C

In literature the same effect is observed with oxygen, in [16], it is stated that the quantity

of oxygen increases with the size of particles and O content increases with the distance from the center of the particle.

2.2.2. Microstructure

A first insight of the microstructure evolution can be obtained by SEM characterization of annealed powders. After a short (5min) annealing at 800°C a completely isotropic microstructure can be evidenced (cf. Figure III.20a). After a longer (20min) annealing at 800°C, the first coarse grains appear at the boundaries of the particles mostly. and also (similarly to what was observed after the 12h@600°C annealing) at the cold weld and highly deformed regions (cf. Figure III.20b).

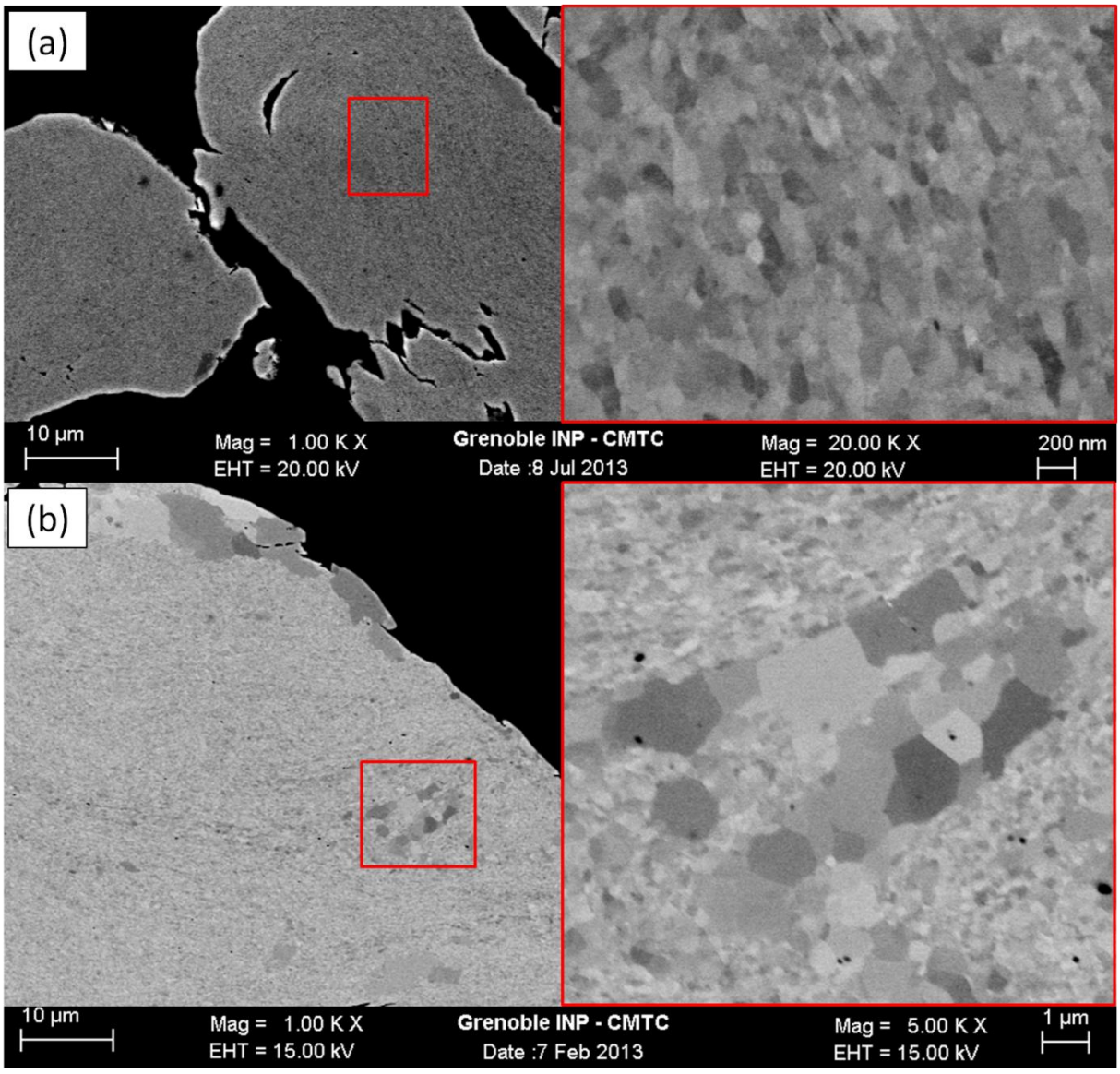

Figure III.20: SEM image of P9073 powders annealed at 800°C (a) for 5min (b) for 20min

Those two abnormal grain growth processes can be respectively explained by different mechanisms:

- At the particles' boundaries, the titanium content is high which means that close to those regions titanium has diffused at the edge of the particle. Therefore it means

that less titanium is available for nanosized yttrium precipitates' formation. However, titanium is used in ODS ferritic steels to refine the yttrium precipitates' size [6,17,18], without titanium, precipitates formed near the particle boundaries will be significantly coarser and the precipitation density will be lower than in the other regions of the particle. This results in less efficient retarding and pinning effects of precipitates on dislocations and grain boundaries' migration. Consequently the recrystallization will be specifically favoured in those regions. To confirm this mechanism, local variation of the precipitation density should be measured.

- The second phenomenon is significantly different. On particular locations of the particle, the grain deformation is particularly important by judging from the particular shape and arrangement of the local grain population. Indeed, according to the classical recrystallization theory [3], high deformation areas are particularly well suited for recrystallization. Whose areas may result from cold welding by judging from the grain shapes and orientation.

SEM imaging of particles annealed at higher temperatures (cf. Figure III.21 for example), all evidence a bimodal grain size distribution demonstrating the abnormal character of further grain growth. The coarse to Ultra Fine Grains (UFGs) surface ratio increases with increasing temperature. To understand the mechanisms leading to this abnormal grain growth, *in-situ* XRD experiments have been performed. Also, the internal grain structure is studied using ACOM-TEM.

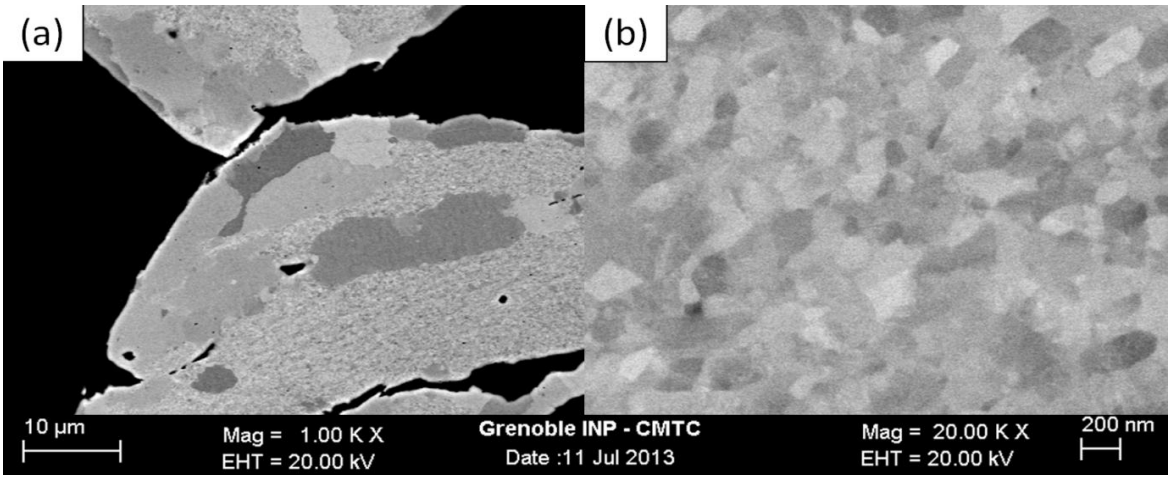

Figure III.21: SEM image of the P9073 powder annealed for 1h@850°C (a) x1K (b) x20K

2.2.2.1. Global microstructure evolution

To study recrystallization, 4 different anisothermal heat treatment studies have been conducted at the beamline Diffabs of the Soleil synchrotron. The as-milled powder P9073, has been heated from room temperature to respectively 800°C for 1h, 850°C for 1h, 900°C for 1h and 1100°C for 20min. Before going further into the results' analysis, it is necessary to stress out that as explained in chapter II, the important part being the insights towards the microstructure evolution the results obtained with the mWA-mWH method allow and not the absolute values obtained.

800°C annealing:

Figure III.22 shows that crystallite size and dislocation density are respectively monotonously increasing and decreasing with the temperature. At 700°C, the crystallite size obtained from the mWA-mWH method shows a significant sigmoid increase. In parallel with this evolution the dislocation density decreases significantly slow down.

This could correspond to a continuous transition from recovery to recrystallization. Indeed the sharp dislocation decrease while the crystallite size increase is slow can be attributed to the incubation time for dislocations and sub-boundaries to rearrange and transform into proper grain boundaries. These two succeeding phenomena (sharp dislocation decrease preceding a sigmoid growth of the crystallite size) can therefore be a strong indication of an ongoing continuous recrystallization. Furthermore, the steady and moderate decrease of the dislocation density may be an indication that no discontinuous phenomena occur.

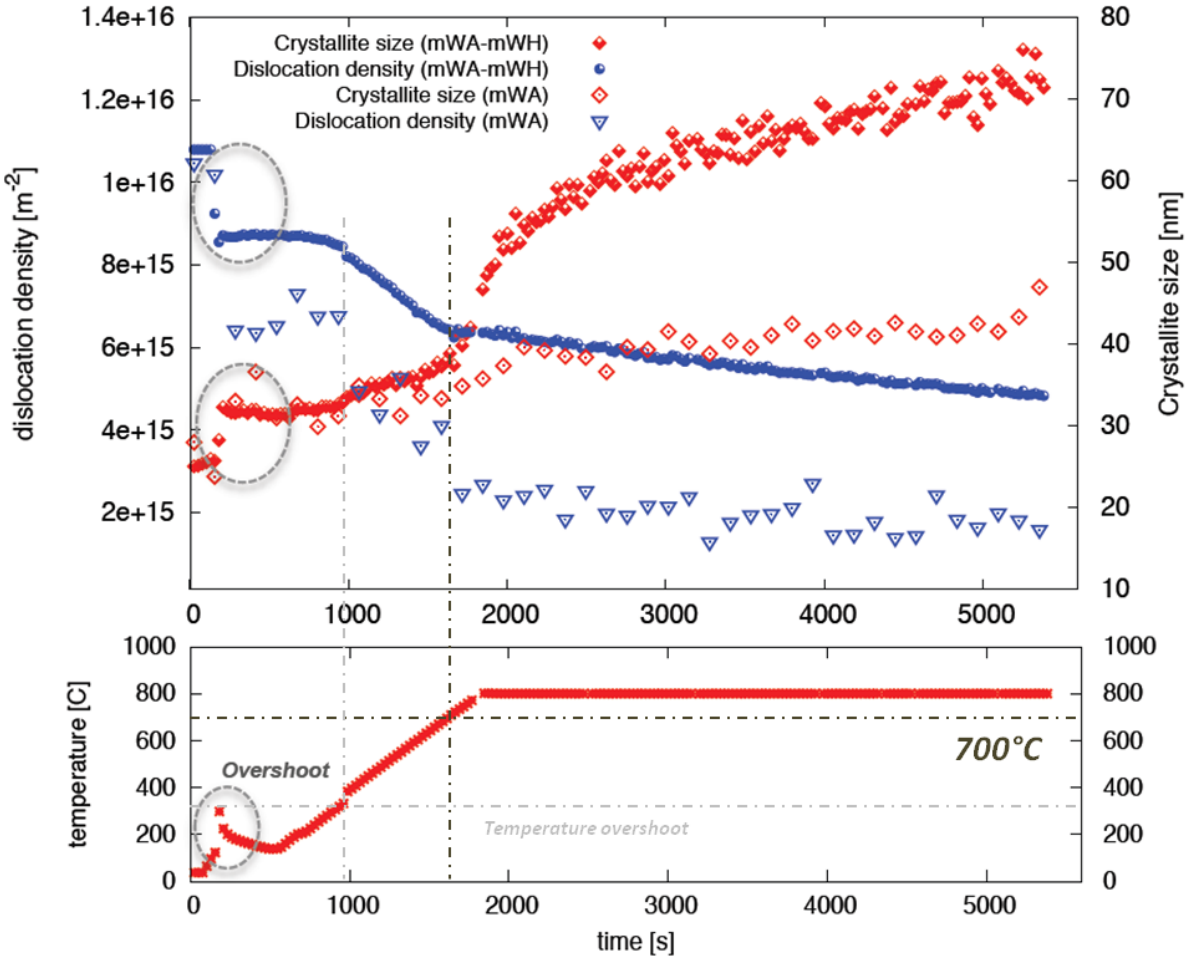

Figure III.22: Dislocation density and crystallite size determined with the coupled mWA-mWH method and the mWA method during heating up to 800°C and consecutive annealing for 1h. During the first minutes of heating, crystallite size sharply increases due to a thermal overshot. This growth is accompanied by a jump of the dislocation density. Following these changes both parameters remain constant until the temperature reaches again the temperature peak value attained during the overshot (300°C)

850°C annealing:

During heating up to 850°C the dislocation density of the average grains (mWA method, cf. II§4.1.3.) continuously decreases from $1.2.10^{16}$ m^{-2} to about 4.10^{15} m^{-2}, while crystallite size increases steadily from 23 nm to 37 nm (cf. Figure III.23).This first part reproduces the recovery behaviour described in §2.1. Starting from 650°C up to 820°C dislocation density shows a plateau around the value of 6.10^{15} m^{-2} for both mWA-mWH and mWA method. In parallel, the mWA-mWH crystallite size follows a sharp increase corresponding to the one observed during the 800°C cycle (i.e. sigmoid increase from 40 nm to 90 nm). The decrease of the dislocation density during the isothermal annealing is faster compared to previous heat treatments (at 600°C and 800°C) and for average grains it reaches the value of about $1.5.10^{15}$ m^{-2} after 1 hour (cf. Figure III.23).

This plateau in dislocation density might, similarly to the interpretation made for the 800°C, correspond to an incubation time for a continuous transition from recovery to recrystallization. Then, during the soaking stage at 850°C, the growth rate of large crystallites continuously increases evidencing the ongoing recrystallization while the average small grain size increases really slowly, showing a high thermal stability. Despite their relative small size (0.2-1µm) UFGs are no longer quantitatively measurable by diffraction peak analysis methods which reach their limits, values obtained above 0.5 µm are no longer reliable. The arrow shows the moment where the growth rate evidenced between mWA and mWA-mWH methods vary, which can be associated to the beginning of abnormal grain growth.

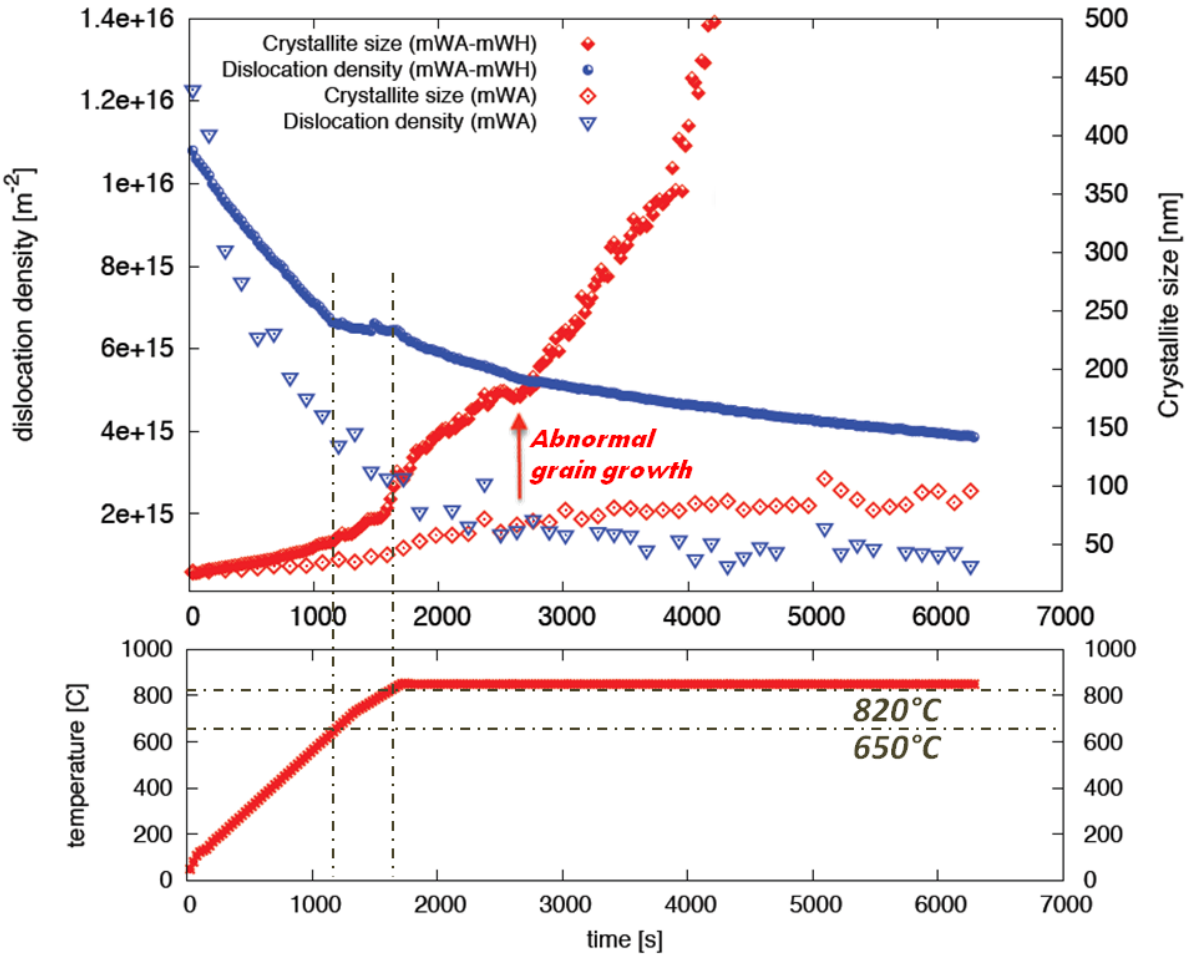

Figure III.23: Dislocation density and crystallite size determined with the coupled mWA-mWH method and the mWA method during heating up to 850°C and consecutive annealing for 1h

900°C annealing:

During the 900°C cycle, the signal evolution allows to follow step by step almost all microstructural transformations within the material (cf. Figure III.24). The recovery part of the cycle is similar to the one observed during previous annealing. The transition step between recovery and recrystallization between 650°C and 800°C is confirmed, however, the length of the plateau is shorter. During this plateau, the grain populations' sizes evidenced by mWA and mWA-mWH are clearly diverging. After 800°C, dislocation density of average grains drops to about 2.10^{15} m^{-2}, significantly more rapidly than what was observed in the two preceding cycles.

It is worth noticing that the dislocation density drops almost concomitantly with the crystallite sharp growth (mWA-mWH data) which begins during the drop in dislocation density and not right after as evidenced earlier (cf. Figure III.22 and Figure III.23). This indicates an acceleration of the transformation kinetics. Then, crystallite size increases drastically and monotonously until abnormal grains prevent exploitable results. After 1h hour annealing, dislocation density reaches $9.0.10^{14}$ m^{-2}. There is no transition from recrystallization to abnormal grain growth, the two phenomena occur simultaneously.

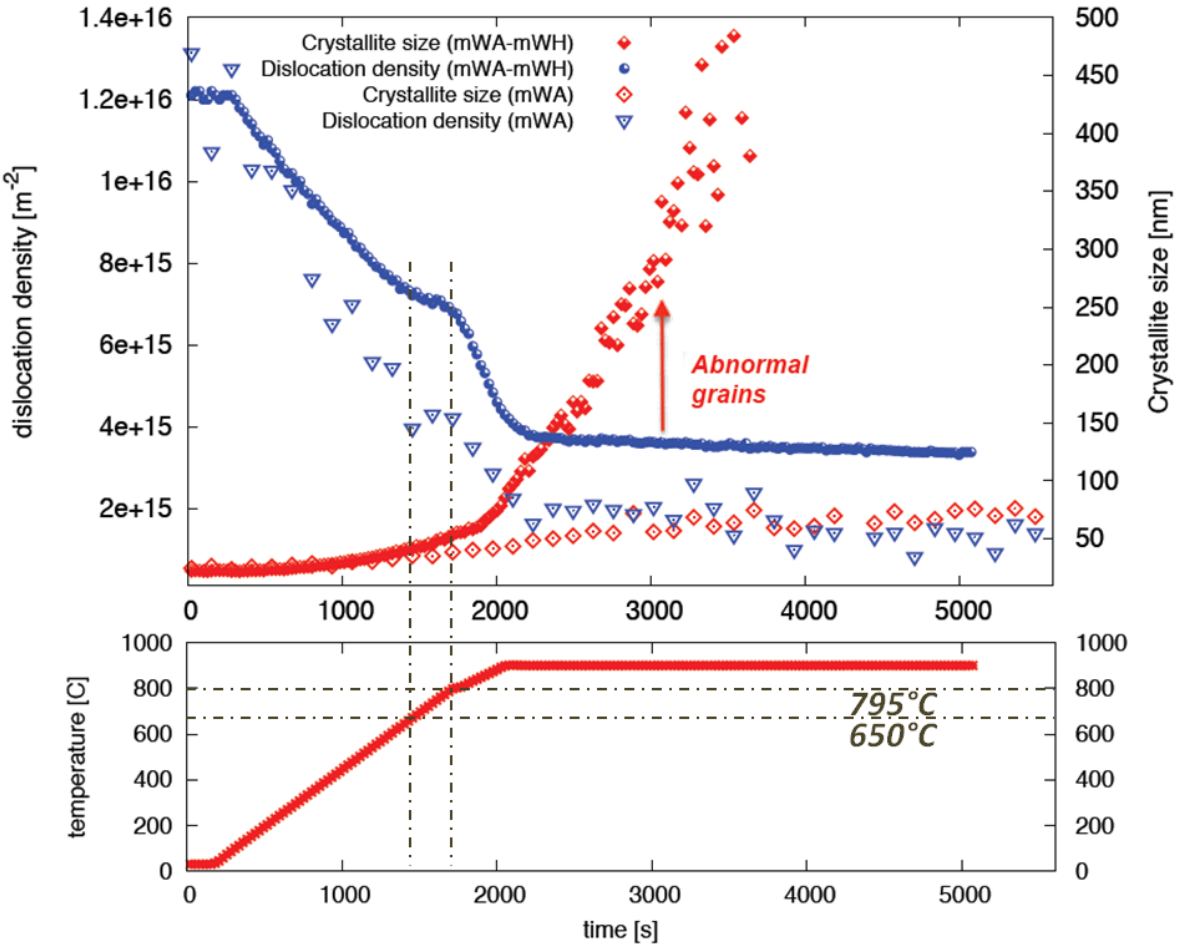

Figure III.24: Dislocation density and crystallite size determined with the coupled mWA-mWH method and the mWA method during heating up to 900°C and consecutive annealing for 1h

1100°C annealing:

1100°C is the typical consolidation temperature for ODS steels processing. Similarly to previous experiments, in the initial as-milled powder, crystallite size and dislocation density are respectively 22 nm and $1.2.10^{16}$ m^{-2}.

A dislocation density plateau is once more observed (for both large and average grains) between 650°C and 800°C, definitively validating the separation between recovery recrystallization and abnormal grain growth. On the contrary, annealing above 900°C leads to a higher drop in dislocation density within the normal grains' growth than what was observed in other cycles, (dislocation density $<8.10^{14}$ m^{-2} at 1000°C) (cf. Figure III.25).

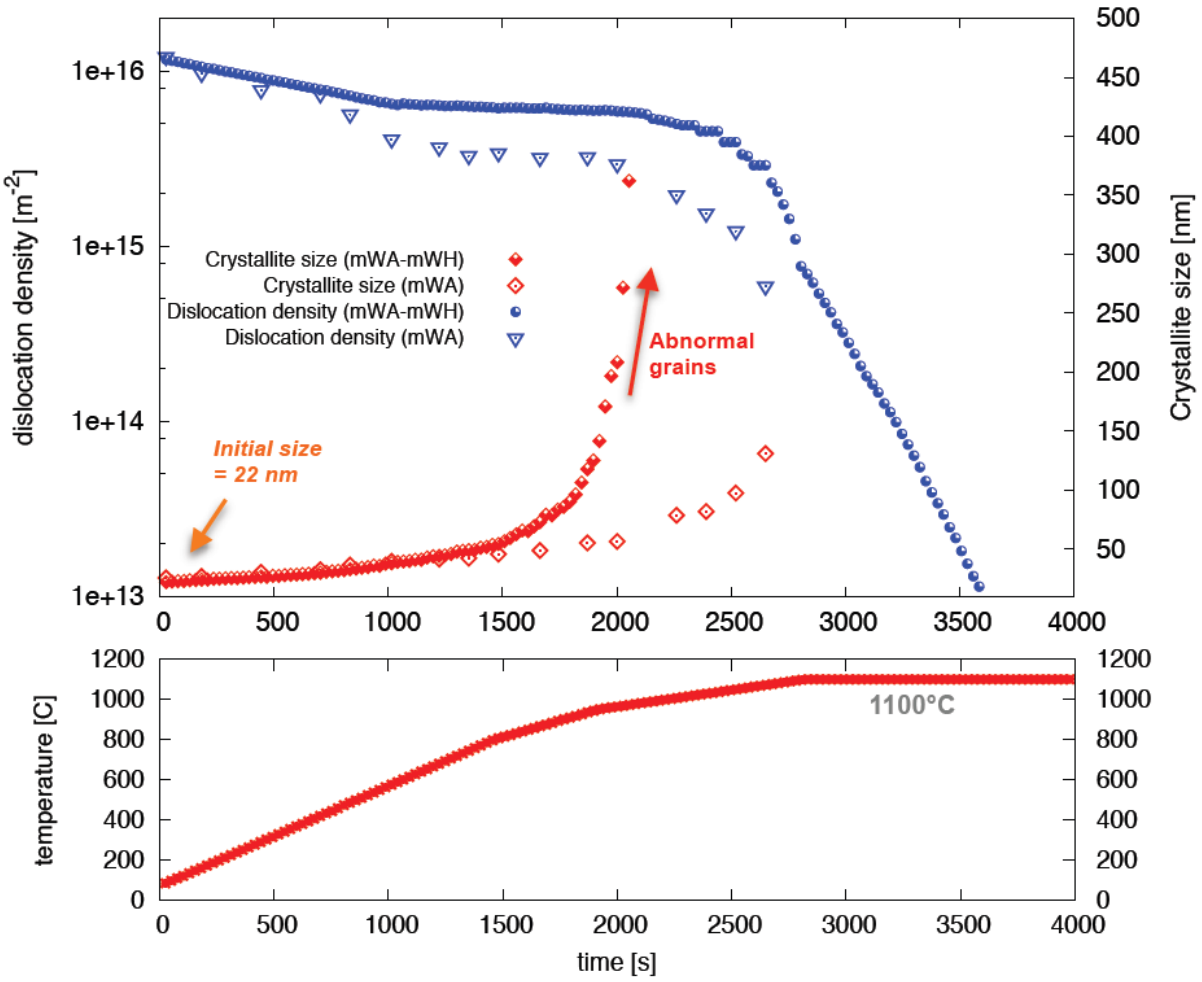

Figure III.25: Dislocation density and crystallite size determined with the coupled mWA-mWH methods and the mWA method during heating up to 850°C and consecutive annealing for 1h

After 800°C and 900°C, crystallites grow very rapidly due to both continuous recrystallization and abnormal grain growth. To be able to follow their evolution even for a high crystallite size, the 2D detected signal has been used. Indeed, as illustrated in Figure II.8, the diffraction rings are no longer homogeneous and become spotty upon heating up to 1100°C, this clearly involves the occurrence of abnormal grain growth. Abnormal grains are therefore identified as individual spots of high intensity. The selected abnormal grains start to grow around 1080 (cf. Figure III.26).

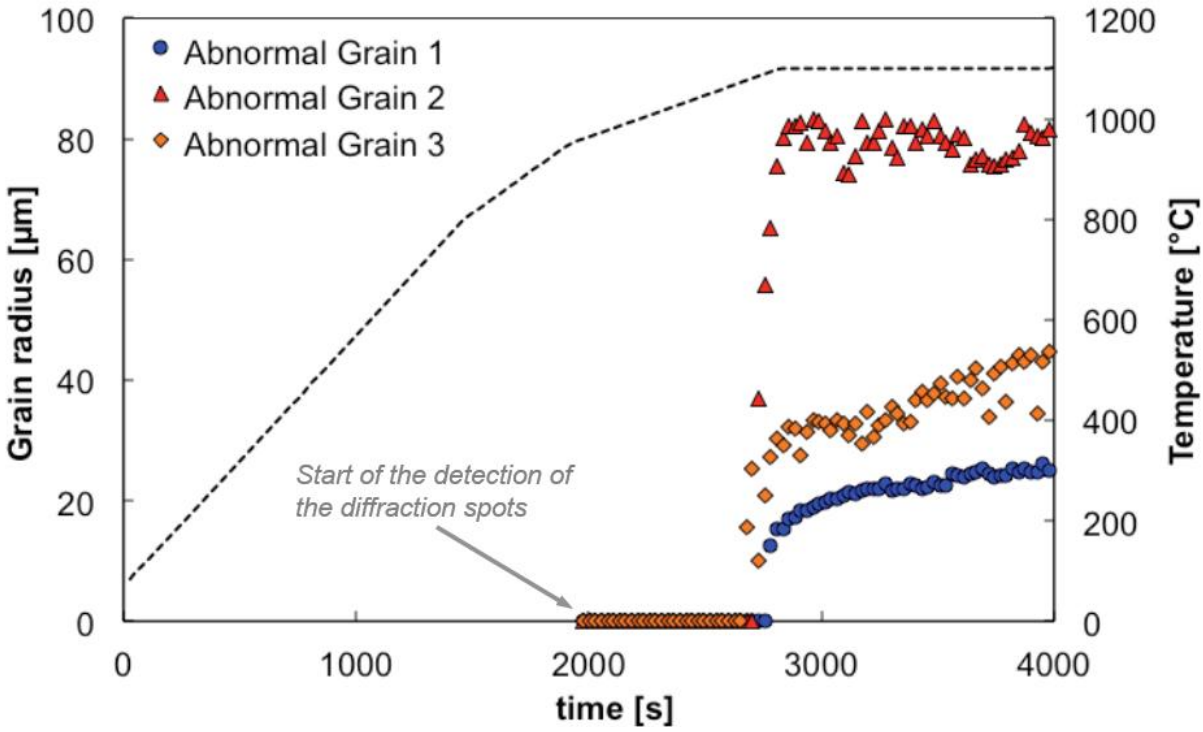

Figure III.26: Growth of three abnormally growing grains during the 1100°C annealing

The growth rate for abnormal growth is much higher than that of the ultrafine grains. Once abnormal grains start to grow, they can reach their final equilibrium size at 1100°C in less than 200s. Given that the diffraction intensity was measured under reflection diffraction conditions and not under transmission, the error of their radius is larger than the grain radius itself. Two grains having the same volume can give rise to various diffraction intensities depending upon the distance between the grain and the free surface, leading to an attenuation factor from 0 to 100%. Thus the detected intensities can be used for detecting the onset of abnormal grain growth and to observe whether they grow rapidly or not, but their volume cannot be quantified accurately.

Abnormal growth occurs so rapidly that the selected grains perform the main part of their growth even before the soaking step at maximum temperature begins.

2.2.2.2. Local microstructure evolution

Since XRD measurement is an indirect global characterization method highly sensitive to the instrumental correction it is important to have local direct measurements. This part of the microstructural evolution study will be done using ACOM-TEM.

For the ACOM-TEM study on recrystallization, it has been chosen to focus on 800°C and 850°C temperatures, which according to the *in-situ* XRD results appear as key states for recrystallization.

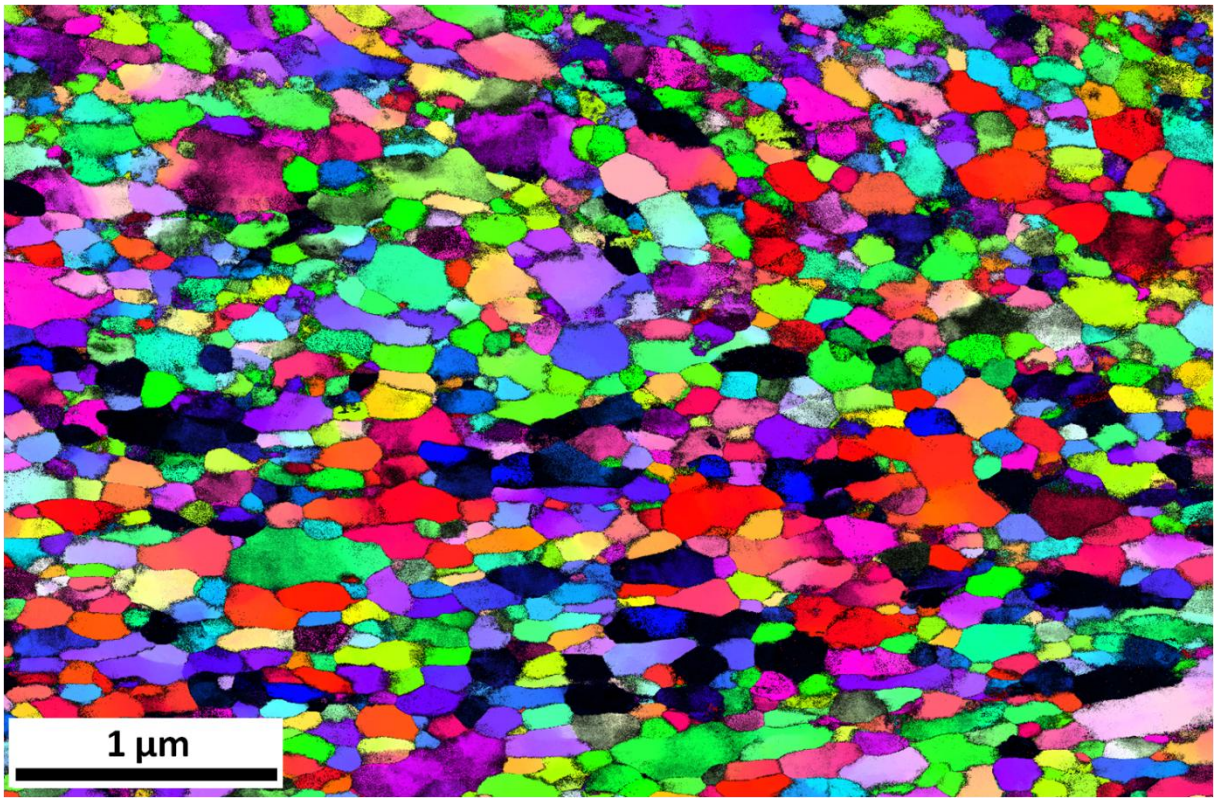

Figure III.27: Microstructure of the P9073 powder after a 5min@800°C annealing

As evidenced on Figure III.27, after a 5min@800°C, the microstructure evolves to become almost isotropic (grain aspect ratio = 2). Indeed, the microstructure is completely transformed compared to the high anisotropic microstructure observed in the as-milled and the 600°C annealed powders states.

The reduction of the shape factor and increase of the mean grain area are consistent with the migration of grain boundaries perpendicularly to the grain elongated dimension. More importantly, it is also consistent with the transformation of the crystallites into proper grains (cf. Figure III.14b) by modification of their former sub-boundaries into proper boundaries. It also strengthens the interpretation in term of the continuous recrystallization made for the interpretation of the *in-situ* XRD synchrotron results.

For longer annealing at the same temperature, grain growth occurs with a reduction grain aspect ratio (1,8). Also as can be noticed on Figure III.28, grains are polygonized. According to the ACOM map no sign of abnormal grain growth can be evidenced during the 800°C annealing and grains seem to grow homogeneously (cf. Figure III.31).

On neither of the two cartographies are the grain morphologies and size modifications accompanied by orientation changes.

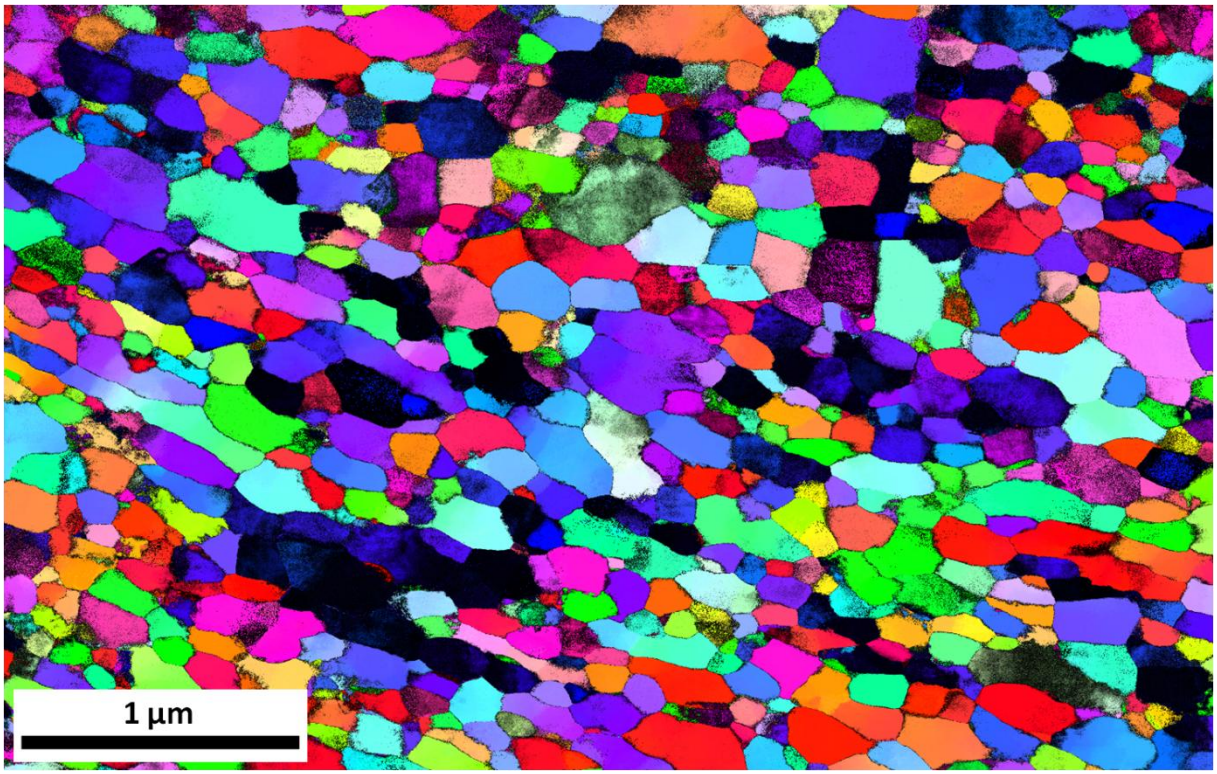

Figure III.28: Microstructure of the P9073 powder after a 20min@800°C annealing

KAM of the 5min@800°C annealed powder is 0.70° which is higher than what was measured for the 600°C annealings and also for the as-milled powder. Indeed, its fraction of low misoriented points is low (18% compared to 30 % in the 1h@600°C heat treated samples and 15 % in the as milled states) (cf. Figure III.29).

During recovery and recrystallization, misorientation usually tends to be reduced when the annealing temperature increases. When repeated on another particle also annealed at 800°C, the same KAM values have been obtained. It has also been checked that all reliability maps were comparable.

Precipitation is evidenced at this annealing temperature on ODS ferritic steels [19,20]. Furthermore, based on the detailed analysis of high resolution image of coherent precipitates, the local lattice rotation in the vicinity of coherent precipitates can range from 0.2 to 0.7° [21]. The misorientation level measured on the 800°C ACOM-TEM maps (i.e. 0.70°) is in agreement with the level of local distortion expected from a dense nanoscale precipitation. It is worth noting that ACOM-TEM cartography can be sensitive to small scale distortions since the scanning uses small step size (i.e. 2.75nm) and data was analysed with a dedicated refinement procedure. In addition to clearly observable precipitates, small particles with no identifiable crystal structures are also found in ODS steels [22]. At intermediate annealing temperature such as 800°C, precipitation may not be complete and numerous pre-precipitates are likely to be found within the material [20]. However, these features can nevertheless induce small strain fields within the matrix and contribute to the misorientation observed on the 800°C annealed ODS ferritic steel powders.

When misorientation is averaged on each grain, few grains appear to be completely free from misorientation, and can therefore be considered as recrystallized. Nevertheless it is

not a general trend and grains with important deformation can be found within each size class.

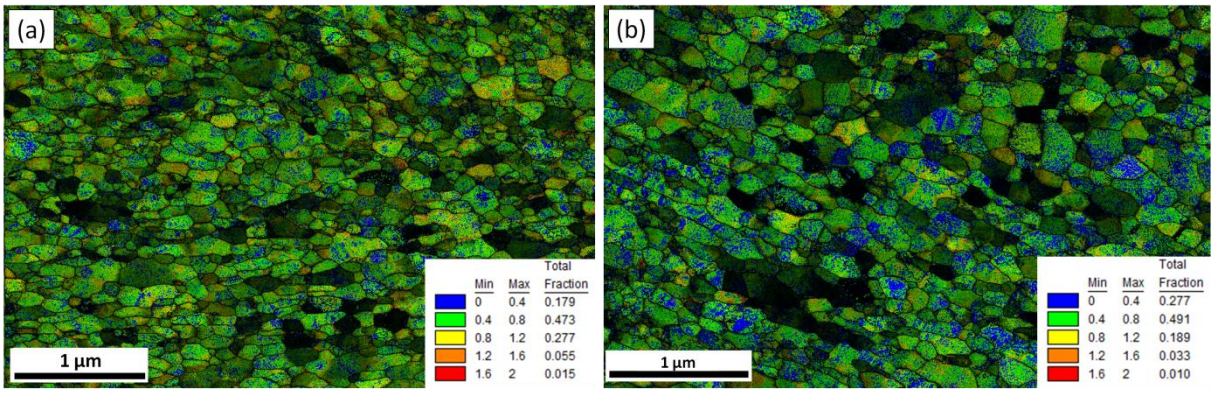

Figure III.29: KAM maps resulting respectively from (a) the 5min and (b) the 20min@800°C annealings

Contrarily to what was observed at 800°C, on ACOM-TEM orientation cartographies gathered at 850°C, abnormal grain growth can be evidenced (cf. Figure III.30). The grain aspect ratio in the rest of the microstructure is nearly unchanged (1,7).

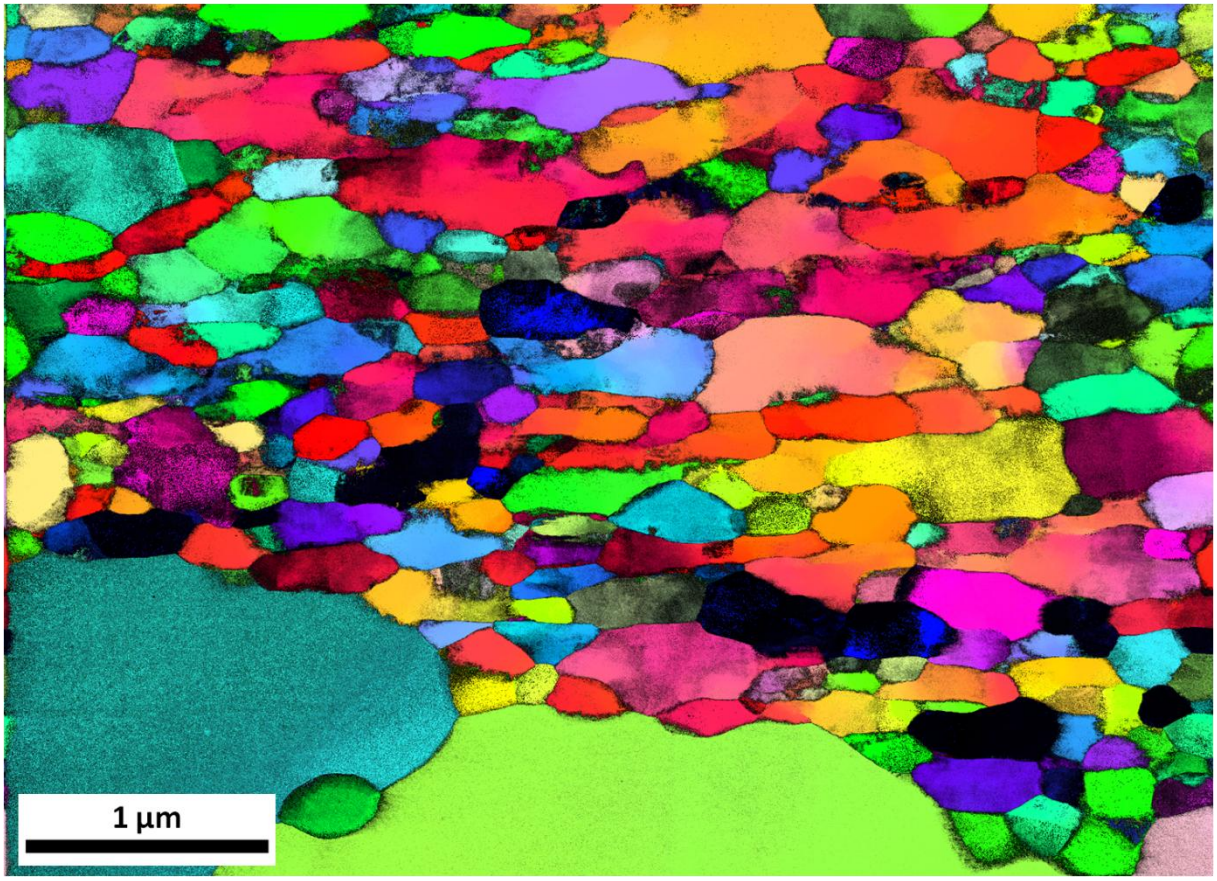

Figure III.30: ACOM-TEM orientation map of a 20min@850°C powder particle

The comparison of grain size distributions of the 800°C and 850°C ACOM-TEM cartographies (cf. Figure III.31) shows that abnormal grain growth occurs between 800°C and 850°C. Also, while during the annealing mean grain population growth is very limited at 800°C, it is important at 850°C. Indeed, apart from the biggest grains, even the size of the rest of the grain population grows at 850°C (cf. Figure III.31). This is in

agreement with what was observed during the analysis of the DRX *in-situ* experiments.

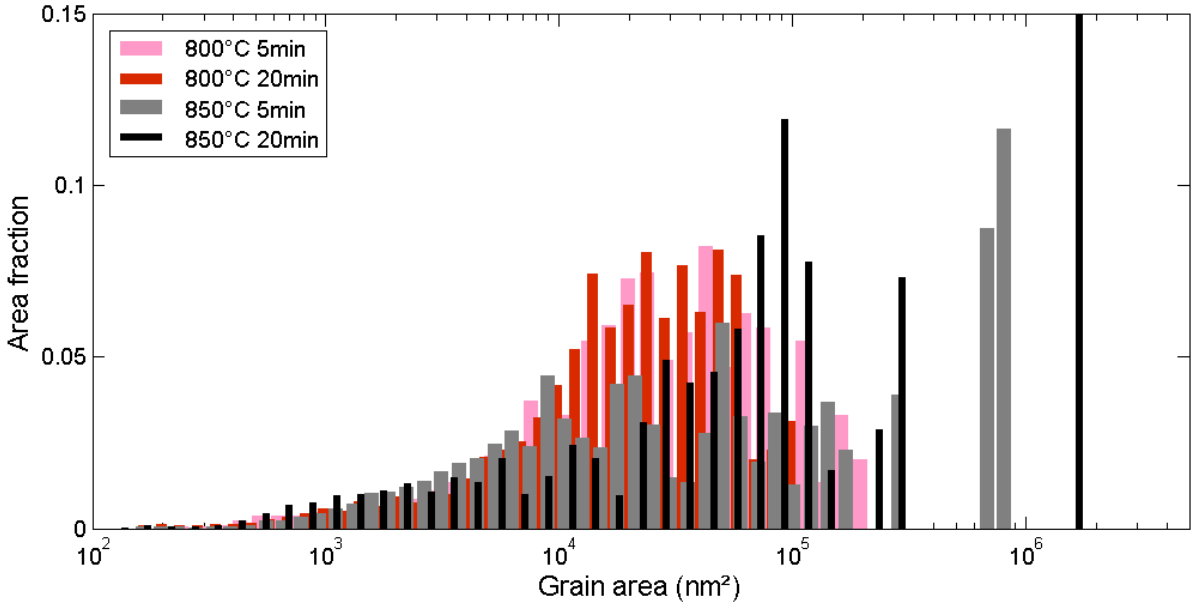

Figure III.31: Grain area distribution comparison of the ACOM-TEM 800°C and 850°C orientation maps

The present study achieves a very detailed description of the microstructure of ODS powder particles and consolidated state using a combination of XRD and ACOM-TEM techniques. Since the ACOM-TEM method is very recent it is not possible to compare our results to equivalent ones from literature. Also, the small scale of the investigation prevents from comparison with similar EBSD studies which cannot address such deformed states and for which the step size is at least five times larger.

2.2.2.3. Precipitation

SANS precipitation measurements

As-milled powder is taken as the reference signal, therefore the SANS scattering intensity on Figure III.32 indicates the occurrence of precipitation in powder annealed at 800°C for different times.

After 5min@800°C, precipitates have a radius equal to ~9.5 Å, precipitates' radii grow to around 10 Å after 20min. Then for longer soaking time the precipitation remains stable. Calculated on the assumption of a precipitation population constituted by Y_2TiO_5 and $Y_2Ti_2O_7$ the volume fractions (~1%) do not vary with increasing annealing time (cf. Table III.2). The signal is therefore very stable during the annealing at 800°C, showing a temperature dependency but no soaking time dependency.

At 1100°C, precipitates have a radius equal to 13.6 Å and a volume fraction of 0.6%. Compared to 600°C and 800°C the precipitate radii has slightly increased while the volume fraction has significantly decreased (cf. Table III.2).

This can be due to the fact that the precipitation evidenced at 800°C has evolved into a bimodal distribution as described in [23,24]. Another possibility is that the shape of the precipitates changed from spherical to cubic with increasing size as evidenced in [25]. The two proposed phenomena could explain the underestimated volume fraction.

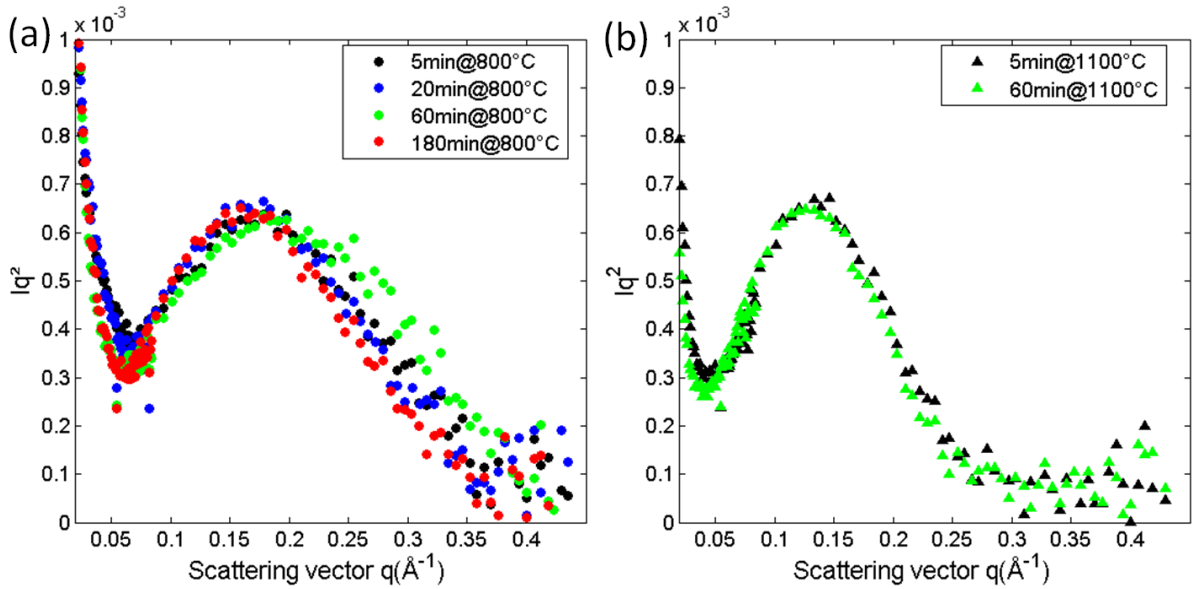

Figure III.32: SANS results obtained on the P9073 powder (a) after 800°C annealings (b) after 1100°C annealings

		5 min	20 min	60 min	180 min
800°C	R_g (Å)	9.62	10.06	10.08	10.05
	f_v (%)	1.07	1.01	1.11	1.06
1100°C	R_g (Å)	13.6	-	13.9	
	f_v (%)	0.64	-	0.51	-

Table III.2: Mean parameters of the precipitate distributions of the 800°C and 1100°C annealed powders.

2.3. Pinning effect

The stability of the microstructure at 600°C which can be attributed to a retarding recrystallization compared to unreinforced ferritic steels, is often accounted for by the pinning effect of the precipitates. The driving forces for recrystallization have been presented in I§2.3.2. In this section, we will estimate the forces exerted on the microstructure considering different microstructural features. In the case of a classical Zener pinning:

Soaking time at 600°C	5min	20min	60min	720min
Zener Pinning (MPa)	10.3	9	9.3	9.5
Boundary pressure (MPa)	16.4	16.7	18.3	16
Driving Force (MPa)	5.5	5.3	4.7	4.3
Net pressure on boundary (MPa)	11.6	12.9	13.8	10.8

Table III.3: Net pressure on boundaries after 600°C annealings

According to Table III.3, the net pressures on boundaries after annealings at 600°C are very high. Nevertheless, no grain growth is observed at this temperature. Therefore, a significant effect acting on grain growth seems to be missing with the classical Zener pinning. The number of possible effects is really high since the Zener pinning involves numerous hypotheses. Given the nanoscale features of the microstructure at 600°C observed during the material characterization and also known from the literature review, the first effect tested to account for the underestimated pinning by classical Zener pinning is the enhanced pinning on special locations such as triple or quadruple junctions [26].

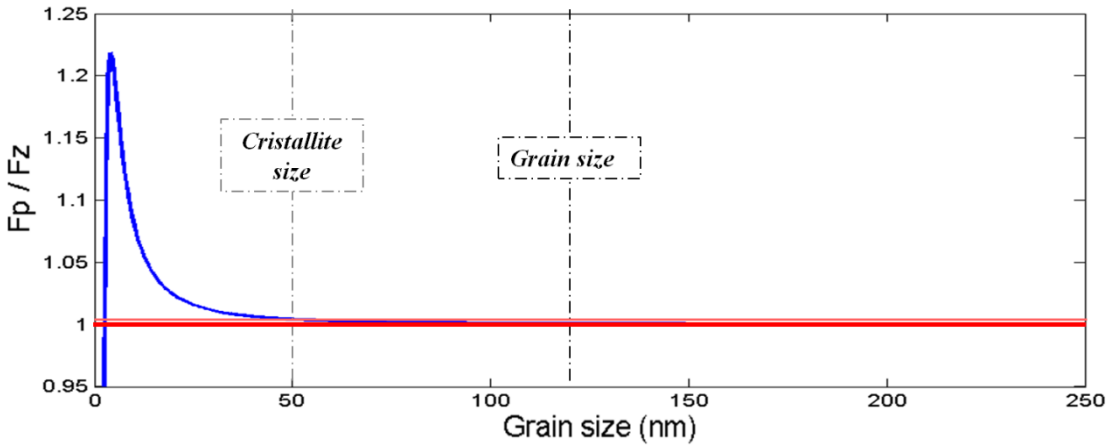

Figure III.33: Special location effect on pinning force. The pinning force considering special location (Fp) over the classical Zener pinning force (Fz) is presented as a function of the grain size. Precipitate volume fraction and mean radius are taken respectively to 1% and 1nm

As observed on Figure III.33, considering the mean grain size (i.e. 120nm), special location precipitation does not influence the pinning effect. Even by taking into account the crystallites, which are ~50nm in size, there is no significant domain size effect. Indeed, precipitate density is so high that the grain size should have been lower than 40 nm for special boundary location to have a significant effect on the pinning efficiency.

The possibility of a cubic precipitation was explored and did not allow to explain the microstructural stability (cf. Table III.4).

Soaking time at 600°C	5min	20min	60min	300min
Pinning force of cubic precipitate (MPa)	12.4	11.0	11.2	10.2
Net pressure on boundary (MPa)	11.4	11.2	9.7	8.1

Table III.4: Net pressure on boundaries after 600°C annealings considering cubic precipitates and special locations

Then, it can be concluded that precipitation is not responsible for the microstructure stability at 600°C.

One of the particular feature that has been identified being the microstructural anisotropy, the grain aspect ratio can explain the retardation of the recrystallization. Classically, the pressure of grain size on boundaries is:

$$P_C = \gamma\left(\frac{1}{\vartheta_1} + \frac{1}{\vartheta_2}\right)$$

With ϑ_1 and ϑ_2 being the principal radii of curvature. Frequent approximations include the spherical character of the grains ($\vartheta_1 = \vartheta_2 = \vartheta$) and grain radius is proportional to ϑ (then $R = C\vartheta$). Which gives, when C is taken as equal to 1:

$$P_C = \frac{2\gamma}{R} \quad \text{(III.1)}$$

To account for the grain anisotropy, several works are based on the following general relation [27–29]:

$$P_C = \frac{\gamma m_V}{S_V}$$

Where, m_V is the grain surface curvature $m_V = \int_{S_V} \frac{1}{2}\left(\frac{1}{\vartheta_1} + \frac{1}{\vartheta_2}\right) dS_V$ and S_V is the surface area per unit volume. In the case of an ellipsoid shape, this equation is extremely complicated to resolve.

Other studies, based on the triple junction geometry, also conclude to a significant retarding effect of the grain morphology on the grain growth rate especially in nanosized grain materials [30,31].

Using the simple assumption that the overall curvature is maximised in the case of a perfectly spherical boundary and minimized in the case of a planar boundary, in this study, it has been chosen to linearly take into account the grain aspect ratio coefficient K_{gar} and to insert it in equation (III.1) as:

$$P_C = \frac{2\gamma}{RK_{gar}} \quad \text{(III.2)}$$

Figure III.34 compares the net pressure at 600 and 800°C with or without taking into account the anisotropy. At 600°C the net pressure is negative considering the anisotropy while it is positive otherwise. The microstructure is therefore stable at 600°C as expected by characterization observations. At 800°C, however, pressure remains positive in both cases which means that growth is allowed. Even if the coefficient and the formula used are debatable, the important points here are that due to the anisotropy effect, the pressure at 800°C is higher than the one calculated at 600°C (of course mobility would need to be more carefully studied too) and that explains both for the slight growth at 800°C and for the stability at 600°C.

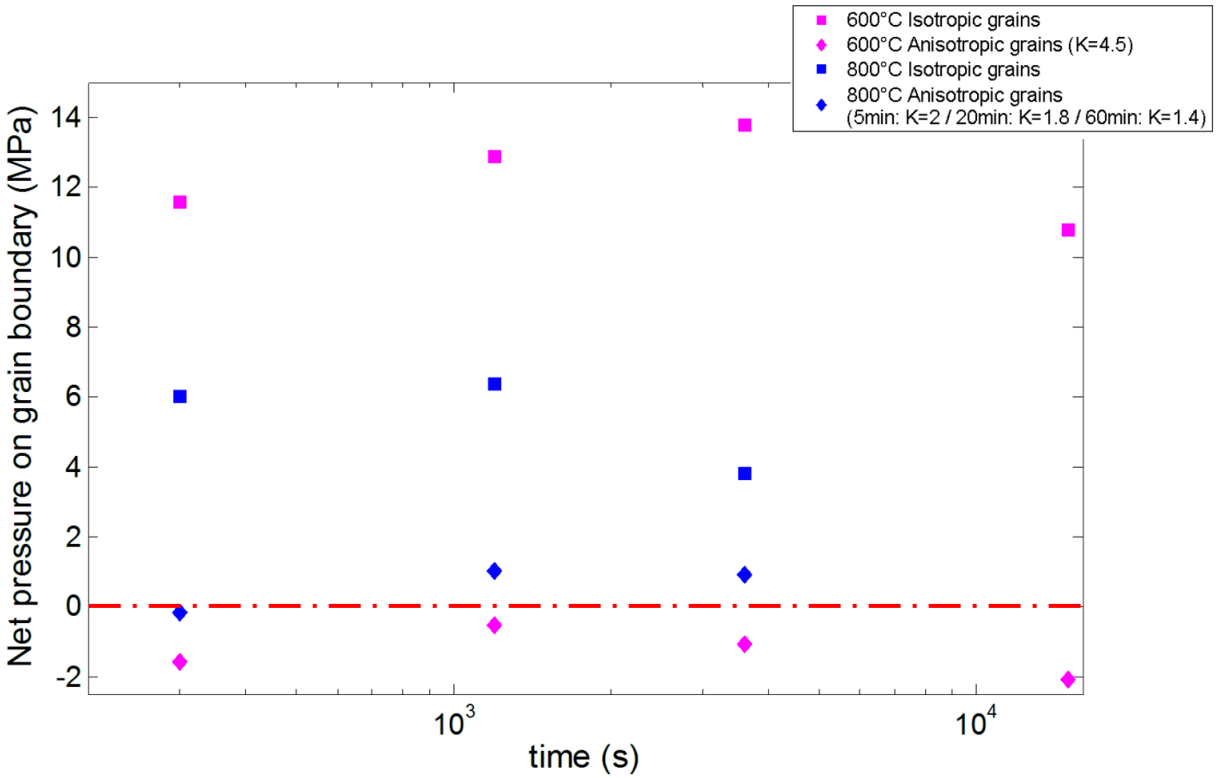

Figure III.34: Effect of the consideration of anisotropic grains on net pressure on grain boundary

Resistance towards recrystallization can therefore be interpreted as being controlled by the morphological anisotropy of the grains while the nanoscaled precipitation becomes a predominant effect for grain growth and abnormal grain growth.

2.4. Microstructure evolution mechanism

Given these results, we can propose a description of the successive mechanisms involved in the microstructure evolution.

2.4.1. Stage I: mechanisms operating at low temperature

The nanocrystalline powder was processed by high-energy mechanical alloying, producing a huge amount of dislocations and highly anisotropic grains. Due to the high stalking fault energy of ferritic steels, these dislocations form cell structures with typical size (determined as the initial crystallize size) of 20-30nm within the highly deformed microstructure. At low temperature, we have identified different recovery mechanisms. Up to 600°C monotonous decrease in dislocation density and monotonous increase of the crystallite size was observed. This is characteristic of recovery when dislocations within cells rearrange and annihilate each other to form thinner cell walls. Therefore, initial growth stage is due to dislocation annihilation within the milled powder. The crystallite growth rate then significantly decreases during the soaking time at 600°C (from $4.0.10^{-3}$ $nm.s^{-1}$ to $4.0.10^{-4}$ $nm.s^{-1}$, cf. Figure III.12) while average grain size remains constant (cf. Figure III.14). Growth of crystallites might be caused by subgrain mobility that either disappears or whose wall areas slightly decrease. Subgrains with a diameter D evolve as:

$$D^n - D_0^n = c \times t \quad \text{(III.3)}$$

where t is the time at 600°C, n and c are constants and D_0 the diameter before subgrain growth occurred (here D_0 33 nm).

A least square method was applied to calculate the best fit exponent n=4.9. Scattered values of n were reported in the literature ($n = 2$ in high purity iron [32]). The value found in our study is rather high indicating a very slow subgrain growth. This suggests that recovery of the nanostructure at low temperature involves only homogeneous recovery with no significant effect on grain growth. The solute drag and eventual yttria clusters coming from mechanical alloying may be the cause of such a slow rate. This reinforces the interpretation that SANS signal in 600°C states is due to the presence of yttria precipitate clusters (cf. Figure III.16).

Recovery is expected to homogeneously reduce the amount of stored energy within the deformed nanostructure. However, recovery at 600°C involves a limited decrease in dislocation density, reaching $4.5.10^{15}$ m^{-2} after 4 hours. The amount of stored energy is therefore still significant and the driving pressure for recrystallization still very high even after long annealing treatment at low temperature. Since the overall solute content within the matrix is far from negligible (17at%), the solute atoms may act as obstacles and largely impede dislocation mobility [33]. It has been shown that at this temperature crystallite slightly increases while the mean grain size slightly decreases. This is a result of the evolution into several grains of the longest grains having a high aspect ratio (>20) and high internal misorientation.

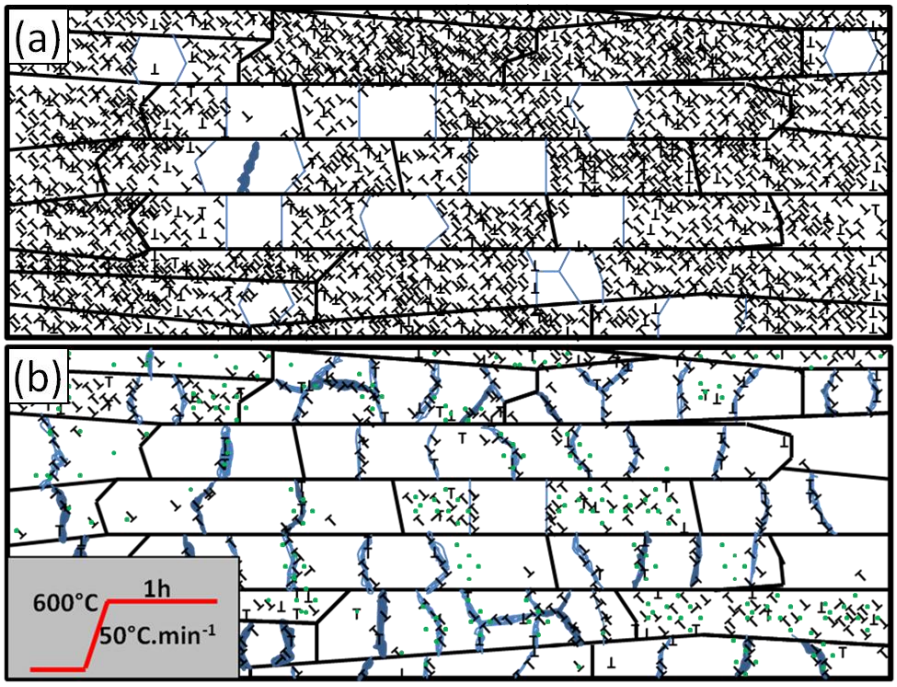

Figure III.35: Schematic diagram of the ODS ferritic steel powder at different stages, high angle boundaries are displayed in black, low angle boundaries in blue, dislocations are displayed by T, green dots are precipitate clusters (a) as-milled powder microstructure (b) Schematic diagram of a 1 h at 600°C annealed sample.

2.4.2. Stage II: mechanisms operating at medium temperatures (600°C-900°C)

When comparing the crystallite size during the soaking time, two distinct evolutions can be observed (cf. Figure III.36a). At low annealing temperature the largest crystallite size reaches almost a plateau (600°C) or increases very slowly (800°C) while at higher temperatures (i.e.: 850 and 900°C) the larger crystallites grow very rapidly. Comparison between this behaviour and the evolution of the dislocation density allows to go further.

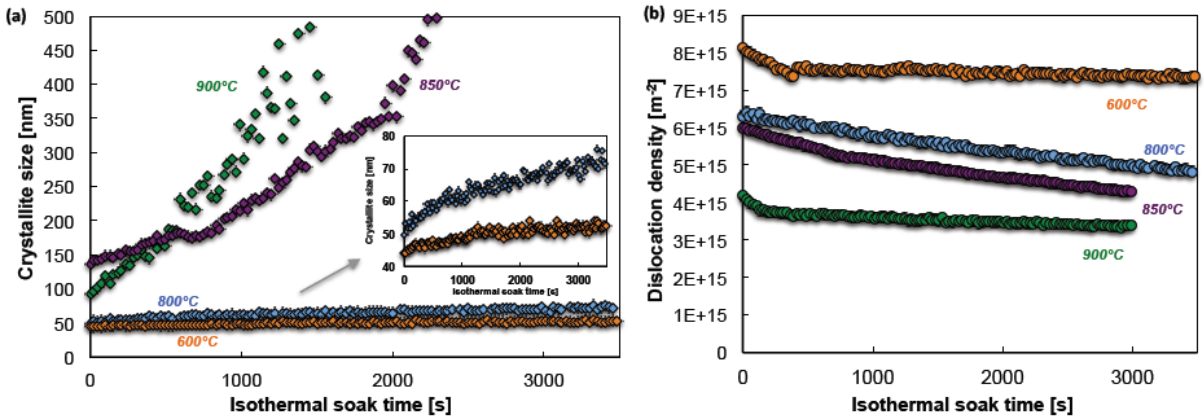

Figure III.36: Comparison of the microstructural evolution during soaking time at different temperatures (a) crystallite size (b) dislocation density.

Indeed, Figure III.36b shows that at 600°C dislocation density is stable while at 800°C, 850°C and 900°C it decreases steadily. The relatively high values (~10^{15} m^{-2}) obtained with the mWA analysis at these temperatures indicates that the UFGs are stable at high temperature.

During high temperature annealing, in the range of 800°C to 1100°C the microstructural evolution is no longer limited to recovery. Nevertheless, a very clear transition is observed between recovery and recrystallization and abnormal grain growth.

First, dislocation density reaches a plateau, from about 650°C to 800°C, while the crystallite size monotonously increases. In this range, ACOM-TEM evidenced a transition from subgrain boundaries of an anisotropic microstructure into grain boundary of an isotropic microstructure. Furthermore, around 750°C, the ultra-fine grains size sharply increase.

Those abrupt evolutions are evidence that recrystallization occurs during this dislocation density plateau. It can be noticed that the higher the temperature, the shorter the dislocation plateau. This can be seen as the integrated energy necessary for the microstructure to transform and to recrystallize. It is the retarding effect of anisotropy on grain boundary mobility.

Therefore, the ongoing phenomenon is very likely to be continuous recrystallization rather than primary recrystallization formation of germs. A further argument supporting this interpretation was put forward by ACOM-TEM maps, where it has been shown that grain growth involves no orientation change within the UFGs regions.

Once the microstructure is recrystallized, the main retarding mechanism for grain growth is boundary pinning by precipitates. Indeed, this effect is very effective at 800°C since the grain growth is very limited at this temperature, except for some specific locations as detailed in §2.2. However, due to abnormal grain growth generalized heterogeneous grain growth is detected around 850°C, when nanosized grain growth stays very limited. At 900°C abnormal grain growth is detected after a shorter annealing time.

After abnormal grain growth, remaining ultra-fine grains are stable at high temperature and the dislocation density within the powder is higher than expected in annealed steels. The retained stored energy is most likely located in the ultra-fine grained zones where abnormal growth has not occurred. When reaching the typical temperature at which recrystallization is activated, recovery is limited to a dislocation density drop of less than one order of magnitude: from $1.0.10^{16}$ to $1.0.10^{15}$ m^{-2}, which is probably due to the dislocation pinning by solute atoms and precipitates. Following $P_D = \alpha\rho Gb^2$ (cf. I§2.5.2), the driving pressure for recrystallization becomes approximately 5MPa. While the Zener pinning pressure due to nanoparticles in ODS steels is close to 8 MPa. These two opposing forces are very important and this situation is very favourable to abnormal grain growth [26]. Therefore while precipitates are pinning the boundaries, the positive pressure on those grain boundaries due to both capillarity and driving pressure is very high. Indeed, boundary pinning by precipitate seems to dominate but the capillarity pressure on grain boundaries has to be taken into account. Moreover, once a grain has taken a growth advantage on its neighbours it will tend to grow very rapidly compared to them.

2.4.3. Stage III: mechanisms operating at high temperature

At high temperature, a rapid growth of grains with specific advantages (such as lower initial stored energy, higher initial grain size, lower boundary pinning force, etc.) occurs. Abnormal grain growth remains difficult to understand as the factors to enable the growth of particular grains to the expense of others can be multiple and not so easily separable. In ODS steels two parameters are more likely to influence this evolution: precipitation which generates a pinning force and stored energy (i.e. dislocation density) heterogeneity.
From a processing point of view, one major conclusion can be emphasized. Whatever the consolidation time, once the process involves a temperature higher than the abnormal growth occurrence temperature, the resulting grain microstructure becomes drastically heterogeneous. Furthermore, the abnormal grain microstructure is thermally stable even at high temperatures. On the powder annealed particles during in situ measurement, the bimodal structure is still observed after heating at 1100°C (cf. Figure III.37). This is consistent with quantitative study (EBSD, cf. [34]) on the same ODS ferritic steel consolidated by either spark plasma sintering (processing time at 1150°C 5min) or hot isostatic pressing (processing time at 1150°C 3hours). Indeed, the high density of nanoparticles dispersed in the ODS steel particles has an efficient Zener pinning on grain

boundaries, resulting in a strong thermal stability of the bimodal microstructure.
Consequently, abnormal grain microstructure might be difficult to avoid by accelerating the consolidation process kinetics (i.e. increased heating rate). However, long annealing treatments performed just below the abnormal growth temperature but above the recrystallization temperature of the materials (i.e. between 750 and 800°C) may result in a significant reduction of the available energy for secondary recrystallization and therefore limit the abnormal growth extend.

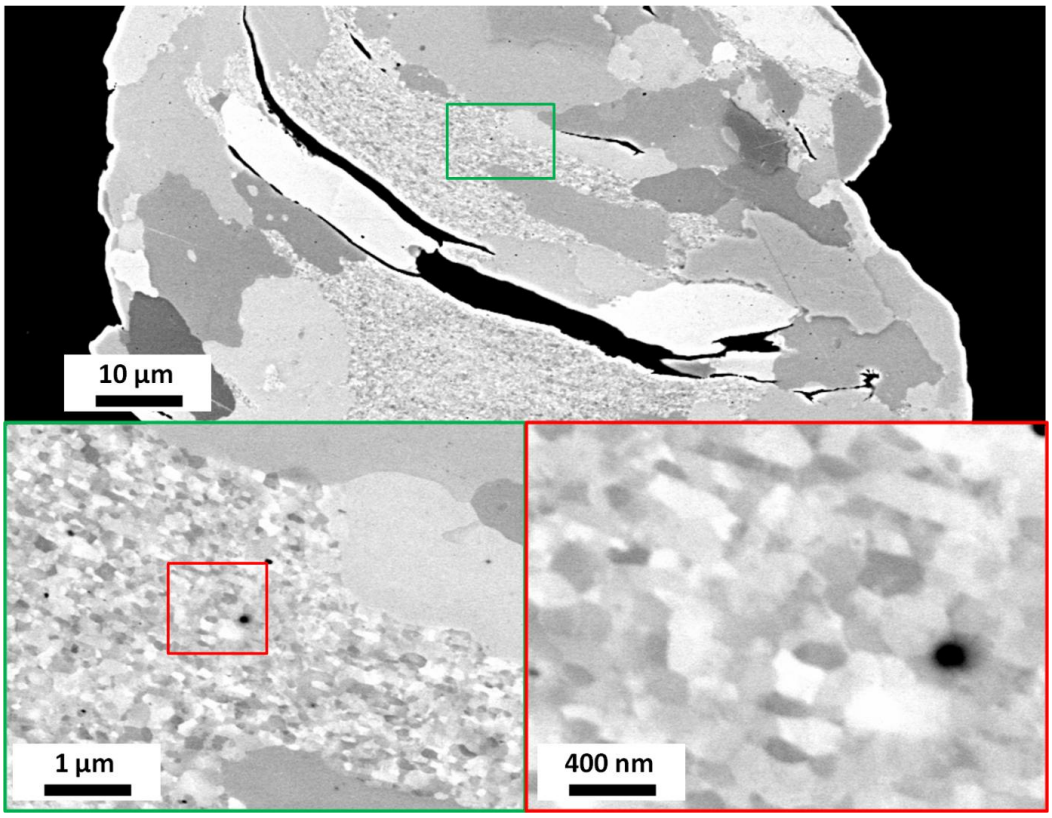

Figure III.37: P9073 1100°C annealed microstructure at various magnifications

2.4.4. Key points

- Recovery: recovery is completed between 600°C and 650°C, it involves the formation of subgrains around 50nm in size.
- Recrystallization: Recrystallization occurs between 750°C and 800°C, it is retarded by the anisotropy of the grains. Once recrystallization has occured the microstructure is isotropic and further grain growth is greatly limited by nanosized pinning precipitates.
- At earlier microstructural evolution stage those precipitates also allows to keep a significant amount of dislocation density. This creates ideal conditions for abnormal grain growth to occur. And indeed abnormal grain growth occurs between 850°C and 900°C.

3. Part II : Effect of solute content on the abnormal grain growth

In §2, the anisotropic nanostructure obtained by mechanical alloying combined with the rapid precipitation during annealing cause abnormal grain growth. The resulting heterogeneous microstructure contributes to the large mechanical anisotropy of the extruded microstructure and low transverse creep strength (cf. introductive chapter). Two main properties of abnormal growth can allow to limit its extend, the temperature at which abnormal grain growth occurs and the nanosized-to-coarse grain ratio. Indeed, from an engineering point of view, the temperature at which abnormal grains appear is a key factor for optimizing the consolidation process. Tailoring the nanosized-to-coarse-grain ratio can by an efficient way to achieve a good compromise between mechanical strength and uniform tensile elongation [35,36].

Precipitation has been identified as a key parameter to control recrystallization and abnormal grain growth. Therefore, to influence the nanosized-to-coarse grain ratio and the abnormal grain growth temperature, a pre-alloyed ferritic powder Fe-14Cr-1W was mechanically alloyed with an increasing content of yttrium and titanium. The recovery, crystallite growth and the occurrence of heterogeneous recrystallization are then studied by *in-situ* anisothermal treatments up to the consolidation temperature (1100°C). In addition, special attention is given to separate the respective influence of grain anisotropy and pinning by precipitate on control of grain growth. On the basis of Zener pinning pressure theory, these results are used to derive rules describing the influence of the precipitation on the microstructure of a ferritic ODS steel.

3.1. Microstructural evolution

Base powders are milled with respectively 0, 0.05, 0.3 and 1 wt% of yttrium and titanium. The microstructure's evolution is studied by XRD performed at the synchrotron using the *in-situ* heating furnace (cf. chapter II §4.1.4), with identical anisothermal treatment from room temperature up to 1100°C on each powder[4].

After annealing, the powder particles are characterized by SEM-FEG (cf. Figure III.38). The first remarkable feature is the important reduction of the initial powder particle size resulting from ball milling as a function of the solute content. Indeed, the fracture strain is expected to be lower with increasing solute content as a result of the solid solution hardening. Therefore, the particle size decreases with increasing solute content.

In §2.2.1, we have evidenced the titanium diffusion from the center of the powder particle to its outer surface. Since the distance to the surface is smaller on the smallest powder particles, the smaller the particles, the more titanium will diffuse. Moreover, titanium is known to refine the precipitate size [6]. Since large precipitates are less efficient to pin boundaries than an identical volume fraction of smaller precipitates, it is then expected that the smaller the powder particles the more likely the formation of coarse grains.

[4] Heat treatment were performed under high vaccum (3.10^{-5} Pa)

Surprisingly, a bimodal microstructure with both fine and coarse grains is observed on the four powders (cf. Figure III.38). The Y-Ti free powder UP49 contains a majority of coarse grains with a diameter of 10 to 50 µm (cf. Figure III.38a). Even its finest grains are quite large, with a diameter ranging from 0.5 to a few microns. The latter are visibly pinned by particles at boundaries, with a high proportion of special location sites occupied by precipitates. It is worth mentioning that these particles were found to be carbides or coarse oxides. The yttrium oxides having been identified as the main cause for abnormal grain growth [26,37] (cf. §2), the bimodal microstructure is therefore expected to disappear in the unreinforced grade.

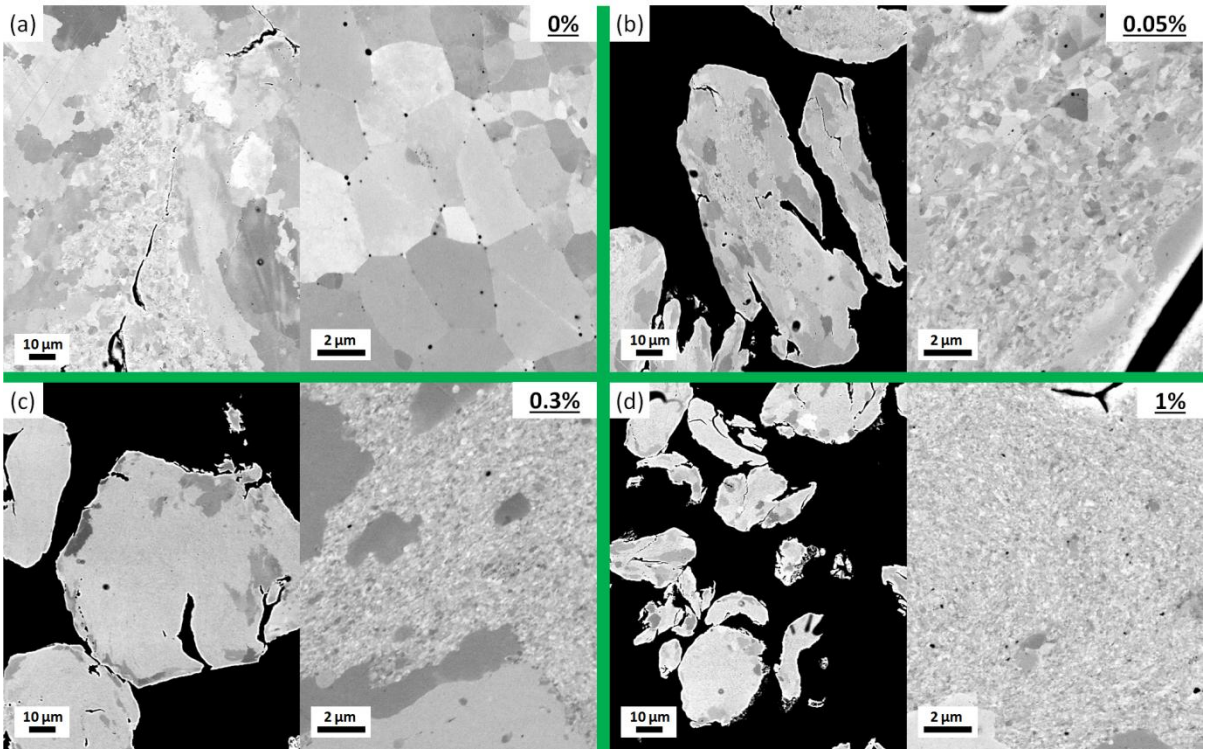

Figure III.38: SEM images of the microstructures of annealed powders: (a) UP49 (unreinforced), (b) UP26 (0.05%), (c) P29 (0.3%) and (d) UP25 (1%)

On the UP26 (0.05%) powder the surface ratio of abnormal grains over the total surface has severely dropped (cf. Figure III.38b). The finest grains are also drastically smaller than those observed in the UP49 (0%), with a mean diameter being smaller than 0.3 µm. Interestingly when the content of yttrium and titanium is further increased to 0.3wt% and 1wt% (UP29 (cf. Figure III.38c), and UP25 (cf. Figure III.38d) powders), microstructure still exhibits some coarse grains even if they are mainly concentrated on the powder particle interfaces. Ultra-fine grains possess higher surface fraction and lower mean size than those in the two powders UP49 and UP26 (0 and 0.05%), which confirms the important role of solute content on this population. Similarly, the powder UP25 (1% of Ti and Y_2O_3 content) shows a limited number of abnormal grains, mainly located on the powder particle edges.

Therefore, the fraction of ultrafine grains increases while the ultrafine grains' mean size decreases with increasing solute content. The differences between the abnormal growth

mechanisms in each powder are the size of both grain populations and the size and nature of pinning particles (at least for the unreinforced grade compared to the others). Also the extent of recrystallization and abnormal grain growth is very limited for most reinforced powders (even if it is interesting to note that whatever the solute content, the abnormal grains have the same size). The kinetic evolution of the four powders obtained from *in situ* X-Ray diffraction will be presented below.

3.1.1. Global microstructure evolution

Figure III.39 reports the evolution of the crystallite size and the dislocation density for the four grades during annealing. This characterization step allows to determine and compare the general microstructural behaviour of the different powder grades.

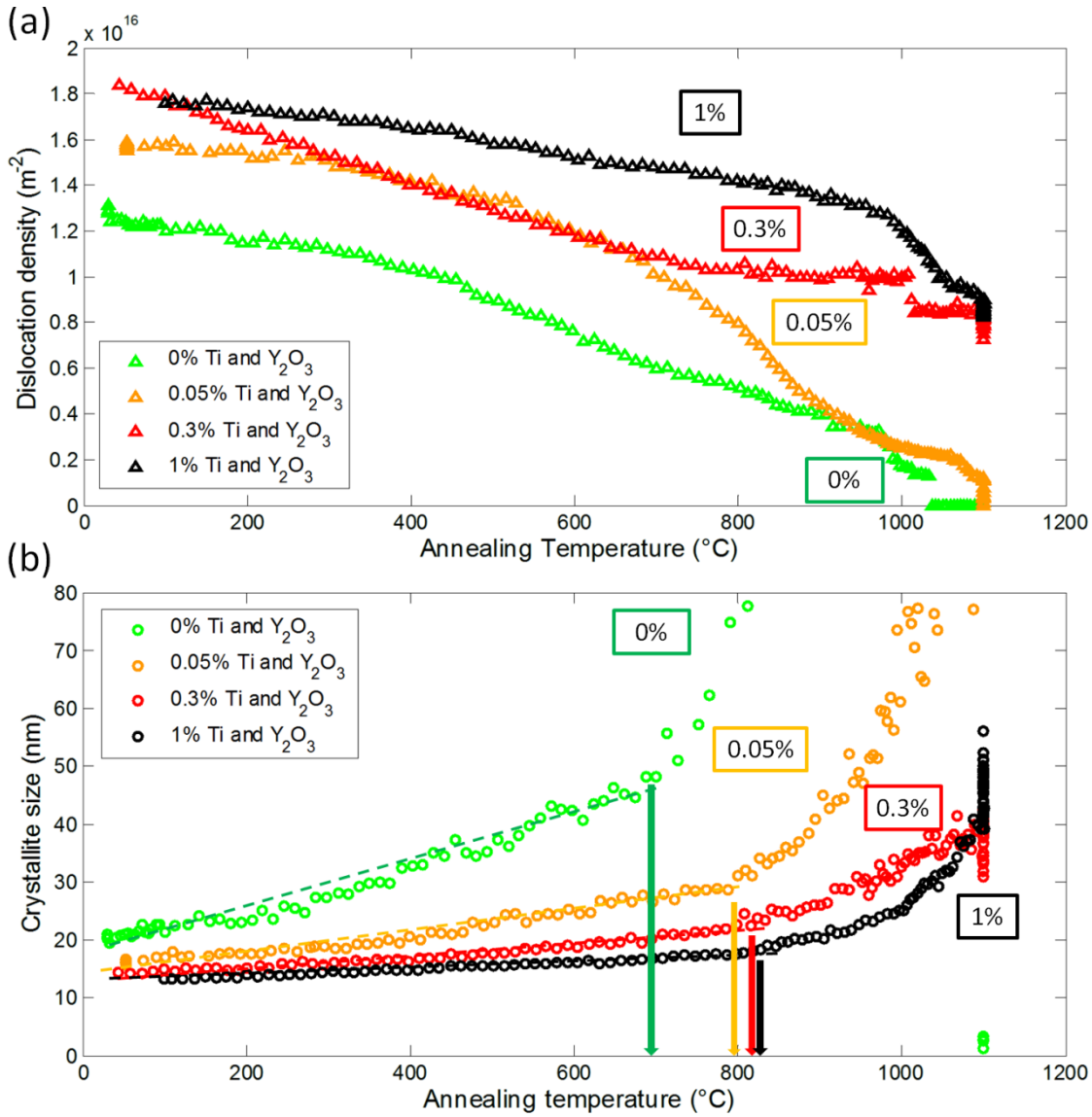

Figure III.39: Comparison of the global microstructure evolution of ODS ferritic powders with varying solute content, (a) dislocation density (b) crystallite size are determined with the coupled mWA-mWH method during heating up to 1100°C and consecutive annealing for 20min

The initial crystallite size is 20.3 nm for the unreinforced grade and 13,2 nm for the most reinforced one (1%). This decrease of the crystallite size with increasing Ti content tends

to prove that increasing the amount of oxide powder during mechanical alloying refines the nanostructure as already reported in [38]. Indeed, mechanical alloying of ODS steels involves the milling of one ductile metallic phase with a brittle oxide. During intensive milling of this kind of system, the ductile powder particles get work hardened and their grain structure is refined [38]. The alloying process intensifies the lattice distortions by adding large solute elements (Y, Ti) at substitutional positions and oxygen atoms at interstitial sites and therefore raises the amount of microstrain. This interpretation is consistent with the detection of a higher dislocation density for the most reinforced powder UP25 ($1.8.10^{16}$ m^{-2}) compared to UP49 ($1.3.10^{16}$ m^{-2}) (Figure III.39b). These values significantly differ from the ones measured on P9073 powder, this can be due to the difference between the milling conditions used during their fabrication.

During the first stage of annealing, up to 700°C, dislocation density of the four different powders linearly decreases (Figure III.39a). The crystallite size also increases linearly in the four powders (Figure III.39b). These continuous evolutions evidence the recovery of the microstructure. Figure III.39b shows that crystallite growth rate is significantly higher for UP49 (0%) than for other powders. Ranging from the unreinforced grade to the 1% reinforced powder, the crystallite growth rate is respectively 0.0251 $nm.s^{-1}$, 0.0088 $nm.s^{-1}$, 0.0051 $nm.s^{-1}$ and 0.0033 $nm.s^{-1}$.

Therefore, the higher the solute content, the lower the grain growth rate. This difference can be attributed to the impurity drag effect that is efficient at low temperature [39–41]. Indeed, the mobility of the crystallite boundaries is altered by solute segregation, which increases with the amount of yttrium and titanium in the powders. The limitation of grain growth at temperatures under 800°C is not only due to pinning effect but probably also to the microstructural anisotropy of the powders (cf. §2.4.4). Therefore, based on the detailed microstructural analysis made on §2, it can be stated that due to the anisotropy of the microstructure, whatever the solute content, recrystallization starts between 700°C and 820°C. Since a higher solute content implies a higher initial dislocation density and a lower crystallite growth rate, it is expected that the recrystallized grain size decreases with increasing solute content [3], which is observed in Figure III.39b.

From 700°C to 800°C, dislocation density in 0% and 0.05% reinforced powders rapidly decreases. This decrease is followed by a drastic increase of their crystallite size. These evolutions for both the dislocation density and the crystallite size traduce the occurrence of recrystallization (cf. §2.2.2.1). Thus, the UP49 (0%) powder crystallite size rapidly reaches 100 nm at 850°C (growth rate ~0.33$nm.s^{-1}$) whereas in the UP26 (0.05%) powder the same crystallite size is reached at 1000°C (growth rate ~0.096$nm.s^{-1}$). At this point, both have a very low dislocation density, corresponding to recrystallized materials (below 2.10^{15} m^{-2}). The crystallite size evolution in Figure III.39b shows that the growth rate increases indicating the beginning of the grain growth stage of a recrystallization mechanism occurs at very close temperatures for the three reinforced grades (~800°C). It means that the occurrence of recrystallization is not controlled by the solute content.

After 800°C however, the 0.05 and the 0.3wt% reinforced powders' microstructural features start to evolve differently. Whereas the crystallite size of both powders increases with a rate corresponding to their respective solute content (~0.096nm.s^{-1} for the 0.05% and ~0.014 nm.s^{-1} for the 0.3%), dislocation density of the 0.05% powder literally drops while the dislocation density of the 0.3% powder remains stable. For most reinforced grades (1%) it can be observed that the dislocation density decrease more slowly compared to the case of other powders. Moreover, despite the fact that the crystallite size growth rate significantly increases after 800°C (from 0.0033 nm.s^{-1} to 0.013 nm.s^{-1}) this decrease is linear from room temperature to ~1000°C.

Here, the effect of the precipitation density on grain boundary migration after recrystallization is observed. Indeed, the low solute content in the UP26 (0.05%) powder leads to a high boundary migration rate and an important drop of dislocation density which rapidly leads to abnormal grain growth. Meanwhile, the dislocation density of the 0.3% reinforced powder remains stable after the beginning of recrystallization, which means that grains are efficiently pinned. Moreover, the linear decrease of the dislocation density and its high level 1.5.10^{16} m^{-2} while the crystallite increases at 800°C, can be interpreted as a partial recovery of the UP25 (1%) microstructure before recrystallization.

To detect the occurrence of abnormal grain growth, the distinct crystallite populations obtained by the mWA and mWA-mWH methods will be used. Indeed, it will be considered that the beginning of abnormal grain growth occurs when the difference between the growth rates observed using mWA and mWA-mWH methods increases.

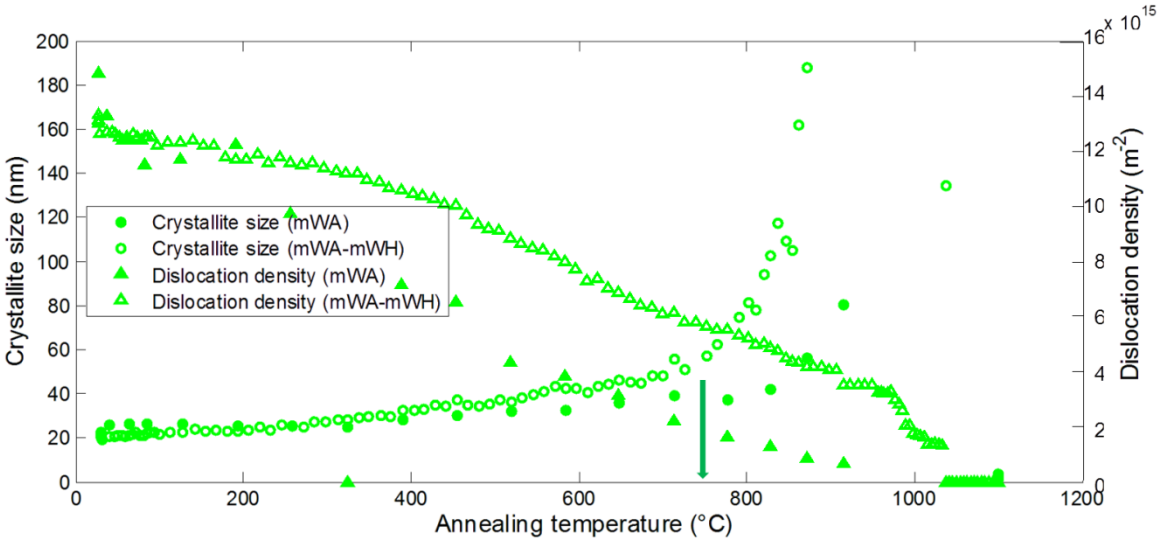

Figure III.40: Microstructure evolution of the unreinforced steel powder (UP49)

The comparison of mWA and mWA-mWH results in Figure III.40 shows the onset of abnormal grain growth occurs around 750°C. It is therefore occurring alongside with recrystallization.

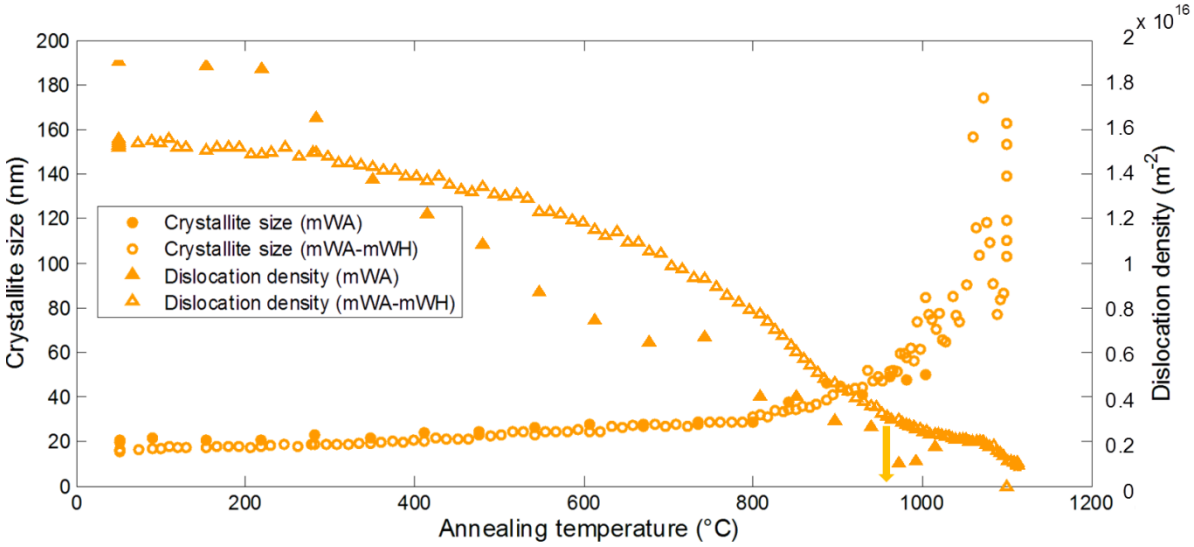

Figure III.41: Microstructure evolution of the 0.05% reinforced steel powder (UP26)

As observed on Figure III.41, the abnormal grain growth of the UP26 (0.05%) occurs around 950°C.

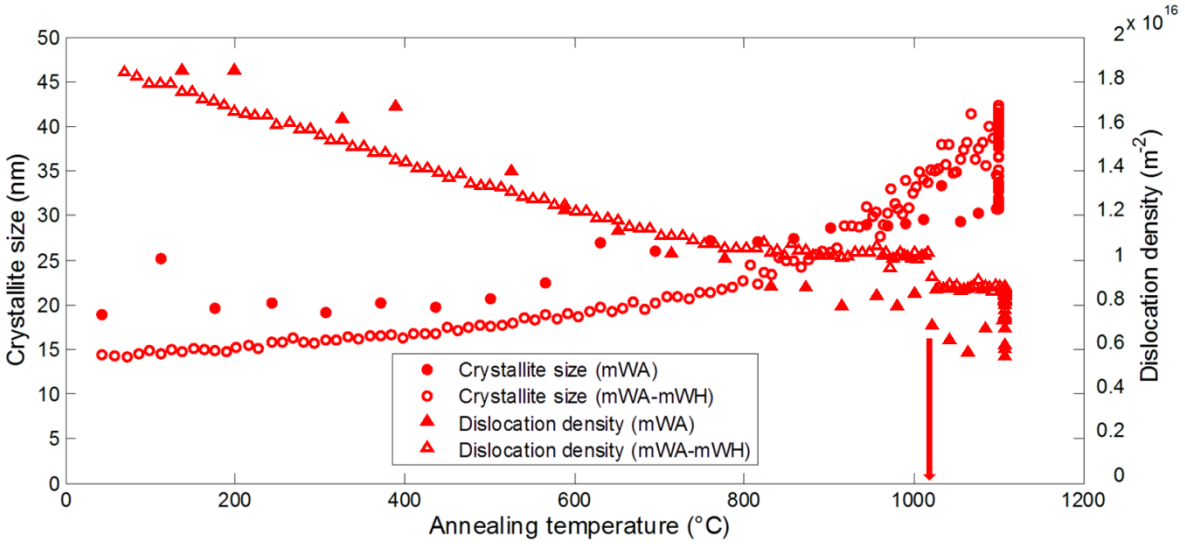

Figure III.42: Microstructure evolution of the 0.3% reinforced steel powder (UP29)

On the UP29 (0.3%, Figure III.42) and UP25 (1%, Figure III.43) powders, it can be evidenced a slight variation between the crystallite sizes growth rate of the mWA and the mWA-mWH methods slightly above 1000°C. This divergence accompanied with a limited but brutal decrease in dislocation density is here again interpreted as abnormal grain growth. Given the SEM images of the Figure III.38, the abnormal grain growth extend is indeed limited.

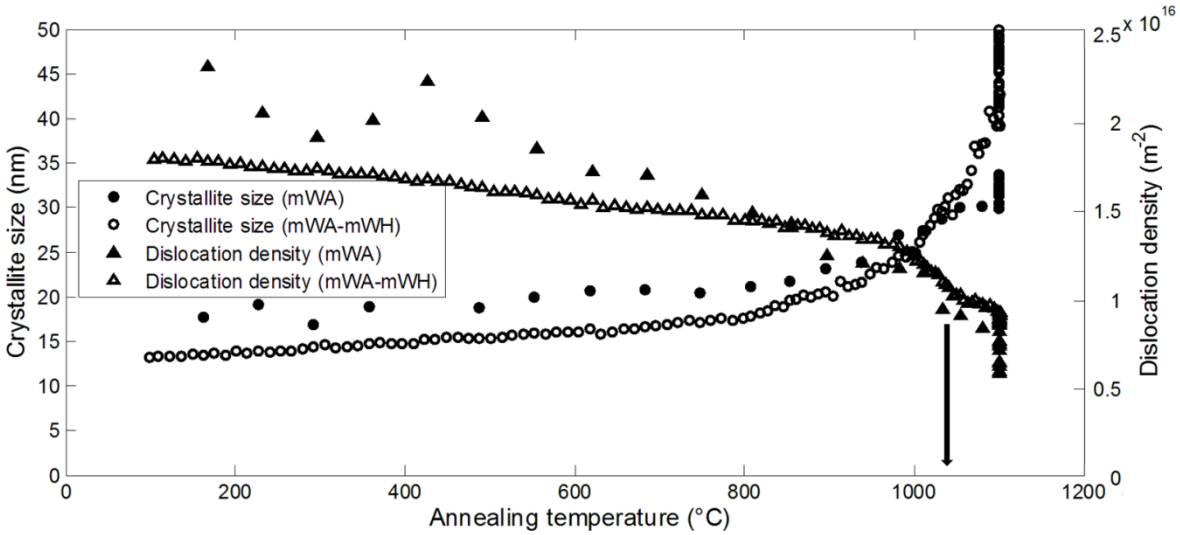

Figure III.43: Microstructure evolution of the 1% reinforced steel powder (UP25)

To conclude on these results, it can be summarized that:

- Recrystallization temperature is then stable whatever the solute content.
- The crystallite growth rate is limited by the solute content.
- Abnormal grain growth temperature increases with increasing solute content.
- Ultra fine grain to coarse grain ratio increases with increasing solute content.

	Y and Ti solute content			
	0%	0.05%	0.3%	1%
Recrystallization	~700°C	~800°C	~800°C	~800°C
Abnormal growth	~750°C	~950°C	~1000°C	~1050°C

Table III.5: Occurrence temperatures of recrystallization and abnormal grain growth for the different solute content.

Therefore, increasing the yttrium and titanium solute content is an efficient solution to limit the occurence of abnormal grains during high-temperature processing. Qualitative effects of solute content on recrystallization and abnormal growth have been studied. In order to finely quantify this effect content, *ex-situ* examination was performed on the annealed powders.

3.1.2. Local microstructure comparison

UFGs mean size are under 100 nm, especially in the most reinforced powders, and require transmission electron microscopy to be quantified. An ACOM-TEM analysis has therefore been performed on each annealed powder (cf. Figure III.44).

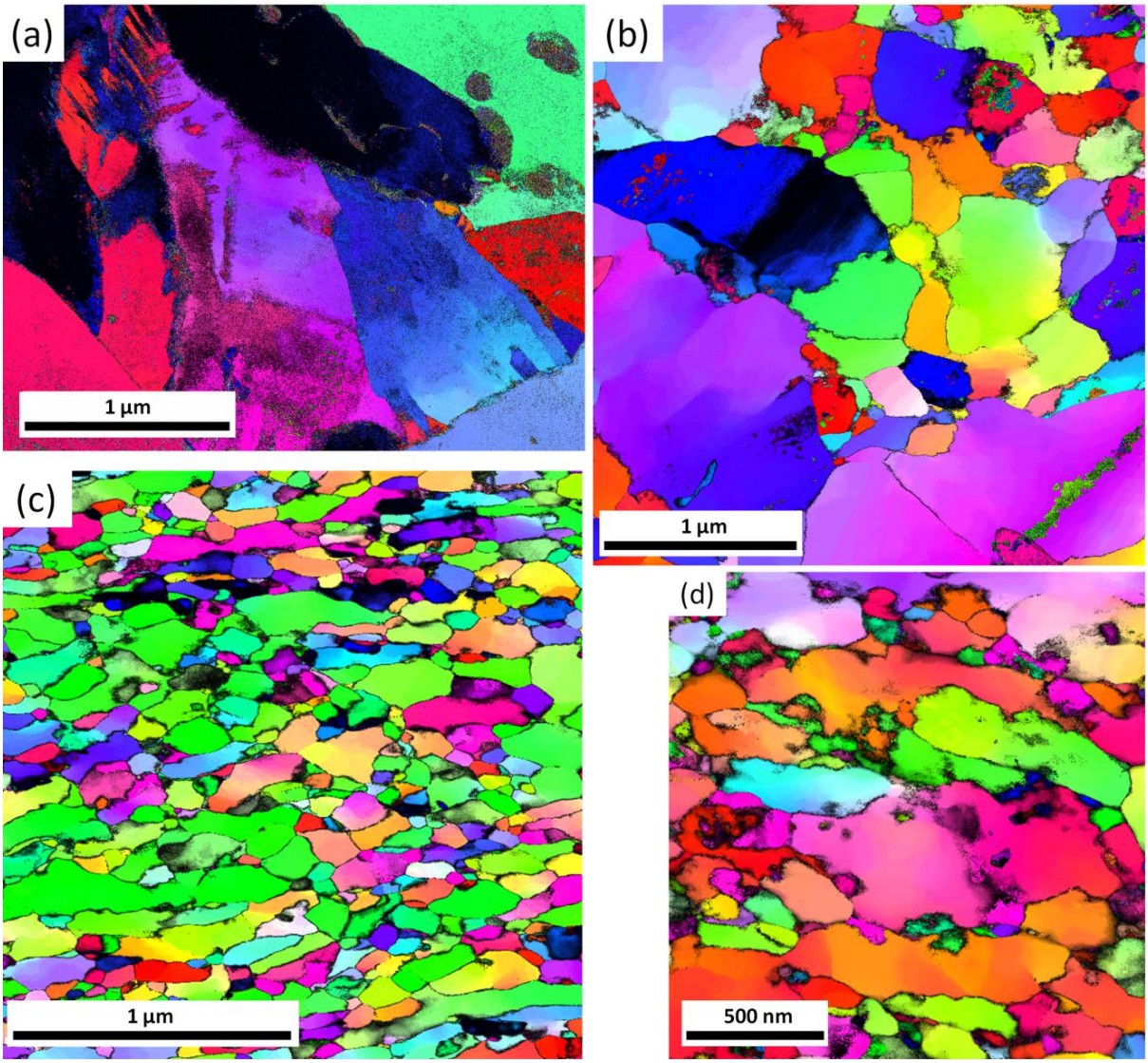

Figure III.44: ACOM-TEM orientation cartography of 1100°C annealed ODS steel powder with varying solute content, (a) unreinforced, (b) 0.05% reinforced, (c) 0.3% reinforced (d) 1% reinforced

In Figure III.44a, grains are large (~1µm) and many areas have a low reliability (black areas). This low reliability can be due to the partial austenitization of the microstructure. Indeed, some of the grains have characteristic shapes indicating austenitization (upper left corner of the figure).

Figure III.44b shows a bimodal microstructure with both ultrafine (~250nm) and coarse grains (~1µm). Also, incoherent orientation features appear in the middle of some of the grains. These features may also indicate austenitization.

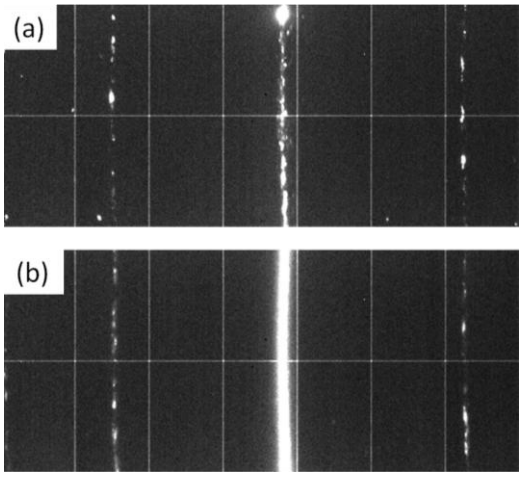

Figure III.45: 2D diffraction rings of the 28°-36° 2θ range taken at 1100°C (a) unreinforced powder (b) 0.05% reinforced powder.

After verification on the 2D diffraction rings, specific peaks corresponding to austenite appear (cf. Figure III.45). What is observed here is a consequence of the both the gamma-phase producting effect of nitrogen and alpha-phase producing effect of titanium [42].
Figure III.44c, shows the ultrafine grain microstructure of the 0.3% reinforced powder after annealing, the mean grain size is 65nm. Moreover, on Figure III.46 it can be observed that the proportion of low angle boundaries is still very high, indicating a partial recrystallization of the microstructure. Those results are in good agreement with *in-situ* XRD.

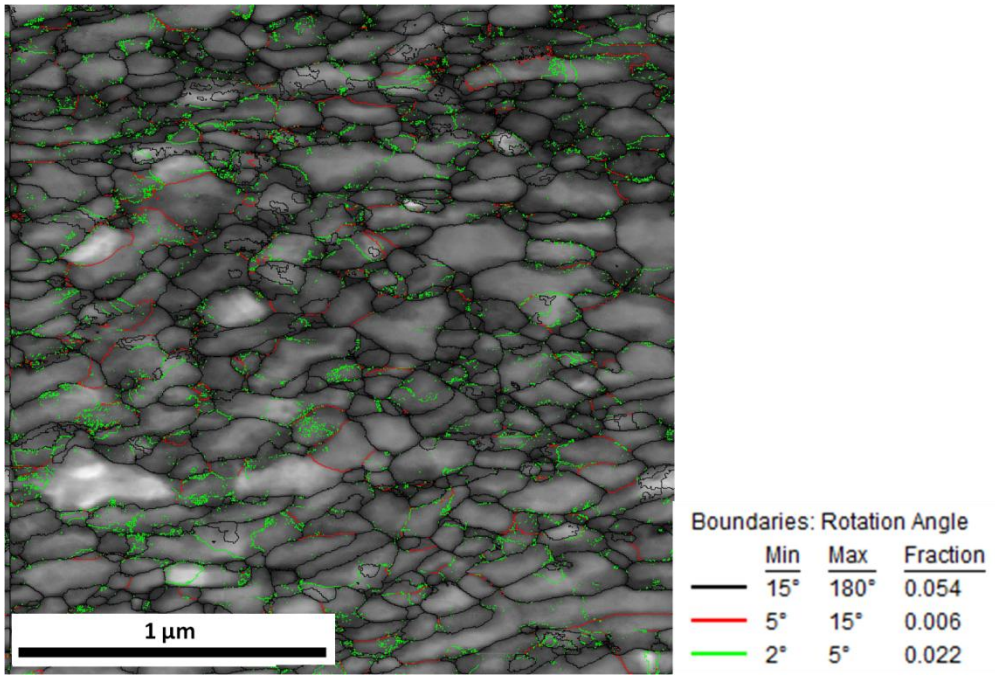

Figure III.46: Cartography of the boundary rotation angles of the 0.3% reinforced powder after annealing

Finally, Figure III.44d, shows that the microstructure of the most reinforced powder is heterogeneous with both large and ultrafine grains. Interestingly, some of the grains are still highly anisotropic (aspect ratio~4), while the misorientation within grains is very high (KAM = 0.8°). Those two features show that not only recrystallization but also the

microstructure recovery are partial in the 1% reinforced powder.

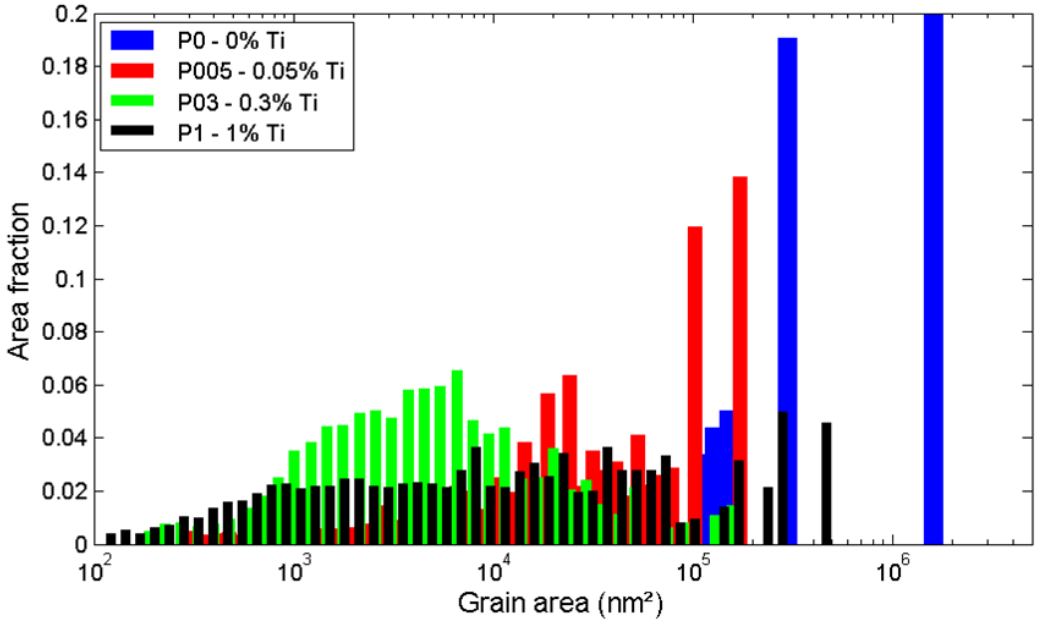

Figure III.47: Grain size distribution of the various reinforced ODS steel powders

Figure III.47 shows the grain size distribution of each annealed powders. It confirms the main observations already made:

- Increasing Y_2O_3 and Ti solute content refine the ultra fine grain size.
- Increasing Y_2O_3 and Ti solute content limits the recrystallization. Indeed, the 0.3% and especially the 1% reinforced powder contain coarse grains which are initial anisotropic grains improperly recrystallized.

3.1.3. Precipitation states in the annealed / consolidated materials

To achieve SAXS measurements the powder has been consolidated. The heating cycle performed during the *in-situ* synchrotron XRD experiment is representative of typical consolidation with hot isostatic pressing (HIP): a non-isothermal treatment from room temperature to around 1100°C with an average heating rate of 30°C.min^{-1} followed by a 20 min annealing at 1100°C and a slow cooling. Hot isostatic pressing (HIP) was carried out at 1100°C for 2 hours under 1900 bar. As illustrated by Figure III.48 powder HIPed at 1100°C and the same powder (0.3%) annealed during the *in situ* synchrotron experiment have indeed very similar microstructures.

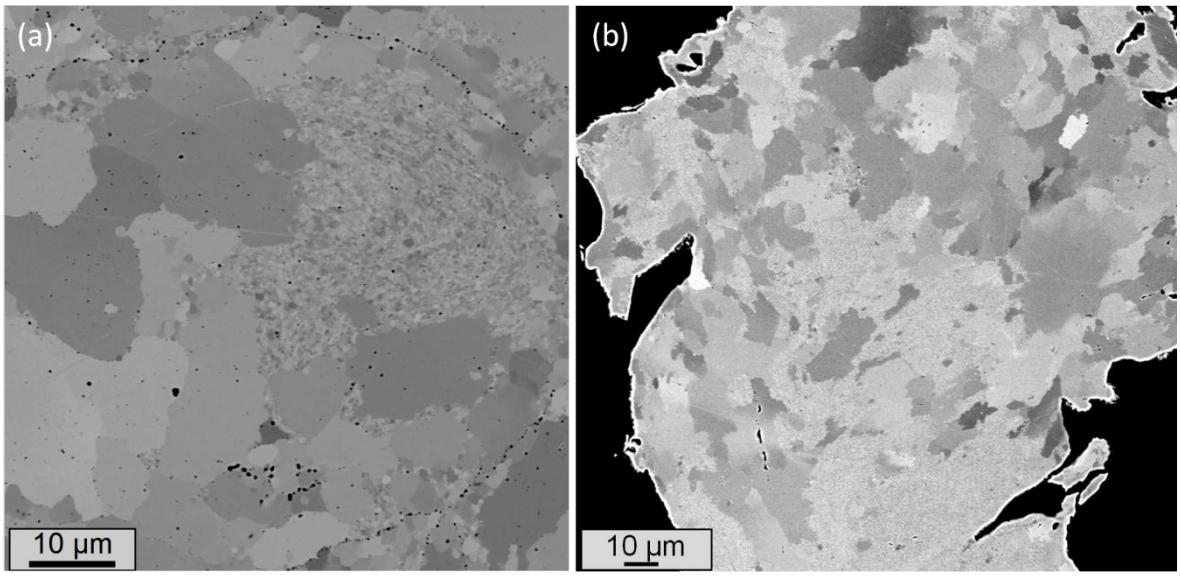

Figure III.48: SEM-FEG image (backscattered electrons) of: (a) the powder P03 processed by HIP at 1100°C and (b) the powder P03 after annealing at 1100°C at the synchrotron. Both have a bimodal microstructure

Both are showing a bimodal microstructure with coarse grains and UFGs with roughly the same fraction. Thus, the microstructure of the annealed powders and HIPed ODS steels are expected to be equivalent both in term of grain size and precipitation. In the following, SAXS study was performed on the 4 different powders processed by HIP at 1100°C.

The precipitate volume fraction and mean radius measured on the series of HIPed powder by SAXS are summarized in Table III.6.

Sample	Volume fraction	Mean radius (nm)	Zener pinning pressure (MPa)
HIP-0%	3.0×10^{-3}	3.0	0.7
HIP-0.05%	3.5×10^{-3}	1.1	2.4
HIP-0.3%	7.2×10^{-3}	1.3	4.2
HIP-1%	1.9×10^{-2}	0.9	15.6

Table III.6: Precipitation state from SAXS experiments and resulting Zener pinning pressure for each HIPed sample using equation (E1) with a grain boundary energy assumed to be $\gamma = 0.5$ J.m^{-2}.[5]

As expected, the precipitate volume fraction increases with the titanium and yttrium content, from 0.3% to 1.9% for the most highly reinforced grade (cf. Table III.6). The average radius of the few nanosized particles detected in the UP49 (0%) powder is 3 nm, whereas the average radius in the three other powders is approximately 1 nm, which is consistent with the precipitation measured on P9073 powders (cf. §2.2.2.3).

These results are also consistent with the presence of coarser oxides or carbide in UP49 while fine Y-Ti-O are expected in the three reinforced powders. The current microstructure features are optimal for a maximal (special) pinning location effect.

[5] Measured with the entire precipitate distribution, the Zener pinning pressure results were very similar to the results given in Table III.6.

Indeed, with a smaller precipitation density than what has been calculated on §2.3 for the P9073 powder, the special location boundary peak effect described by Figure III.33 will be shifted to the right. Furthermore, since the crystallite and grain sizes are smaller, their location will be shifted to the left of the graph. Therefore, the risk of abnormal grain growth is extremely high.

Given the volume fraction and mean radius of the precipitate populations, the Zener pinning pressure has been calculated on each powder (Table III.6). The Zener pressure is 0.7MPa for the unreinforced grade and increases up to 15.6MPa for the 1% Y_2O_3 and Ti solute content powder.
This is particularly interesting since the Zener pinning pressure P_z in the reinforced powders can therefore be easily tailored by the precipitation fraction at constant mean radius.

3.2. Microstructure evolution mechanism

3.2.1. Critical size of ultrafine grains

A large part of ODS steels' interest is the spectacular stability of utrafine grains under thermal treatment at high temperature [43,44]. Indeed, UFGs may be responsible for Hall-Petch hardening and are of key interest. From the SAXS experiment, the volume fraction and precipitate radius have been measured and the corresponding Zener pinning forces calculated for the series of HIPed samples. From this information, it is possible to derive the critical size resulting from the competition between the driving pressure and the retarding pressure. When the driving force due to dislocation density is neglected[6], the critical grain size is reached when Zener pinning pressure is equal to the driving pressure:

$$\sum P_i = P_C - P_Z = \gamma\left(\frac{2}{R} - \frac{3f_p}{2r_p}\right) = 0 \qquad \text{(III.4)}$$

Which allows to derive the critical size that is reached by UFG when Zener pinning pressure and driving pressure are equal:

$$R_C^{Zener} = {}^{4r_p}\!/_{3f_P} \qquad \text{(III.5)}$$

It is worth noticing that Rios modified Zener's theory, resulting in a critical grain size 8 times smaller [45]:

$$R_C^{Rios} = {}^{r_p}\!/_{6f_P} \qquad \text{(III.6)}$$

The critical size of ultrafine grains was measured using the Small-Angle X-ray Scattering (SAXS) data on the four powders consolidated by Hot Isostatic Pressing at 1100°C (cf. Table III.6). Figure III.49 shows that the calculated critical sizes are consistent with the

[6] This approximation may seem to be severe but dislocation density induced by driving forces results from the local difference of the dislocation density. Therefore, its effect is maximal considering undeformed abnormal grain growth over ultrafine grains. In the case of two competing ultrafine grains, this approximation is then acceptable.

measured UFG size for all samples. Given the experimental errors, the measured radii of the ultrafine grains are well accounted by the theory of competing pressures and are included in the interval defined by the Zener and Rios calculated values.
Indeed, the size of the ultrafine grains follows, within the investigated range of the solute content, the criterion:

$$R_{measured}^{ODS} = 0.71\ {}^{r_p}\!/_{f_p}$$

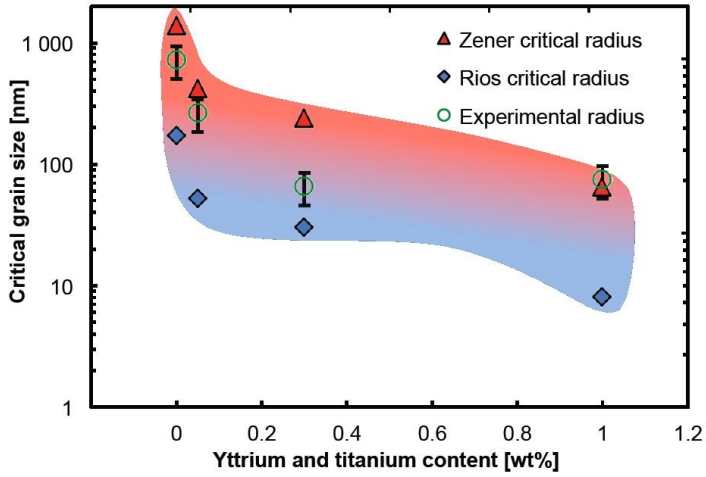

Figure III.49: Critical size calculated from Zener's and Rios's theories based on the precipitation state determined on each grade. Measurements of ultrafine grain (UFG) size are from ACOM-TEM

When dealing with low fractions of second-phase particles, more efficient pinning by particles located at multiple grain junctions is most likely responsible for reducing the grain size [26]. However, the calculated critical size of the ultrafine grains reasonably matches the UFG size measured by TEM. Then, as can be seen in Figure III.50, the precipitation density is so high even considering the unreinforced steel that the effect of special location pinning is not expected to be important in the present case.

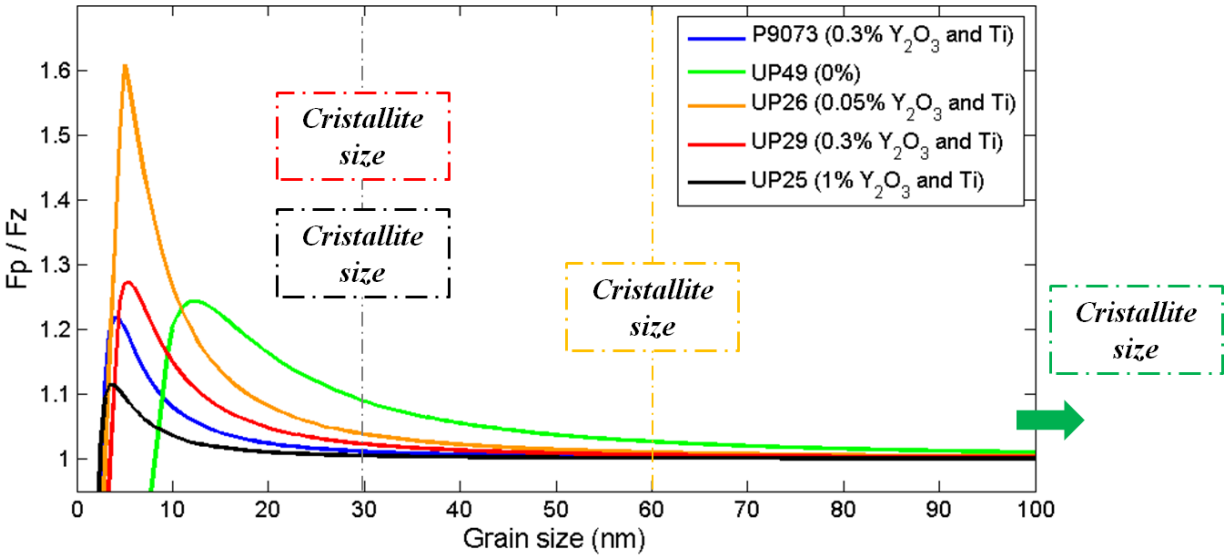

Figure III.50: Special precipitate location effect on pinning force. The pinning force considering special location (Fp) over the classical Zener pinning force (Fz) is presented as a function of the grain size for the different powders studied

The measured grain size of UP25 (1%) powder is slightly larger than the critical ultra fine grain size calculated using Zener pinning pressure. This is due to the fact that the high precipitation density impedes the complete recrystallization of the microstructure. Therefore, the grain size is larger than what it should be in the case of a perfect recrystallization.

Nevertheless, one can conclude that only UFGs are effectively pinned by the fine particles whereas grain boundaries of large abnormal grains are able to migrate more easily.

3.2.2. Abnormal grain growth

The second relevant result that needs to be discussed is the appearance of the bimodal microstructure that was observed whatever the titanium and yttrium content. This phenomenon seems to be not entirely governed by the precipitation state. Indeed, abnormal grains do not fit the Zener model based on the competition between pinning and capillary driving pressures. Since the plastic deformation on each powder is severe, this gives rise to a high level of stored energy. The latter is directly related to the driving pressure of what is called strain-induced boundary migration (SIBM). This effect can be interpreted by an increase of grain boundary mobility due to the difference in stored energy between two neighbouring grains. Therefore, the grain boundary will move into the more deformed grains, resulting in the growth of the least deformed one. It has a great importance on the onset of the abnormal grains. The SIBM pressure may result in a continuous recrystallization when the crystallite sub-boundaries evolve into grain boundaries despite the retardation by precipitate or solute pinning. This evolution reduces the anisotropy of the grains and allows grain growth at rates controlled by precipitation pinning. Then, grains with the lower amount of stored energy will grow at the expense of their closest neighbours. This driving pressure combined with the capillary driving pressure *Pc* will compete with the pinning pressure. Therefore, the formation and further growth of the abnormal grains will be controlled be the local variations in dislocation density and affected by the precipitation state. This mechanism is emphasized by the increase in the abnormal grain growth temperature with titanium and yttrium content.

3.3. Key points on the effect of Ti and Y solute content

- Initial dislocation density increases with the amount of titanium and yttrium.
- Crystallite growth rate reduces with increasing solute content.
- Except for the unreinforced powder for which the recrystallization occurs at 700°C, recrystallization temperature is ~800°C for the three reinforced grades (0.05, 0.3 and 1%).
- Abnormal growth during heating is observed for each powder. The abnormal growth temperature depends on the solute content. Then, if this temperature is higher than that necessary to consolidate the powder, abnormal growth can be avoided and a homogeneous and ultrafine microstructure can be obtained.

- Increasing the content of titanium and yttrium increases the precipitate fraction while the precipitates mean radius remains stable. Therefore the Zener pinning pressure on grain boundaries increases with increasing solute content. This is a key parameter to control the microstructure.
- Also, increasing the solute content gives rise to an increase in the ratio between ultrafine and coarse grains and a decrease in the size of the UFG. The critical grain size of ultrafine grained ODS steel responds to the following criterion:

$$\begin{cases} R_c^{ODS} = C^{ODS}\ {r_p}/{f_p} \\ C^{Zener} = {4}/{3} \leq\ C^{ODS} \approx 0.71 \leq C^{Rios} = {1}/{6} \end{cases}$$

- The fraction and the size of the UFG in bimodal structured metallic materials can govern the mechanical properties. Therefore, a comprehensive relationship between the solute content and the UFG can be of great importance. This could be applied to tailor the mechanical properties of ODS ferritic steels.

General conclusion of the chapter

Based on a study of ODS steel powder particles' microstructural evolution at different temperatures (600, 800, 850, 900 and 1100°C) and on a study of the microstructural evolution of ODS powder particles with different titanium and yttrium solute content (0, 0.05, 0.3 and 1%), it has been possible to identify the different mechanisms involved in the microstructural evolution of the ODS ferritic powder:

- From room temperature to 750°C, the recovery of the microstructure is ongoing. The mechanism is controlled by the anisotropy of the microstructure.
- Then recrystallization occurs, and the microstructure becomes isotropic. The grain growth rate and the final ultrafine grain size is then controlled by precipitation.
- Varying the solute content is an efficient way to control the abnormal grain growth temperature. Nevertheless, the phenomenon occurs whatever the solute content and is controlled by the difference of the dislocation density stored energy between neighbouring grains.
- The ultrafine to coarse grain ratio as well as the critical ultrafine grain size can also be controlled by the solute content. However the abnormal grains have the same size whatever the solute content.

Chapter III bibliography

[1] Alinger M.J., Odette G.R. et Hoelzer D.T. (2009) On the role of alloy composition and processing parameters in nanocluster formation and dispersion strengthening in nanostuctured ferritic alloys. *Acta Materialia*, **57**, 392‑406.

[2] Brocq M., Radiguet B., Poissonnet S., Cuvilly F., Pareige P. et Legendre F. (2011) Nanoscale characterization and formation mechanism of nanoclusters in an ODS steel elaborated by reactive-inspired ball-milling and annealing. *Journal of Nuclear Materials*, **409**, 80‑5.

[3] Humphreys F.J. et Hatherly M. (2004) Recrystallization and Related Annealing Phenomena. Elsevier.

[4] Calcagnotto M., Ponge D., Demir E. et Raabe D. (2010) Orientation gradients and geometrically necessary dislocations in ultrafine grained dual-phase steels studied by 2D and 3D EBSD. *Materials Science and Engineering: A*, **527**, 2738‑46.

[5] Gao H., Huang Y., Nix W.D. et Hutchinson J.W. (1999) Mechanism-based strain gradient plasticity— I. Theory. *Journal of the Mechanics and Physics of Solids*, **47**, 1239‑63.

[6] Ratti M., Leuvrey D., Mathon M.H. et de Carlan Y. (2009) Influence of titanium on nano-cluster (Y, Ti, O) stability in ODS ferritic materials. *Journal of Nuclear Materials*, **386–388**, 540‑3.

[7] Alinger M.., Odette G.. et Hoelzer D.. (2004) The development and stability of Y–Ti–O nanoclusters in mechanically alloyed Fe–Cr based ferritic alloys. *Journal of Nuclear Materials*, **329–333, Part A**, 382‑6.

[8] Zhang H., Gorley M.J., Chong K.B., Fitzpatrick M.E., Roberts S.G. et Grant P.S. (2014) An in situ powder neutron diffraction study of nano-precipitate formation during processing of oxide-dispersion-strengthened ferritic steels. *Journal of Alloys and Compounds*, **582**, 769‑73.

[9] Hatzoglou C. (2015) Etude des aciers ODS par Sonde Atomique et MET. Compréhension de l'évolution nanostructurale en température et sous irradiation. Université de Rouen. PhD thesis.

[10] Gao Y., Nakata K., Nagatsuka K., Liu F.C. et Liao J. (2015) Interface microstructural control by probe length adjustment in friction stir welding of titanium and steel lap joint. *Materials & Design*, **65**, 17‑23.

[11] Ghosh M. et Chatterjee S. (2003) Diffusion bonded transition joints of titanium to stainless steel with improved properties. *Materials Science and Engineering: A*, **358**, 152‑8.

[12] Koch C.C. (1993) The synthesis and structure of nanocrystalline materials produced by mechanical attrition: A review. *Nanostructured Materials*, **2**, 109‑29.

[13] Fecht H.-J. (1995) Nanostructure formation by mechanical attrition. *Nanostructured Materials*, **6**, 33‑42.

[14] Koch C.C. (1997) Synthesis of nanostructured materials by mechanical milling: problems and opportunities. *Nanostructured Materials*, **9**, 13‑22.

[15] Hin C. et Wirth B.D. (2011) Formation of oxide nanoclusters in nanostructured ferritic alloys during anisothermal heat treatment: A kinetic Monte Carlo study. *Materials Science and Engineering A*, **528**, 2056‑61.

[16] Liu Y., Fang J., Liu D., Lu Z., Liu F., Chen S. et Liu C.T. (2010) Formation of oxides particles in ferritic steel by using gas-atomized powder. *Journal of Nuclear Materials*, **396**, 86‑93.

[17] Ukai S. et Fujiwara M. (2002) Perspective of ODS alloys application in nuclear environments. *Journal of Nuclear Materials*, **307–311, Part 1**, 749‑57.

[18] Klimiankou M., Lindau R. et Möslang A. (2004) TEM characterization of structure and composition of nanosized ODS particles in reduced activation ferritic–martensitic steels. *Journal of Nuclear Materials*, **329–333, Part A**, 347‑51.

[19] Alinger M.J., Wirth B.D., Lee H.-J. et Odette G.R. (2007) Lattice Monte Carlo simulations of nanocluster formation in nanostructured ferritic alloys. *Journal of Nuclear Materials*, **367–370, Part A**, 153‑9.

[20] Williams C.A., Unifantowicz P., Baluc N., Smith G.D.W. et Marquis E.A. (2013) The formation and evolution of oxide particles in oxide-dispersion-strengthened ferritic steels during processing. *Acta Materialia*, **61**, 2219‑35.

[21] Hernández-Rivera J.L., Rivera J.J.C., Koch C.T., Özdöl V.B. et Martínez-Sánchez R. (2012) Study of coherence strain of GP II zones in an aged aluminum composite. *Journal of Alloys and Compounds*, **536, Supplement 1**, S159‑64.

[22] Brandes M.C., Kovarik L., Miller M.K. et Mills M.J. (2012) Morphology, structure, and chemistry of nanoclusters in a mechanically alloyed nanostructured

ferritic steel. *Journal of Materials Science*, **47**, 3913‑23.

[23] Ratti M. (2009) Evaluation de nouvelles nuances d'aciers ferritique/martensitique pour le gainage d'éléments combustibles des RNR. PhD thesis.

[24] Couvrat M. (2013) Fabrication d'aciers ODS à haute performance: relation procédé, microstructure, propriétés mécaniques. CEA Saclay, Direction des systèmes d'information. PhD thesis.

[25] Ribis J. et de Carlan Y. (2012) Interfacial strained structure and orientation relationships of the nanosized oxide particles deduced from elasticity-driven morphology in oxide dispersion strengthened materials. *Acta Materialia*, **60**, 238‑52.

[26] Bréchet Y. et Militzer M. (2005) A note on grain size dependent pinning. *Scripta Materialia*, **52**, 1299‑303.

[27] Rhines F.N., Craig K.R. et DeHoff R.T. (1974) Mechanism of steady-state grain growth in aluminum. *Metallurgical Transactions*, **5**, 413‑25.

[28] Doherty R.D. (1975) Discussion of "mechanism of steady-state grain growth in aluminum". *Metallurgical Transactions A*, **6**, 588‑90.

[29] Atkinson H.V. (1988) Overview no. 65: Theories of normal grain growth in pure single phase systems. *Acta Metallurgica*, **36**, 469‑91.

[30] Gottstein G. et Shvindlerman L.S. (2006) Grain boundary junction engineering. *Scripta Materialia*, **54**, 1065‑70.

[31] Gottstein G., Shvindlerman L.S. et Zhao B. (2010) Thermodynamics and kinetics of grain boundary triple junctions in metals: Recent developments. *Scripta Materialia*, **62**, 914‑7.

[32] Smith C.J.E. et Dillamore I.L. (1970) Subgrain growth in high purity iron. *Metal Science*, **4**, 161‑7.

[33] Hayoune A. et Hamana D. (2010) A dilatometric and high-temperature X-ray diffraction study of cold deformation effect on the interaction between precipitation, recovery and recrystallization reactions in Al–12 wt.% Mg alloy. *Materials Science and Engineering: A*, **527**, 7261‑4.

[34] Boulnat X., Perez M., Fabregue D., Douillard T., Mathon M.-H. et Carlan Y. de. (2014) Microstructure Evolution in Nano-reinforced Ferritic Steel Processed By Mechanical Alloying and Spark Plasma Sintering. *Metallurgical and Materials*

Transactions A, 1‑13.

[35] Dapeng Z., Yong L., Feng L., Yuren W., Liujie Z. et Yuhai D. (2011) ODS ferritic steel engineered with bimodal grain size for high strength and ductility. *Materials Letters*, **65**, 1672‑4.

[36] Wen Y., Liu Y., Hirata A., Liu F., Fujita T., Dou Y., Liu D., Liu B., Liu Z. et Liu C.T. (2012) Innovative processing of high-strength and low-cost ferritic steels strengthened by Y–Ti–O nanoclusters. *Materials Science and Engineering: A*, **544**, 59‑69.

[37] Novikov V.Y. (2012) Grain growth and disperse particles: Impact of triple junctions. *Materials Letters*, **84**, 136‑8.

[38] Suryanarayana C. (2001) Mechanical alloying and milling. *Progress in Materials Science*, **46**, 1‑184.

[39] Cahn J.W. (1962) The impurity-drag effect in grain boundary motion. *Acta Metallurgica*, **10**, 789‑98.

[40] Lücke K. et Stüwe H.P. (1971) On the theory of impurity controlled grain boundary motion. *Acta Metallurgica*, **19**, 1087‑99.

[41] Hillert M. et Sundman B. (1976) A treatment of the solute drag on moving grain boundaries and phase interfaces in binary alloys. *Acta Metallurgica*, **24**, 731‑43.

[42] Tanno T., Ohtsuka S., Yano Y., Kaito T., Oba Y., Ohnuma M., Koyama S. et Tanaka K. (2013) Evaluation of mechanical properties and nano-meso structures of 9–11%Cr ODS steels. *Journal of Nuclear Materials*, **440**, 568‑74.

[43] Miao P., Odette G.R., Yamamoto T., Alinger M. et Klingensmith D. (2008) Thermal stability of nano-structured ferritic alloy. *Journal of Nuclear Materials*, **377**, 59‑64.

[44] Cunningham N., Wu Y., Klingensmith D. et Odette G.R. (2014) On the remarkable thermal stability of nanostructured ferritic alloys. *Materials Science and Engineering: A*, **613**, 296‑305.

[45] Rios P.R. (1987) Overview no. 62: A theory for grain boundary pinning by particles. *Acta Metallurgica*, **35**, 2805‑14.

Chapter IV
A model to predict abnormal grain growth

In this chapter, a numerical modelling of abnormal grain growth coupled to precipitation is described. In order to predict the occurrence of abnormal grain growth for different thermal treatments, the model was applied to the ferritic ODS steel case and adapted to take the influence of the dislocation density into account.

1. Coupled abnormal grain growth and precipitation model

The physical basis of both abnormal grain growth and precipitation models as well as the coupling between these phenomena is presented in this section.

1.1. Abnormal grain growth model

The abnormal grain growth model allows to account for the differential growth of the coarse grains compared to the mean grain size by taking into account the effect of precipitation pinning. The model has originally been developed for low alloy steels [1–4]. Therefore, as suggested by [5], precipitation controlled abnormal grain growth (AGG) is more likely to occur than any other scenario involving exaggerated energy or mobility anisotropy. The basis that leads to the AGG model developed at the MATEIS laboratory has been recalled in chapter I §2.7. Mathematical derivation allowing to obtain an AGG criterion will be detailed in the section. The model assumptions are:

- Grains are assumed to be isotropic and have high angle boundaries.
- Solute drag force is assumed to be comparatively smaller than precipitate induced pinning force. Solute drag, and its possible evolution while precipitation occur thus depleting the solid solution, will not be considered.
- Precipitation is homogeneous, no segregation is considered in the system.

These assumptions allow to formulate the AGG model with a reduced number of variables while preserving the fundamental mechanism of grain growth.

Grain size pressure

Grain growth theory is based on the decrease of grain boundary interfacial energy. In the case of AGG, the potential energy decrease for the abnormal grain growth is higher than for their neighbouring grains, therefore abnormal grains drain them.

Grains are represented as spheres (cf. Figure IV.1) with coarse grains (D_{ab}) surrounded by normal sized grains (D_n). The total work necessary to move the system from state 1 to

state 2 is $\delta W = E_1 - E_2$. It determines the driving pressure for abnormal grain to grow as $\delta W = P_{ab}\delta V$. Here, δV is the abnormal grain volume change from state 1 to state 2, $\delta V = \lambda_{ab} D_{ab}^2 \delta D_{ab}/2$, where λ_{ab} is a geometric factor (π for a sphere).

The number n_g of normal grains surrounding an abnormal grain varies as a function of D_n and D_{ab}:

$$n_g = \rho_{eff} \frac{\lambda_{ab}(D_{ab} + D_n)^2}{\lambda_p \lambda_n D_n^2} = 4\mu \frac{\lambda_{ab}}{\lambda_n} \frac{(D_n + D_{ab})^2}{D_n^2} \quad \text{(IV.1)}$$

Where ρ_{eff} is the compact efficiency factor, λ_n is a geometric factor (π for a sphere), λ_p is the ratio between the projected surface over the actual surface of the normal grain ($\lambda_p = 1/4$ for a plane) and $\mu = \rho_{eff}/(4\lambda_p)$. According to a parametric study [4], the same value $\mu = 0.56$ was obtained for different initial microstructural parameters.

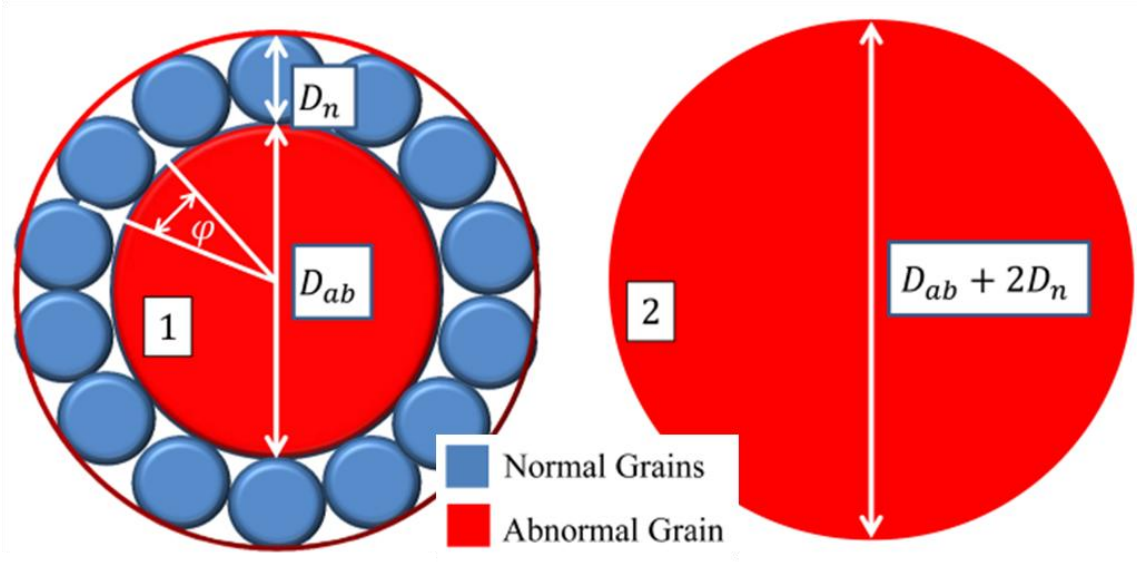

Figure IV.1: Schematic representation of an abnormal grain of diameter D_{ab} surrounded by normal grains of diameter D_n. The abnormal grain is growing from state 1 to state 2 by consuming all the surrounding normal grains and increasing its diameter by $2D_n$ [6]

The total interfacial energy of state 1 is given by:

$$E_1 = \frac{\gamma_g}{2}\left[\lambda_{ab} D_{ab}^2 + n_g \lambda_n D_n^2\right] = \frac{\gamma_g \lambda_{ab}}{2}\left[D_{ab}^2 + 4\mu(D_{ab} + D_n)^2\right] \quad \text{(IV.2)}$$

Where γ_g is the grain boundary energy. Similarly, total interfacial energy of the state 2 is:

$$E_2 = \frac{\gamma_g \lambda_{ab}}{2}[D_{ab} + 2D_n]^2 \quad \text{(IV.3)}$$

The driving pressure for a volume increase of the abnormal grain by δV, can be written as:

$$P_{ab} = \frac{\delta W}{\delta V} = \frac{E_1 - E_2}{\delta D_{ab}} \frac{\delta D_{ab}}{\delta V} = \frac{E_1 - E_2}{2D_n} \frac{2}{\lambda_{ab} D_{ab}^2} \quad \text{(IV.4)}$$

Using equations (IV.2)to (IV.4):

$$P_{ab} = \frac{2\gamma_g}{D_n}\left[\mu - (1-\mu)\left(\frac{D_n}{D_{ab}}\right)^2 + (2\mu - 1)\frac{D_n}{D_{ab}}\right] \quad \text{(IV.5)}$$

Zener pinning pressure

The effect of second phase particles on grain boundary migration has already been detailed in chapter I §2.6. It consists in a pinning effect on grain boundaries that will reduce the driving pressure for growth. Hence, the abnormal grain growth rate can be reduced by the following expression [7–9]:

$$\frac{dD_{ab}}{dt} = M\left(P_{D_{ab}} - P_Z\right) \tag{IV.6}$$

Where M is the mobility of the grain boundary. The same expression holds for a normal grain growth rate:

$$\frac{dD_n}{dt} = M\left(P_{D_n} - P_Z\right) \tag{IV.7}$$

Precipitate distribution and corner pinning pressure

The special pinning location (corner pinning) effect is detailed in chapter I §2.6. Here only the particular consideration of the entire particle size distribution will be described.

Considering a particle distribution $n_i(r_i)$ with a total number of precipitates $n_n = \sum_i n_i$ and following the Bréchet-Militzer hypothesis that larger particles reside primarily in special locations, smaller ones are located on classical boundaries (Zener pinning), there is a critical radius r_c of the particle classes which separates the precipitates contributing to the Zener or to the special boundary pinning. As shown in [5] and reported in chapter I §2.6, the pinning force is dependent on the number of corner points available in the system. With N^* the number of corner points, if $n_n < N^*$:

$$P_C = \sum_i \frac{n_i}{N^*} \frac{K_0 \alpha k_s \gamma_g r_i}{K_A D_n^2} = \frac{K_V \alpha k_s \gamma_g}{K_A} D_n \sum_{i=1}^{n} n_i r_i \tag{IV.8}$$

If $n_n > N^*$, the total pinning is given not only by P_C but also by P_Z:

$$P_C = \frac{K_V \alpha k_s \gamma_g}{K_A} D_n \sum_{i=i^*}^{n} n_i r_i \text{ and } P_Z = 2k_s\gamma_g \sum_{i=1}^{i^*} n_i r_i^2 \tag{IV.9}$$

Here, i^* is the index of the precipitate class for which the precipitate can be either on a special location or lying on a classical Zener boundary.

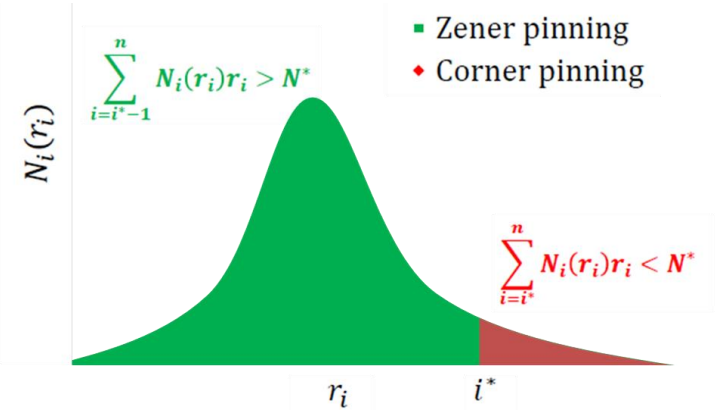

Figure IV.2: Precipitate class distribution. Small precipitates (green part of the distribution) contribute to Zener pinning, while large precipitates contribute to Corner pinning (red part of the distribution)

It should be noted that i^* depends on D_n, indeed, the larger the grain size is, the smaller is

the number of special locations and consequently the larger the index i^*.
Then considering both Zener and special location pinning, equation (IV.7) becomes:

$$\frac{dD_n}{dt} = M\left(P_{D_n} - P_C - P_Z\right) \tag{IV.10}$$

$$\frac{dD_{ab}}{dt} = M\left(P_{D_{ab}} - P_C - P_Z\right) \tag{IV.11}$$

Abnormal Grain Growth condition

To establish a criterion for AGG in a real microstructure, a condition for abnormal grain growth has to be introduced. A simple one is to consider that, for abnormal grain growth to occur, larger grains have to grow faster than the normal grain population. As detailed in chapter I §2.6 this leads to (if $D_{ab}/D_n > 0$):

$$\begin{aligned}\frac{d}{dt}\left(\frac{D_{ab}}{D_n}\right) &= \frac{1}{D_n}\frac{dD_{ab}}{dt} - \frac{D_{ab}}{D_n^2}\frac{dD_n}{dt} \\ &= \frac{2\gamma_g M}{D_n^2}\left[\mu - (1-\mu)\left(\frac{D_n}{D_{ab}}\right)^2 + (2\mu - 1)\frac{D_n}{D_{ab}}\right. \\ &\left. - \frac{\lambda}{2}\frac{D_{ab}}{D_n}\right] - \frac{M}{D_n}\left(\frac{D_{ab}}{D_n} + 1\right)(P_C + P_Z)\end{aligned} \tag{IV.12}$$

For a given precipitation density, this condition is only true when $D_n/D_n^l > 1$ with D_n^l as the critical grain size:

$$D_n^l = \lambda k_v \Big/ \left(2k_s \sum_{i^*}^{n} n_i r_i^2\right) \tag{IV.13}$$

1.2. Precipitation modelling

A description of the precipitation model based on Classical Nucleation and Growth Theories CNGTs established by Langer and Schwartz [10] and modified by Kampmann and Wagner [11] is presented here. This presentation will allow to evidence the parameters that are necessary to model the yttrium precipitation.

1.2.1. Model assumptions

The presented precipitation model is based on the main following simplifications:

- Precipitate growth is controlled by long distance solute diffusion in the matrix.
- Precipitates are assumed to be spherical. This has the great advantage to simplify precipitation modelling into one dimension parameter equations (radius) to handle it in the calculation;
- Precipitates do not induce strain field in the matrix;
- Precipitate interfacial energy depends on neither the precipitate size nor the temperature.

- Local equilibrium is assumed for the interfacial condition (i.e. given by the solubility product obtained from the phase diagram) and is corrected by the Gibbs-Thomson effect.
- The solute concentration profile is stationary around the precipitates.

1.2.2. Analytical description and numerical modelling

In this description, the general form of two special stoichiometric precipitates A_xB_y will be used.

Thermodynamics:

For an ideal solution model, elements' activities in a solid solution can be approximated by their atomic proportion. Then, the driving force for precipitation is:

$$\Delta G^* = k_b T \ln([X_A]^x [X_B]^y) \tag{IV.14}$$

Where X_A and X_B are respectively the atomic fractions of A and B in the bulk and $[X_A]^x[X_B]^y$ is the solubility product K_s.

Nucleation:

Formation of a precipitate in a supersaturated solid solution is associated with the change in volume and interfacial energy induced by this precipitate [2,11]. In the case of a spherical precipitate of radius R, the driving force for precipitation is given by (cf. Figure IV.3):

$$\Delta G^*(R) = \frac{4}{3}\pi R^3 \Delta g + 4\pi R^2 \gamma_p \tag{IV.15}$$

Where Δg is the driving force for precipitation per unit volume and γ_p the specific interfacial energy between matrix and precipitate.

The nucleation rate is given as [11]:

$$\frac{dN}{dt} = N_0 Z \beta^* exp\left(-\frac{\Delta G^*}{k_b T}\right) exp\left(-\frac{\tau}{t}\right) \tag{IV.16}$$

Where N_0 is the number of nucleation sites per unit volume, Z is the Zeldovich factor, β^* is the condensation rate of solute atoms in a cluster of radius R^* and τ is the incubation time. The expressions for these values are:

$$Z = \frac{v_{at}^p}{2\pi R^{*2}} \sqrt{\frac{\gamma_p}{k_B T}} \tag{IV.17}$$

$$\beta^* = \frac{4\pi R^{*2}}{a^4} \left(\sum_i \frac{X_i^p}{D_i^m X_i^m} \right)^{-1} \tag{IV.18}$$

$$R^*_{k_b T} = R^* + \frac{1}{2} \sqrt{\frac{k_b T}{\pi \gamma}} \tag{IV.19}$$

$$\tau = \frac{4}{2\pi\beta^* Z^2} \tag{IV.20}$$

These equations include the following parameters: the mean atomic volume within precipitates v_{at}^{p}, the critical radius for stable precipitates R^*, the diffusion coefficient of atoms D, the solute atom fraction in the matrix X_i^m, precipitate constituent atomic fraction X_i^p and the lattice parameter a .

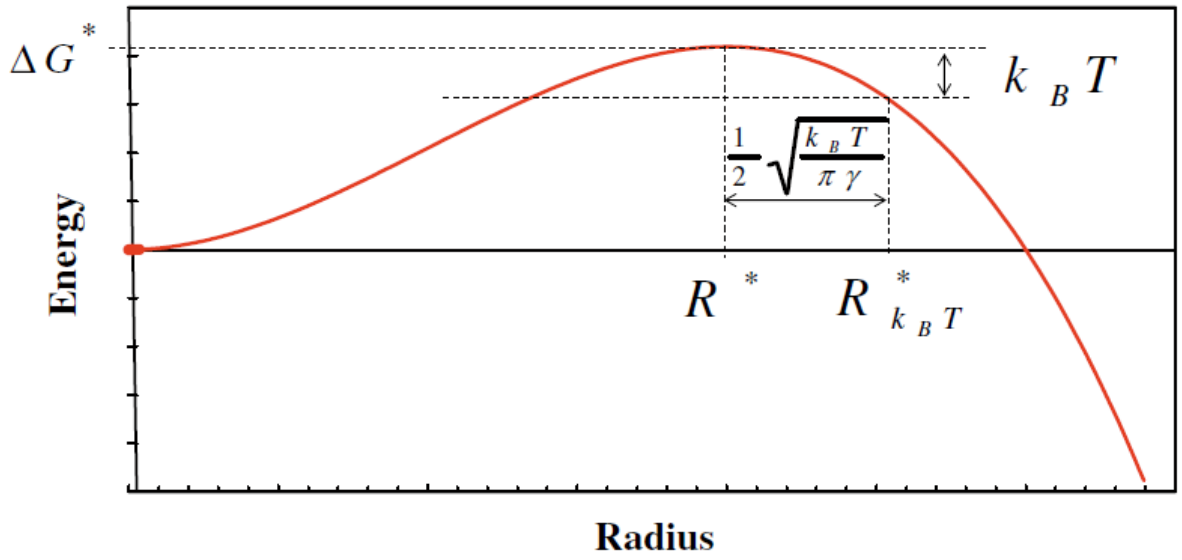

Figure IV.3: Schematic representation of the Gibbs energy changes associated with precipitate formation as a function of their radius *R* in the classical nucleation theory [12]

For a large precipitation volume fraction ($f_v \gg 0.1$), the number of nucleation sites is reduced. To take it into account, the number of nucleation sites is expressed as:

$$N_0' = N_0\left(1 - \frac{v_{at}^{M}}{v_{at}^{p}} f_v\right) \tag{IV.21}$$

Growth:

After their nucleation precipitates can grow and coarsen while the nucleation rate in solid solution progressively decreases with the supersaturation level. Due to the interface between precipitates and the matrix, the local equilibrium is modified by the curvature effect which is known as the Gibbs-Thomson effect. The solubility product then becomes:

$$K_s exp\left[\frac{R_0}{R}\right] = X_A^I X_B^I \tag{IV.22}$$

The diffusion controlled growth rate of spherical precipitates, under the assumption of small supersaturation ($X^0 - X^i \ll \alpha X^p - X^i$) and local equilibrium, can be described by Fick's law:

$$\frac{dR}{dt}|_A = \frac{D_A^m}{R} \frac{X_A^m - X_A^I(R)}{\alpha_r X^p - X_A^I(R)} \tag{IV.23}$$

$$\frac{dR}{dt}|_B = \frac{D_B^m}{R}\frac{X_B^m - X_B^I(R)}{\alpha X^p - X_B^I(R)} \quad \text{(IV.24)}$$

Where, $\alpha_r = v_{at}^M / v_{at}^P$ is the ratio of matrix to precipitate atomic volumes, X^I is the equilibrium atomic concentration of solute atoms at the precipitate matrix interface.

The growth of the precipitate is unique, therefore $\frac{dR}{dt}|_A = \frac{dR}{dt}|_B$. To simplify the equation system, it is often considered that one of the solute atom diffuses much faster than the other ($D_B^m \gg D_A^m$). Then, the precipitation growth rate is controlled only by the diffusion of A solute atoms. This assumption leads to:

$$X_B^I(R) = X_B^m \quad \text{(IV.25)}$$

Then the equation system can be solved as there are two equations and two unknowns (dR/dt and X_A^I).

1.2.3. Numerical implementation of the precipitation model

Numerical implementation to solve the CNGTs is performed using "Lagrange-like" multi class approach described in [13]. The precipitate size distribution is discretised, which allows to independently solve a variable number of differential equations giving the nucleation and growth rate of each precipitate class at each time [2,12,13].

$$R_i(t + \Delta t) = R_i(t) + \frac{dR_i}{dt}\Delta t \quad \text{(IV.26)}$$

New classes are added to the pre-existing n number of classes, if the nucleation rate is positive

$$N_{n+1} = \frac{dN}{dt}\Delta t \quad \text{(IV.27)}$$

$$R_{n+1} = R^*_{k_B T} \quad \text{(IV.28)}$$

A complete description of the precipitation distribution is then possible.

1.3. Coupled modelling

The influence of precipitation on the occurrence of normal or abnormal grain growth is taken into account by coupling precipitation and abnormal grain growth models dynamically [4]. Dynamic Coupled Modelling (DCM) is defined by the interaction between the AGG model described in §1.1 and the precipitation evolution model described in §1.2 which are preformed at the same time scale.

Evolution of the mean grain size and precipitation condition will change both the pinning conditions and the available energy for AGG. Then, the evolution of the precipitation state and grain growth is interconnected. In the current model, time and temperature dependent evolution of the physical parameters are studied collectively.

1.3.1. Model assumption

- Mean grain size is evolving with time at a particular temperature

- Precipitate nucleation and growth occur homogeneously
- Larger precipitates lie in the special boundary locations. During grain growth, grain boundary triple points move with the grain boundary and the precipitate located in it.

1.3.2. Numerical implementation of the coupled model

At each time step, the precipitation distribution is taken as an input data in the AGG model. Then, the AGG model calculates the precipitate induced pinning and mean grain growth as:

$$D_n^i = D_n^{i-1} + dD_n/dt \times \Delta t \quad \text{(IV.29)}$$

A schematic representation of the dynamic modeling strategy is given in Figure IV.4.

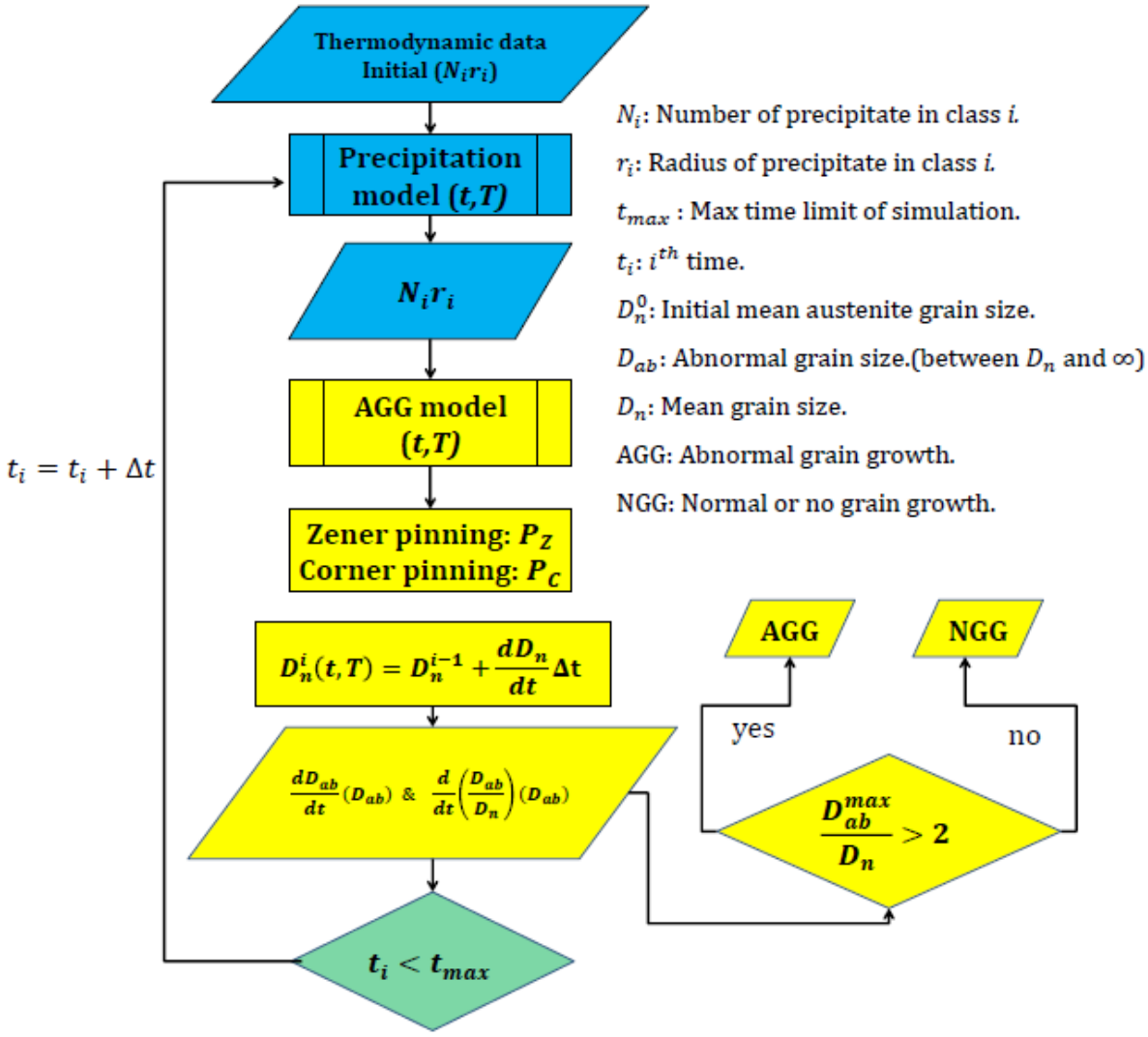

Figure IV.4: Schematic representation of dynamic coupling between precipitation and abnormal grain growth model [4]

2. Adaptation of the model to ODS ferritic steels

Originally, the coupled precipitation and abnormal grain to the growth model detailed on

the previous section has been developed to be used in austenitic low alloy steels. In this section, the modifications made to account for the ODS ferritic steel microstructure are presented.

2.1. Matrix parameters

Compared to the austenitic matrix, Ferritic matrix's main parameters are significantly different. In the model, the following parameters will be used:

Parameter	Value	Reference
Atomic volume	$2.38.10^{-29}$ m^{-3}	
Lattice parameter	$2.876.10^{-10}$ m	
Molar mass	56.58 $g.mol^{-1}$	
Pre-exponential factor for grain boundary mobility (M_0)	58.10^{-3} $m^2.s^{-1}$	[14,15]
Grain boundary mobility Activation energy (Q)	140 $kJ.mol^{-1}$	[14,15]

Table IV.1: Input parameters of the ferritic matrix

2.2. Precipitation

In order to account for the pinning effect as a retardation force for grain growth in ferritic ODS steels, precipitation is considered. As a first stage of implementation it is proposed here to consider and describe the kinetic evolution of Y_2O_3. Indeed, as stated in §1.2.2, growth rate of precipitates is controlled by the slowest diffusing species. Yttrium being the species with the lowest diffusion coefficient, it controls the precipitates growth rate. Therefore the evolution of $Y_xTi_yO_z$ precipitates of the ODS steels should be efficiently accounted for by the Y_2O_3 precipitation. This assumption has already been proposed in [16] and proved to be able to reproduce the precipitate thermal stability observed experimentally [17–20]. In the present study, a 0.3 Y_2O_3 %wt is considered (as in the P9073 powder studied in Chapter III).

Precipitates parameters:

The key parameters for precipitation modelling are the interfacial energy, the diffusion coefficient of the slowest diffusing species within the matrix (here yttrium in ferrite), and the solubility product K_s as a function of the temperature which is assumed to have the following form:

$$\ln K_{Y_2O_3} = -\frac{A}{T} + B \qquad \text{(IV.30)}$$

Parameter		Value	Reference
Yttrium diffusion	$D_{0_Y}^{m\alpha}$	1.10^{-5}	[21]
	$Q_Y^{m\alpha}$	309.9 kJ.mol^{-1}	[21]
Yttrium at%		0.15	
Oxygen diffusion	$D_{0_O}^{m\alpha}$	4.10^{-5}	[21]
	$Q_O^{m\alpha}$	167.1 kJ.mol^{-1}	[21]
Oxygen at%		0.3	
Y_2O_3 atomic volume		$1.19.10^{-27}$ m^{-3}	
Y_2O_3 interfacial energy		0.4 J.m^{-2}	[21]
Y_2O_3 solute product parameter	A	29200 K	[21]
	B	1.33	[21]

Table IV.2: Input parameters for precipitation model

2.3. Implementation

To account for the validity of the abnormal grain growth prediction of the model, occurrence of abnormal grain growth is tested at a temperature for which abnormal grain growth was observed during the characterization campaign (800°C, 850°C and 900°C). To avoid numerical issues, simulations are performed at each temperature for 300s. The same precipitate size distribution is used for each simulation, normal and abnormal grain sizes are issued from corresponding experimental observation for each simulation temperature.

2.3.1. Precipitate size distribution

Given the experimental results obtained concerning precipitation, the initial precipitation distribution is described by a lognormal function with the following parameters (corresponding to the precipitation distribution obtained experimentally for the 800°C annealings (cf. II§2.2.2.3)):

Thermal treatment	Mean precipitate radius (m)	Standard deviation	Volume fraction (%)
800 5min	$9.62.10^{-10}$	0.35	1.07
800 20min	$1.06.10^{-9}$	0.33	1.01
800 60min	$1.08.10^{-9}$	0.45	1.11
average	$1.03.10^{-9}$	0.37	1.06

Table IV.3: parameters of the lognormal distribution used to model the initial precipitate distribution

2.3.2. Normal and abnormal grains

Abnormal and normal grain parameters are given as input parameters.

Thermal treatment	Mean grain radius Dn (nm)	Abnormal grain radius Dab (nm)	Experiment
800 5min	120	250	ACOM + SEM
800 20min	120	250	ACOM + SEM
800 60min	120	250	ACOM + SEM
850 5min	150	300	ACOM + SEM
850 20min	160	350	ACOM + SEM
850 60min	200	600	SEM
900 5min	180	400	SEM
900 20min	200	850	SEM
900 60min	250	1000	ACOM + SEM

Table IV.4: parameters of the lognormal distribution used to model the initial precipitate distribution

The parameter μ that depends on the compact efficiency factor and the ratio between projected surface over the actual surface of the normal grain is set to 0.56. according to [4].

3. Results

In section 3.1, the results correspond to the application of the model as it is described above. Then, in section 3.2 the modelling is improved by the introduction of the dislocation density.

3.1. First results

Thermal treatment		Model				Experimental			
		dD_n/dt	dD_{ab}/dt	dD_{ab}/D_n	Prediction	dD_n/dt	dD_{ab}/dt	dD_{ab}/D_n	observation
800°C	5 min	0	0	0	NGG	>0	>0	~1	NGG
	20 min	0	0	0	NGG	~0	~0	~1	NGG
	60 min	0	0	0	NGG	~0	~0	~1	NGG
850°C	5 min	0	0	0	NGG	>0	>0	~1	NGG
	20 min	0	0	0	NGG	~0	>0	>2	AGG
	60 min	0	0	0	NGG	~0	>0	>2	AGG
900°C	5 min	0	0	0	NGG	>0	>0	>2	AGG
	20 min	0	0	0	NGG	>0	>0	>2	AGG
	60 min	0	0	0	NGG	>0	>0	>2	AGG

Table IV.5: Comparison between coupled precipitation and AGG model and experimental observations

Table IV.5 shows that no matter the temperature or the initial microstructure, the simulation does not allow for any growth, contrarily to what is observed experimentally. The initial results obtained with the coupled precipitation / abnormal grain growth proved to be out of scale.

While developing the model, Perez and coll. [1,3,4] always made clear that the model was designed for fully recrystallized materials. However, as observed in Chapter III, this is far from being the case on the ODS ferritic steel particles annealed between 800°C and 900°C on which a high dislocation density was calculated.

3.2. Stored energy driving pressure

Therefore the model has been modified to take into account the driving pressure arising from the dislocation density stored energy. As stated before, the driving pressure does not arise from the driving pressure itself but from the difference in stored energy between two neighbouring grains. In order to keep the model as simple as possible, the following assumptions are made:

- Dislocation density between normal grains is homogeneous.

- Dislocation density between abnormal grains is homogeneous.
- Dislocation density is considered to be present only in the normal grains, therefore the dislocation density in coarse grains is set to 0.

As a consequence the grain growth equations (IV.31) and (IV.32) have been modified as follow:

$$\frac{dD_n}{dt} = M\left(P_{D_n} - P_C - P_Z\right) \quad \text{(IV.31)}$$

$$\frac{dD_{ab}}{dt} = M\left(P_{D_{ab}} - P_C - P_Z + P_\rho\right) \quad \text{(IV.32)}$$

Where $P_\rho = \alpha\rho Gb^2$, with ρ is the dislocation density, G is the shear modulus, and b Burgers' vector, for ferrite, $G = 69GPa$ and $b = 2.49.10^{-10}$ m.

Using the values obtained in chapter III §2.2.2.1 dislocation density is implemented according to Table IV.6:

Temperature	Dislocation density evolution as a function of time (m^{-2})
800°C	$2.34.10^{15} - 2.034.10^{11} \times t$
850°C	$2.10^{15} - 2.09.10^{11} \times t$
900°C	$2.14.10^{15} - 2.82.10^{11} \times t$

Table IV.6: linear evolution of the dislocation density as calculated in chapter III

This modification of the code deeply modifies the results obtained with the model as it can be seen in Table IV.7.

Thermal treatment		Model				Experimental			
		dD_n/dt	dD_{ab}/dt	dD_{ab}/D_n	Prediction	dD_n/dt	dD_{ab}/dt	dD_{ab}/D_n	observation
800°C	5 min	0	0	0	NGG	>0	>0	~1	NGG
	20 min	0	0	0	NGG	~0	~0	~1	NGG
	60 min	0	0	0	NGG	~0	~0	~1	NGG
850°C	5 min	0	0	0	NGG	>0	>0	~1	NGG
	20 min	0	$9.1.10^5$	∞	AGG	~0	>0	>2	AGG
	60 min	0	$1.5.10^6$	∞	AGG	~0	>0	>2	AGG
900°C	5 min	0	$1.8.10^6$	∞	AGG	>0	>0	>2	AGG
	20 min	0	3.10^6	∞	AGG	>0	>0	>2	AGG
	60 min	0	1.10^6	∞	AGG	>0	>0	>2	AGG

Table IV.7: Comparison between modified coupled precipitation and AGG model and experimental observations

The major result evidenced on Table IV.7 is the fact that now the model correctly predicts the occurrence of normal or abnormal grain growth. It can also be noticed that once abnormal grains start to grow, they grow very rapidly. Growth is faster at 900°C than it is at 850°C. Also, the abnormal grain growth rate decreases with increasing soaking time.
This reproduces quite well the experiments presented in chapter III in which it was observed that when abnormal grain growth starts it grows very fast.
However, the absolute value obtained for abnormal growth is very unlikely and does not correspond to what is observed experimentally.
More importantly, absolutely no growth is detected for normal sized grain. Experimentally, even if the growth of ultrafine grains was limited, it occurs nonetheless. This can be due to the fact that here, both precipitation and dislocation density have been distributed equally for each grains. Therefore, since precipitation pinning is high enough to freeze the microstructure and no local heterogeneities are available, growth is completely impeded.

4. Limits and perspectives

The model strongly depends on the input parameters and is currently unable to account for eventual mean grain size evolution. It is not a predictive modelling. Indeed, grain growth (AGG or NGG) only occurs when the initial grain sizes allows it.
However most importantly, the model validates the fact that as observed in chapter III abnormal grain growth in ODS ferritic steels is controlled by stored energy.
To numerically evaluate the influence of the solute content on the AGG initiation, different precipitate size distributions have to be tested with the model.
In order to go further and allow the model to account for the mean grain size evolution, it is intended to account for the entire grain size distribution within the model. Then the driving pressure could be more finely integrated with a respective dislocation density attributed to each grain size class.

Chapiter IV bibliography

[1] Acevedo-Reyes D. (2007) Evolution de l'état de précipitation au cours de l'austénitisation d'aciers microalliés au vanadium et au niobium. INSA de Lyon. PhD thesis

[2] Perez M., Dumont M. et Acevedo-Reyes D. (2008) Implementation of classical nucleation and growth theories for precipitation. *Acta Materialia*, **56**, 2119‑32.

[3] Leguen C. (2010) Prior Austenite Grain Size Controlled by Precipitates. INSA de Lyon. PhD thesis

[4] Razzak M. (2013) Precipitation and abnormal grain growth in low alloy steels. INSA

de Lyon. PhD thesis.

[5] Bréchet Y. et Militzer M. (2005) A note on grain size dependent pinning. *Scripta Materialia*, **52**, 1299‑303.

[6] Razzak M. abdur, Perez M., Sourmail T., Cazottes S. et Frotey M. (2012) A simple model for abnormal grain growth. *ISIJ International*, **52**, 2278‑82.

[7] Hillert M. (1965) On the theory of normal and abnormal grain growth. *Acta Metallurgica*, **13**, 227‑38.

[8] Gladman T. (1966) On the Theory of the Effect of Precipitate Particles on Grain Growth in Metals. *Proceedings of the Royal Society of London Series A Mathematical and Physical Sciences*, **294**, 298‑309.

[9] Humphreys F.J. et Hatherly M. (2004) Recrystallization and Related Annealing Phenomena. Elsevier.

[10] Langer J.S. et Schwartz A.J. (1980) Kinetics of nucleation in near-critical fluids. *Physical Review A*, **21**, 948‑58.

[11] Wagner R., Kampmann R. et Voorhees P.W. (2006) Homogeneous Second-Phase Precipitation. *Materials Science and Technology*, Wiley-VCH Verlag GmbH & Co. KGaA.

[12] Perez M., Dumont M. et Acevedo-Reyes D. (2009) Corrigendum to “Implementation of classical nucleation and growth theories for precipitation” [Acta Materialia 56 (2008) 2119–2132]. *Acta Materialia*, **57**, 1318.

[13] Maugis P. et Gouné M. (2005) Kinetics of vanadium carbonitride precipitation in steel: A computer model. *Acta Materialia*, **53**, 3359‑67.

[14] Krielaart G.P. et van der Zwaag S. (1998) Simulations of pro-eutectoid ferrite formation using a mixed control growth model. *Materials Science and Engineering: A*, **246**, 104‑16.

[15] S. V. S. Narayana Murty S.T. (2005) Ferrite Grain Size Formed by Large Strain-High Z Deformation in a 0.15C Steel. *Materials Transactions*, **46**, 2454‑60.

[16] Hin C. et Wirth B.D. (2010) Formation of Y_2O_3 nanoclusters in nano-structured ferritic alloys: Modeling of precipitation kinetics and yield strength. *Journal of Nuclear Materials*, **402**, 30‑7.

[17] Alinger M.., Odette G.. et Hoelzer D.. (2004) The development and stability of Y–Ti–O nanoclusters in mechanically alloyed Fe–Cr based ferritic alloys. *Journal of Nuclear Materials*, **329–333, Part A**, 382‑6.

[18] Miao P., Odette G.R., Yamamoto T., Alinger M. et Klingensmith D. (2008) Thermal stability of nano-structured ferritic alloy. *Journal of Nuclear Materials*, **377**, 59‑64.

[19] Ratti M., Leuvrey D., Mathon M.H. et de Carlan Y. (2009) Influence of titanium on nano-cluster (Y, Ti, O) stability in ODS ferritic materials. *Journal of Nuclear Materials*, **386–388**, 540‑3.

[20] Cunningham N., Wu Y., Klingensmith D. et Odette G.R. (2014) On the remarkable thermal stability of nanostructured ferritic alloys. *Materials Science and Engineering: A,* **613**, 296‑305.

[21] Hin C. et Wirth B.D. (2011) Formation of oxide nanoclusters in nanostructured ferritic alloys during anisothermal heat treatment: A kinetic Monte Carlo study. *Materials Science and Engineering a-Structural Materials Properties Microstructure and Processing*, **528**, 2056‑61.

Chapter V
From powder to extruded materials

This chapter reports a detailed comparison of the microstructures of the consolidated samples and annealed powders. This study is made in order to examine whether or not the mechanisms presented in the previous chapter apply to the case of the actual material processing. Furthermore, in this chapter, the interaction between precipitates and grain boundaries in the case of a ferritic ODS steel will also be investigated.

1. Material consolidation: impact of the process on the microstructure

The impact of consolidation on the microstructure is studied in this section in order to differentiate between thermally and thermo-mechanically driven processes.

1.1. Chemical distribution

Chemical maps carried out by EPMA method on the P9073 annealed powder have evidenced a significant titanium segregation at the boundaries between powder particles (cf. III §2.2.1). This segregation was attributed to the presence of the particle free zones close to the surfaces that allowed the free titanium to react with oxygen. Titanium is attracted to the free surface of particles because of the presence of oxygen.

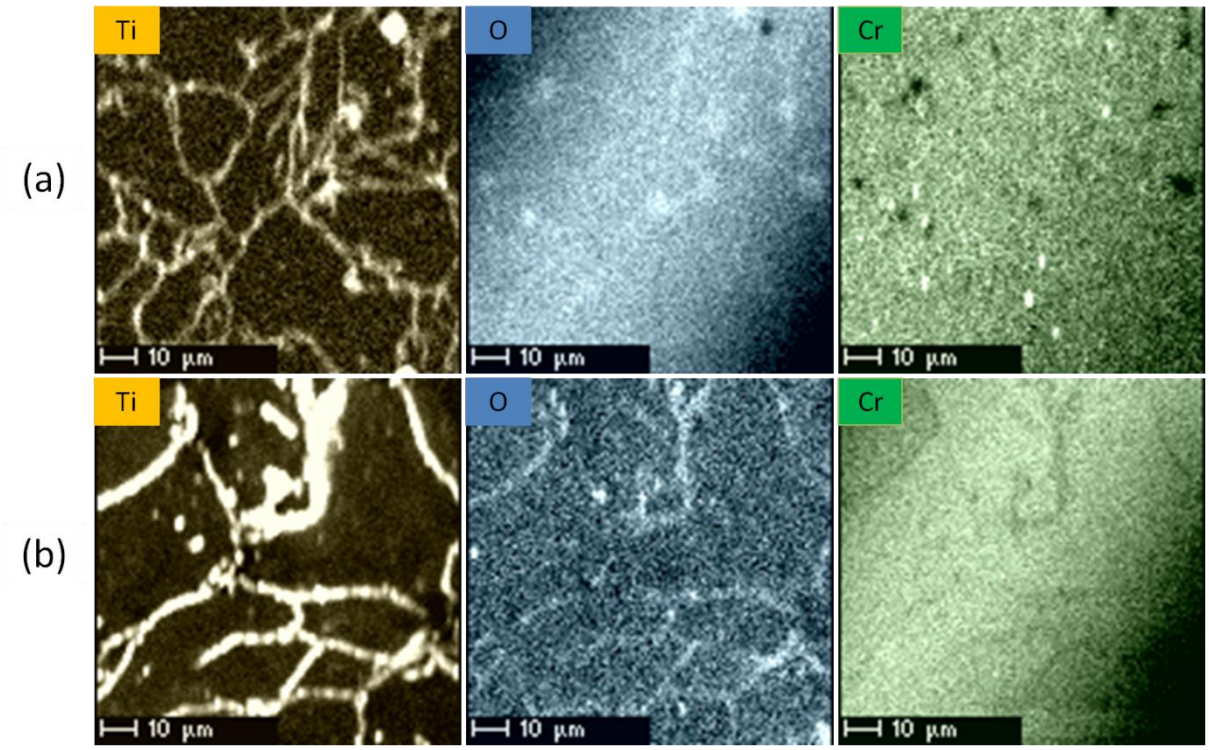

Figure V.1: Electron microprobe elemental maps of consolidated samples (a) K10 (1h@850°C) (b) –HIP-INSA (3h@1100°C)

On consolidated samples, titanium enriched areas are also observed at the surface of the particles, or rather at the Prior Particle Boundaries (PPB). Moreover, oxygen rich areas show a good correlation with the titanium rich areas (cf. Figure V.1).

It has been observed that Yttrium precipitates with a high content of titanium are finer than other yttrium precipitates (cf. §I.1.2.2). Therefore the size of the precipitates is expected to be heterogeneous within the consolidated material due to the chemical heterogeneity.

1.2. Microstructure

1.2.1. Intermediate consolidation temperature

SEM images of the 1h@850°C consolidated sample show a very fine and homogeneous microstructure (cf. Figure V.2). In Figure V.2, the important residual porosities indicate that the consolidation is not complete.

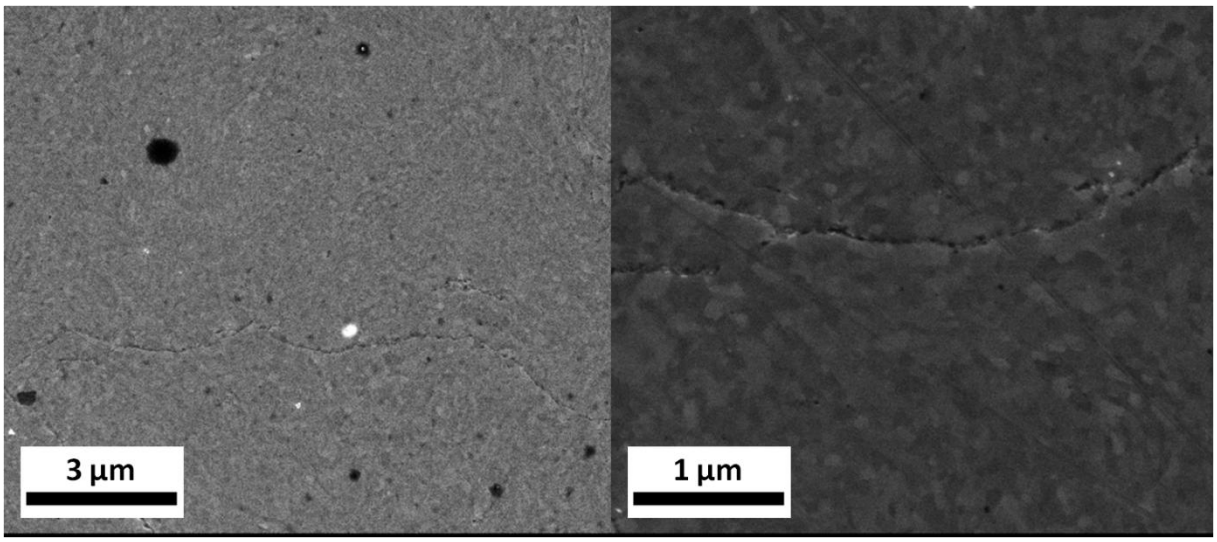

Figure V.2: SEM images of the K10 sample (HIP 1h@850°C)

Due to both the small grain size and the high misorientation level of the microstructure, the internal grain structure can be studied only by ACOM-TEM.

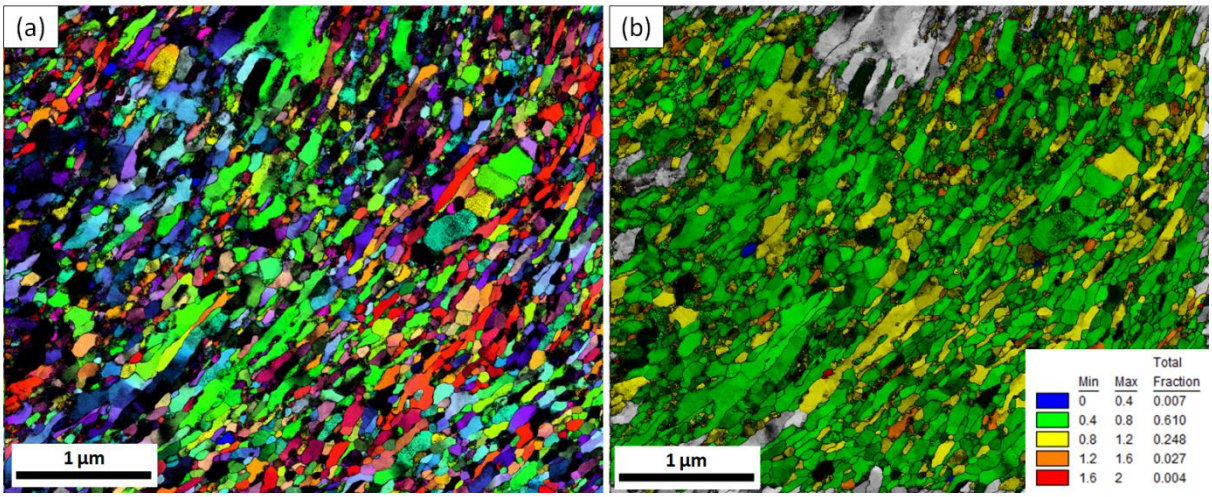

Figure V.3: ACOM-TEM study of the K10 sample (a) orientation map (b) GAM map

The mean grain area of the 1h@850°C consolidated sample is 10 000 nm² (0.01 µm²) and the mean grain aspect ratio is 2.7, with both very anisotropic (aspect ratio >20) and large isotropic grains (cf. Figure V.3a). This microstructure is close to the one observed in the as-milled powder (cf. III§1). To compare with the as-milled powder and the annealed powder particles, the mean grain area was 0.01 µm² for as milled powder and 0.1 µm² for the 20@850°C annealed powder, the mean grain aspect ratio was 5 for the as-milled powder and 1,4 for the 20min@850°C annealed powder.

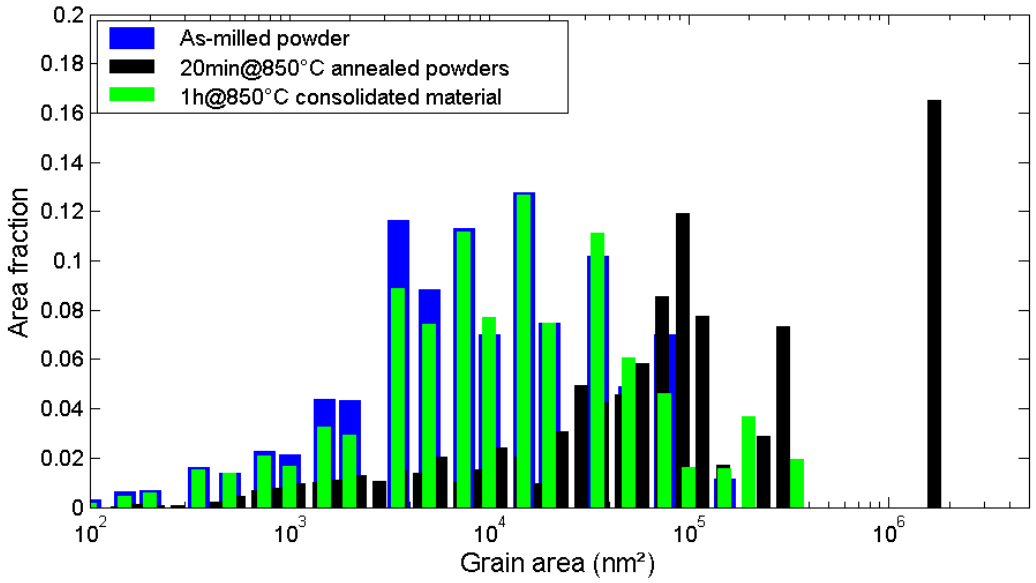

Figure V.4: Grain area distribution comparison between the HIP sample, the 20min@850°C annealed powder particles and the as-milled powder

The comparison of the grain area distribution in Figure V.4, shows that the HIP consolidation at 850°C does not substantially modify the microstructure produced by ball-milling.

According to Figure V.3a and b, the microstructure is very heterogeneous: some small isotropic grains can be highly distorted while others exhibit very low distortion. These low distorted small isotropic grains can be interpreted as recrystallization nuclei (cf. blue grains on the GAM map in Figure V.3b). Large isotropic grains are also observed. Since the microstructure of the ODS steels consolidated at higher temperature shows a pronounced bimodal distribution with a large component of coarse grains [1,2], these few large grains correspond most probably to early stages of abnormal grain growth. These large grains have a high distortion level which seems to be in disagreement with classical recrystallization theory [3]. Here, this high distortion value can be due to the precipitation effect presented in III.§2.2.2.2. The high distortion can also be partially attributed to the deformation induced by the compression of the material if abnormal grain growth occurs before the deformation step is completed.

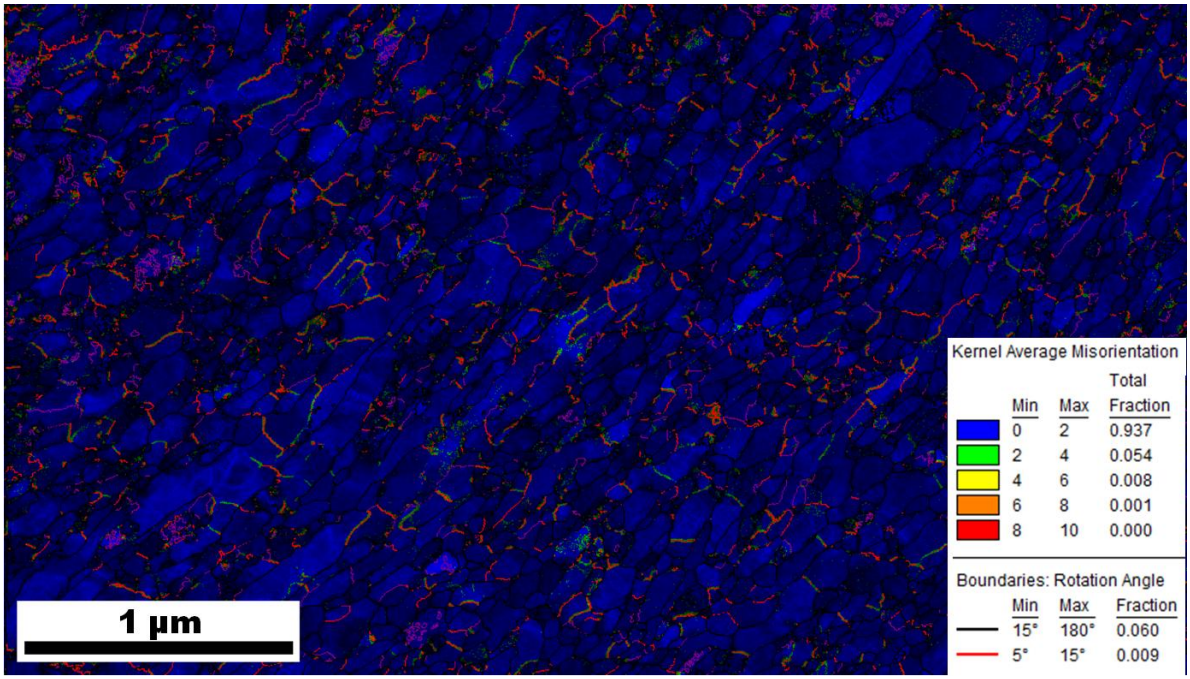

Figure V.5: Kernel average misorientation map and boundaries angle rotation in the K10 (1h@850°C) sample

Furthermore, the misorientation map displaying the high angle sub boundaries (5-15°) (cf. Figure V.5) reveals an important substructure within the grains with a high number of sub-boundaries. These 5° to 15°sub-boundaries are mainly surrounded by KAM values from 2 to 4°, (in green in the Figure V.5) forming thick sub-boundaries. Therefore the sub-boundaries structure is still very important in the material.

These overall results indicate that during consolidation only partial recovery and partial recrystallization occur. This strongly differs from the evolution observed for equivalent thermal treatments on annealed powder particles.

Two main factors can be put forward to account for these differences. Firstly, the Ti content is higher on the K10 sample, which, as demonstrated in chapter III§3 can significantly contribute to the impediment of the recrystallization and the recovery of the microstructure. Secondly, the deformation induced during the processing of the material will impose strain primarily on the recrystallized or the less deformed grains. Therefore, the driving pressure resulting from the dislocation density difference between neighbouring grains tends to decrease with increasing deformation.

2. Classical consolidation temperature: effect of the extrusion process

The classical consolidation processes for ferritic ODS steels are achieved at 1100°C. This temperature allows an easier mechanical processing and the completion of the consolidation process.

2.1. Hot Isostatic Pressure (HIP) consolidation

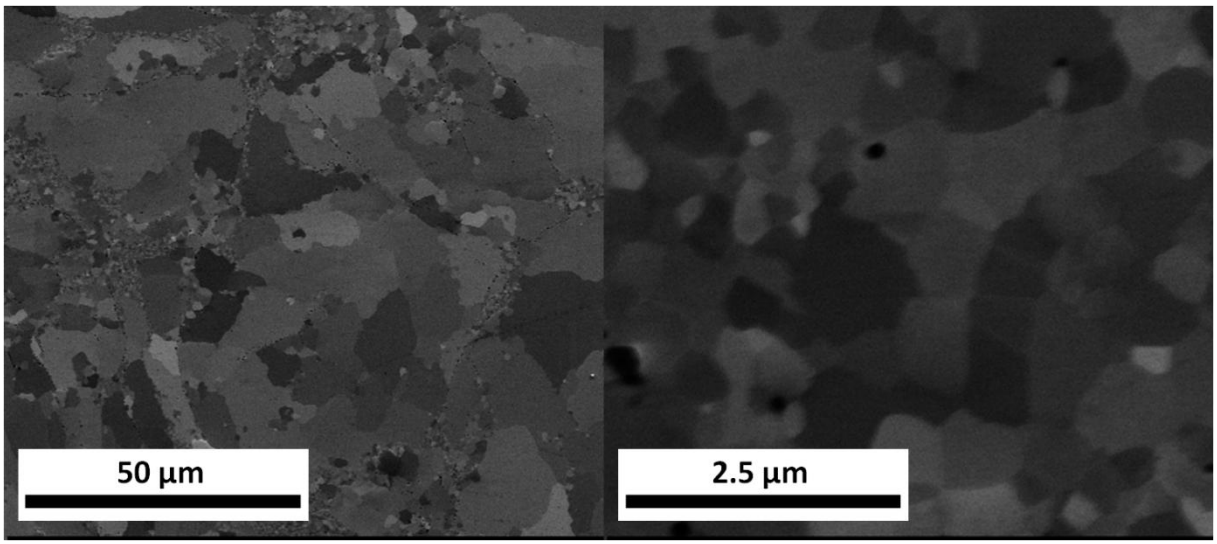

Figure V.6: SEM images of the INSA-HIP sample (3h@1100°C) (a) global microstructure showing a grain bimodal distribution (b) high magnification image recorded on an Ultra Fine Grains (UFGs) area

Figure V.6 and Figure V.7 show the microstructure of the 3h@1100°C consolidated sample (HIP). On both images a large number of coarse grains is observed (~20 µm). Nevertheless, nanosized grains (<500 nm) are also seen in large proportions.

It is worth noticing that this bimodal distribution of UFGs and coarse grains strongly reminds the one observed on annealed powders (cf. III§2.4.3). Furthermore, the respective sizes and ratio of UFGs / coarse grains seem to be very similar as well. Therefore, the effect of the deformation during the consolidation process seems to be limited.

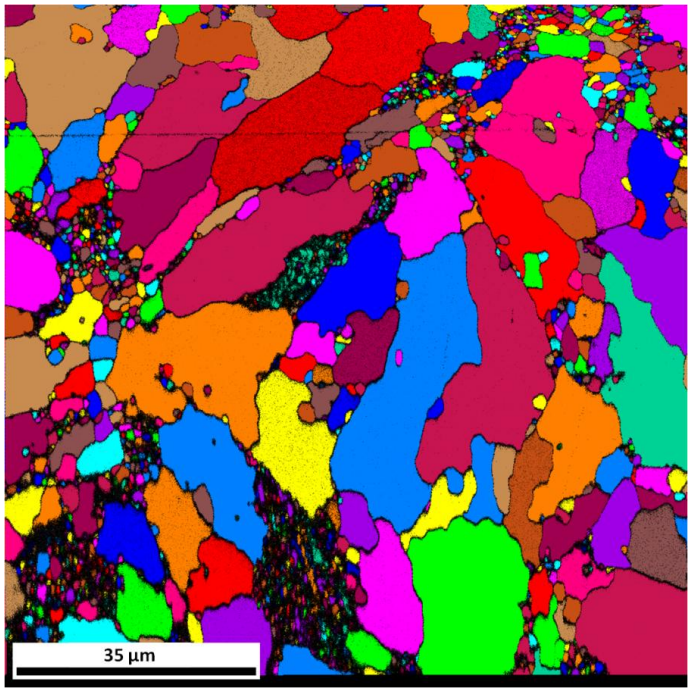

Figure V.7: EBSD orientation map of the HIP-INSA sample (consolidated @ 1100°C for 3h)

Figure V.8a shows the map of the boundary rotation angles for the 1100°C HIPed

microstructure. It can be observed that the number of low and medium angle boundaries (2-15°) within the coarse grains is very low. On the contrary, in the UFGs areas, low angle boundaries (2-5°) are numerous. On the KAM map in Figure V.8b, the global level of misorientation is very low. Indeed, within the coarse grains almost no misorientation is observed. Nevertheless, an important misorientation is still observed in the UFGs.
According to those observations it can be concluded that the recrystallization is complete in the coarse grains while it is still incomplete in the UFGs.

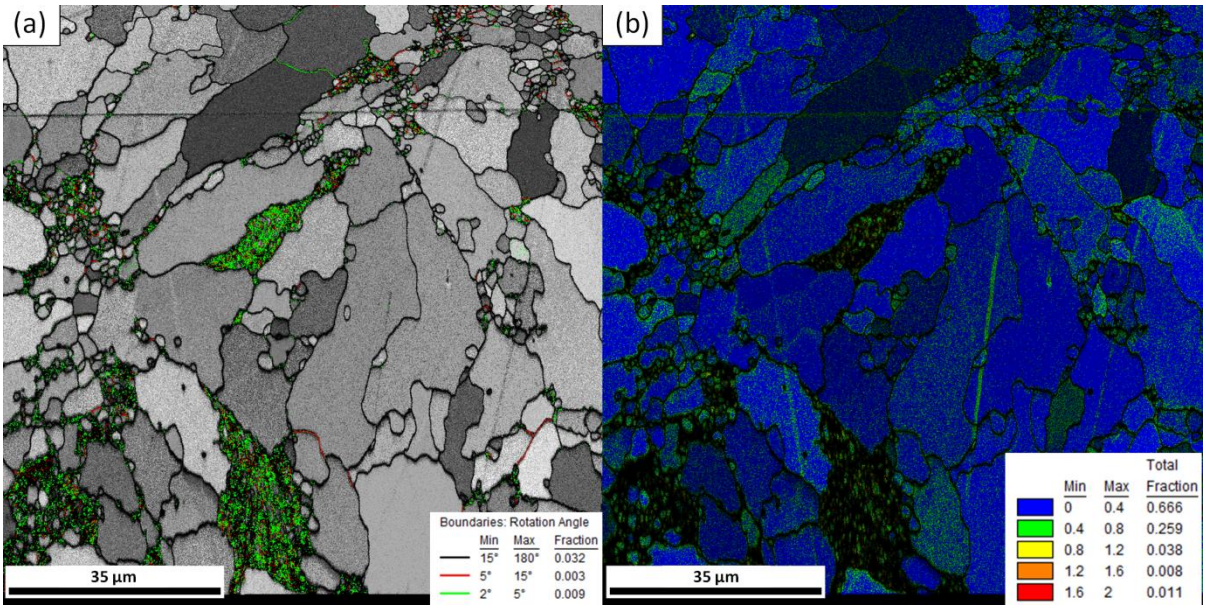

Figure V.8: EBSD study of the 1100°C consolidated sample (a) Grain boundary rotation angle (b) KAM map

2.2. Consolidation by extrusion

The extrusion process is essential to achieve the final form required for SFR cladding tubes. The microstructure of the 1100°C extruded sample J27 is presented in the following section.

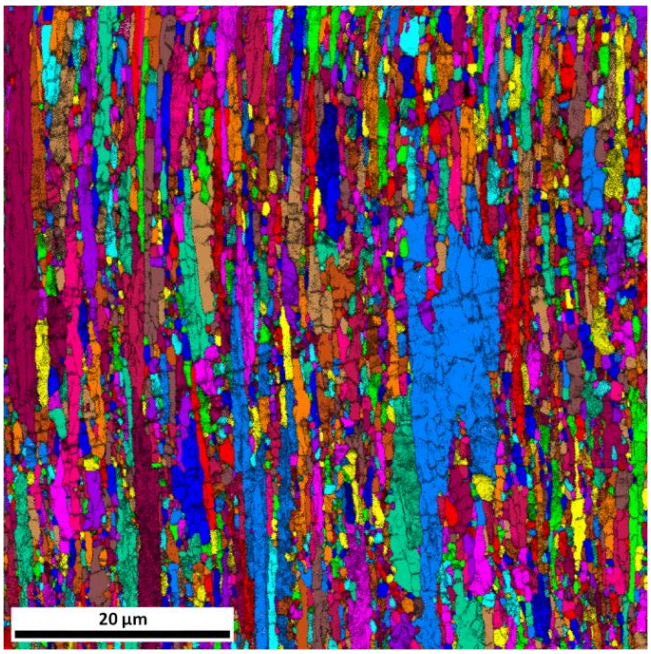

Figure V.9: EBSD orientation of the 1100°C extruded sample J27

Figure V.9 shows a highly anisotropic and heterogeneous microstructure. For the same length, the width of these elongated grains varies from 0.5 to 15 µm. On Figure V.10a a high number of both low (2-5°) and medium (5-15°) angle boundaries are observed. This high concentration of sub-boundaries is probably linked to dynamic recrystallization.

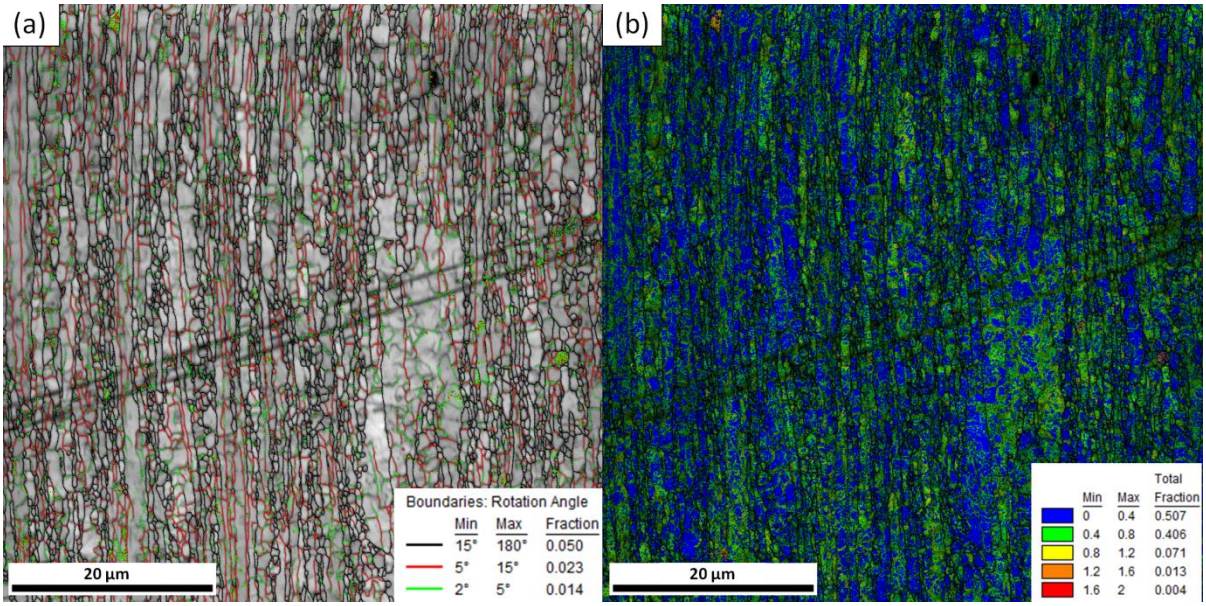

Figure V.10: EBSD study of the 1100°C extruded sample (a) Grain boundary rotation angle (b) KAM map

Figure V.10b shows that the deformation is homogeneously distributed within the material, contrarily to what is observed on the consolidated sample. No correlation is found between the size of the grains and their local misorientation.

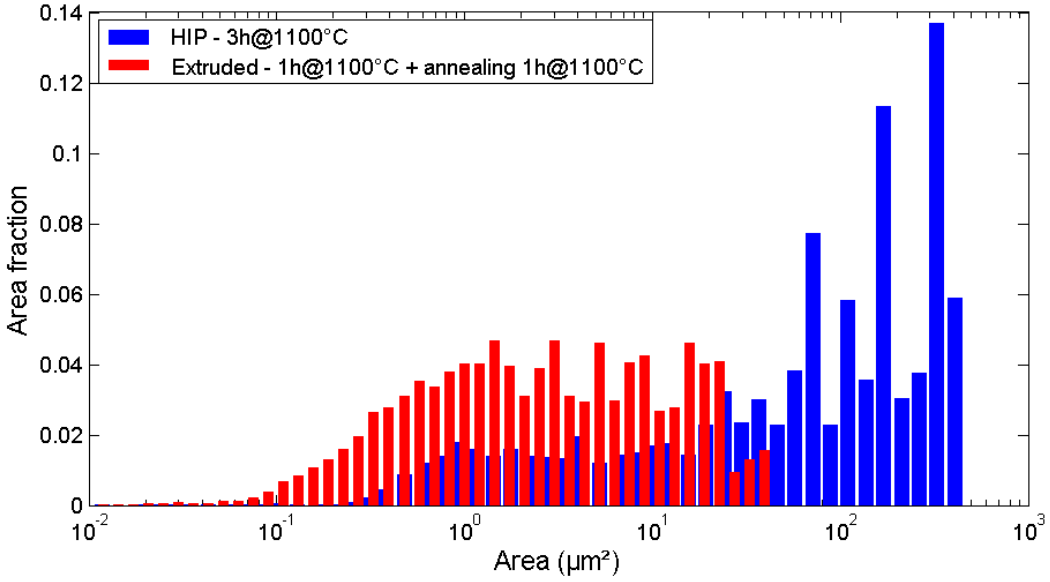

Figure V.11: Grain area distribution comparison between the consolidated and the extruded samples @1100°C

Figure V.11 shows that the grain size distribution of the extruded sample is reduced compared to the consolidated one. Particularly, large grains are no longer present in the microstructure. This can be due to the fact that during the extrusion, deformation is introduced in the material while the high processing temperature allows its reorganization into grain and subgrain boundaries. Such evolution corresponds to the occurrence of a

dynamic recrystallization process during the extrusion of the material.

2.3. Precipitation

To investigate the precipitation states SAXS experiments have been carried out on the three bulk samples (HIP 1h@850°C, HIP 3h@1100h and extruded 1h@1100°C and further annealed 1h@1050°C) (cf. Figure V.12).

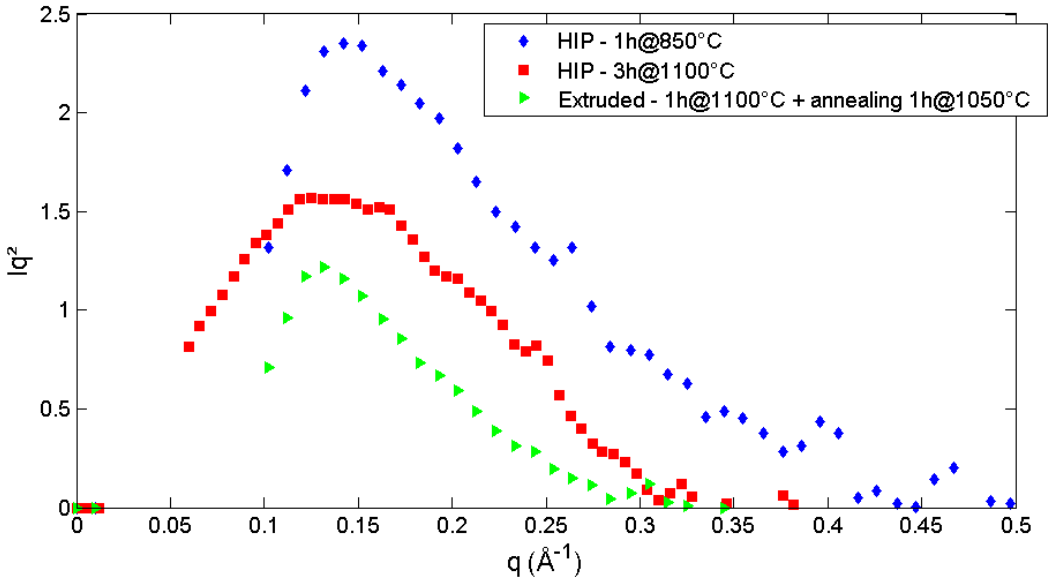

Figure V.12: SAXS intensity signal, precipitation state comparison between consolidated samples. Results are obtained from a laboratory source (Mo, E = 5.98keV)

The first important point obtained from the SAXS data analysis summarized in Table V.1 is that the precipitate mean radius increases with increasing temperature used for HIP processing. Also, the mean radius increases during the extrusion and further softening.

	R_g (Å)	Q_0
HIP 850°C - K10	12.19	$3.98.10^{-1}$
HIP-1100°C - INSA	12.64	$2.61.10^{-1}$
Extruded-1100°C J27	13.12	$1.31.10^{-1}$

Table V.1: Mean parameters of the precipitate distributions of the bulk materials studied

Furthermore, if we assume the precipitate composition and structure are stable during the annealing, the fact that the invariant Q_0 decreases at each advancing step indicates that the volume fraction decreases accordingly (cf. Table V.1). Particularly, the invariant Q_0 is very low for the extruded sample. This can partially be due to the fact that larger precipitates (R >35 Å) are not taken into account by the SAXS study.

These results are similar to what is observed for the precipitate evolution on the annealed powders, that is to say an increasing mean radius and a decreasing volume fraction with an increasing temperature.

In literature, it has been shown that increasing the consolidation temperature leads to an increase in precipitate mean radius and a decrease in precipitate volume fraction [4,5]. Also, Miao et al. [6] show that after extrusion, a further softening at 900°C leads to an

increase in volume fraction and precipitate number density. In [6], this evolution occurs while no grain size evolution is observed. On the contrary, in our case, the decrease of the precipitate volume fraction was observed in a state characterized by major grain size evolution and grain boundary migration.

Therefore, since these observations suggest a possible effect of that grain boundary migration on precipitate population evolution, specific interest has been given to the interaction between precipitates and grain boundaries. It is worth mentioning that the direct impact of extrusion on the precipitate evolution is seldom studied on the ODS ferritic steels.

3. Precipitates and boundaries interaction in ferritic ODS steels

Studying the interaction between boundaries and precipitates during extrusion was motivated by the observations reported above as well as the earlier ones carried out at the beginning of the thesis on the J27 sample (i.e. a 1100°C extruded and annealed 1h@1050°C).

3.1. Preliminary observations performed on a 14Cr ODS extruded alloy (J27):

As illustrated by Figure V.13, a remarkable feature noticed on the extruded material is the presence of coherent precipitation in every place even though grain boundaries have migrated during extrusion (cf. V§2.2).

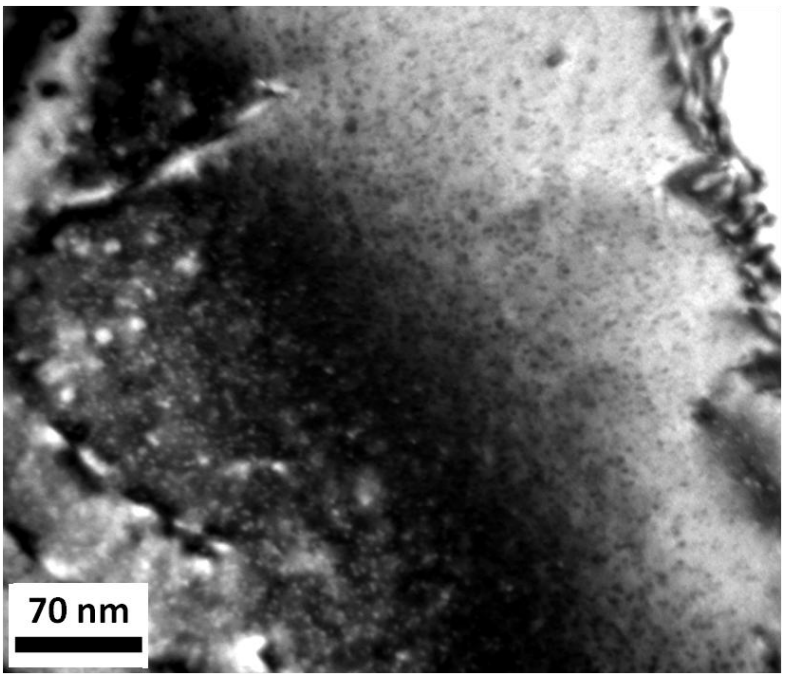

Figure V.13: TEM image of the J27 sample. Black and white dots arise from a structure factor contrast which is typically seen in the case coherent precipitates imaged in 2 beam conditions [7].

TEM investigation on extruded ferritic ODS steels shows a high density of nanosized coherent precipitates (cf. Figure V.13). The precipitates display a uniform black or white

contrast. This specific uniform contrast produced by nanoprecipitates arises from the difference between the structure factors of the precipitates and the matrix. In 2-beam conditions, this contrast is reversed from black to white depending on the thickness fringes as shown by Ashby and Brown in 1963 [7]. This so-called structure factor contrast can only be observed in the case of coherent precipitates.
Figure V.14, (a) and (b) are images from the same area containing several grain boundaries. On both sides of the grain boundaries, precipitates revealed by the structure factor contrast can be observed. The diffraction patterns recorded on each grain attest of the high misorientation between the grains. Indeed the coherency of the small nanosized precipitates (2-5 nm) in extruded ODS steel has already been noticed by several authors [8–10].

As extrusion must involve the migration of the grain boundaries, the observation of such coherent precipitates suggests a particular relation between precipitation and boundary migration since the maximal precipitation density is observed between 800°C and 900°C (cf. III§2.2.2.4, V§1.3 or even in [4–6]) while extrusion occurs at 1100°C.

Generally speaking, if a grain grows after precipitate nucleation, when the grain boundary passes the precipitates, precipitates should lose their coherency since they necessarily end up in another matrix orientation. However, nanosized precipitates are observed to be coherent despite the modification of the surrounding matrix orientation during the migration of the grain boundaries. In order to study better this particular interaction between precipitates and grain boundary during extrusion, an interrupted extrusion sample was prepared to access the microstructure at different steps of the process.

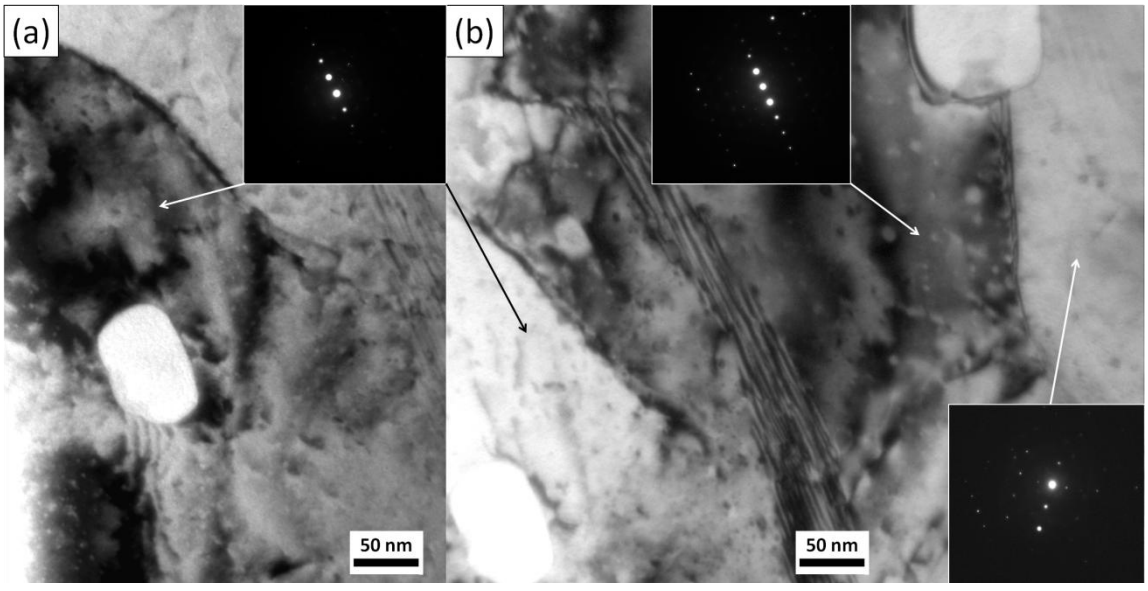

Figure V.14: TEM images of the same region at different tilt angles in an extruded and softened 1h @ 1050°C ferritic ODS steel (J27). In every regions of the images, dots are visible. They arise from a structure factor contrast which is typically seen in the case of coherent precipitates [7]. Diffraction patterns account for the different grain orientations.

3.2. Microstructure of the interrupted extrusion sample

As described in chapter II§1.4, the extrusion of a ferritic ODS steel has been interrupted, then TEM samples are taken out from three different areas (consolidated, extrusion cone, extruded) as sketched by the insert in Figure V.15 to 19. In this section, a TEM study of these samples is presented.

3.2.1. Consolidated area

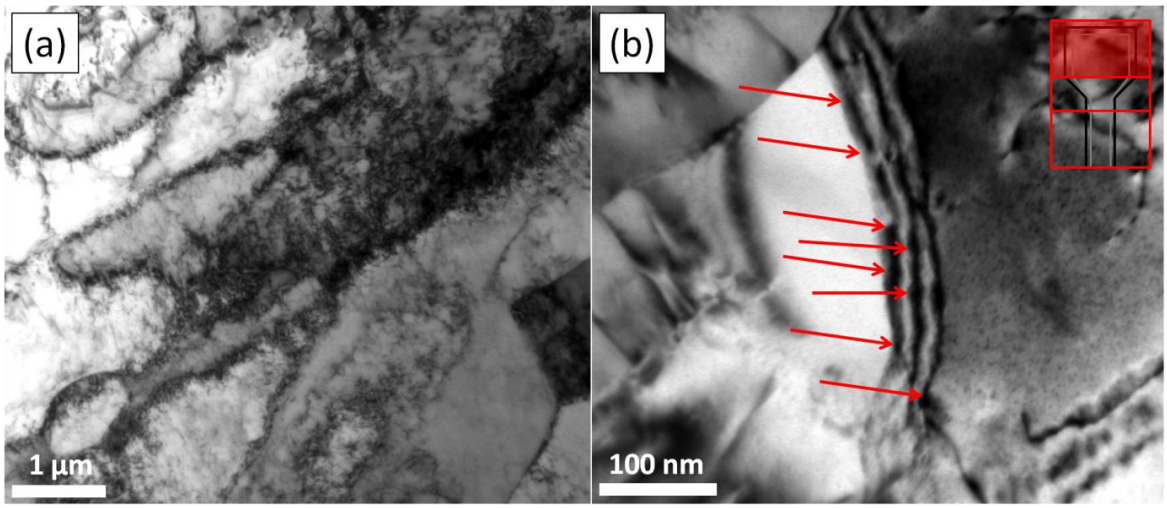

Figure V.15: TEM image of the material before the extrusion. (a) notes the high dislocation density and dislocation cell formation, (b) coherent nanosized precipitates and slightly larger precipitates (pointed by red arrows) on the grain boundary.

The first sample studied is the upper part of the material that can be assimilated to a consolidated sample. Despite the high temperature of the process (i.e. 1100°C), a large amount of dislocations is observed on Figure V.15a, dislocation cells are even visible. Fine coherent precipitates are found within the grains while larger ones are observed on the grain boundaries (cf. Figure V.15b). In such microstructure, the energy stored by dislocations provides an important driving force for grain boundary migration. In the same time, the very dense precipitation will highly impede any grain migration.

3.2.2. Extrusion cone area

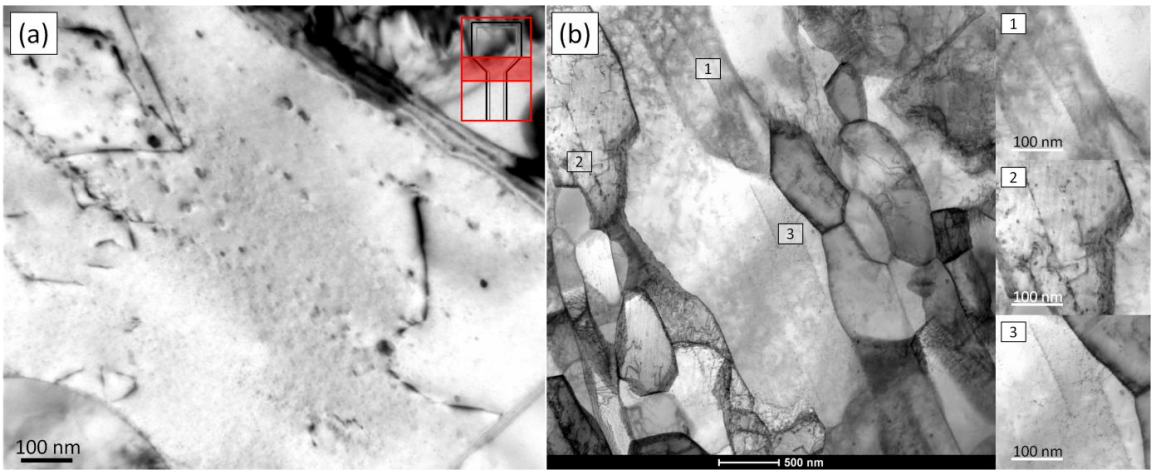

Figure V.16: Images of the in-extrusion area. Precipitate alignments and precipitate free zones are visible all over the images. Aligned precipitates are larger than the average precipitate population. (a) TEM, (b) STEM.

On the sample taken from the extrusion cone area, numerous precipitate alignments of several hundreds of nanometers are visible (Figure V.16) especially on the largest grains. These alignments are parallel to the grain boundaries and are made of medium sized precipitates (10-50nm). Along with those alignments, we can observe precipitate free zones (PFZs) that have a thickness of about 100 nm (cf. Figure V.16a). Figure V.16b (1), (2) and (3) show different alignment features. From those pictures we cannot determine if the depleted zones are ahead or behind the grain migration.

3.2.3. Extruded area

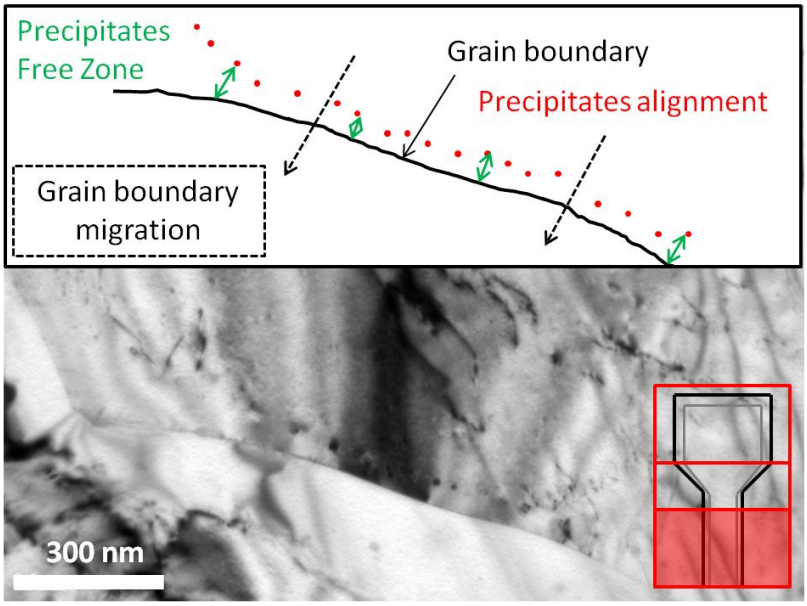

Figure V.17: TEM image from the extruded area of the ferritic ODS steel. For clarity, a sketch of precipitate alignment and Precipitate Free Zone (PFZ) is also presented

On the completely extruded area, Precipitate Free Zones (PFZ) and precipitate alignments are observed (cf. Figure V.17). Here, the PFZ is observed between the grain boundary and the precipitate alignments.

The pinning effect of coarse precipitates is low compared to the one produced by the nanoprecipitates, the PFZ should therefore be formed after the grain boundary during migration as sketched in Figure V.17.

The main phases usually precipitating in ferritic ODS steel are yttrium-titanium oxides. In order to confirm the presence of yttrium precipitates and also to examine the effective presence of a PFZ, a chemical study of the samples by APT and TEM-EDX was performed.

3.3. Chemical composition of precipitates

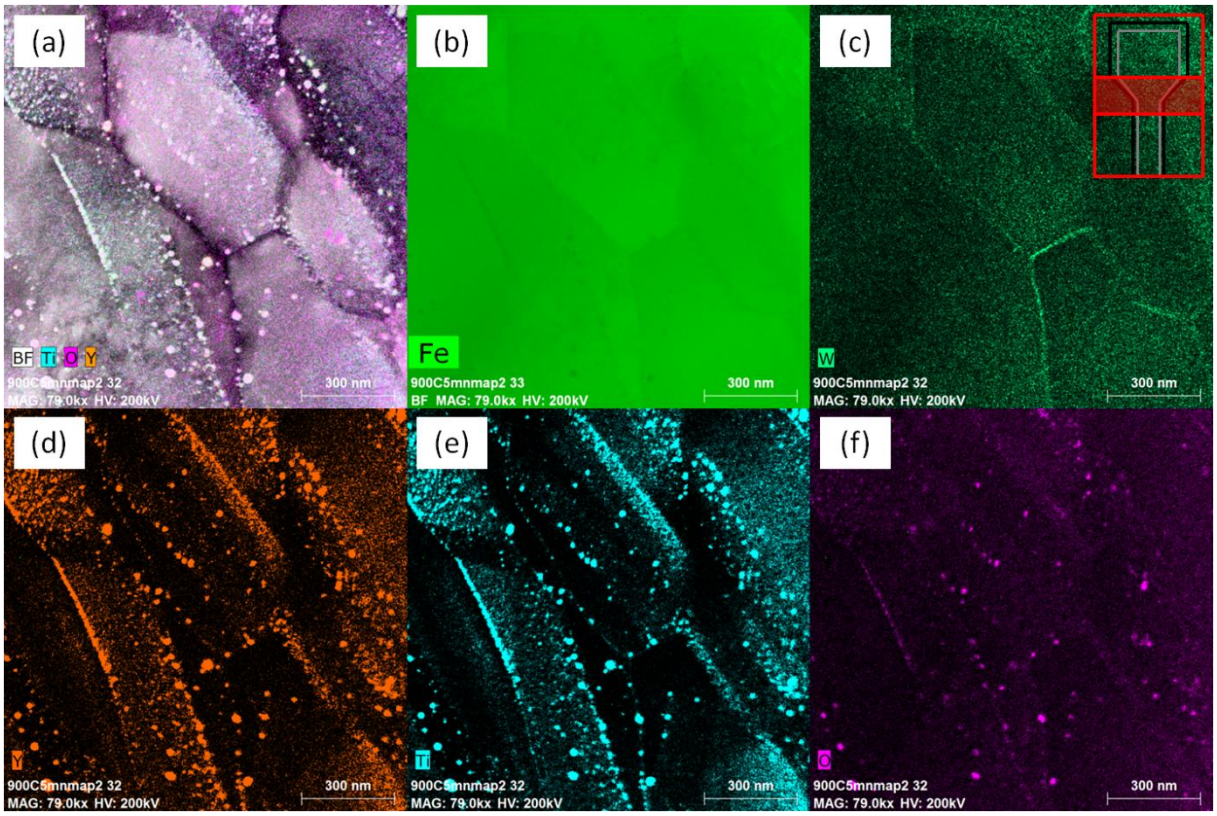

Figure V.18: EDX maps performed around the area 3 of the Figure V.16b. Alignments of precipitates and the PFZs are observable. Y, Ti and O locations correlate with each other and are heterogeneous. (a) BF STEM image+Y+O+Ti chemical maps (b) Fe (c) W (d) Y (e) Ti (f) O

EDX chemical maps displayed in Figure V.18 show that the distribution of the alloying elements is highly heterogeneous within the material. This is a confirmation of the previous observations for both precipitates alignments and depleted zones. The correlation between Y, Ti and O elements respectively evidenced by Figure V.18d, e, and f, confirms that precipitates can be described as $Y_xTi_yO_z$. Precipitate free zones are observed both along grain boundaries and in the grain between precipitate alignments parallel to the grain boundaries. The density of precipitates seems to depend on their distance from grain boundaries and precipitate alignments. Moreover it is interesting to note that even if some large precipitates (~20-30nm) are observed on grain boundaries, precipitate alignments are not located on grain boundaries.

Therefore, in the likely hypothesis that large precipitates are formed on grain boundaries, these observations are consistent with grain boundary migration and precipitate alignments left behind.

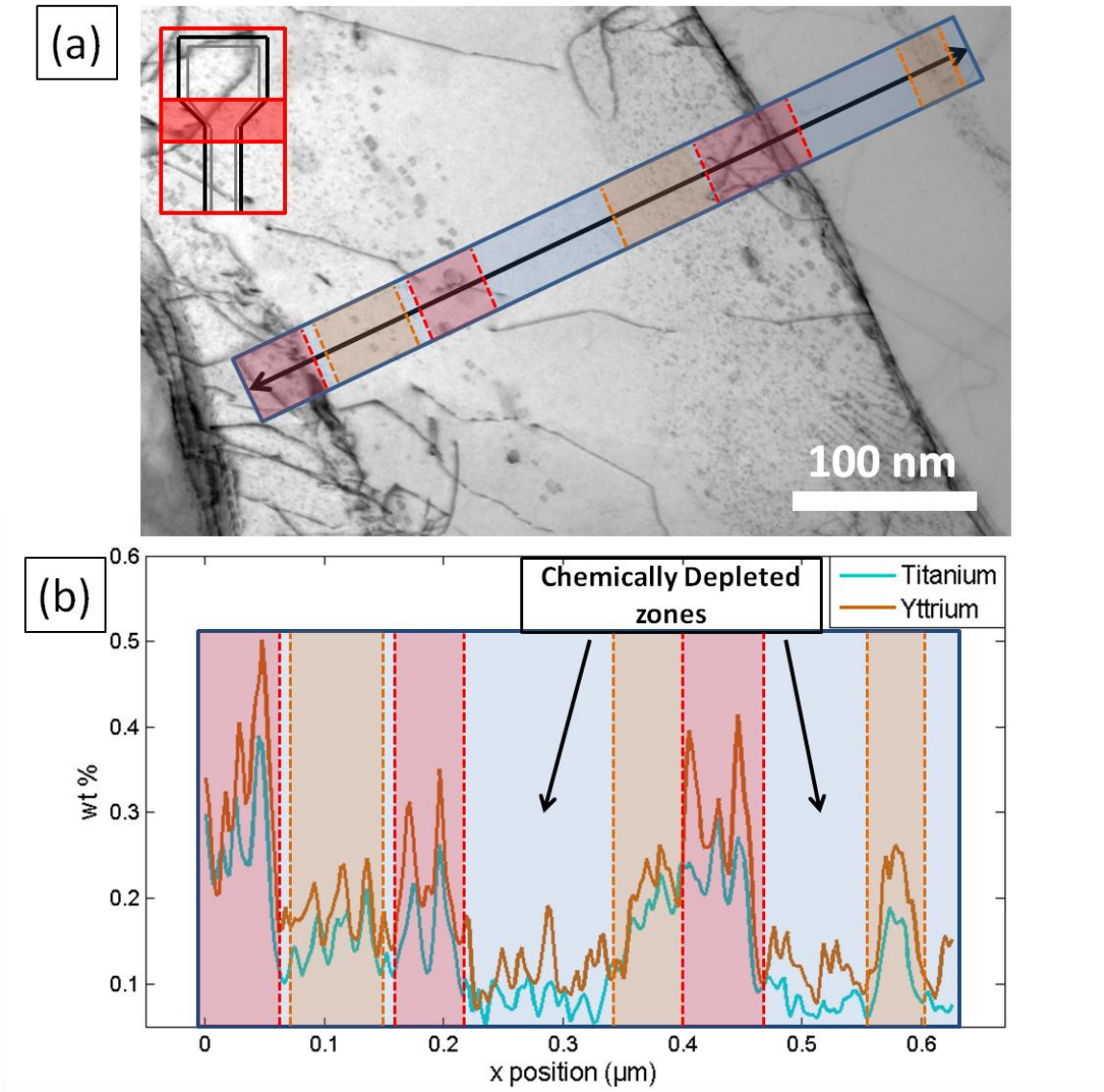

Figure V.19: (a) STEM image of the in-extrusion sample (b) Y and Ti elements concentration profile corresponding to the black arrow on (a), coloured areas correspond respectively to: blue areas - depleted zones, orange areas - nanosized precipitates, red areas - grain boundaries and large precipitate alignments.

Figure V.19 shows another area presenting both precipitates alignments and PFZs. On this area a concentration profile has been taken (cf. Figure V.19b) that confirms the correlation between titanium and Yttrium content. The precipitate depleted zones have the lowest yttrium and titanium content, ranging from 0.05 to 0.1wt%. In areas where nanoprecipitates are observed Y and Ti content is in the 0.12 to 0.22wt% range; a concentration higher than 0.25wt% is obtained for areas containing coarse precipitates.

According to the TEM observations of the extruded sample, the precipitate microstructure can be described as a bimodal distribution with small nanosized coherent precipitates and larger ones (10-40 nm) forming alignments showing PFZ in their vicinity.

3.4. Effect of the softening treatment

The extruded sample was further annealed for 1h@1050°C and is referred to as “BR1 F1 R1” in the following. This softening treatment is supposed to ease the later cold rolling of

the tube.

Tips for Atom Probe Tomography (APT) have been cut in order to specifically examine the distribution of precipitates with respect to grain boundaries.

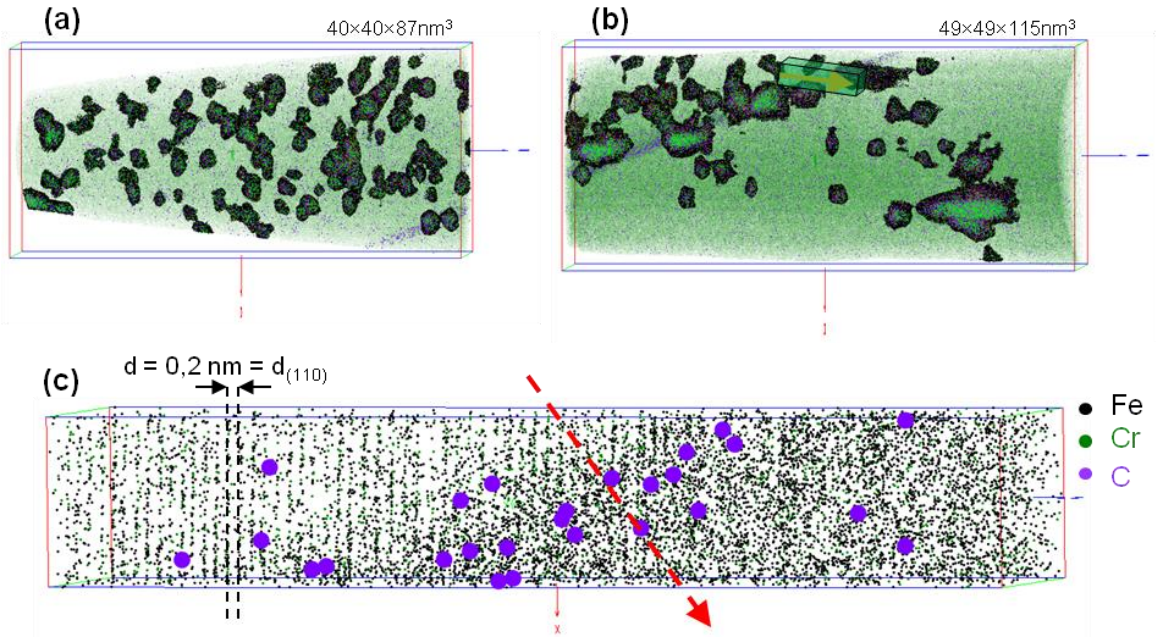

Figure V.20: APT volume reconstruction of the extruded sample after 1h@1050°C annealing. (a) and (b) are the two parts of the same volume. Orange arrow in the green rectangle is associated with the (c) volume. (c) shows a different crystallography from each part of the carbon enrichment, it confirms the presence of a grain boundary. Courtesy of C. Hatzoglou, GPM Rouen

In the sample tip shown in Figure V.20a, medium sized precipitates are observed on the grain boundary. Here, a precipitate alignment is observed at a grain boundary separating two areas very different in terms of precipitate density ($3,0 \pm 0,9.10^{23}m^{-3}$ / $12,0 \pm 0,2.10^{23}m^{-3}$). On the right side of the grain boundary the ATP volume is almost free from precipitation, whereas on the left side, the precipitate density is very high.

These APT results, though limited to small volumes, provide complementary information to the ones obtained by TEM. In particular, this method is appropriate to give chemical information and confirms the existence of the precipitate free zone and the heterogeneity in precipitation density across boundaries.

4. Dissolution mechanism

As previously mentioned, several experimental studies have demonstrated the coherency of the nanosized precipitation and the appearance of coarser incoherent precipitates after recrystallization and grain growth [8–10]. Indeed, such bimodal precipitation distribution is also often observed in ODS steels [2].

The main observations previously reported are the following:

- Nanosized coherent precipitates (2-5 nm) are observed in all grains

- There are coarse precipitate (10-40 nm) alignments parallel to the grain boundaries
- Some precipitate free zones are found to be parallel to the precipitate alignments and located behind migrating grain boundaries

To interpret these observations, a mechanism involving precipitate dissolution as will be presented below has been devised. The main issue is to explain the coherency of the nanosized precipitates on the entire material (cf. Figure V.13, [8,10]). There are two main possibilities: either precipitation occurs entirely after grain boundary migration, or migrating grain boundaries dissolve nanosized precipitates that eventually re-precipitate coherently later. The first possibility can be rejected since we know that precipitation occurs at moderate temperatures, i.e. between 600 to 650°C (cf. chapter III§2.1.3, [11]), while grain growth is known to occur mostly over 800°C (cf. chapter III§2.2.2.4, [12]). This leaves us with the possibility of the yttrium precipitate dissolution within the ferritic ODS steel. $Y_xTi_yO_z$ nanoprecipitates are reported to be extremely stable even at high temperatures [13,14].

Nevertheless, yttrium-oxide particles have already been reported to dissolve at grain boundaries in Ti alloys [15,16]. In [15] and [16], yttrium precipitates (Y_2O_3) dissolve in a Ti-Y-O alloy with 0.74wt% Y and 0.6wt% in oxygen. Following this dissolution hypothesis, the alignments of medium sized precipitates are due to coarsening of precipitates on grain boundaries when the solubility limit is reached and the dissolution is no longer possible. The proposed mechanism can be described as follows:

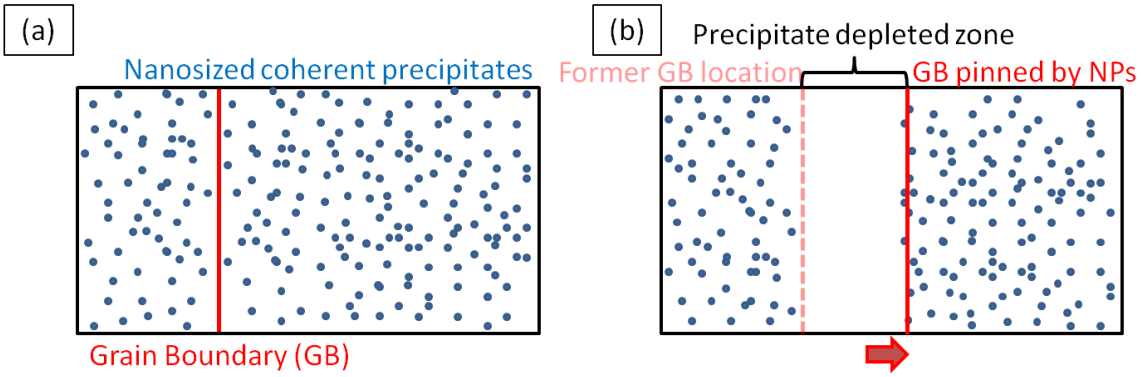

Figure V.21 : (a) Schematic diagram of the initial situation within the grain. (b) Schematic diagram of a grain boundary pinned by nanoprecipitates.

Figure V.21 presents the simplified initial situation: high density precipitation and a grain boundary. If the grain boundary is to migrate, it needs a driving force. On Figure V.16 and Figure V.17, migrating grains are shown with a flat interface and migrating perpendicularly to the center of the grain. In such a case, boundary surface pressure tends to be negligible. Therefore the driving pressure on the Grain Boundary (GB) relies almost entirely on the dislocation stored energy [3]. Nevertheless, for the sake of clarity, dislocations are not represented here.

As the GB migrates, nanoprecipitates are assumed to dissolve ahead of the grain

boundary. This assumption is supported by the results on PFZ formation widely studied in the case of Nickel superalloys or Al alloys [17,18]. The GB is generally admitted to have a higher solubility than the alloying elements. In the present case, the solubility of Y in Fe_α matrix is supposed to be of only 0,05% at 1000°C [19], the atomic radius of Y is more than 45% larger than the one of Fe. Due to this important size effect, the solubility of Y at grain boundaries is expected to be enhanced at GB. This will attract Y atoms at the GB and create a Y depleted zone just ahead of the grain boundary. Dissolution of the precipitates will occur in this depleted region due to the modification of the local composition by the moving GB (cf. Figure V.21b). In classical dissolution theories, the resulting solute concentration profile is asymmetrical when a grain boundary is moving [20,21].

As the grain boundary migrates, its concentration in solute atoms increases until it reaches the limit of solubility. At this point precipitates do not dissolve any more. When the GB encounters new precipitates, it can drag them, but the Zener force increases and the GB will soon find itself stopped by the pinning effect (cf. Figure V.22a).

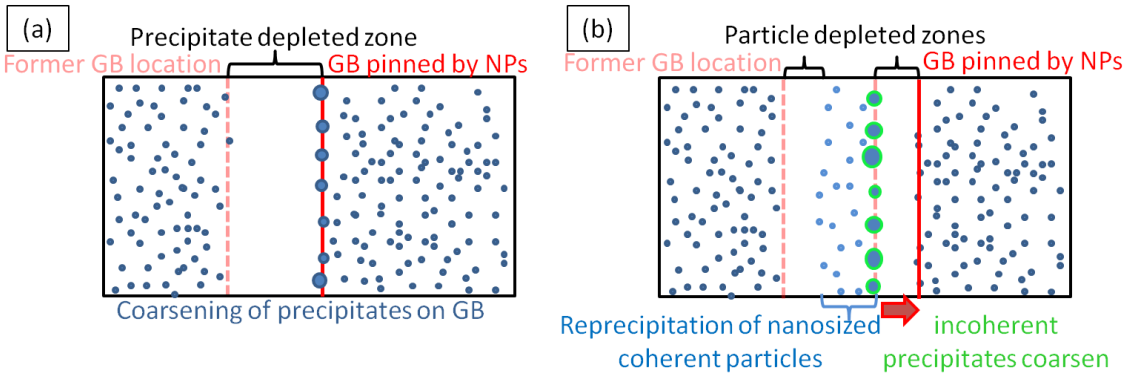

Figure V.22 : (a) Schematic diagram of the coarsening of the precipitates on the grain boundary. (b) Schematic diagram dissolution process – 2nd step.

Precipitates on grain boundary undergo an accelerated coarsening due to the enhanced diffusivity at GB (cf. Figure V.22). The coarsening is rather due to Ostwald ripening governed by the interface diffusion than by the bulk diffusion. Indeed, during this step, concentration in Yttrium is no longer asymmetrical and grain boundary vicinity is no longer depleted in solute. Therefore, there is no reason for the solute atoms to diffuse to the grain boundaries.

As the precipitates coarsen, the grain boundary moves out from the pinned position because of the decrease of the Zener force. It will dissolve and drag once again other small precipitates before it is stopped by pinning effect. Solubility limit decreases when the boundary is moving [3]. As the GB moves, it releases oversaturated solute atoms in every directions. This leads to the reprecipitation of new coherent nanoparticles on both sides of the boundary. Half of them will be rapidly dissolved by the migrating grain boundary or directly absorbed depending on the reprecipitation kinetics compared to the grain boundary migration velocity. Medium sized precipitates, being now incoherent with

the matrix, can lead to a further coarsening as explained in [8]. This mechanism can be repeated several times. However, the driving force will gradually decrease (following the dislocation density decrease) until reaching a value for which grain boundary migration becomes impossible.

The mechanism involving precipitate dissolution is consistent with the TEM observations on the extruded material as well as the partially extruded states. It is quite similar with the one proposed by Bouchaud et al. [16] to account for the microstructure of the heat treated cold rolled Ti alloys containing nanoprecipitates (Naka et al. [15]). This dissolution mechanism is also consistent with the evolution of the volume fraction with heat treatment and extrusion reported above (V§3.2).

5. Synthesis and prospects

A mechanism based on the dissolution and the alignments of nanosized $Y_xTi_yO_z$ particles induced by boundary migration has been proposed. It achieves to explain for the following experimental observations: the coherency of nanoparticles on both sides of the migrating grain boundary, the asymmetrical precipitate free zones and the presence of medium size precipitate alignments.

This mechanism can be a major contribution in the understanding of the mechanical behaviour of the ODS ferritic steels. Indeed, it could account for the intergranular ductile behaviour of the ODS ferritic steels reported by many authors.

To study this mechanism further, a modelling of the dissolution phenomenon will be proposed. For example, the phase field simulation model developed by M. Militzer et al. [22,23] can be used as an efficient starting basis for modelling such precipitate / grain boundary interaction.

Chapter V bibliography

[1] Unifantowicz P., Oksiuta Z., Olier P., de Carlan Y. et Baluc N. (2011) MICROSTRUCTURE AND MECHANICAL PROPERTIES OF AN ODS RAF STEEL FABRICATED BY HOT EXTRUSION OR HOT ISOSTATIC PRESSING. *Fusion Engineering and Design*, **86**, 2413‑6.

[2] Sornin D., Grosdidier T., Malaplate J., Tiba I., Bonnaillie P., Allain-Bonasso N. et Nunes D. (2013) MICROSTRUCTURAL STUDY OF AN ODS STAINLESS STEEL OBTAINED BY HOT UNI-AXIAL PRESSING. *Journal of Nuclear Materials*, **439**, 19‑24.

[3] Humphreys F.J. et Hatherly M. (2004) RECRYSTALLIZATION AND RELATED ANNEALING PHENOMENA. Elsevier.

[4] Alinger M.J., Odette G.R. et Hoelzer D.T. (2009) ON THE ROLE OF ALLOY COMPOSITION AND PROCESSING PARAMETERS IN NANOCLUSTER FORMATION AND DISPERSION STRENGTHENING IN NANOSTUCTURED FERRITIC ALLOYS. *Acta Materialia*, **57**, 392‑406.

[5] Williams C.A., Unifantowicz P., Baluc N., Smith G.D.W. et Marquis E.A. (2013) THE FORMATION AND EVOLUTION OF OXIDE PARTICLES IN OXIDE-DISPERSION-STRENGTHENED FERRITIC STEELS DURING PROCESSING. *Acta Materialia*, **61**, 2219‑35.

[6] Miao P., Odette G.R., Yamamoto T., Alinger M. et Klingensmith D. (2008) THERMAL STABILITY OF NANO-STRUCTURED FERRITIC ALLOY. *Journal of Nuclear Materials*, **377**, 59‑64.

[7] Ashby M.F. et Brown L.M. (1963) ON DIFFRACTION CONTRAST FROM INCLUSIONS. *Philosophical Magazine*, **8**, 1649‑76.

[8] Ribis J., Lescoat M.-L., Zhong S.Y., Mathon M.-H. et de Carlan Y. (2013) INFLUENCE OF THE LOW INTERFACIAL DENSITY ENERGY ON THE COARSENING RESISTIVITY OF THE NANO-OXIDE PARTICLES IN TI-ADDED ODS MATERIAL. *Journal of Nuclear Materials*, **442**, S101‑5.

[9] Ribis J. et de Carlan Y. (2012) INTERFACIAL STRAINED STRUCTURE AND ORIENTATION RELATIONSHIPS OF THE NANOSIZED OXIDE PARTICLES DEDUCED FROM ELASTICITY-DRIVEN MORPHOLOGY IN OXIDE DISPERSION STRENGTHENED MATERIALS. *Acta Materialia*, **60**, 238‑52.

[10] Hsiung L.L., Fluss M.J. et Kimura A. (2010) STRUCTURE OF OXIDE NANOPARTICLES IN FE–16CR MA/ODS FERRITIC STEEL. *Materials Letters*, **64**, 1782‑5.

[11] Hin C. et Wirth B.D. (2011) FORMATION OF OXIDE NANOCLUSTERS IN NANOSTRUCTURED FERRITIC ALLOYS DURING ANISOTHERMAL HEAT TREATMENT: A KINETIC MONTE CARLO STUDY. *Materials Science and Engineering: A*, **528**, 2056‑61.

[12] Boulnat X., Perez M., Fabregue D., Douillard T., Mathon M.-H. et de Carlan Y. (2014) MICROSTRUCTURE EVOLUTION IN NANO-REINFORCED FERRITIC STEEL PROCESSED BY MECHANICAL ALLOYING AND SPARK PLASMA SINTERING. *Metallurgical and Materials Transactions A*, 1‑13.

[13] Sakasegawa H., Legendre F., Boulanger L., Brocq M., Chaffron L., Cozzika T., Malaplate J., Henry J. et de Carlan Y. (2011) STABILITY OF NON-STOICHIOMETRIC CLUSTERS IN THE MA957 ODS FERRTIC ALLOY. *Journal of Nuclear Materials*, **417**, 229‑32.

[14] Lescoat M.-L., Ribis J., Gentils A., Kaïtasov O., de Carlan Y. et Legris A. (2012) IN SITU TEM STUDY OF THE STABILITY OF NANO-OXIDES IN ODS STEELS UNDER ION-IRRADIATION. *Journal of Nuclear Materials*, **428**, 176‑82.

[15] Naka S., Octor H., Bouchaud E. et Khan T. (1989) REPRECIPITATION OBSERVED IN Y_2O_3 DISPERSED TITANIUM DURING HEAT TREATMENT AFTER COLD ROLLING. *Scripta Metallurgica*, **23**, 501‑5.

[16] Bouchaud E., Bouchaud J.-P., Naka S., Lapasset G. et Octor H. (1992) DISSOLUTION OF PRECIPITATES BY MIGRATING GRAIN BOUNDARIES. *Acta Metallurgica et Materialia*, **40**, 3451‑8.

[17] Jha S.C., Sanders Jr T.H. et Dayananda M.A. (1987) GRAIN BOUNDARY PRECIPITATE FREE ZONES IN AL-LI ALLOYS. *Acta Metallurgica*, **35**, 473‑82.

[18] Krol T., Baither D. et Nembach E. (2004) THE FORMATION OF PRECIPITATE FREE ZONES ALONG GRAIN BOUNDARIES IN A SUPERALLOY AND THE ENSUING EFFECTS ON ITS PLASTIC DEFORMATION. *Acta Materialia*, **52**, 2095‑108.

[19] Kalokhtina O. (2012) STUDY OF THE FORMATION OF NANO-PARTICLES IN ODS AND NDS STEELS BY ATOM PROBE TOMOGRAPHY. Université de Rouen. PhD thesis.

[20] Cahn J.W. (1962) THE IMPURITY-DRAG EFFECT IN GRAIN BOUNDARY MOTION. *Acta Metallurgica*, **10**, 789‑98.

[21] Grönhagen K. et Ågren J. (2007) GRAIN-BOUNDARY SEGREGATION AND DYNAMIC SOLUTE DRAG THEORY—A PHASE-FIELD APPROACH. *Acta Materialia*, **55**, 955‑60.

[22] Militzer M. (2011) PHASE FIELD MODELING OF MICROSTRUCTURE EVOLUTION IN STEELS. *Current Opinion in Solid State and Materials Science*, **15**, 106‑15.

[23] Militzer M., Hoyt J.J., Provatas N., Rottler J., Sinclair C.W. et Zurob H.S. (2014) MULTISCALE MODELING OF PHASE TRANSFORMATIONS IN STEELS. *JOM*, **66**, 740‑6.

General Conclusion

Main results and conclusion

Oxide Dispersion Strengthened (ODS) ferritic steels are materials of particular interest for nuclear applications as fuel claddings due to their high resistance to both high temperature creep and irradiation swelling. During elaboration, Abnormal Grain Growth (AGG) occurs before tube forming and results in detrimental transverse mechanical properties. Yet, after having been investigated for decades, the causes for AGG to occur are not fully understood. The main objective of this thesis was to evaluate and understand the causes leading to AGG. In order to obtain information on the microstructural evolution at the earliest elaboration stages, ODS steel powder particles in the as milled states and after heat treatment corresponding to the processing have been investigated. This study involves both experimental characterization and numerical modelling.

Using innovative characterization, namely the ACOM-TEM method and specifically adapted analysis of *in-situ* XRD experiments, in the heat treated powder particles the successive mechanisms leading to abnormal grain growth have been identified:

- Microstructural anisotropy evidenced for the first time on as-milled powders, induces a high stability of the microstructure that does not experience any significant grain growth before 700°C.

- Recrystallisation, which leads to an isotropic microstructure is identified to occur between 750°C and 800°C. Extend of the recrystallization (% of the microstructure actually recrystallized) and grain growth rate are controlled by precipitation pinning.

- Recrystallization leads to significant dislocation stored energy heterogeneities within the material. These heterogeneities are responsible for the abnormal grain growth that occurs around 900°C.

To account for the occurrence of abnormal grain growth, a model has been developed that accurately reproduces the experimental observation on abnormal grain growth. This model built on classical assumptions (grain growth driven by the decrease in interfacial energy, dislocation density entirely and homogeneously distributed in ultrafine grains) emphasizes on specific geometrical considerations concerning the microstructure: precipitates are evenly distributed at the boundaries with larger precipitates at special boundary locations such as quadruple points.

A systematic study of the interaction of grain boundaries with precipitation is pursued on consolidated and extruded materials.

To further investigate the microstructure evolution during processing, consolidated ODS powder, partially extruded and extruded material have been considered in a second part of the thesis. This study is specifically focussed on the interaction of the grain boundaries with precipitates in the consolidated and extruded materials. Based on the following observations on consolidated samples:

- Nanosized precipitates (2-5 nm) are coherent in all grains of the extruded material
- Coarse precipitate (10-40 nm) alignments are parallel to the grain boundaries
- Precipitate free zones are parallel to the precipitate alignments and located behind migrating grain boundaries

A mechanism based on the precipitate dissolution by migration grain boundary has been proposed and accounts for those observations.

Prospects

In the prospect of designing new processing routes for the ODS steels, complementary heat treatments should be carried out. For instance, specific thermal treatments around 750-800°C, a temperature that allows for a slight grain growth while avoiding any abnormal grain growth should be explored. The goal is to obtain an isotropic microstructure that could allow the extrusion of the material (indeed due to the Hall-Petch effect, a microstructure with too small grains is very difficult to consolidate and extrude).

Concerning the understanding of the microstructure evolution, the effect of anisotropy in the case of a microstructure pinned by precipitates deserves deeper investigation. For example, the vertex method used by D.Weygand et al. [1] can be used to obtain a parametrical modelling that could account for the anisotropy effect as a function of the grain aspect ratio.

Regarding the modelling of Abnormal Grain Growth (AGG), the present model should be used to examine in more details the effect of solute content. Also the AGG model could be improved with the integration of the entire grain size distribution.

Interaction of grain boundaries and precipitates involving precipitate dissolution was proposed here based on experimental evidence. To examine in more details the validity of this mechanism, the phase field simulation model developed by M. Militzer et al. [2,3] can be used as an efficient starting basis for modelling such precipitate / grain boundary interaction.

Finally, within the frame of the CPR ODISSEE, this thesis allowed to obtain numerous experimental values that could to be used in models developped by other colleagues. Notably, quantitative information concerning precipitation and dislocation density can be of interest for the modelling of precipitation in model alloys carried out within the CPR

and also for works currently in progress at INSA Lyon in collaboration with CEA-SRMA. The knowledge of the microstructure and more specifically the heterogeneities of precipitate distribution within the grain can contribute to the understanding of the mechanical behaviour of the ODS steels which is also studied within the CPR ODISSEE.